

ELECTROCATALYST DEVELOPMENT AND MODELING OF
NONISOTHERMAL TWO-PHASE FLOW FOR PEM FUEL CELLS

A THESIS SUBMITTED TO
THE GRADUATE SCHOOL OF NATURAL AND APPLIED SCIENCES
OF
MIDDLE EAST TECHNICAL UNIVERSITY

BY

BERKER FIÇICILAR

IN PARTIAL FULFILLMENT OF THE REQUIREMENTS
FOR
THE DEGREE OF DOCTOR OF PHILOSOPHY
IN
CHEMICAL ENGINEERING

MAY 2011

Approval of the thesis:

**ELECTROCATALYST DEVELOPMENT AND MODELING OF
NONISOTHERMAL TWO-PHASE FLOW FOR PEM FUEL CELLS**

submitted by **BERKER FIÇICILAR** in partial fulfillment of the requirements for
the degree of **Doctor of Philosophy in Chemical Engineering Department,**
Middle East Technical University by,

Prof. Dr. Canan Özgen
Dean, Graduate School of **Natural and Applied Sciences**

Prof. Dr. Deniz Üner
Head of Department, **Chemical Engineering**

Prof. Dr. İnci Eroğlu
Supervisor, **Chemical Engineering Department, METU**

Examining Committee Members:

Prof. Dr. Işık Önal
Chemical Engineering, METU

Prof. Dr. İnci Eroğlu
Chemical Engineering, METU

Prof. Dr. Zeynep İlsen Önsan
Chemical Engineering, Boğaziçi University

Prof. Dr. İsmail Tosun
Chemical Engineering, METU

Prof. Dr. Nurcan Baç
Chemical Engineering, Yeditepe University

Date: _____

I hereby declare that all information in this document has been obtained and presented in accordance with academic rules and ethical conduct. I also declare that, as required by these rules and conduct, I have fully cited and referenced all material and results that are not original to this work.

Name, Last Name: BERKER FIÇICILAR

Signature :

ABSTRACT

ELECTROCATALYST DEVELOPMENT AND MODELING OF NONISOTHERMAL TWO-PHASE FLOW FOR PEM FUEL CELLS

Fiçıcılar, Berker

Ph.D., Department of Chemical Engineering

Supervisor : Prof. Dr. İnci Eroğlu

May 2011, 214 pages

A macro-homogeneous, nonisothermal, two-phase, and steady state mathematical model is developed to investigate water and thermal management in polymer electrolyte membrane (PEM) fuel cells. An original two-phase energy balance approach is used to catch the thermal transport phenomena in cases when there is a significant temperature difference between the fuel cell temperature and the reactants inlet temperatures like during cold start-up. Model considers in depth electrode kinetics for both anode and cathode reactions. External and internal mass transfer resistances on fuel cell performance are accounted by means of a thin-film and agglomerate approach.

Developed model accounts for all substantial transport phenomena including diffusion of multi-component gas mixtures in the porous media, electrochemical reactions in the catalytic regions, water and proton transport through the solid polymer electrolyte, transport of electrons within the solid matrix, heat transport in the gas and solid phases, phase change and transport of water through porous diffusion media and catalyst layers. In this study, it is truly shown how significant heat and water transport

are to overall fuel cell performance. Model predictions are validated by comparison with experimental data, involving polarization curves, saturation and temperature gradients.

For optimal electrode kinetics purposes, an alternative novel hollow core mesoporous shell (HCMS) carbon supported Pt and Pt-Pd electrocatalysts were synthesized by microwave irradiation. HCMS carbon spheres were produced by two different carbon precursors with the template replication of solid core mesoporous shell (SCMS) silica spheres. Compared to Pt/VX and ETEK[®] electrocatalysts, HCMS carbon based Pt and Pt-Pd electrocatalysts showed promising cathode and anode electrochemical performance in the fuel cell environment.

Keywords: PEMFC, Water and thermal management, Two-phase energy balance, HCMS carbon sphere, Electrocatalyst

ÖZ

PEM YAKIT PİLİ İÇİN ELEKTROKATALİZÖR GELİŞTİRİLMESİ VE İZOTERMAL OLMAYAN İKİ FAZLI AKIŞIN MODELLENMESİ

Fıçıcılar, Berker

Doktora, Kimya Mühendisliği Bölümü

Tez Yöneticisi : Prof. Dr. İnci Eroğlu

Mayıs 2011, 214 sayfa

Polimer elektrolit zarlı (PEM) yakıt pillerinde su ve ısı yönetimini araştırmak için makro-türdeş, izotermal olmayan, iki fazlı, kararlı durum matematiksel modeli geliştirilmiştir. Özgün, iki fazlı enerji denkliği yaklaşımı kullanılarak, reaktant giriş sıcaklıkları ve yakıt pili sıcaklığı arasında önemli sıcaklık değişimi olduğu soğuk çalıştırma gibi durumlardaki ısı aktarım olgularının yakalanması amaçlanmıştır. Modelde anot ve katot tepkimeleri için ayrıntılı elektrot kinetiği göz önünde bulundurulmuştur. Dış ve iç kütle aktarım dirençlerinin yakıt pili verimine etkileri ince tabaka ve topak yaklaşımı kullanılarak incelenmiştir.

Geliştirilen model, gözenekli ortamda çoklu bileşen gaz karışımlarının difüzyonu, katalitik bölgelerdeki elektrokimyasal tepkimeler, katı polimer elektrolitte su ve proton aktarımı, katı matriste elektron aktarımı, gaz ve katı fazlarda ısı aktarımı, gözenekli difüzyon bölgesi ve katalizör tabakalarında faz değişimi ve su aktarımı gibi bütün önemli aktarım olgularını içermektedir. Bu çalışmada, ısı ve su aktarımının yakıt pili verimi için ne kadar önemli olduğu açıkça gösterilmiştir. Model tahminleri, kutuplaşma

eğrileri, doyma ve sıcaklık deęiřimi sonuçlarının deneysel verilerle karřılařtırılmasıyla doęrulanmıřtır.

En uygun elektrot kinetięi verimini saęlamak için alternatif ii boř kabuęu orta gzenekli (HCMS) karbon destekli yeni Pt ve Pt-Pd elektrokatalizrler mikrodalga yntemi ile sentezlenmiřtir. HCMS karbon krecikleri iki farklı karbon kaynaęı kullanılarak ii katı kabuęu orta gzenekli (SCMS) silika kreciklerinin kalıp kopyalamasıyla retilmiřtir. Yakıt pili ortamında, HCMS karbon destekli Pt ve Pt-Pd elektrokatalizrler Pt/VX ve ETEK[®] elektrokatalizrlerle karřılařtırıldıęında umut verici katot ve anot elektrot kinetięi verimi gsterdięi bulgulanmıřtır.

Anahtar Szckler: PEM yakıt pili, Su ve ısı ynetimi, İki fazlı enerji denkliği, HCMS karbon krecik, Elektrokatalizr

To My Family,

ACKNOWLEDGMENTS

I would first like to thank the major funding sources for this study, METU ÖYP and BAP projects through grant numbers BAP-08-11-DPT2002K120510, BAP-03-04-2009-06, and TÜBİTAK project through grant number 109M221. Financial support was provided by the Commission of the European Communities, 6th Framework Program, Priority 6, Sustainable Energy Systems (019825 HYVOLUTION).

TÜBİTAK ULAKBİM, High Performance and Grid Computing Center (TR-Grid e-Infrastructure) supported some of the numerical calculations reported in this dissertation. The author gratefully acknowledges TÜBİTAK BİDEB-2214 research exchange program and the University of Kansas for making the short term research exchange possible and excellent support throughout the research.

I wish to express my gratitude to my thesis advisor Prof. Dr. İnci Eroğlu for her supervision and guidance throughout this study. I would like to thank my advisor Prof. Dr. Trung Van Nguyen at the University of Kansas. It has been my great pleasure and privilege to work with him. I would also like to thank my thesis committee members, Professors Işık Önal, Zeynep İlsen Önsan, İsmail Tosun, and Nurcan Baç, for their time in reading and evaluating this dissertation.

I thank the past and present members of Fuel Cell Research group at the Middle East Technical University, with whom I spent several years working on polymer electrolyte membrane fuel cells. Special thanks are due to Serdar Erkan, Ayşe Bayrakçeken, and Burcu Güvenatam for their enduring assistance in hard times. I would like to thank the Electrochemical Engineering Laboratory group, Venkata Yarlagadda, Xuhai Wang, and Yan Gao, at the University of Kansas for their support and friendship.

Finally, I would like to thank my mother and father; it would be impossible to complete this dissertation without their endless support and understanding. Above all, I would like to thank my brother, without whom I would have never gotten off the ground.

TABLE OF CONTENTS

ABSTRACT	iv
ÖZ	vi
ACKNOWLEDGMENTS	ix
TABLE OF CONTENTS	x
LIST OF TABLES	xv
LIST OF FIGURES	xviii
LIST OF SYMBOLS	xxiv
LIST OF ABBREVIATIONS	xxxii
PREFACE	xxxii
CHAPTERS	
1 INTRODUCTION	1
1.1 Fuel Cell Technology	1
1.2 Overview of Fuel Cell Components	2
1.3 Basic PEM Fuel Cell Operation	5
1.4 Effective PEMFC Operation Strategies	6
1.5 Motivation and Research Objectives	9
2 LITERATURE REVIEW	13
2.1 PEM Fuel Cell Models	13
2.1.1 Empirical Models	14
2.1.2 Mechanistic Models	14
2.2 Optimal PEM Fuel Cell Operation	15
2.2.1 Water Management and Cathode Flooding	15
2.2.2 Thermal Management and Cold Start up	18

2.2.3	Electrode Kinetics	20
2.3	Electrocatalyst Design	20
2.3.1	Electrocatalyst Support Development	21
2.3.2	Pt Based Electrocatalysts	23
2.3.3	Bimetallic Electrocatalysts	24
3	GENERAL MODELING APPROACH	25
3.1	Two-phase Flow Modeling	25
3.2	Mathematical Modeling Strategy	27
3.3	Governing Equations and Boundary Conditions	29
3.4	PEM Fuel Cell Performance Limitations	30
3.4.1	PEM Fuel Cell Polarization Curve	31
3.4.2	Electrochemically Active Surface Area	33
4	PROTON EXCHANGE MEMBRANE FUEL CELL MODEL	36
4.1	Model Description	36
4.1.1	Physical Domain for PEM Fuel Cell	38
4.1.2	Mathematical Model Assumptions	39
4.2	Model Development	40
4.2.1	Two Phase Flow	40
4.2.1.1	Gas Phase Species Conservation	40
4.2.1.2	Liquid Phase Species Conservation	43
4.2.1.3	Transport of Water inside the Electrolyte	47
4.2.2	Anode Electrode Kinetics	52
4.2.2.1	Butler–Volmer Type HOR Rate	52
4.2.2.2	Linearized Reaction Rate at the Anode	53
4.2.2.3	Hydrogen Oxidation Reaction Mechanism	53
4.2.2.4	CO Poisoning Mechanism	55
4.2.3	Cathode Electrode Kinetics	56
4.2.3.1	Butler–Volmer Type ORR Rate	56
4.2.3.2	Tafel Kinetics at the Cathode	57
4.2.3.3	Oxygen Reduction Mechanism	57

4.2.4	Thin-film and Agglomerate Approach	59
4.2.4.1	Thermodynamic PEM Fuel Cell Potential	61
4.2.4.2	Dissolved Oxygen Concentration	61
4.2.5	Two Phase Energy Balance	63
4.2.6	Charge Conservation	64
4.2.6.1	Ionic Phase Charge Conservation	64
4.2.6.2	Solid Phase Charge Conservation	65
4.3	Summary of Governing Equations	66
4.4	Summary of Boundary Conditions	67
4.5	PEM Fuel Cell Model Parameters	73
5	NUMERICAL SIMULATION	77
5.1	Numerical Solution Strategy	77
5.2	Description of the Computational Domain	80
5.3	Finite Volume Method	81
5.4	Single Phase Flow	82
5.5	Multiphase Flow	82
6	EXPERIMENTAL	84
6.1	Carbon Support Development	84
6.1.1	Solid Core Mesoporous Shell (SCMS) Silica	84
6.1.2	Hollow Core Mesoporous Shell (HCMS) Carbon	85
6.1.2.1	HCMS1 Carbon Synthesis: Phenolic Resin Route	86
6.1.2.2	HCMS2 Carbon Synthesis: Divinylbenzene Route	87
6.2	Electrocatalyst Development	87
6.2.1	Synthesis of Pt/HCMS Electrocatalysts	88
6.2.2	Synthesis of Pt-Pd/HCMS Electrocatalysts	89
6.2.3	Carbon Black Supported Electrocatalysts	89
6.3	Characterization of Carbon Supports and Electrocatalysts	89
6.4	Characterization of PEM Fuel Cell Diffusion Media	90
6.5	Ionic Conductivity Measurement	90

6.6	Capillary Transport Mechanism	92
6.7	Electrochemical Characterization	94
6.7.1	Cyclic Voltammetry Tests	95
6.7.2	PEM Fuel Cell Performance Tests	95
7	PEM FUEL CELL ELECTROCATALYST DEVELOPMENT	98
7.1	Solid Core Mesoporous Shell Silica	99
7.2	Hollow Core Mesoporous Shell Carbon	101
7.3	Ex situ Characterization of the Carbon Supports and Pt/C Electrocatalysts	103
7.4	Electrochemical Characterization of Pt/C Electrocatalysts	111
7.5	PEMFC Performance Tests for Pt/C Electrocatalysts	114
7.6	Ex situ Characterization of the Pt-Pd/HCMS Electrocatalysts	116
7.7	PEMFC Performance Tests for Pt-Pd/HCMS Electrocatalysts	124
7.8	Characterization of Fuel Cell Components	129
8	PEM FUEL CELL MODEL PREDICTIONS	133
8.1	0-D Model Predictions of PEM Fuel Cells	133
8.2	PEM Fuel Cell Performance	135
8.3	Single Phase and Two-phase Flow Model Predictions	137
8.4	Effect of Temperature on PEM Fuel Cell Performance	139
8.5	Effect of Pressure on PEM Fuel Cell Performance	141
8.6	Effect of Cathode Humidity on PEM Fuel Cell Performance	143
8.7	Ionic Phase Potential Distribution at PEM Fuel Cell Cathode	145
8.8	Liquid Water Transport in PEM Fuel Cells	146
8.8.1	Humidity Effect on Liquid Water Transport	147
8.8.2	Pressure Effect on Liquid Water Transport	147
8.8.3	Temperature Effect on Liquid Water Transport	149
8.9	Thermal Effects in PEM Fuel Cells	152
9	CONCLUSIONS AND RECOMMENDATIONS	157
	REFERENCES	161
	APPENDICES	

A	PROPERTIES AND CORRELATIONS FOR THE PEMFC MODEL .	179
A.1	Physical Properties of Water	179
A.2	Water Vapor Saturation Pressure	179
A.3	Capillary Pressure Measurement	180
A.4	Water Uptake of the Electrolyte	181
A.5	Proton Exchange Membrane Ionic Conductivity	181
B	ELECTROCHEMICAL REACTION MECHANISMS	184
B.1	Oxygen Reduction Reaction Mechanism	184
B.2	Hydrogen Oxidation Reaction Mechanism	187
C	ELECTROCATALYST SYNTHESIS ROUTE	191
D	EXPERIMENTAL DATA FOR PEM FUEL CELL TESTS	192
E	NONLINEAR FIT FOR A LUMPED PEM FUEL CELL MODEL . .	204
F	FCSIMULATOR PROGRAM	206
F.1	FCSIMULATOR Program	206
F.2	FCSIMULATOR Code Architecture	207
F.2.1	File Information	207
F.2.2	Program Input Parameter Module	208
VITA	214

LIST OF TABLES

TABLES

Table 1.1	Overview of substantial differences of the fuel cell types	2
Table 1.2	Comparison of electrochemical reactions for the six fuel cell technologies	3
Table 1.3	Order of layer thickness of PEM fuel cell components	4
Table 4.1	Governing equations for anode side and membrane	68
Table 4.2	Governing equations for cathode side	69
Table 4.3	Source terms for the governing equations	70
Table 4.4	Boundary conditions for anode side	71
Table 4.5	Boundary conditions for cathode side	72
Table 4.6	Gas diffusion layer properties used in the base case	73
Table 4.7	Microporous layer properties used in the base case	74
Table 4.8	Catalyst layer properties used in the base case	74
Table 4.9	Solid polymer electrolyte properties used in the base case	75
Table 4.10	PEM fuel cell operation conditions for the base case	75
Table 7.1	Structural properties of the carbon supports and the electrocatalysts	104
Table 7.2	XPS data of carbon supported platinum electrocatalysts	108
Table 7.3	Electrochemical and total surface area of the synthesized electrocatalysts	113
Table 7.4	PEMFC performance of the platinum based electrocatalysts for vari- ous carbon supports	115
Table 7.5	Structural properties of the Pt-Pd/HCMS2 electrocatalysts	117
Table 7.6	PEMFC performance of the synthesized cathode electrocatalysts at 0.6 V and 0.4 V	126

Table 7.7 Fuel cell performance comparison of the anode and cathode HCMS2 carbon supported electrocatalysts at 0.6 V	128
Table 7.8 Structural properties of SGL carbon papers	129
Table 7.9 Structural properties of Toray carbon papers	130
Table 8.1 0-D Model nonlinear fit parameters for Pt/C electrocatalysts	133
Table A.1 Physical properties of water	179
Table D.1 Experimental H ₂ /O ₂ PEM fuel cell test data for the polarization curve (Anode catalyst: 20% Pt/C (E TEK [®]), Cathode catalyst: 20% Pt/HCMS1, T=70 °C, P=1 atm, RH _a =100%, RH _c =100%, H ₂ Flow Rate = 100 cm ³ /min, O ₂ Flow Rate = 100 cm ³ /min)	193
Table D.2 Experimental H ₂ /O ₂ PEM fuel cell test data for the polarization curve (Anode catalyst: 20% Pt/C (E TEK [®]), Cathode catalyst: 20% Pt/HCMS2, T=70 °C, P=1 atm, RH _a =100%, RH _c =100%, H ₂ Flow Rate = 100 cm ³ /min, O ₂ Flow Rate = 100 cm ³ /min)	193
Table D.3 Experimental H ₂ /O ₂ PEM fuel cell test data for the polarization curve (Anode catalyst: 20% Pt/C (E TEK [®]), Cathode catalyst: 20% Pt/VX, T=70 °C, P=1 atm, RH _a =100%, RH _c =100%, H ₂ Flow Rate = 100 cm ³ /min, O ₂ Flow Rate = 100 cm ³ /min)	194
Table D.4 Experimental H ₂ /O ₂ PEM fuel cell test data for the polarization curve (Anode catalyst: 20% Pt/C (E TEK [®]), Cathode catalyst: 20% Pt/Regal, T=70 °C, P=1 atm, RH _a =100%, RH _c =100%, H ₂ Flow Rate = 100 cm ³ /min, O ₂ Flow Rate = 100 cm ³ /min)	194
Table D.5 Experimental H ₂ /O ₂ PEM fuel cell test data for the polarization curve (Anode catalyst: 20% Pt/C (E TEK [®]), Cathode catalyst: 20% Pt/BP2000, T=70 °C, P=1 atm, RH _a =100%, RH _c =100%, H ₂ Flow Rate = 100 cm ³ /min, O ₂ Flow Rate = 100 cm ³ /min)	195
Table D.6 Experimental H ₂ /O ₂ PEM fuel cell test data for the polarization curve (Anode catalyst: 20% Pt/C (E TEK [®]), Cathode catalyst: 20% Pt/C (E TEK [®]), T=70 °C, P=1 atm, RH _a =100%, RH _c =100%, H ₂ Flow Rate = 100 cm ³ /min, O ₂ Flow Rate = 100 cm ³ /min)	195

Table D.7	Experimental H ₂ /O ₂ PEM fuel cell test data for the polarization curve (Anode catalyst: 20% Pt/C (E TEK [®]), Cathode catalyst: Pt(15)Pd(5)/HCMS1 (E TEK [®]), T=70 °C, P=1 atm, RH _a =100%, RH _c =100%, H ₂ Flow Rate = 100 cm ³ /min, O ₂ Flow Rate = 100 cm ³ /min)	196
Table D.8	Experimental H ₂ /O ₂ PEM fuel cell test data for the polarization curve (Anode catalyst: 20% Pt/C (E TEK [®]), Cathode catalyst: Pt(10)Pd(10)/HCMS1 (E TEK [®]), T=70 °C, P=1 atm, RH _a =100%, RH _c =100%, H ₂ Flow Rate = 100 cm ³ /min, O ₂ Flow Rate = 100 cm ³ /min)	197
Table D.9	Experimental H ₂ /O ₂ PEM fuel cell test data for the polarization curve (Anode catalyst: 20% Pt/C (E TEK [®]), Cathode catalyst: Pt(5)Pd(15)/HCMS1 (E TEK [®]), T=70 °C, P=1 atm, RH _a =100%, RH _c =100%, H ₂ Flow Rate = 100 cm ³ /min, O ₂ Flow Rate = 100 cm ³ /min)	198
Table D.10	Experimental H ₂ /O ₂ PEM fuel cell test data for the polarization curve (Anode catalyst: 20% Pt/C (E TEK [®]), Cathode catalyst: 20% Pd/HCMS1 (E TEK [®]), T=70 °C, P=1 atm, RH _a =100%, RH _c =100%, H ₂ Flow Rate = 100 cm ³ /min, O ₂ Flow Rate = 100 cm ³ /min)	199
Table D.11	Experimental H ₂ /O ₂ PEM fuel cell test data for the polarization curve (Anode catalyst: 20% Pt/C (E TEK [®]), Cathode catalyst: Pt(15)Pd(5)/HCMS2 (E TEK [®]), T=70 °C, P=1 atm, RH _a =100%, RH _c =100%, H ₂ Flow Rate = 100 cm ³ /min, O ₂ Flow Rate = 100 cm ³ /min)	200
Table D.12	Experimental H ₂ /O ₂ PEM fuel cell test data for the polarization curve (Anode catalyst: 20% Pt/C (E TEK [®]), Cathode catalyst: Pt(10)Pd(10)/HCMS2 (E TEK [®]), T=70 °C, P=1 atm, RH _a =100%, RH _c =100%, H ₂ Flow Rate = 100 cm ³ /min, O ₂ Flow Rate = 100 cm ³ /min)	201
Table D.13	Experimental H ₂ /O ₂ PEM fuel cell test data for the polarization curve (Anode catalyst: 20% Pt/C (E TEK [®]), Cathode catalyst: Pt(5)Pd(15)/HCMS2 (E TEK [®]), T=70 °C, P=1 atm, RH _a =100%, RH _c =100%, H ₂ Flow Rate = 100 cm ³ /min, O ₂ Flow Rate = 100 cm ³ /min)	202
Table D.14	Experimental H ₂ /O ₂ PEM fuel cell test data for the polarization curve (Anode catalyst: 20% Pt/C (E TEK [®]), Cathode catalyst: 20% Pd/HCMS2 (E TEK [®]), T=70 °C, P=1 atm, RH _a =100%, RH _c =100%, H ₂ Flow Rate = 100 cm ³ /min, O ₂ Flow Rate = 100 cm ³ /min)	203

LIST OF FIGURES

FIGURES

Figure 1.1 Depiction of a basic PEM fuel cell system	4
Figure 1.2 Traditional parallel flow field design for flow channels of PEM fuel cells	7
Figure 1.3 Serpentine flow field design for flow channels of PEM fuel cells . . .	8
Figure 1.4 Interdigitated flow field design for flow channels of PEM fuel cells .	8
Figure 3.1 Illustration of polymer electrolyte membrane fuel cell polarization curve	31
Figure 3.2 Depiction of cyclic voltammogram of PEMFC (fuel cell anode/cathode: H ₂ /N ₂)	34
Figure 4.1 Illustration of 2-D physical domain for PEM Fuel Cell	38
Figure 4.2 Capillary pressure curve for Toray 090 paper using Leverett function at 80 °C	47
Figure 4.3 Chemical structure of Nafion [®] electrolyte	48
Figure 4.4 Conceptual illustration of proton transport within the Nafion [®] mem- brane	48
Figure 4.5 Depiction of Schroeders paradox for the solid polymer electrolyte .	51
Figure 4.6 Depiction of dual site attack of hydrogen atoms onto Pt surface . .	54
Figure 4.7 Representative models for O ₂ configuration over active metals: (a) Griffiths Model, (b) Pauling Model, (c) Bridge Model	58
Figure 4.8 Depiction of single site attack of oxygen molecules onto Pt surface .	59
Figure 4.9 Illustration of (a) Electrocatalyst agglomerates inside the catalyst layers, (b) Hollow core mesoporous shell carbon supported Pt electrocatalyst particle coated with ionomer	60

Figure 4.10 Illustration of heat transfer mechanisms inside porous diffusion media and catalyst layers: (1) Solid phase conduction, (2) Gas phase conduction and convection, (3) Gas-Solid heat exchange, (4) Irreversible heat generation by ORR or HOR, (5) Heat generation due to entropy change by ORR or HOR, (6) Joule heating in the solid and ionic phase, (7) Heat transfer due to phase change	63
Figure 5.1 Flowchart for the numerical solution algorithm	79
Figure 5.2 Two dimensional adaptive PEMFC grid illustration for numerical simulation	80
Figure 5.3 Staggered structured finite volume grid	81
Figure 6.1 Depiction of silica template synthesis route for HCMS carbon	86
Figure 6.2 Experimental setup for ionic conductivity measurement	91
Figure 6.3 Conductivity cell for proton conductivity measurement (a) Left view, (b) Right view	91
Figure 6.4 Experimental setup for capillary measurement	93
Figure 6.5 Experimental setup for cyclic voltammetry	94
Figure 6.6 Single cell PEM Fuel Cell test station	96
Figure 7.1 SEM micrograph of solid core mesoporous shell (SCMS) silica	100
Figure 7.2 TEM micrograph of solid core mesoporous shell (SCMS) silica	100
Figure 7.3 N ₂ adsorption/desorption isotherms and the corresponding pore size distribution for SCMS silica	101
Figure 7.4 TEM images of (a) HCMS1 carbon and (b) HCMS2 carbon	102
Figure 7.5 N ₂ adsorption/desorption isotherms and the corresponding pore size distribution for HCMS carbon	103
Figure 7.6 Pore size distribution of the carbon supports	105
Figure 7.7 Pore size distribution of the 20% Pt/C electrocatalysts	106
Figure 7.8 The XRD patterns of 20% Pt/C electrocatalysts	107
Figure 7.9 Pt 4f XPS spectra for 20% Pt/C electrocatalysts	108
Figure 7.10 XPS survey spectra for 20% Pt/C electrocatalysts	109

Figure 7.11 TGA data of (a) 20% Pt/HCMS1, 20% Pt/HCMS2 and 20% Pt/C (E TEK [®]), (b) BP2000 and 20% Pt/BP2000, (c) Regal and 20% Pt/Regal, (d) VX and 20% Pt/VX	110
Figure 7.12 Cyclic voltammograms for the catalysts prepared with the synthesized carbon supports and commercial catalyst (Pt/C E TEK [®]) in 0.1M HClO ₄ in N ₂ atmosphere at a scan rate of 50 mVs ⁻¹	111
Figure 7.13 Cyclic voltammograms for the catalysts prepared with the carbon black supports in 0.1M HClO ₄ in N ₂ atmosphere at a scan rate of 50 mVs ⁻¹	112
Figure 7.14 PEMFC polarization curves for Pt/HCMS1 cathode catalysts synthesized with different microwave durations (anode catalyst is 20% Pt/C, E TEK [®])	114
Figure 7.15 PEMFC performance test for Pt/C cathode electrocatalysts (anode catalyst is 20% Pt/C, E TEK [®])	117
Figure 7.16 SEM (a) and TEM (b) micrograph of 20% Pt/HCMS2 electrocatalyst	119
Figure 7.17 TEM micrographs of (a) Pd/HCMS2 (20), (b) PdPt/HCMS2 (15:5), (c) PdPt/HCMS2 (10:10), (d) PdPt/HCMS2 (5:15)	120
Figure 7.18 The XRD patterns of as-synthesized SCMS silica and HCMS2 carbon	121
Figure 7.19 The XRD patterns of Pt-Pd/HCMS2 electrocatalysts	121
Figure 7.20 Pt 4f XPS spectra for HCMS2 based electrocatalysts	122
Figure 7.21 Pd 3d XPS spectra for HCMS2 based electrocatalysts	123
Figure 7.22 XPS survey spectra for Pt/HCMS2, PtPd/HCMS2 (10:10) and Pd/HCMS2 electrocatalysts	124
Figure 7.23 PEMFC performance test for Pt-Pd/HCMS1 cathode electrocatalysts (anode catalyst is 20% Pt/C, E TEK [®])	125
Figure 7.24 PEMFC performance test for Pt-Pd/HCMS2 cathode electrocatalysts (anode catalyst is 20% Pt/C, E TEK [®])	127
Figure 7.25 PEMFC polarization curve of the HCMS2 based anode catalysts (cathode catalyst is 20% Pt/C, E TEK [®])	128
Figure 7.26 Pore size distribution for various diffusion media components for PEM fuel cells	131

Figure 7.27 SEM micrograph of SGL 30BC (a) Gas diffusion layer (b) Microporous Layer	132
Figure 7.28 SEM micrograph of a used membrane electrode assembly (Diffusion Media: SGL 30BC, Membrane: Nafion 112, Anode Catalyst Layer: 20% Pt/C, ETEK [®] , and Cathode Catalyst Layer: 20% Pt/HCMS2)	132
Figure 8.1 Zero dimensional model validation for PEMFC with 20% Pt/HCMS2 cathode electrocatalyst (T=70 °C, P _a =1 atm, P _c =1 atm, Anode RH= 100 %, Cathode RH= 100 %)	134
Figure 8.2 Steady state isothermal polarization and power curve for H ₂ /Air PEMFC (T=60 °C, P _a =1 atm, P _c =1 atm, Anode RH= 100 %, Cathode RH= 100 %)	136
Figure 8.3 Steady state isothermal polarization and power curve for H ₂ /Air PEMFC (T=70 °C, P _a =1 atm, P _c =1 atm, Anode RH= 100 %, Cathode RH= 100 %)	137
Figure 8.4 Steady state isothermal polarization and power curve comparison for different oxidant feeds (T=70 °C, P _a =1 atm, P _c =1 atm, Anode RH= 100 %, Cathode RH= 100 %)	138
Figure 8.5 PEM fuel cell performance comparison for single phase and two-phase flow at isothermal and steady state conditions (T=70 °C, P _a =1 atm, P _c =1 atm, Anode RH= 100 %, Cathode RH= 10 %)	139
Figure 8.6 Effect of cell temperature on PEM fuel cell performance for isothermal and steady state operation (P _a =1 atm, P _c =1 atm, Anode RH= 100 %, Cathode RH= 10 %)	140
Figure 8.7 Effect of cathode feed pressure on PEM fuel cell performance for single phase flow at isothermal and steady state operating conditions (T=70 °C, P _a =1 atm, Anode RH= 100 %, Cathode RH= 10 %)	141
Figure 8.8 Effect of cathode feed pressure on PEM fuel cell performance for two phase flow at isothermal and steady state operating conditions (T=70 °C, P _a =1 atm, Anode RH= 100 %, Cathode RH= 10 %)	142
Figure 8.9 Variation of PEM fuel cell performance with cathode relative humidity (T=60 °C, P _a =1 atm, Anode RH= 100 %)	144

Figure 8.10 Variation of PEM fuel cell performance with cathode relative humidity (T=70 °C, P _a =1 atm, Anode RH= 100 %)	145
Figure 8.11 Ionic phase potential distribution at cathode for the base case (T=60 °C, P _a =1 atm, Anode RH= 100 %, Cathode RH= 10 %)	146
Figure 8.12 Variation of liquid phase saturation with cathode relative humidity at a cell potential of (a) 0.6 V (b) 0.4 V (T=60 °C, P _a =1 atm, Anode RH= 100 %)	148
Figure 8.13 Variation of liquid phase saturation with cathode pressure at a cell potential of 0.3 V (T=70 °C, P _a =1 atm, Anode RH= 100 %, Cathode RH= 10 %)	149
Figure 8.14 Liquid phase saturation distribution for different cell potentials (T=60 °C, P _a =1 atm, P _c =1 atm, Anode RH= 100 %, Cathode RH= 10 %)	150
Figure 8.15 Isothermal liquid phase saturation distribution for different cell potentials (T=80 °C, P _a =1 atm, P _c =1 atm, Anode RH= 100 %, Cathode RH= 10 %)	151
Figure 8.16 Nonisothermal liquid phase saturation distribution for different cell potentials (T=80 °C, P _a =1 atm, P _c =1 atm, Anode RH= 100 %, Cathode RH= 10 %)	151
Figure 8.17 Steady state isothermal and nonisothermal polarization and power curve for H ₂ /Air PEMFC (T=80 °C, P _a =1 atm, P _c =1 atm, Anode RH= 100 %, Cathode RH= 100 %)	153
Figure 8.18 Steady state isothermal and nonisothermal polarization and power curve for H ₂ /O ₂ PEMFC (T=80 °C, P _a =1 atm, P _c =1 atm, Anode RH= 100 %, Cathode RH= 100 %)	153
Figure 8.19 Effect of cell temperature on PEM fuel cell performance for nonisothermal and steady state operation (P _a =1 atm, P _c =1 atm, Anode RH= 100 %, Cathode RH= 100 %)	154
Figure 8.20 Nonisothermal steady state temperature profile in the cathode PEM fuel cell (T=50 °C, P _a =1 atm, P _c =1 atm, Anode RH= 100 %, Cathode RH= 100 %)	155

Figure 8.21 Nonisothermal steady state temperature profile in the cathode PEM fuel cell ($T=80\text{ }^{\circ}\text{C}$, $P_a=1\text{ atm}$, $P_c=1\text{ atm}$, Anode RH= 100 %, Cathode RH= 100 %)	155
Figure A.1 Saturation pressure of water vapor at low temperatures	180
Figure A.2 Capillary pressure variation with respect to liquid phase saturation level for different components at ambient temperature	181
Figure A.3 Water content of Nafion [®] 117 membrane as function of water activity at $30\text{ }^{\circ}\text{C}$	182
Figure A.4 Ionic conductivity of Nafion [®] 117 membrane as function of water content at $30\text{ }^{\circ}\text{C}$	182
Figure C.1 PEM fuel cell electrocatalyst synthesis and characterization route .	191
Figure E.1 Zero dimensional model validation for PEMFC with 20% Pt/HCMS1 cathode electrocatalyst ($T=70\text{ }^{\circ}\text{C}$, $P_a=1\text{ atm}$, $P_c=1\text{ atm}$, Anode RH= 100 %, Cathode RH= 100 %)	205
Figure E.2 Zero dimensional model validation for PEMFC with 20% Pt/BP2000 cathode electrocatalyst ($T=70\text{ }^{\circ}\text{C}$, $P_a=1\text{ atm}$, $P_c=1\text{ atm}$, Anode RH= 100 %, Cathode RH= 100 %)	205

LIST OF SYMBOLS

Latin Letters

a_1	Coefficient in capillary pressure data		
a_2	Coefficient in capillary pressure data		
A_e	External surface area of agglomerate	cm^2	L^2
a_i	Activity of species i		
$a_{Pt}^{a,agg}$	Catalyst surface area per volume	cm^2/cm^3	$\frac{\text{L}^2}{\text{L}^3}$
a_w	Activity of water		
b	Coefficient in capillary pressure data	Pa	$\frac{\text{M}}{\text{L}t^2}$
c	Coefficient in capillary pressure data		
C_f	Fixed site charge concentration	mol/cm^3	$\frac{\text{N}}{\text{L}^3}$
$C_{\text{H}_2}^{ref}$	Reference hydrogen concentration	mol/cm^3	$\frac{\text{N}}{\text{L}^3}$
$C_{\text{O}_2}^m$	Oxygen concentration in ionomer	mol/cm^3	$\frac{\text{N}}{\text{L}^3}$
$C_{\text{O}_2}^{ref}$	Reference oxygen concentration	mol/cm^3	$\frac{\text{N}}{\text{L}^3}$
$C_{\text{O}_2}^w$	Oxygen concentration in water	mol/cm^3	$\frac{\text{N}}{\text{L}^3}$
$\bar{C}_{p,g}$	Average gas phase specific heat capacity	J/g K	$\frac{\text{L}^2}{\text{T}t^2}$
C_t	Total concentration in the gas phase	mol/cm^3	$\frac{\text{N}}{\text{L}^3}$
C_w^m	Water concentration within the electrolyte	mol/cm^3	$\frac{\text{N}}{\text{L}^3}$
d	Coefficient in capillary pressure data	Pa	$\frac{\text{M}}{\text{L}t^2}$
d_p	Pore diameter	cm	L

D_c	Capillary diffusion coefficient	cm^2/s	$\frac{L^2}{t}$
$D_{i,j}$	Binary diffusivity in the gas phase	cm^2/s	$\frac{L^2}{t}$
$D_{i,j}^{eff}$	Effective binary diffusivity	cm^2/s	$\frac{L^2}{t}$
D_K	Knudsen diffusivity	cm^2/s	$\frac{L^2}{t}$
D_t	Composite diffusivity	cm^2/s	$\frac{L^2}{t}$
D_w^m	Water diffusivity within the electrolyte	cm^2 / s	$\frac{L^2}{t}$
F	Faraday's constant	C/mol	$\frac{It}{N}$
$A_{g,s}$	Heat transfer area of the porous media	cm^2/cm^3	$\frac{L^2}{L^3}$
$h_{g,s}$	Gas-solid heat transfer coefficient	$\text{W} / \text{cm}^2 \text{ K}$	$\frac{M}{Tt^3}$
$H_{O_2}^m$	Henry's coefficient for O_2 and ionomer	$\text{atm cm}^3/\text{mol}$	$\frac{ML^2}{Nt^2}$
$H_{O_2}^w$	Henry's coefficient for O_2 and water	$\text{atm cm}^3/\text{mol}$	$\frac{ML^2}{Nt^2}$
i_m	Ionic phase current density	A/cm^2	$\frac{I}{L^2}$
i_s	Solid phase current density	A/cm^2	$\frac{I}{L^2}$
J	Jacobian matrix of the nonlinear PDEs		
j_a	Anode current density	A/cm^3	$\frac{I}{L^3}$
$j_{o,a}^{ref}$	Anode exchange current density	A/cm^3	$\frac{I}{L^3}$
$J(s)$	Leverett function for capillary pressure		
k_c	Condensation rate constant for water	$1/\text{s}$	$\frac{1}{t}$
k_e	Evaporation rate constant for water	$1/\text{atm s}$	$\frac{Lt}{M}$
k_g^{eff}	Effective gas phase thermal conductivity	$\text{W}/\text{cm K}$	$\frac{ML}{Tt^3}$
Kn	Knudsen number		
k_s^{eff}	Effective solid phase thermal conductivity	$\text{W}/\text{cm K}$	$\frac{ML}{Tt^3}$
K_w	Liquid water permeability	cm^2	L^2
K_w^m	Electrolyte liquid water permeability	cm^2	L^2

$K_{w,o}$	Permeability of water at 100% saturation	cm^2	L^2
M_i	Molecular weight of species i	g/mol	$\frac{M}{N}$
M_j	Molecular weight of species j	g/mol	$\frac{M}{N}$
M_w	Molecular weight of water	g/mol	$\frac{M}{N}$
n_d	Electro-osmotic drag coefficient		
N_i	Molar flux of species i	$\text{mol/cm}^2 \text{ s}$	$\frac{N}{L^2 t}$
n_k	Number of transferred e^- in reaction k		
N_w	Liquid water flux	$\text{mol/cm}^2 \text{ s}$	$\frac{N}{L^2 t}$
N_w^m	Water flux within the electrolyte	$\text{mol/cm}^2 \text{ s}$	$\frac{N}{L^2 t}$
P	Pressure	atm	$\frac{M}{L t^2}$
P_c	Capillary pressure in the porous matrix	atm	$\frac{M}{L t^2}$
P_g	Gas phase pressure	atm	$\frac{M}{L t^2}$
P_{H_2O}	Partial pressure of water vapor	atm	$\frac{M}{L t^2}$
$P_{H_2O}^{sat}$	Saturation pressure of water vapor	atm	$\frac{M}{L t^2}$
$P_{c,i}$	Critical pressure of species i	atm	$\frac{M}{L t^2}$
$P_{c,j}$	Critical pressure of species j	atm	$\frac{M}{L t^2}$
P_l	Pressure of liquid water	atm	$\frac{M}{L t^2}$
P_{O_2}	Oxygen partial pressure	atm	$\frac{ML}{t^2}$
q_t	Total heat flux generated by rxn	W/cm^2	$\frac{M}{t^3}$
R	Universal gas constant	J/molK	$\frac{ML^2}{NTt^2}$
\bar{R}_m^{eff}	Ionic phase effective resistivity	ohm cm	$\frac{ML^3}{I^2 t^3}$
\bar{R}_s^{eff}	Solid matrix effective resistivity	ohm cm	$\frac{ML^3}{I^2 t^3}$
R_{H_2O}	Interfacial molar rate of the water	$\text{mol/cm}^3 \text{ s}$	$\frac{N}{L^3 t}$
R_i	Generation rate of species i	$\text{mol/cm}^3 \text{ s}$	$\frac{N}{L^3 t}$

r_p	Pore radius	cm	L
s	Liquid phase saturation		
S_{ϕ_m}	Proton transport source term	A/cm ³	$\frac{I}{L^3}$
S_{ϕ_s}	Electron transport source term	A/cm ³	$\frac{I}{L^3}$
S_s	Source term for solid phase energy balance	W/cm ³	$\frac{M}{Lt^3}$
T	Average temperature in the porous media	K	T
T_g	Average temperature in the gas phase	K	T
$T_{c,i}$	Critical temperature of species i	K	T
$T_{c,j}$	Critical temperature of species j	K	T
T_s	Average temperature in the solid phase	K	T
D_i	Diffusion coefficient of species i	cm ² /s	$\frac{L^2}{t}$
u	Superficial velocity	cm/s	L/t
U_{eq}^a	Anode thermodynamic potential	V	$\frac{ML^2}{It^3}$
U_{eq}^c	Cathode thermodynamic potential	V	$\frac{ML^2}{It^3}$
\mathbf{u}_g	Gas phase superficial velocity	cm/s	$\frac{L}{t}$
U°	Reversible cell potential	V	$\frac{ML^2}{It^3}$
U_H	Thermoneutral potential	V	$\frac{ML^2}{It^3}$
V	Applied cell potential	V	$\frac{ML^2}{It^3}$
V_p	Volume of the pellet	cm ³	L ³
y_i	Mole fraction of species i		
z_i	Charge number of species i		

Greek Letters

ΔG	Gibbs free energy	J/mol	$\frac{ML^2}{Nt^2}$
ΔH	Enthalpy change of reaction	J/mol	$\frac{ML^2}{Nt^2}$
ΔH_{H_2O}	Heat of vaporization of water	J/mol	$\frac{ML^2}{Nt^2}$
ΔS_k	Entropy change of reaction k	J/molK	$\frac{ML^2}{NTt^2}$
ε_o	Intrinsic porosity of the porous matrix		
η_a	Anode overpotential	V	$\frac{ML^2}{It^3}$
η_c	Cathode overpotential	V	$\frac{ML^2}{It^3}$
η_k	Overpotential in the anode or cathode	V	$\frac{ML^2}{It^3}$
κ_m^{eff}	Effective ionic conductivity	S/cm	$\frac{I^2t^3}{ML^3}$
κ_s^{eff}	Effective electronic conductivity	S/cm	$\frac{I^2t^3}{ML^3}$
λ	Water content in the electrolyte	mol H ₂ O/mol SO ₃ ⁻	N/N
λ^{eq}	Equilibrium water uptake of electrolyte		
λ_m	Molecular mean free path	cm	L
μ_w	Viscosity of the liquid water	g/cms	$\frac{M}{Lt}$
ϕ_m^a	Anode ionic phase potential	V	$\frac{ML^2}{It^3}$
ϕ_m^c	Cathode ionic phase potential	V	$\frac{ML^2}{It^3}$
ϕ_s^a	Anode solid phase potential	V	$\frac{ML^2}{It^3}$
ϕ_s^c	Cathode solid phase potential	V	$\frac{ML^2}{It^3}$
ρ_g	Density of the gas phase	g /cm ³	$\frac{M}{L^3}$
ρ_w	Density of the liquid water	g /cm ³	$\frac{M}{L^3}$
σ	Surface tension for gas-water system	N/m	$\frac{M}{t^2}$

τ	Tortuosity of the porous media	
θ_c	Contact angle of the porous media	◦
φ	Thiele modulus	
ξ	Effectiveness factor	

Superscripts

<i>eff</i>	Effective transport property
<i>n</i>	Total number of gas species
<i>sat</i>	Saturation

Subscripts

<i>c</i>	Critical or condensation
<i>e</i>	Evaporation
<i>g</i>	Gas phase
<i>H₂O</i>	Water species in the gas phase
<i>i</i>	Gas or liquid species
<i>j</i>	Gas or liquid species
<i>k</i>	Anode or cathode electrochemical reaction
<i>l</i>	Liquid phase
<i>m</i>	Membrane phase or ionic phase
◦	Initial or bulk value
<i>s</i>	Solid phase or region s

t Total value
 w Liquid water

LIST OF ABBREVIATIONS

AFC Alkaline Fuel Cell. 1

C18TMS Octadecyl trimethoxysilane. 85

HCMS Hollow Core Mesoporous Shell. 23

HOR Hydrogen Oxidation Reaction. 22

LBV Langmuir-Butler-Volmer. 36

MCFC Molten Carbonate Fuel Cell. 1

MEA Membrane Electrode Assembly. 11

ORR Oxygen Reduction Reaction. 22

PAFC Phosphoric Acid Fuel Cell. 1

PEMFC Polymer Electrolyte Membrane Fuel Cell. 1

SCMS Solid Core Mesoporous Shell. 85

SOFC Solid Oxide Fuel Cell. 1

TEOS Tetraethyl orthosilicate. 85

PREFACE

This dissertation has two major sections including experimental studies related to synthesis and characterization of Proton Exchange Membrane (PEM) fuel cell electrocatalysts and modeling and simulation of PEM fuel cells. These two major field of research are broken down into several subsections. Experimental and modeling sections can be read separately without losing any detail of the research. It is up to the reader to decide whether they want to read about foundations related to the electrocatalyst synthesis and characterization or the reader may want to focus on the modeling and simulation of fuel cells.

General introduction to PEM fuel cell is given in Chapter 1. This chapter is essentially a short description of the fuel cells and also some pitfalls encountered during the commercialization of fuel cells are explained briefly. There is a short subsection which emphasize the motivation behind this research and several goals regarding to the Ph.D. study are highlighted. This section should be read by all users before they proceed further into the text.

In Chapter 2, up to date literature on PEM fuel cell modeling is presented in the first part. Most commonly used models are discussed and presented to introduce the reader to strong and weak parts of the pioneer models. The need for a new kind of model is described to understand the details of electrode kinetics. Emphasis is given to the nonisothermal models. In the second part, first literature on the supporting materials for PEM fuel cell electrocatalysts are reviewed. Second, most common and alternative electrocatalysts and their impact on PEM fuel cells are discussed. Recent developments in electrocatalyst design are overviewed and promising electrocatalysts are presented considering their synthesis route.

Chapter 3 deals with the general features of the PEM fuel cell model. Modeling approach and strategy are outlined. This chapter can be considered as an overlook

to the fundamental processes within a PEM fuel cell. Some global assumptions are presented and their relative importance are discussed in the text.

In Chapter 4, mathematical model is described in depth. All governing equations are explained extensively for all fuel cell components. Appropriate boundary conditions are given for fuel cell layer interfaces and proper inlet conditions are also discussed. Almost every model introduces some uncertainty within the limits of the assumptions made. Therefore, the reliability and applicability of the model are also addressed.

Chapter 5 covers the numerical simulation of the mathematical model presented. Method of discretization of the governing equations and boundary conditions are outlined. Implementation of the numerical solution algorithm to the FORTRAN 90 is described in detail.

In Chapter 6, experimental procedures for the synthesis of the carbon support and electrocatalyst are covered. Various characterization methods for the synthesized nanomaterials are explained further to help understand the methodology of the electrocatalyst design.

Results of experimental part, electrocatalyst development, are given in Chapter 7. Synthesized carbon supported Pt and Pt-Pd electrocatalysts are compared and discussed for various synthesis conditions. Electrochemical characterization and fuel cell performance of the electrocatalysts are investigated and major findings are presented in the text.

Chapter 8 deals with the model results for various operating condition scenarios. Model predictions are validated through the experimental data presented and thermal and water management issues are addressed.

In Chapter 9, main conclusions that can be drawn from this research are presented. To help improve the electrocatalyst design some possible synthesis methods are recommended. In addition, key issues for the development of robust models are covered.

Appendices include the details related to the estimation of some physical properties. In addition, some experimental data are also tabulated in this section. Furthermore, some brief information on programming is given in the final part.

CHAPTER 1

INTRODUCTION

Hydrogen is considered to be the energy carrier of the near future. Dependence on fossil fuels can be overcome through novel technologies enabling the efficient production, storage, and use of hydrogen. One key technology taking part in hydrogen energy system is fuel cells. Fuel cells are electrochemical energy conversion devices with high efficiency and power density. These electrochemical devices produce electricity, heat, and water by utilizing the fuel and oxygen in the air with low environmental impact. When hydrogen is used as fuel, water is the only emitted product.

There are multiple benefits of fuel cells over conventional energy producing systems. First, there is no Carnot efficiency limit in fuel cells due to direct conversion of chemical energy to electrical energy. For this reason, these devices are two or three folds more efficient than internal combustion engines in transforming fuel to useful power. Second, fuel cells operate quietly with minimal impurity emission. In addition, modular design feature of fuel cell systems facilitates scale-up for specific applications.

1.1 Fuel Cell Technology

Various fuel cells are in development stage for distinct applications. Generally, fuel cells are classified according to the electrolytes used between anode and cathode. Specific properties of these electrolytes determine some fuel cell specific properties like the process operating temperature. Alkaline Fuel Cell (AFC), Polymer Electrolyte Membrane Fuel Cell (PEMFC), Phosphoric Acid Fuel Cell (PAFC), Molten Carbonate Fuel Cell (MCFC), and Solid Oxide Fuel Cell (SOFC) are the five common fuel cell technologies

that are currently being developed. Having different process temperatures make these fuel cells best suited to special applications. Table 1.1 lists the major differences in different fuel cell types [1].

Table 1.1: Overview of substantial differences of the fuel cell types

	AFC	PEMFC	PAFC	MCFC	SOFC
Electrolyte	KOH in asbestos	PFSA membranes	H ₃ PO ₄ in SiC	Liquid MC in LiAlO ₂	Perovskites (Ceramics)
Mobile ion	OH ⁻	H ⁺	H ⁺	CO ₃ ²⁻	O ²⁻
Electrodes	Transition metals	Carbon	Carbon	Ni and NiO	Perovskite & metal cermet
Catalyst	Platinum metal	Platinum metal	Platinum metal	Electrode material	Electrode material
Temperature	65-220 °C	60-100 °C	175-200 °C	600-1000 °C	600-1000 °C

Since process temperature is one of the critical parameters affecting fuel cell system, a significant distinction results from the operating temperature of the various fuel cell types. Other varieties considered are due to electrolytes, mobile ion transferred through electrolyte, and cathode and anode electrocatalysts.

Useful life time and operating pressure of the fuel cells specify the properties of the materials required in cell components like electrodes, electrolyte, and current collector. A comparison of the electrochemical reactions for different fuel cell technologies are presented in Table 1.2 [2].

1.2 Overview of Fuel Cell Components

A typical single cell polymer electrolyte membrane fuel cell requires five significant components to function properly. Figure 1.1 shows the simplified two dimensional view of a single cell PEM fuel cell. Solid matrix of the fuel cell consists of bipolar plate, gas diffusion layer, microporous layer, and catalyst layer. On the other hand, electrolyte, which is a thin solid polymer membrane, is placed in the middle of the cell and acts as the ionic phase.

Each component has a different role to help optimal operation of PEM fuel cell. To be-

Table 1.2: Comparison of electrochemical reactions for the six fuel cell technologies

Fuel Cell	Electrochemical Reactions
AFC	Anode: $\text{H}_2 + 2 \text{OH}^- \rightarrow 2 \text{H}_2\text{O} + 2 \text{e}^-$ Cathode: $\frac{1}{2} \text{O}_2 + \text{H}_2\text{O} + 2 \text{e}^- \rightarrow 2 \text{OH}^-$ <hr/> Cell: $\text{H}_2 + \frac{1}{2} \text{O}_2 \rightarrow \text{H}_2\text{O}$
PEMFC	Anode: $\text{H}_2 \rightarrow 2 \text{H}^+ + 2 \text{e}^-$ Cathode: $\frac{1}{2} \text{O}_2 + 2 \text{H}^+ + 2 \text{e}^- \rightarrow \text{H}_2\text{O}$ <hr/> Cell: $\text{H}_2 + \frac{1}{2} \text{O}_2 \rightarrow \text{H}_2\text{O}$
DMFC	Anode: $\text{CH}_3\text{OH} + \text{H}_2\text{O} \rightarrow 6 \text{H}^+ + 6 \text{e}^- + \text{CO}_2$ Cathode: $\frac{3}{2} \text{O}_2 + 6 \text{H}^+ + 6 \text{e}^- \rightarrow 3 \text{H}_2\text{O}$ <hr/> Cell: $\text{CH}_3\text{OH} + \frac{3}{2} \text{O}_2 \rightarrow 2 \text{H}_2\text{O} + \text{CO}_2$
PAFC	Anode: $\text{H}_2 \rightarrow 2 \text{H}^+ + 2 \text{e}^-$ Cathode: $\frac{1}{2} \text{O}_2 + 2 \text{H}^+ + 2 \text{e}^- \rightarrow \text{H}_2\text{O}$ <hr/> Cell: $\text{H}_2 + \frac{1}{2} \text{O}_2 \rightarrow \text{H}_2\text{O}$
MCFC ^a	Anode: $\text{H}_2 + \text{CO}_3^{2-} \rightarrow \text{H}_2\text{O} + \text{CO}_2 + 2 \text{e}^-$ Cathode: $\frac{1}{2} \text{O}_2 + \text{CO}_2 + 2 \text{e}^- \rightarrow \text{CO}_3^{2-}$ <hr/> Cell: $\text{H}_2 + \frac{1}{2} \text{O}_2 + \text{CO}_2 \rightarrow \text{H}_2\text{O} + \text{CO}_2$
SOFC	Anode: $\text{H}_2 + \text{O}^{2-} \rightarrow \text{H}_2\text{O} + 2 \text{e}^-$ Cathode: $\frac{1}{2} \text{O}_2 + 2 \text{e}^- \rightarrow \text{O}^{2-}$ <hr/> Cell: $\text{H}_2 + \frac{1}{2} \text{O}_2 \rightarrow \text{H}_2\text{O}$

^a CO_2 is produced at anode and consumed at cathode

gin with, fuel and oxidant flow channels are machined into bipolar plate with a specific channel architecture. Usually graphite is used as the bipolar plate material. These plates provide mechanical stability, electrical conductivity and they can be considered as nonporous and impermeable to gas flow. Major function of these plates to supply reactant feed by forcing the convective flow over the diffusion media and remove the product streams at the anode and cathode by way of sophisticated flow fields.

When a number of single cells are combined together to form a fuel cell stack or module, there is usually a need for coolant channels to remove the excess heat produced. In the case of designing of a fuel cell stack, coolant channels are also machined into bipolar plates. In a standard fuel cell stack, one side of the bipolar plate acts as the anode, whereas the other side serves as the cathode.

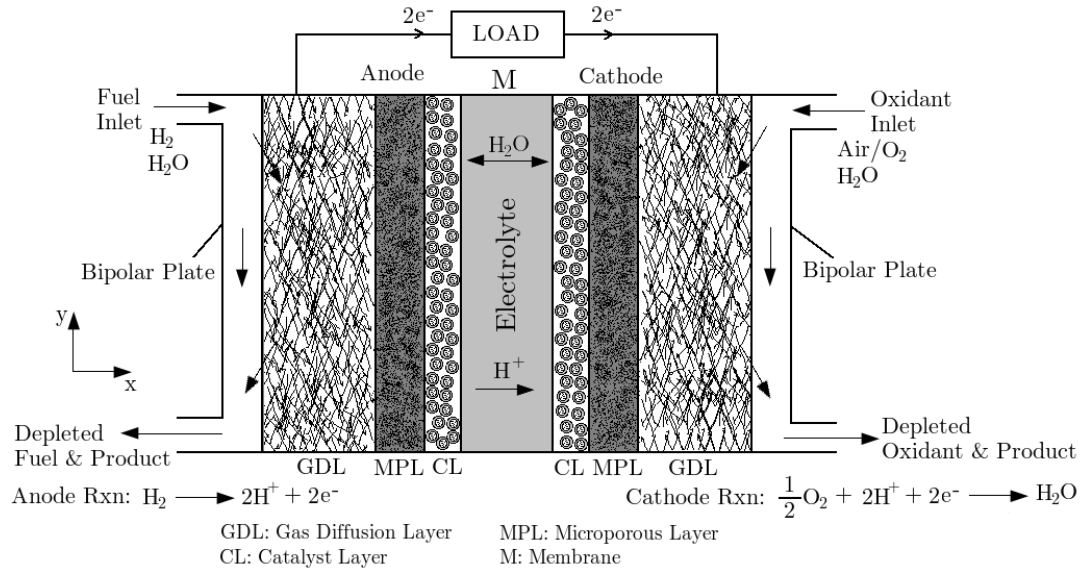


Figure 1.1: Depiction of a basic PEM fuel cell system

Table 1.3 presents the order of dimension of fuel cell components (in x direction, see Figure 1.1) so as to give an insight to the scale of physical system. Bipolar plate thickness given in Table 1.3 is a minimum thickness so as to fabricate flow channels easily into bipolar plate. Flow channel depth is usually about 1000 μm .

Table 1.3: Order of layer thickness of PEM fuel cell components

PEMFC Layer	Component Thickness (μm)
Bipolar Plate	$\sim\text{O}(5000-6000)$
Gas Diffusion Layer (GDL)	$\sim\text{O}(200-300)$
Electrolyte (M)	$\sim\text{O}(25-50)$
Microporous Layer (MPL)	$\sim\text{O}(20-30)$
Catalyst Layer (CL)	$\sim\text{O}(5-20)$

Porous diffusion media, adjacent to bipolar plate, may contain only gas diffusion layer (macroporous structure) or it may involve both the gas diffusion layer and microporous layer together. Material selection is usually made considering the specific fuel cell application. Carbon paper or carbon cloth is the standard material for gas diffusion layer. GDL is a critical component of fuel cell and plays a major role for the proper operation of PEMFC. GDL provides a mechanical and electrical contact to CL. Major

function of GDL is to evenly distribute reactants towards CL and remove the produced water effectively through capillaries. In most of the cases materials like PTFE is added to the GDL structure to provide a hydrophobic pathway for water removal.

Microporous layer may or may not be included in the PEM fuel cell. However, it is well known that inclusion of MPL only at the cathode side improves PEMFC performance tremendously. MPL has similar properties as compared to GDL and involves a microporous carbon material with high hydrophobicity. With high hydrophobicity, MPL acts as a pump and liquid water is pumped from cathode catalyst layer to cathode channels by capillary flow as well as to anode through membrane by back diffusion.

Catalyst layer includes an electrocatalyst support, usually mesoporous or macroporous carbon, electroactive metals (e.g. Platinum or palladium), ionomer solution, and sometimes PTFE may be added considering a similar purpose as described with MPL. Hydrogen oxidation and oxygen reduction reactions take place in the catalyst layers. Electrons are transferred through the solid matrix and protons are transferred through the ionomer phase.

Conventional electrolytes are Perfluorosulfonic Acid (PFSA) based solid polymers. Typical electrolyte functioning at relatively low temperatures require humidification to ionically conduct positive ions from anode to cathode. Electrolyte can be considered gas impermeable (very low reactant permeation rate). Electrons can not pass through the electrolyte, therefore, electrons follow the solid matrix (generates electricity) to meet with the protons at the cathode.

1.3 Basic PEM Fuel Cell Operation

Among the several fuel cell types, PEM fuel cells have attracted much more attention for both portable and stationary applications due to its beneficial characteristics such as high power density at relatively lower temperatures, lightweight, and compactness [3]. During the operation of fuel cell, hydrogen gas flows through porous diffusion media and reaches electrochemically active sites at the anode catalyst layer by diffusion. Over the three-phase boundary, where active nanometal particles (e.g. Platinum), ionomer, and gas pores are all connected, hydrogen oxidation reaction takes place and hydrogen

gas is separated into electrons and protons (hydrogen ions).

Similarly, on cathode side, oxygen in the air diffuses through gas diffusion media and reaches three-phase boundary at the cathode catalyst layer. Concurrently, produced hydrogen ions pass through the solid polymer electrolyte (membrane) and reach to the cathode active sites. Oxygen, protons, and electrons combine over the electrocatalyst surface producing electricity and heat. The electrons, which can not pass through the electrolyte, follows an external path from anode to cathode containing electronic load or motor, which consumes the power generated by the PEM fuel cell.

For optimal fuel cell operation, voltage from one single cell is on the order of 0.7 volts - almost sufficient for a bulb. Therefore, cells are stacked into series to increase fuel cell voltage to meet the design voltage of the system. Similarly, active area of the single cell may be increased to provide higher current to the appliance.

1.4 Effective PEMFC Operation Strategies

Among the fuel cell performance limiting factors, water removal and management has vital importance for optimum PEM fuel cell performance. Water is transported from anode to cathode by electroosmosis and water is produced at the cathode catalyst layer by oxygen reduction reaction. Back diffusion of water from cathode to anode might also take place together with hydraulic pressure effects when there is a pressure gradient between the two electrodes.

One may control and enhance the water distribution throughout the fuel cell by flow field design, auxiliary system design (e.g. efficient humidification system at anode or even at cathode) or material engineering, that is, with the introduction of new materials that are capable of ejecting liquid water by creating hydrophobic pathways (pump effect).

To prevent flooding at the cathode electrode, generally three major flow field designs are in use depending on the design criteria of the fuel cell system. Figure 1.2 is an illustration for the traditional parallel flow field design considered for polymer electrolyte membrane fuel cells. This standard parallel flow field geometry is well suited for fuel cells with high feed flow rates and low pressure drop. This type of flow

field forces reactants to diffuse through macroporous and microporous layer. Since electrochemical activity is limited by reactant transport rate to the electroactive sites, in some cases, reactant starvation may be a major issue for parallel flow field.

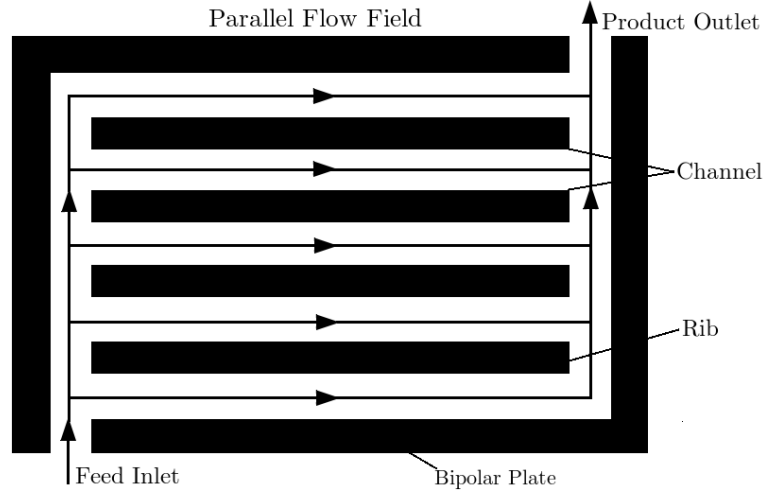


Figure 1.2: Traditional parallel flow field design for flow channels of PEM fuel cells

One of the most common PEM fuel cell flow field architecture is single or multiple parallel serpentine channels. Figure 1.3 depicts the single serpentine flow channel geometry. Gas mixture flow is substantially along the channel. If sufficient pressure gradient develops in each successive turn, gas mixture may flow back to the next serpentine turn, which may enhance the flow hydrodynamics within the fuel cell channels.

To overcome cathode electrode flooding, Trung Van Nguyen suggested the use of interdigitated flow field architecture [4] as shown in Figure 1.4. With the inclusion of dead ended inlet and outlet channels, gas is forced to flow into the porous media and back diffuse to the flow channels. Additionally, capillary force driven liquid water may well be swept through the gas shear force created at the channel-diffusion media interface.

Convective flow hydrodynamics of the interdigitated flow field together with diffusional flow characteristics usually provide the best fuel cell performance. However, compared to conventional designs relatively higher pressure must be supplied to direct the flow of gas into the porous diffusion media. In cases of using dry feed streams, one may observe electrode and/or electrolyte dehydration due to high mass transfer rates provided with this flow field at low current density region.

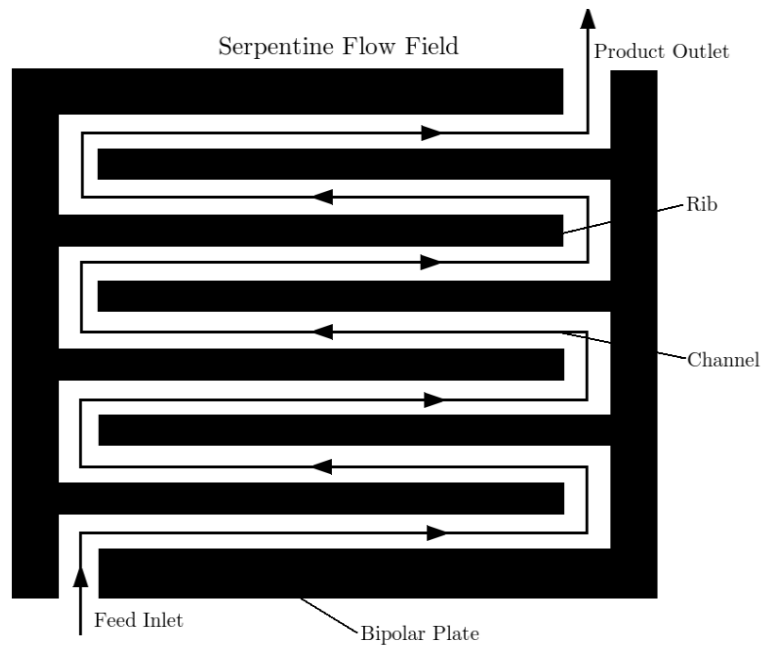


Figure 1.3: Serpentine flow field design for flow channels of PEM fuel cells

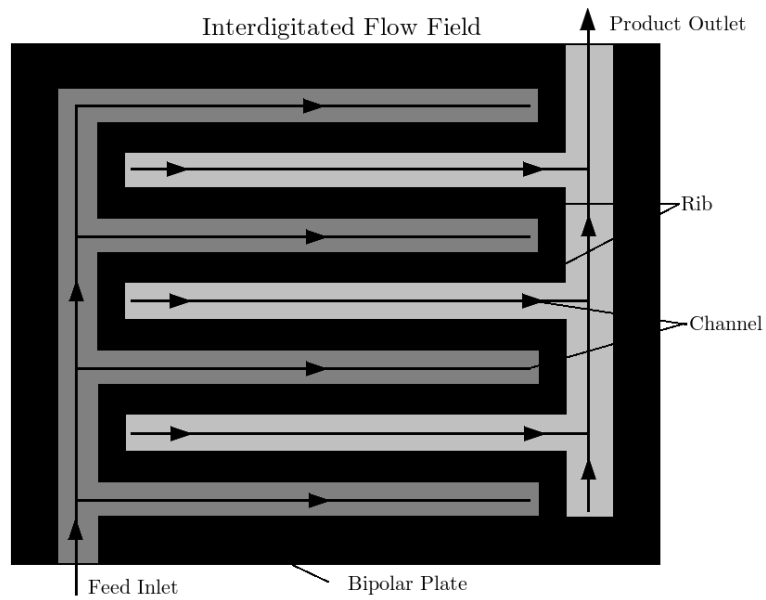


Figure 1.4: Interdigitated flow field design for flow channels of PEM fuel cells

Since most of the electrolytes require hydration to supply sufficient positive ion conductivity and, conversely, electroosmosis from anode to cathode may cause anode dehydration, control of water requires a delicate dynamic balance during the course of fuel cell operation. Another possibility for water management is the control of humidification system at anode or cathode. This may be achieved by traditional humidification, liquid water injection, vapor injection, and hydrogen recirculation at anode. Traditional humidification is the supply of feed streams by circulating gas through water bed at a certain temperature and humidification is limited by the saturation pressure of water. Each external humidification system introduces additional complication and cost to the fuel cell system design [5].

New rising trend is the use of novel materials like microporous layers to control the water dumping and keep a target phase saturation dispersion within the all fuel cell components. With the engineering of diffusion media [6] and catalyst layer [7], a better performance by internal control may be achieved.

1.5 Motivation and Research Objectives

Correct thermal and water management strategies are needed for PEM fuel cells to attain high power density and effective energy utilization. Conventionally, thermal and water management has been treated with fuel cell system design. This methodology usually downgrades the total system efficiency with additional auxiliary process inputs leading to increased order of complexity and cost [5]. Now, fuel cell technology has come to a new breakthrough providing new routes to resolve cost and durability issues through material improvement and engineering.

Several competing transport processes take place during the operation of a PEM fuel cell. These processes occur in three different phases, namely gas, liquid, and solid. In fact, solid phase is comprised of porous media and solid polymer electrolyte and each can be treated as separate sub-solid phase. In order to design efficient heat removal processes throughout the cell, one must have knowledge related to possible temperature distributions under different load cycles. It is almost impossible to detect the true temperature profile experimentally due to difficulties encountered in probing temperatures at every location. Experimental measurements of global temperatures

(e.g. probing local maximum temperature) will likely to mislead the direction and development of thermal management strategies.

In the last two decade, many researchers have addressed the problems associated with the thermal management through thermal models. However, almost all of the researchers have used a lumped heat evolution approximation. In other words, they solved the energy balance in single phase (e.g. solid phase) to find out the temperature profile in their models. The present study is motivated by the need to develop a proper mathematical model capable of capturing cold start up characteristics of a PEM fuel cell. With this purpose, an original two-phase energy balance approach for solid and gas phases is suggested to catch more accurate temperature distributions throughout the fuel cell as well as to predict the location of possible ice formation in cases of cold start. Nonlinearly coupled water and thermal management issues are discussed with evidence.

Liquid water is transported through capillary transport mechanisms within the porous media including catalyst layers, microporous layers, and macroporous layers. While developing mathematical model equations explaining liquid water flux inside the porous media, many researchers have implemented Leverett function to model the capillary pressure change with liquid water saturation levels. Leverett function originated from sand/rock type porous media and it is not very convenient to use this type of correlation for PEM fuel cells to describe the evolution and ejection of water from the porous matrix. Recently, experimental studies have been conducted to investigate the change of phase saturation with capillary pressure for various fuel cell components.

Another substantial goal of this Ph.D. study was to develop a two-fluid model to understand transport and removal of water from the fuel cell. In this dissertation, a gas-liquid two-phase flow based mathematical model is suggested to explore water profiles within the fuel cell by using experimentally measured capillary curves. Proper water management strategies are discussed in the text. Moreover, effect of wet-proof gas diffusion layer on fuel cell performance has been investigated.

Up to now, Butler-Volmer or Tafel type reaction rate expressions have been proposed commonly to model and simulate the cathode and the anode catalyst layers considering the electron transfer step being the rate limiting. In this work, Langmuir-Butler-

Volmer (LBV) type reaction rate expressions, derived from reaction mechanisms, are suggested to understand the effect of both the adsorption/desorption and the electron transfer steps involved in the reaction mechanisms on the overall PEM fuel cell performance. Anode and cathode rate expressions are coupled with agglomerate and thin film approach to investigate electrode kinetics in detail.

Anode and cathode electrochemical reactions cause significant voltage drop to develop during the course of fuel cell operation. Especially, oxygen reduction reaction at the cathode over common electrocatalysts (e.g. Pt/Vulcan[®] XC72) is sluggish with slow kinetics and creates several folds higher activation overpotential compared to hydrogen oxidation reaction at the anode. An understanding and development of the catalyst layers through both experimentation and modeling are essential.

Over the last decade, comprehensive research on the development of proton exchange membrane fuel cells resulted in significant increase in the catalytic performance of Membrane Electrode Assembly (MEA). Considering efficiency and cost requirements, one major challenge is arising from the electrocatalytic layers of the PEMFCs. For hydrogen oxidation and oxygen reduction reactions in these electrocatalytic layers, uniform and homogeneous dispersion of active metal catalysts as nanoparticles over electronically conductive carbon support is necessary to provide effective catalyst utilization. Catalytic activity of the fuel cell electrocatalysts depends on several parameters such as metal particle shape and size as well as particle size distribution resulting from catalyst preparation technique, structure of the catalyst support, and precursor properties. Accessibility of the active metal on the carbon support is also an important parameter [8].

There are various ongoing research studies related to the problems regarding the catalyst layers of PEM fuel cells for the enhancement of overall performance. Engineering of the catalyst layer by introducing some hydrophobic materials in correct proportions with respect to the carbon and ionomer is one possibility [7, 9]. This strategy helps improve water and thermal management throughout the fuel cell by providing hydrophilic and hydrophobic pathways facilitating two-phase transport. Another possibility is to lower platinum loading onto the active area so as to increase the utilization of platinum nanoparticles. Furthermore, for cost reduction and performance improvement, design

of binary and ternary electrocatalysts or non-platinum electrocatalysts with suitable catalyst support materials are important research fields.

To provide enhanced electrode kinetics, especially ORR electrocatalysis, through material engineering and system design is a challenging field in the fuel cell era. In the experimental part of the dissertation, to alleviate problems associated with the poor electrode kinetics, a novel ordered mesoporous carbon electrocatalyst support synthesis by template replication of silica was proposed as an alternative support material to conventional carbon black supports. Pt and Pt-Pd electrocatalysts were produced over these new highly porous carbon materials by microwave irradiation technique. Ex situ and in situ characterization of these nanomaterials were conducted through systematic analysis. PEM fuel cell performance of these promising electrocatalysts were reported in the results section of the dissertation.

CHAPTER 2

LITERATURE REVIEW

2.1 PEM Fuel Cell Models

The idea behind the mathematical modeling of proton exchange membrane fuel cells is to capture dominant transport mechanisms for each fuel cell component and to develop a basic understanding and an insight for further improvement of the fuel cells. This has to be done to reduce experimentation time and to focus on the major losses occurring during the course of the fuel cell operation. Only through a robust and reasonable model (realistic), one can fully gather information from the model so as to investigate and modify fuel cells to design in a more efficient and economical way. Modeling is an important tool that will not only help evaluate the feasibility of new fuel cell components through material engineering but also it will help improve fuel cell performance through system design.

Starting from the early 1990s, there have been various fuel cell modeling efforts reported in the literature, but quite a few of those models are versatile when the real phenomenon is concerned. Even for the today's modeling studies, researchers use the experimental data fits based on the early modeling studies even without demonstrating the accuracy of those previously conducted experiments. For this reason, several studies are dependent to the precision level of the experimental measurements performed in the past.

Historically, first fuel cell models [10–13] were developed for phosphoric acid fuel cells considering diffusion fluxes and reaction source terms in the porous diffusion media and catalyst layers respectively. These particular systems are resembling PEM fuel cells

in terms of their diffusion media and catalyst layers, however, the electrolyte treated is liquid (e.g. concentrated H_3PO_4) in nature. Based on the early PAFC models, various empirical or zero dimensional models and multi-dimensional models have been proposed in the last two decades.

2.1.1 Empirical Models

As a result of experimental observations under various operating conditions, researchers have proposed a number of zero dimensional models in the past [14–18]. These models were essentially composed of a single equation (for example see equation 3.6) predicting fuel cell performance with the experimental data fit.

Zero dimensional models are easy to use and one may obtain fairly reasonable rapid model predictions explaining the experimental data in an acceptable agreement. These empirical models may provide an insight for the order of some important model parameters like cell resistance, exchange current density or charge transfer coefficient. Researchers have gained valuable information by analyzing and interpreting the physical significance of these model parameters with the variation of some fuel cell components or with a change in operating condition. Some fundamental PEM fuel cell models were developed and improved with the help of these 0-D fit models.

2.1.2 Mechanistic Models

From the early empirical models, the two main fundamental models were derived. Bernardi and Verbrugge [19, 20] and Springer et al. [21] have proposed pioneer fuel cell models in the early 1990s. They have treated the fuel cell sandwich, composed of electrolyte, diffusion media, and catalyst layers. These models were isothermal and simplified, however, they served as a basis for today's models.

Bernardi and Verbrugge model assumes a fully hydrated membrane and incorporates porous-electrode equations and Stefan-Maxwell diffusion in the diffusion media and catalyst layers [19]. The model of Springer et al. did not use porous-electrode equations but did consider changing water content in the membrane for the first time. This allows for variable properties in the membrane such as conductivity and the water diffusion

coefficient [21]. Most models trace their roots back to these models.

Natarajan and Nguyen [22] have proposed a pseudo three-dimensional mathematical model for liquid water transport in the cathode gas diffusion layer. To capture transport effects that occur in the flow direction, the authors simulated their two dimensional model in succession, with each new solution using boundary conditions obtained by the previous solution. The authors have adjusted their previously developed constitutive relation explaining experimental capillary pressure data and they showed a comparison illustrating how the model results change with the capillary flow mechanism.

2.2 Optimal PEM Fuel Cell Operation

Although polymer electrolyte membrane fuel cells have the potential to become effective electricity generating devices, practical application of knowledge has not yet met those targets. Fuel cell cost and durability are the two substantial bottlenecks to be overcome prior to commercialization. For this reason, fundamental breakthroughs are required to design and engineer novel electrocatalysts, diffusion media, electrolyte, and bipolar plates. On the other hand, water and thermal management are coupled issues that play a significant role on the PEM fuel cell efficiency. For optimal operation, one must strike a balance between water and temperature distributions within the fuel cell environment [23].

2.2.1 Water Management and Cathode Flooding

In polymer electrolyte membrane fuel cells, control and transport of water is predominantly critical issue includes phenomena with contradicting outcomes on the fuel cell performance. Increased level of humidification is necessary in the solid polymer electrolyte to enhance ionic conductivity of the ionomer. Concurrently, hydrogen and oxygen must flow through the porous diffusion media and reach electroactive sites with minimal transport losses. To provide high level of hydration in the membrane, fuel and oxidant feed streams are generally humidified depending on the desired fuel cell performance characteristics. On the other hand, water generated with the oxy-

gen reduction reaction along with the water transferred from anode to cathode due to electro-osmotic drag alter the effective available gas pores at the cathode gas diffusion layer and microporous layer. This pore occlusion by water transport in the diffusion media inhibits the capability of oxygen to diffuse over the active three-phase boundary [24] within the electrocatalyst agglomerate. This phenomenon so called as *flooding* of the electrode causes to develop limiting current densities. Furthermore, clogging up of the flow channels by liquid water is associated to the durability issues [25] in the fuel cells. As a result of inadequate local reactant supply, specific potential deviations develop in the cell and this leads to severe carbon corrosion in the electrodes [26].

Water management strategies must involve several interrelated phenomena such as multiphase transport in the flow channels and MEA, transport of water between the fuel cell layers, and temperature gradient induced phase change of water. There are some technical hurdles for experimental detection of water saturation levels within the fuel cell environment. Some researchers have investigated the levels of saturation discontinuity at the porous diffusion media and catalyst layer interfaces by using in-situ neutron imaging [27, 28] and synchrotron X-ray radiography [29, 30]. For example, one may probably observe a saturation discontinuity at the GDL/CL interface and, however, a phenomena called *eruptive water ejection* will likely to occur at the channel/GDL interface causing droplets to form, grow, and accumulate. Difficulty in using experimental techniques have lead the researchers develop two-phase flow models from direct experimental knowledge.

Accurate two-phase model development necessitates the experimental measurement of capillary pressure data as function of different liquid phase saturation levels. Previously, most of the fuel cell researchers have used the Leverett function [31], originally derived for sand/rock type porous media, to express capillary pressure for the prediction of capillary transport mechanism through porous solid matrix (e.g. GDL, MPL, and CL) [32, 33]. In addition, Nam and Kaviany suggested a modified type of Leverett function to account for the hydrophobicity in the porous diffusion media [34].

Optimal diffusion media development and measurement of some bulk properties were reported in the last decade [35–40]. Only recently, there have been some attempts for the measurement of capillary pressure curves using some methods that are more realis-

tic and well suited for the diffusion media of the fuel cells. Kumbur et al. developed a capillary pressure-saturation expression with the use method of standard porosimetry (MSP) [41–43]. This approach provided a more precise prediction with the inclusion of wettability of the porous media. Wang et al. [44] proposed a gravimetric method to measure capillary pressure experimentally for catalyst layer, microporous layer, and macroporous layer. As a result of the efforts made in the last five years, an acceptable capillary pressure database have been formed for the estimation of two-phase flow. Now, researchers have directed their focus on the effect of temperature and compression on capillary pressure, which still remains as an important topic.

Cathode flooding phenomena and significance of liquid water levels in fuel cell components to the overall PEM fuel cell performance have enlivened a widespread research focus on liquid water transport. In order to develop a better mathematical model, it is essential to have some experimental insight for liquid water transport within the fuel cell diffusion media. Over the past few years, several researchers have concentrated on the visualization of liquid water in an operating PEM fuel cell. This knowledge of phase saturation distribution within the fuel cell is quite helpful to understand the capillary transport mechanism and so as to improve and tune the current two-phase PEM fuel cell models [45].

Liquid water visualization in an operating PEMFC is a challenging topic. One needs sophisticated in situ visualization methods due to the opaque character of diffusion media and bipolar plate materials. High temporal and spatial resolution of water can be provided through direct optical visualization methods. Neutron imaging [28] is one popular method for in situ water detection due to sensitivity of neutrons to hydrogen containing compounds and insensitive to traditional fuel cell components. However, limited availability (only a few place in the world, NIST, PSI, etc.) of this technique is a major problem. In addition, other techniques such as nuclear magnetic resonance (NMR) [46], X-ray microtomography [47], synchrotron X-ray radiography [29], environmental scanning electron microscopy (ESEM) [34, 48], and fluorescence microscopy [49] may provide beneficial visual information on the transport characteristics of liquid water in an operating PEM fuel cell.

2.2.2 Thermal Management and Cold Start up

In the last decade, many researchers have focused on water management strategies to optimize and understand the operation of polymer electrolyte membrane fuel cells. Controlling liquid water and water vapor gradients in each fuel cell component is very critical for achieving optimal performance with longer life times. Recently, mathematical modeling of PEM fuel cells is moving towards more on thermal models. To develop more realistic and accurate models, one must consider the strongly coupled interaction between the thermal and two-phase flow models.

Produced and transported water evaporates in the cathode catalyst layer due to heat generation resulting from the electrochemical reactions. Water vapor follows the temperature gradient and vapor starts condensing as it moves along the temperature gradient. In other words, this temperature difference induces phase change and results in mass transfer of water. Condensation of water occurs due to the exponential change in vapor pressure with temperature. This dynamic phase change of water with temperature gradient is sometimes called "*heat pipe effect*" in the open literature [50]. When fuel cell is operated at elevated temperatures in the high current density region with low levels of humidification, this phenomena becomes very significant due to larger temperature gradients observed throughout the MEA.

Difficulties encountered in the measurement of water saturation levels as well as probing dynamic temperature gradients in the fuel cell environment directed the researchers to develop nonisothermal models for the prediction of the effects of this coupled behavior. Recently, many thermal models have been published in the literature. Most of these models only accounted for the efficiency losses due to heat generation resulting from electrochemical reaction and joule heating. Lately, some researchers have addressed the impact of coupled water and thermal management issues on fuel cell performance by investigating temperature gradients with sophisticated nonisothermal models.

Nonisothermal modeling efforts for PEM fuel cells have started in the early 1990s. Fuller and Newman [51] analyzed the effects of temperature on fuel cell performance by assuming the fuel cell sandwich isothermal due to its small thickness compared

to channels. In their analysis, heat evolution occurs with the heat generation in the MEA and these thermal gradients create efficiency losses throughout the fuel cell. They showed that the rate of heat removal is a critical controlling parameter for the optimal operation.

Nguyen and White [52] assumed a uniform and constant temperature within the solid region due to high thermal conductivities. They explored the effect of heat transport from the solid phases to the gases and vice versa along the flow channels. They proved that back diffusion of water from cathode to anode is inadequate to maintain solid polymer electrolyte hydrated at high current densities. Accordingly, anode fuel feed must be humidified to keep membrane ionically conductive and prevent dehydration. In addition, they also addressed the need for humidification at the cathode stream in cases of supplying air instead of pure oxygen.

For optimum start up of a PEM fuel cell from a subzero temperature, a proper balance of heat and water removal rate must be provided. Before all the porous matrix in the cathode catalyst layer is filled with frost or ice, the fuel cell stack temperature must be elevated to freezing point. Ice formation theory at the electrode interface suggests that ice formation at the cathode catalyst layer is the key process controlling parameter that limits the start up characteristics of the fuel cell and causes a considerable potential drop throughout the cell [53].

Nandy et al. [54] stressed the effect of cold start up on PEM fuel cell performance characteristics from subzero temperatures. Nandy et al. conducted experimental and theoretical work on the impact of catalyst layer pore volume for isothermal and non-isothermal operation. They pointed out a self start up criteria relating electrolyte thickness, cell thermal mass, and ambient start up temperature with the use of ultra thin catalyst layers. In their work, they assume a spatially uniform cell temperature for the cold start problem and consequently they used lumped thermal modeling approach to predict the effect of temperature for fuel cells operating at subzero conditions.

In this dissertation, instead of using a single phase lumped thermal model, a two phase energy balance approach is suggested between gas and solid phases to capture the influence of several competing heat transfer mechanisms on overall fuel cell performance. Although liquid water moves over the solid matrix and heat transfer occurs between

solid and liquid, it is assumed that local equilibrium holds for solid and liquid phases. Hence, liquid temperature is considered to be same with the solid phase temperature. This original two-phase energy balance approach is a better representation of the physical system under investigation [55].

2.2.3 Electrode Kinetics

In PEM fuel cells, catalyst layers are multi-phase layers including solid carbon matrix, ionomer, and electroactive nanometal particles. Recently, researchers from the University of Kansas [7] proposed incorporation of Teflon based hydrophobic materials as an additional nanomaterial to overcome electrode flooding at the cathode. Addition of Teflon and ionomer (e.g. Nafion[®]) was achieved in a two-step process. Addressing the water management issue, this novel method of preparation will provide continuous hydrophobic pathways for the flow of reactants and hydrophilic pathways for the water transport within the catalyst layers. In modeling such a complex catalyst layer structure, global rate expression should be modified to account for the external mass transfer resistance due to the inclusion of additional hydrophobic layer.

2.3 Electrocatalyst Design

Development of fuel cell electrocatalyst plays a critical role in the commercialization of the PEMFCs in the aspects of the cost and the performance. Platinum is the most active metal for the anode and the cathode electrochemical reactions of PEMFCs. However, high cost of platinum, lack of availability of platinum, possibility of catalyst poisoning (e.g. CO poisoning), stability and durability issues are some of the critical problems that hinder the electrochemical reactions of the polymer electrolyte membrane fuel cells [56]. Platinum should be uniformly distributed over a porous conductive support material to increase the electrochemically active area. Supporting material for the PEM fuel cell electrocatalyst plays a significant role for the enhancement of the electrochemical reactions at the anode and cathode catalytic regions. Carbon supported Pt nanoparticles exhibit improved fuel cell performance in comparison to unsupported platinum catalysts [57].

2.3.1 Electrocatalyst Support Development

In PEM fuel cell environment, well-developed porosity, high surface area, good crystallinity, functional oxygen surface groups, stability under reactive environment, and chemical inertness are some critical key structural properties for carbon materials that directly control electrocatalyst preparation as well as sintering and electrocatalytic activity. Carbon support material should provide an extremely distributed electroactive phase to enhance electrode kinetics. In addition, electrical and thermal conductivity of the support material must be reasonably high to provide path for electron transfer and resolve thermal management issues.

Carbon is chemically stable in acidic and basic media and the structure can withstand elevated temperatures. For various carbon materials, desired pore size distribution can be supplied by adapting the pore structure. Most carbon structures possess hydrophobic character, however, modification of carbon surface can provide hydrophilicity. During the operation of a fuel cell, considering water management strategies, hydrophobic/hydrophilic character of the supporting material becomes very important especially at high current densities, where more water is produced. Cost of carbon support is lower compared to several other catalyst support materials. Additionally, active dispersed phase (e.g. Pt, Pd nanoparticles) can easily be recovered through burning away the carbon support. This feature is very critical since fuel cells usually contain precious metals for catalyzing the electrochemical reactions [58].

Microstructural characteristics of carbon may facilitate the interaction at the electrode–electrolyte–reactant interface (three phase boundary) resulting in an increased fuel cell performance. In carbon supported catalysts, the structure of the carbon support affects the catalyst properties such as the particle size, dispersion, metal–support interaction and the accessibility of the reactants to the active metal [59]. A proper catalyst support, usually carbon, must exhibit good electronic conductivity to create a pathway for the flow of electrons throughout the solid matrix [60]. Structure of the electrocatalyst support has a great impact on the PEM fuel cell performance. Pore texture of the carbon material should provide a pathway for the reactants and products from the active catalytic sites to the bulk of the fluid. This issue becomes especially critical at elevated currents, that is, when the water production rate is accelerated [61, 62]. Another im-

portant feature of the support material is that the support must have reasonably high surface area to increase the reaction rate for both the Hydrogen Oxidation Reaction (HOR) and the Oxygen Reduction Reaction (ORR) such that one must avoid the pore clogging phenomena by ionomer solution (e.g. Nafion[®] electrolyte solution) [63].

In PEMFC, the electrolyte is a solid polymer. To provide a network between the catalyst and the membrane, commonly Nafion[®] solution is used in the catalyst ink. There is also a need for an ordered macro/meso bimodal pore structure to provide an efficient pathway for the flow of protons from the active sites to the membrane. In case of carbon supports having a high percentage of micropores, addition of the Nafion[®] solution can inhibit the access of the reactants to the metal which will result in a decrease in the fuel cell performance. However, use of high surface area carbon supports with increased mesoporosity provides a high accessibility to the active dispersed phase of the electrocatalyst.

Considering high availability and lower costs, carbon black materials, like Vulcan XC72R, Black Pearl 2000, Regal 330, are the conventional electrocatalyst supports that are commonly used in low temperature fuel cells. It has random pores with varying sizes, which may lead to an inefficient multiphase transfer of reactants and products. In recent years, various carbon materials have been proposed as PEM fuel cell electrocatalyst support. Among these carbon supports, carbon nanotubes [64], ordered mesoporous carbons [65, 66], carbon aerogels [67], carbon nanofibers [68], carbon nanohorns [69], and carbon nanocoils [70] have attracted much more attention due their flexibility in pore texture tailoring, good mechanical properties, and improved electrical conductivities. Alternatively, polycrystalline boron-doped diamond (BDD) also provides appropriate properties for use in PEM fuel cells as electrocatalyst supports. Compared to the conventional carbon supports, BDD based materials can resist high current densities in alkaline and acidic environments and these materials possess excellent stability and corrosion resistance [71, 72].

Gallezot et al. [73] studied high surface area graphite support materials for the Ruthenium based catalysts. These graphitized materials are promising supports with good electronic conductivity and a moderate BET surface area of around 300 m²/g. One can also produce graphitized carbon blacks through recrystallization of the carbon black

at high temperatures (ca. 2500 °C). For this particular subclass of carbon materials, crystallization temperature sets the degree of graphitization.

Yoon et al. [74] reported the new class of Hollow Core Mesoporous Shell (HCMS) carbon materials with 2-5 nm uniform ordered average pore size. These spherical carbon particles were synthesized by using sub-micrometer size silica spheres [75] as templates. Structure of HCMS carbons can be altered by using different carbon precursors [76] and/or silica templates. For the proper passage of reactants and products with increased electrocatalysis, bimodal (meso/macro) and adjustable pore structure of HCMS carbon can facilitate the diffusion of hydrogen and oxygen as well as the water transport within the fuel cell [77].

2.3.2 Pt Based Electrocatalysts

Platinum on carbon (Pt/C) is one of the most effectively utilized electrocatalyst for PEM fuel cell applications [78–80]. In order to obtain optimal platinum loading, it is generally incorporated as nanoparticles on an electronically conductive material such as high surface area carbon supports. Optimization of the electrocatalyst particle diameter is a critical issue since the activity of an electrocatalyst increases as the reaction surface area of the catalytic material increases [61, 62]. To further increase the active surface area for the anode and cathode reactions, one must reduce the electrocatalyst particle diameter. However, local activity of the metal nanoparticles may decrease with shrinking catalyst particles. This phenomenon is known as particle-size effect. This effect is minimized by distributing catalyst nanoparticles over a high surface area supporting material [81].

Among the other catalyst preparation techniques [82, 83], microwave irradiation seems to be a promising method because of being time and energy efficient. Microwave irradiation has a wide variety of applications in chemistry. Many chemical reactions can be accelerated by the utilization of the microwave field which depends on the material having high dielectric constant. In the literature, it is shown that microwave irradiation can be used to prepare catalysts for different applications [84–86]. In this study, we revealed that microwave irradiation method can be effectively used to prepare considerably active electrocatalysts such as Pt, Pt–Ru or Pt–Pd incorporated over

carbon supports [87, 88].

2.3.3 Bimetallic Electrocatalysts

For the carbon supported fuel cell catalysts, carbon–metal interactions occur and additional active metal incorporation to the supported platinum catalysts may improve the platinum–carbon configuration [89]. Bimetallic Pt-Co/C cathode catalysts improved the durability in PEMFCs by reducing Pt dissolution and migration during the course of operation [90, 91]. Bimetallic Pt-Ru/C catalysts improved the carbon dioxide tolerance of PEMFCs. There are several ways to deposit metal alloys over the carbon supports. Of all the other catalyst preparation techniques, microwave irradiation is gaining an increasing attention because of being energy and time efficient.

Pd is another noble metal (widespread in the earth crust) with significant electrocatalytic activity towards anode and cathode electrochemical reactions of PEM fuel cells. It is less expensive and stable in acidic solutions. In the present work, palladium nanoparticles are studied for the possible replacement of active platinum nanoparticles.

CHAPTER 3

GENERAL MODELING APPROACH

There are several approaches for the mathematical modeling of polymer electrolyte membrane fuel cells. One distinction could be the level of interest in terms of the dimensions of the system under consideration. For example, a detailed surface electrode kinetics studies may be performed through molecular modeling and this type of modeling may provide some useful electrochemical reaction parameters.

Microscopic models focus on pore level modeling and one can gain very useful information through observing spatial and temporal change of system variables at the pore scale with the use of rigorous simulations. However, microscopic models require detailed information on the microstructure of the physical system. Most of the time, gathering such in depth knowledge, if not impossible, is not an easy task. In addition, conducting high resolution complete microscopic model simulations are realistic but computationally expensive. One other useful modeling strategy could be continuum models developed through averaging of the pore level models. These models are macroscopic models and may help investigate the global change of system variables.

3.1 Two-phase Flow Modeling

In PEM fuel cells, two-phase flow is the interactive flow occurring between liquid and gas phases inside flow channels and porous diffusion media at anode or cathode (e.g. GDL, MPL, and CL). For PEMFCs, liquid phase is always water, whereas gas phase is hydrogen and water vapor mixture at anode and air and water vapor mixture at cathode. It is reasonably assumed that there is no gas phase present within the

electrolyte. Moreover, dissolved water is considered to be transported (or dragged) within the solvation shells together with protons inside the solid polymer electrolyte.

Design, improvement, and optimization of flow channels necessitates the prediction of flow phases and flow characteristics depending on the interfaces formed between liquid and gas phases. Based on this information, pressure drop at anode or cathode and heat transfer nature of fuel cell system can then be determined.

Two-phase flow models can be categorized into separated flow models and homogeneous flow models. In this dissertation, considering a separated flow model approach, two distinct phase transport equations are written for the species in the liquid and gas phases. Solid, liquid and gas phase interactions play a significant role in heat and mass transfer inside the fuel cell components. Additionally, governing equations must involve source terms to account for phase change between liquid and gas phase [92].

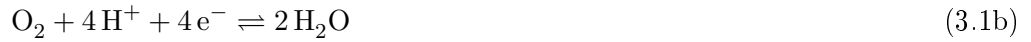
PEMFC model equations are generally derived for multiphase porous media based on volume-averaged Navier-Stokes equations. With the assumption of non-inertial flow, the basic and most general approach is the use of multifluid models (MFM) [26, 93–95]. Due to complexities involved in the multifluid models, researchers generally attempt to model PEM fuel cell system considering either multiphase mixture model (MMM) [96, 97] or unsaturated flow theory (UFT) [22, 98]. MFM treats the phases separately including the details of each phase, whereas MMM sums each phase and converts the system variables to mass-averaged counterparts.

In this dissertation, unsaturated flow theory is considered for the two-phase flow model. UFT is the reformulation of MFM with additional assumptions. In UFT, capillary pressure in the porous media is assumed to be the function of phase saturation in the liquid phase and gas phase pressure is assumed to be equal to the hydrostatic pressure of the gas. Although accurate models must rely on multifluid models, unsaturated flow theory based flow models give reasonable model predictions. Efforts are underway for the development of a multifluid model to simulate two-phase flow within the fuel cells.

3.2 Mathematical Modeling Strategy

In this study, a macro-homogeneous modeling approach is used to develop a mathematical model for PEM fuel cells. Although some information related to the real system is lost through averaging process, it is possible to model and simulate the fuel cell system with reduced number of variables such as diffusion media porosity or electrocatalyst agglomerate area per unit volume. In the macroscopic modeling strategy, properties are averaged over the microscopic level and it is assumed that physical domain is isotropic.

Before proceeding with the details of modeling strategy, an understanding on the nature of electrochemical reactions are required. Considering a single cell PEM fuel cell with pure hydrogen as fuel and oxygen or air as the oxidant, reactants go through the following half cell reactions at the prespecified operating conditions:



As a result of hydrogen oxidation reaction (HOR) at the anode and oxygen reduction reaction (ORR) at the cathode, water, electricity, and heat are generated by the following overall PEM fuel cell reaction:



Since goal is to produce electricity through the flow of electrons over a load, water and heat generated through reactions are the two critical issues to be controlled for optimized PEM fuel cell operation. Indeed, water and thermal management strategies are central focus of this dissertation. Depending on the local conditions liquid water or water vapor is produced at the cathode catalyst layer in the stoichiometric amount dictated by the system demand, say current draw rate. A simple energy balance over

the fuel cell system may demonstrate the amount of heat generated throughout the cell. Total heat flux generated through reaction may be defined as follows:

$$q_t = i(U_H - V) \tag{3.3}$$

where q_t is the total heat generated per superficial active area, i is the current density, V is the applied or observed cell potential, and U_H is the thermoneutral potential or more conveniently enthalpy potential. Enthalpy potential for the PEM fuel cell reaction reads:

$$U_H = -\frac{\Delta H}{2F} \tag{3.4}$$

Proton exchange membrane fuel cells directly convert the electrochemical energy of fuel and oxidant into electricity and the balance of the fuel cell system is released as heat. For example, a fuel cell operating at around 0.7 volts will almost release total amount of heat equal to the power drawn from the fuel cell. Thus, for large-scale applications like transportation, fuel cell stack will release much more heat at high current density and thermal effects on PEMFC performance become quite important.

Having identified the problems with water and thermal management, one develops a macro-homogeneous mathematical model considering two phase flow to explore water saturation profiles within the fuel cell sandwich. Heat flux given in equation (3.3) is oversimplified and, in fact, this expression can not be used to predict the exact locations of heat generation throughout the fuel cell. Thermal modeling approach is especially critical to improve heat removal through system design in cases like cold start. In the present work, a two-phase energy balance is proposed to gain useful information related to temperature distributions within the PEM fuel cell.

In evaluating the overall fuel cell performance, understanding the electrode kinetic parameters is necessary. To date, there have been significant efforts in modeling catalyst

layers with the agglomerate and thin film approach. Present work combines suggested reaction mechanisms with a global rate expression including effectiveness factor as well as thin-film approach for ionomer and water build up covering catalyst particles.

3.3 Governing Equations and Boundary Conditions

Mathematical model presented here is based on an Eulerian continuum modeling approach with a fixed domain rather than a Lagrangian frame. All PEM fuel cell components are considered excluding the flow channels, where the nature of the model equations vary sharply. Therefore, all governing, phenomenological or auxiliary equations are derived within the porous media and solid polymer electrolyte matrix.

Maxwell-Stefan type molar diffusion flux expressions are developed to account for the variation of multicomponent gas mixtures at the anode and cathode. Molar flux equations reduce to Fickian type diffusion at the anode with the assumption of only hydrogen and water vapor exist. A capillary transport mechanism approach is suggested for the transport of liquid water in the pores of gas diffusion layer, microporous layer, and catalyst layer. Rate of water exchange between liquid and gas phase is accounted with respect to variation of local vapor pressure with respect to saturation pressure. In general species transport equations, source terms due to electrochemical reactions (e.g. Butler Volmer equation) are incorporated with agglomerate and thin-film approach.

Transport mechanism of dissolved water within the electrolyte is generally induced by means of three mechanisms: electro-osmosis, diffusive flux due to concentration gradient, Darcy based hydraulic pressure effect due to water permeability in the membrane. Hydraulic pressure component of water flux equation inside the membrane may be neglected at equal and low anode and cathode pressures. However, electroosmosis and diffusive dissolved water flux play a significant role in the hydration level of the electrolyte.

Solid and gas phase energy balances are used to investigate the temperature effects on fuel cell performance. It is assumed that there is a thermal equilibrium between solid and liquid phase. Several heat generation source terms are accounted and included in the solid phase energy balance.

Ionic and solid phase charge transport equations are based on Ohm's Law. They describe proton transfer in the electrolyte and electron transfer in the porous diffusion media respectively. Since the solid matrix (carbon paper, microporous carbon, and Pt/C electrocatalyst) exhibit sufficiently high electrical conductivity, it is reasonable to omit the potential variation in the solid phase.

Initial and inlet operating conditions (e.g. Temperature, pressure, and relative humidity) are set at the channel gas diffusion layer interface. Boundary conditions are defined at fuel cell component layer interfaces, continuous fluxes for the transfer of variables into the adjacent physical domain. Since diffusivities of oxygen and hydrogen are small within the electrolyte, gas cross-over is ignored and gas phase fluxes are set to zero within the electrolyte phase.

In order to solve for local variable profiles, one must know the exact pore structure through serious porosimetry experiments and visualization techniques coupled with stochastic modeling. Since gas pores are function of liquid phase saturation, it is a difficult task to capture true structure during the course of operation of a PEM fuel cell. For this reason, mathematical model variables presented in the dissertation are volume averaged quantities for the porous media. For example, considering average temperature in the solid phase or gas phase, some information will be lost due to averaging process, however, still useful information might be provided for the control volume representing the typical pore structure for gas diffusion layer or microporous layer. For additional information, Stephen Whitaker [99] provided brief derivations on volume averaging of the transport equations for various cases including flow in porous media.

3.4 PEM Fuel Cell Performance Limitations

Nonlinearly coupled water and thermal management are critical to achieve optimal performance during the course of fuel cell operation. Efficiency of a fuel cell may be limited by flooding with liquid water at the cathode or, conversely, drying of anode is another route for decrease in overall cell performance. Flooding or inadequate water removal leads to important mass transfer limitation within the electrodes. In other words, fuel and oxidant starving at the electrocatalytic regions may occur due to

limited mass transfer.

Moreover, insufficient heat removal especially at elevated temperatures and current densities might result in significant losses in fuel cell performance. Therefore, elegant heat removal techniques are required to optimize the cell operation. Electrochemical reactions taking place at anode and cathode catalyst layers create overpotential and cause a voltage drop depending on the electrode kinetics. Particularly, slow kinetics of oxygen reduction reaction at cathode sets a severe limitation to fuel cell performance.

3.4.1 PEM Fuel Cell Polarization Curve

Total fuel cell performance is characterized by polarization and power curves. Figure 3.1 depicts the typical polarization curve with cell potential limits and significant performance affecting factors. As shown in the figure, thermoneutral potential is described as the available highest input energy and it is sometimes referred to as enthalpy potential as shown in equation (3.4).

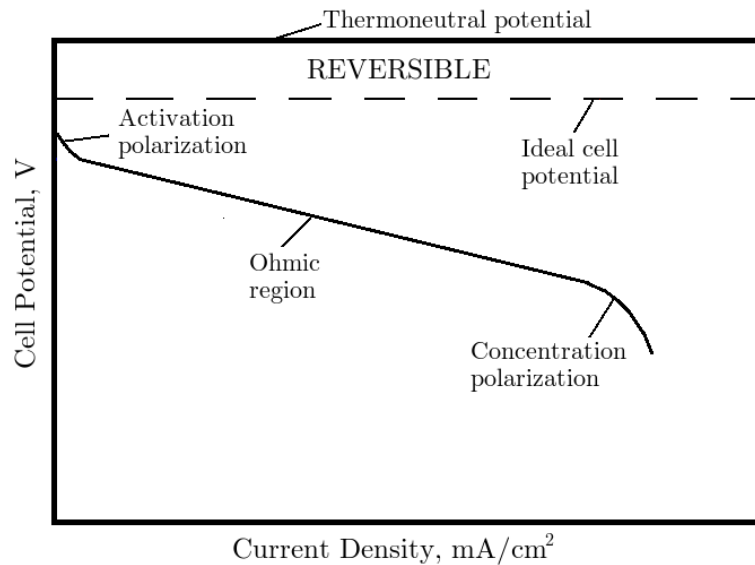


Figure 3.1: Illustration of polymer electrolyte membrane fuel cell polarization curve

Reversible ideal cell potential is defined in terms of useful chemical input energy to the fuel cell system. One can define the reversible cell potential through Gibbs free

energy as follows:

$$U^\circ = -\frac{\Delta G}{2F} \quad (3.5)$$

Activation polarization region, ohmic region, and mass transport region are the three distinct regions (Figure 3.1) exhibiting the relative impact of losses on fuel cell performance. Only through careful analysis of the polarization curve, one can gain a useful perception and understanding related to the operation of the particular fuel cell system run under certain conditions.

At low current density region, activation losses occur due to the rates of anode and cathode electrode kinetics. High cathode overpotential of the oxygen reduction is the dominant portion of the losses resulting from activation polarization. A similar effect may be observed at the anode if the fuel is not pure and contains small amounts of CO for example. In fact, one major ongoing research field is on electrocatalyst development to overcome sluggish cathode reaction for PEM fuel cells.

At moderate current densities, ohmic losses dominate leading to a gradual potential drop with the current. This rather linear region directly correlates with the cell resistance due to ionic, contact, and electronic losses. Ohmic losses are primarily from ionic losses within the electrolyte and catalyst layers. In some cases, depending on the operating conditions and cell architecture, electronic and contact resistances may play an important role in lowering fuel cell performance in ohmic region.

When high currents are drawn from the PEM fuel cell, concentration polarization region dominates due to mass transfer limitations. Mass transfer limitation occurs when fuel and oxidant are unable to access electroactive sites in the catalytic regions. This effect becomes severe at cathode due to flooding by liquid water and oxygen can not reach electrocatalyst surface and causes a major limitation. In addition, positive ion and electron transfer may also act as a barrier in the mass transfer region leading to a performance limitation resulting in the maximum possible current density (limiting current density).

The following zero dimensional model equation [100] can be used to estimate the fuel cell polarization curve. Some useful electrode parameters and an overall cell resistance might be evaluated with quick predictions of the system behavior for the experiments conducted.

$$E = U^\circ - \frac{RT}{\alpha F} \ln \frac{i}{i_o} - R_{ohm} i - \frac{RT}{nF} \ln \frac{i_L}{i_L - i} \quad (3.6)$$

where E is the cell voltage, i is the superficial current density of the fuel cell, α is the charge transfer coefficient, i_o is the exchange current density, R_{ohm} is the ohmic cell resistance, n is the number of electrons transferred in the reaction, and i_L is the limiting current density.

First term in equation (3.6) is standard cell potential at the operating temperature and pressure. Second term represents the activation polarization loss due to electrochemical reaction based on Tafel kinetics. Third term reflects the overall cell resistance with an approximation to the linear region of the polarization curve. Finally, the last term signifies the relative importance of reactants mass transfer. The limiting current density is introduced as a model parameter. Limiting current density is the maximum possible current density that can be attained in an operating PEM fuel cell. Due to severe flooding, reactions cannot proceed beyond limiting current density and fuel cell dies out.

3.4.2 Electrochemically Active Surface Area

Cyclic voltammetry (CV) is a well-established diagnostic tool for characterizing the electrocatalytic layers of polymer electrolyte membrane fuel cells. A standard catalyst layer includes carbon supported active nanometals (e.g. Pt, Pd) and a proton conducting ionomer such as Nafion[®]. The electrochemical activity of the anode or cathode electrode is directly related to the extent of formation of a three-phase boundary where fuel or oxidant, proton conducting ionomer, and electroactive catalyst sites (e.g. Platinum surface) are in contact with one another [101].

Fuel cell catalyst layers may be explored for their electrocatalytic activity by *in situ*

or *ex situ* cyclic voltammetry experiments [102, 103]. A two-electrode configuration is used in the case of *In situ* experiments. One of the electrodes serves as both reference and counter electrode, whereas the other one is the working electrode, usually cathode, used for investigating the electrocatalytic activity. Figure 3.2 demonstrates a typical cyclic voltammogram for an anode Pt electrode.

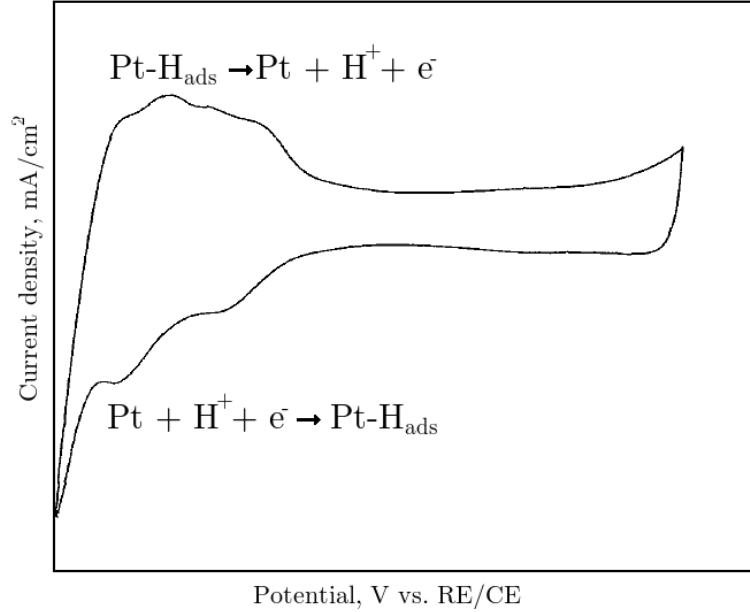


Figure 3.2: Depiction of cyclic voltammogram of PEMFC (fuel cell anode/cathode: H_2/N_2)

On the other hand, *ex situ* experiments are conducted to examine the electrode kinetic properties usually with a three-electrode cell configuration dipped into an acid solution (e.g. 0.5 M HClO_4) serving as electrolyte to simulate membrane in PEM fuel cells. For example, considering the following reduction of positive ions (H^+) and subsequent adsorption of hydrogen atoms on the electrocatalyst surface, one can calculate the electrochemically active surface area.



Hydrogen atom adsorption charge density, q , for the reaction (3.7) can be computed using the cyclic voltammetry scans. The electrochemical active surface area (ESA) of

the platinum electrocatalyst may be calculated with the following equation:

$$\text{ESA}(\text{cm}^2 \text{ Pt} / \text{g Pt}) = \frac{q}{\Gamma m_{Pt}} \quad (3.8)$$

where $\Gamma=210 \mu\text{C}/\text{cm}^2$ is the well-known charge density quantity for the reduction of a monolayer of protons on Pt and m_{Pt} is the electrocatalyst loading. In addition, electrocatalyst utilization may be found by calculating the ratio of ESA to the specific area of the active platinum metal. This fraction indicates the availability of the electrocatalyst for the electrode reaction [104, 105].

CHAPTER 4

PROTON EXCHANGE MEMBRANE FUEL CELL MODEL

Mathematical model is developed for the understanding of various transport and electrochemical reaction phenomena occurring during the operation of PEM fuel cells. Among these transport processes, major focus is given to the modeling of catalyst layers with detailed hydrogen oxidation and oxygen reduction reaction kinetics at the anode and cathode respectively. Besides the electrochemical reactions, water and thermal management are quite important to optimize and design fuel cells. In order to capture these phenomena correctly, two-phase mass and heat transport model equations are proposed.

4.1 Model Description

A non-isothermal, two-phase, steady state PEM fuel cell mathematical model is developed with detailed electrode kinetics. Up to now, Butler-Volmer type reaction rate expressions have been proposed commonly to model and simulate the cathode and the anode catalyst layers considering the electron transfer step being the rate limiting. In this work, Langmuir-Butler-Volmer (LBV) type reaction rate expressions are suggested to understand the effect of both the adsorption/desorption and the electron transfer steps involved in the reaction mechanisms on the overall PEM fuel cell performance.

Previously, Vogel et al. [106] proposed and validated that the dual site adsorption of hydrogen onto active platinum sites (Tafel reaction) might be the rate limiting step for the hydrogen oxidation reaction. Adžić from Brookhaven National Laboratory

[107] reviewed several possible reaction mechanisms for the oxygen reduction reaction. Among these ORR reaction mechanisms, one possible route involves the single site adsorption of oxygen onto platinum sites as the rate determining step.

In the present study, reaction mechanisms are suggested for both hydrogen oxidation and oxygen reduction reactions considering the adsorption of the reactant gases being the rate limiting. This novel catalyst layer modeling approach will enable us to understand the comparative effects of several electrode kinetics parameters on performance of the PEM fuel cells.

Catalyst agglomerates are assumed to be formed in the anode and cathode catalyst layers. Catalyst agglomerates are assumed to be in the spherical shape including a porous carbon support and active metal nanoparticles (e.g. Pt nanoparticles) that are homogeneously distributed over the meso/macro bimodal porous carbon support structure. This structure forms the primary reactive agglomerate particle. Particle size and cluster size may differ depending on the preparation and operating conditions. Different number and diameter of the electrocatalyst agglomerates form the agglomerate clusters. Several agglomerate clusters are in contact with each other and binded with a proton conducting ionomer.

An effectiveness factor relation is developed for the reactions considering the internal mass transfer resistances for the electrocatalyst structure. Agglomerates and agglomerate clusters are assumed to be surrounded by some random fraction of a thin Nafion ionomer film. Through the reaction, back-diffusion, electro-osmotic drag and humidification levels of the transport medium at the fuel cell operating conditions, a thin layer of liquid water may build up around the clusters and this may act as a barrier to the diffusion of oxygen at the cathode and even hydrogen at the anode.

Understanding the cold start characteristics of a PEM fuel cell is critical to design and develop fuel cells that are capable of surviving at subzero temperatures. If the internal fuel cell temperature falls below freezing point during the start up, ice may form and hinder the transport of reactants inside the pores. It is also known that the cyclic exposure of fuel cell to cold start has a negative effect on the fuel cell durability [53]. Therefore, thermal management, electrochemical and water management issues must be resolved and optimized simultaneously to overcome several possible performance

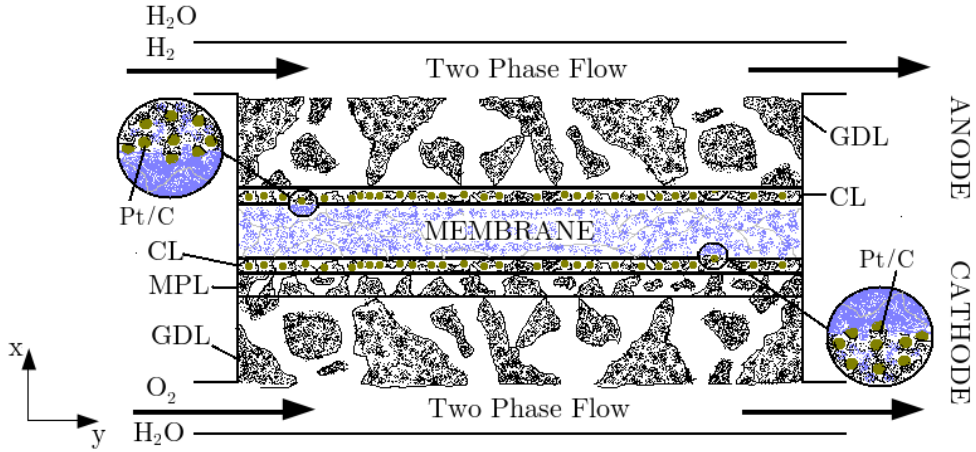


Figure 4.1: Illustration of 2-D physical domain for PEM Fuel Cell

losses.

To be able to capture the effect of several heat transfer mechanisms on fuel cell performance, a two phase energy balance is suggested between gas and solid phases. Liquid phase temperature is considered equal to the solid phase temperature. Two phase energy balance approach becomes much more important when there is a significant temperature difference between the fuel cell temperature and the reactant inlet temperature. A parametric analysis will be presented to reflect the comparative effects of different heat transfer mechanisms on the electrode kinetics.

4.1.1 Physical Domain for PEM Fuel Cell

Physical domain for PEM fuel cell mathematical model contains macroporous and microporous diffusion media, catalyst layer at the cathode and a macroporous diffusion media and catalyst layer at the anode. In addition, there is a thin solid polymer membrane (e.g. Nafion[®]) in between anode and cathode acting as electrolyte for the fuel cell. Figure 4.1 is a simplified illustration of the physical system in two dimensional Cartesian system.

4.1.2 Mathematical Model Assumptions

There are several assumptions imposed during the development of the mathematical model. Some of them may critically affect the system behavior and their effects on overall performance are discussed in Chapter 8. Other assumptions are reasonable within the limits of the mathematical model. The following assumptions are assumed to hold for a low temperature polymer electrolyte fuel cell operating at atmospheric pressure:

1. Gas phase is assumed to obey the ideal gas law.
2. Pressure drop in the gas phase in porous medium is insignificant.
3. Fuel cell operates at steady-state conditions.
4. Flow in the channels are considered laminar.
5. Liquid phase and solid phase are in thermal equilibrium.
6. Solid polymer electrolyte is assumed to be impermeable to gas flow (no gas cross over).
7. Electrocatalyst pellets are in spherical geometry in the catalyst layers.
8. Electrocatalyst pellets are covered with the ionomer film and form spherical agglomerates.
9. Electrocatalyst agglomerates are covered with liquid water.
10. Water produced in the electrocatalyst agglomerate film at the cathode catalyst layer is assumed to be in the liquid phase.
11. Uniform physical properties (electrical conductivity and thermal conductivity) are assumed in x and y directions. Isotropic and homogeneous diffusion media, catalyst layers, and membrane are considered.
12. Electronic phase potential drop in the electronically conductive solid porous matrix is negligible.

4.2 Model Development

There are several coupled and interrelated transport phenomena occurring during the operation of polymer electrolyte membrane fuel cell. Emphasis is given to the development of mathematical model equations for two-phase flow, two-phase energy balance, and detailed electrode kinetics considering various external and internal resistances.

4.2.1 Two Phase Flow

Sluggish oxygen reduction rate at the cathode is one major performance limiting factor for PEM fuel cell. If water management is inadequate during the course of operation, cathode side of the fuel cell will become flooded. This usually happens when the amount of water generated by the reaction and the water transported by the electro-osmotic drag is higher than the back diffusion of water to the anode and removal of water from cathode to the channels by evaporation and through liquid water transport by capillary mechanism. Therefore, to capture the real phenomena, two-phase flow analysis of the PEM fuel cell is essential for systems especially operating at low temperatures.

4.2.1.1 Gas Phase Species Conservation

Species conservation equation can be written for the porous media including gas diffusion layer, microporous layer, and catalyst layer. Similar equations are developed for both anode and cathode regions. Rate term, R_i , (source term) in the general species equation could be written for hydrogen oxidation reaction rate, oxygen reduction reaction rate. Moreover, source term could also be the rate of water production in the liquid phase species (liquid water) conservation or gas phase species (water vapor) conservation. Generalized species conservation equation, based on molar fluxes, can be written at steady state as follows [108]:

$$-\nabla \cdot N_i + R_i = 0 \tag{4.1}$$

Molar flux, N_i , of gas phase species at the anode and cathode could be derived by considering various diffusional terms. Although Knudsen diffusion may play some significant role in the transport of species, in this work, this particular effect is neglected. Binary (anode) and ternary (cathode) gradient of mole fractions of gas phase species are accounted with the following form of Maxwell-Stefan equations [109]:

$$\nabla y_i = \sum_{j=1}^n \left[\frac{1}{C_t D_{i,j}^{eff}} (y_i N_j - y_j N_i) \right] \quad (4.2)$$

For binary gas mixtures at low pressures, binary diffusivity, $D_{i,j}$, is inversely proportional to the pressure, increases with increasing temperature and it is almost independent of composition for a given gas pair. The following Slattery and Bird approximation can be used for the computation of binary diffusion coefficients at low pressure [110]:

$$PD_{ij} = a \left(\frac{T}{\sqrt{T_{c,i} T_{c,j}}} \right)^b (P_{c,i} P_{c,j})^{\frac{1}{3}} (T_{c,i} T_{c,j})^{\frac{5}{12}} \left(\frac{1}{M_i} + \frac{1}{M_j} \right)^{\frac{1}{2}} \quad (4.3)$$

Available gas pores for the flow of gaseous mixtures are directly related to the liquid water saturation level in the pores. Tortuosity of the porous media is a critical parameter affecting the transport of gas phase species. To account for the tortuosity of the diffusion media, generally accepted Bruggemann correction factor is used. Bruggemann correlation is not an accurate representation for the tortuosity but it is rather easy to implement and gives reasonable predictions. Considering the liquid phase saturation dependent porosity change and the Bruggemann factor[111], binary diffusivities can be corrected to account for the effective diffusivity in the porous medium:

$$D_{i,j}^{eff} = \left[\varepsilon_o (1 - s)^{1.5} \right] D_{i,j} \quad (4.4)$$

where ε_o is the intrinsic porosity of the porous media including gas diffusion layer, microporous layer or catalyst layer. Generally, diffusion of a gas through a capillary may take place by molecular diffusion and Knudsen diffusion. For equimolar counter-current diffusion and also for dilute systems composite diffusivity can be formulated with the Bosanquet formula:

$$\frac{1}{D_t} = \frac{1}{D_{i,j}} + \frac{1}{D_K} \quad (4.5)$$

Diffusion is a dominant transport mechanism in the fuel cell environment in the porous media. Effective diffusivity of the gas is an interplay between Knudsen diffusion and molecular diffusion. The Knudsen number is defined as the ratio between the molecular mean free path and the pore diameter.

$$Kn = \frac{\lambda_m}{d_p} \quad (4.6)$$

Using the kinetic theory of gases, one can estimate the Knudsen diffusion coefficient as [108]:

$$D_{K,i} = \frac{2}{3} \left(\frac{8RT}{\pi M_i} \right)^{\frac{1}{2}} r_p \quad (4.7)$$

Effective diffusivity is related to the composite diffusivity by the following relation:

$$D^{eff} = D_t \frac{\varepsilon}{\tau} \quad (4.8)$$

Composite diffusivity is a function of pore radius if the Knudsen diffusion is important. In that case, effective diffusivity can be computed using the following relation:

$$D^{eff} = \frac{1}{\tau} \int_0^\infty D_t(r_p) f(r_p) d(r_p) \quad (4.9)$$

Source terms appearing in the gas phase species conservation equation (4.1) are due to the electrochemical reactions in the catalyst layers and the phase change throughout the porous medium. If the gas phase species is water vapor, the source term is the rate of water vapor produced or depleted depending on the local temperature and pressure. Interfacial molar rate of the water due to phase change can be defined as [22, 98]:

$$R_{H_2O} = \begin{cases} \frac{k_e \varepsilon_o s \rho_w}{M_w} (P_{H_2O} - P_{H_2O}^{sat}) & P_{H_2O} < P_{H_2O}^{sat} \\ \frac{k_c \varepsilon_o (1-s) y_{H_2O}}{RT_g} (P_{H_2O} - P_{H_2O}^{sat}) & P_{H_2O} > P_{H_2O}^{sat} \end{cases} \quad (4.10)$$

where k_c and k_e are the water condensation and evaporation rate constants respectively. The direction of mass transfer from liquid phase to gas phase or gas phase to liquid phase is defined with pressure gradient, which controls the evaporation or the condensation rate with respect to saturation pressure of water.

Some of the physical properties of liquid water are listed in Appendix A.1. Following correlation is the exponential nonlinear fit for the saturation pressure of water with respect to temperature. Considering the exponential behavior of the curve, this saturation pressure data significantly affects the fuel cell behavior under the operating conditions (see Appendix A.2).

$$\ln P_{H_2O}^{sat} = -5.0937 + 7.1081 \times 10^{-2} T_g - 2.5155 \times 10^{-4} T_g^2 + 5.0125 \times 10^{-7} T_g^3 \quad (4.11)$$

4.2.1.2 Liquid Phase Species Conservation

Liquid water transport in the porous matrix of the fuel cell is dominantly driven by capillary force. Liquid water ejection mechanism through catalyst layers and diffusion media can be represented with an average flux expression. Molar flux of liquid water in the porous media reads:

$$N_w = -\frac{\rho_w K_w}{M_w \mu_w} \nabla P_l \quad (4.12)$$

where K_w is the liquid phase saturation dependent liquid water permeability and P_l is the liquid phase pressure. ρ_w , μ_w , and M_w are the density, viscosity, and molecular weight of liquid water respectively. Liquid and gas phase pressures are related through the capillary pressure:

$$P_c = P_g - P_l \quad (4.13)$$

Gas phase pressure, P_g , change is considered as insignificant in the physical domain of interest. Therefore, using equation 4.13 liquid water molar flux can be rewritten in terms of capillary pressure, P_c , as follows:

$$N_w = -\frac{\rho_w K_w}{M_w \mu_w} \nabla (-P_c) \quad (4.14)$$

Capillary pressure is function of liquid phase saturation and experimentally measured capillary transport data is implemented to predict the liquid water transport through the porous medium. Liquid water permeability is dependent on the saturation level. There are various relations proposed for the relation of liquid water permeability with the liquid phase saturation. As a first estimate, the following linear expression is used for $K_w(s)$:

$$K_w = K_{w,o} s \quad (4.15)$$

where $K_{w,o}$ is the permeability of liquid water at 100% saturation level. As another approximation to relate liquid water permeability as function of saturation, the following cubic version of liquid permeability empirical correlation can be used in the

mathematical modeling of PEM fuel cells [112].

$$K_w = K_{w,o}s^3 \quad (4.16)$$

With the developed liquid water visualization techniques, recent studies have shown that cubic permeability relation (4.16) predicts a higher liquid permeability especially at the low saturation conditions [113, 40]. In that case, a higher order relation (equation (4.17)) may be used together with a cubic correlation such that one of the correlations can be selected depending on the saturation level of the media.

$$K_w = K_{w,o}s^{4.5} \quad (4.17)$$

Inserting linear permeability expression 4.15 into liquid water flux expression, the final form of the flux can be written as:

$$N_w = -\frac{\rho_w K_{w,o}}{M_w \mu_w} \left(-\frac{dP_c}{ds} \right) s \nabla s \quad (4.18)$$

It is convenient to express capillary transport variables in a lumped parameter so called as capillary diffusivity. Capillary diffusivity is a measure of liquid water transport capability of the specific porous media and it is dependent on the experimental capillary gradient data. Capillary diffusivity can be defined as:

$$D_c = -\frac{K_w}{\mu_w} \frac{dP_c}{ds} \quad (4.19)$$

In order to investigate the two-phase flow characteristics inside the porous media, one needs capillary pressure data for the variation of liquid phase saturation level within the macropores or micropores. In the early two-phase flow models, Leverett J function have been used very frequently for the capillary function expression in porous media.

Although this empirical correlation gives reasonable predictions to some extent, this correlation was originally proposed for sand/rock type porous media [31, 32]. Therefore, it is not physically accurate representation of the capillary pressure within the diffusion media and catalyst layers of PEM fuel cells. Capillary pressure in the fuel cell porous media is related by the Leverett function as follows [33, 96]:

$$P_c = \sigma \cos(\theta_c) \left(\frac{\varepsilon_o}{K_{w,o}} \right)^{1/2} J(s) \quad (4.20)$$

where $J(s)$ is the Leverett function. Considering wettability of the diffusion media (e.g. contact angle), Leverett function can be related to the liquid phase saturation level with a piecewise function as follows [114]:

$$J(s) = \begin{cases} 1.417(1-s) - 2.120(1-s)^2 + 1.263(1-s)^3 & \theta_c < 90^\circ \\ 1.417s - 2.120s^2 + 1.263s^3 & \theta_c > 90^\circ \end{cases} \quad (4.21)$$

Figure 4.2 illustrates the capillary curve for Toray 090 gas diffusion layer [40, 115, 116]. Toray 090 material was hydrophobized to facilitate the removal of water and this gas diffusion material exhibits a contact angle of about 112° .

There are some recent experimental studies to investigate the dependence of the capillary pressure on saturation level for the porous media including gas diffusion layer, microporous layer, and catalyst layer. In the majority of the previously reported PEM fuel cell models, Leverett function were used to define the capillary pressure as function of liquid phase saturation.

Typical capillary pressure change with liquid water saturation level is provided in Appendix A.3. The following form of capillary pressure correlation can be used for the liquid water transport within the porous media and catalyst layers [44]:

$$P_c = d \left[e^{-a_1(s-c)} - e^{a_2(s-c)} \right] + b \quad (4.22)$$

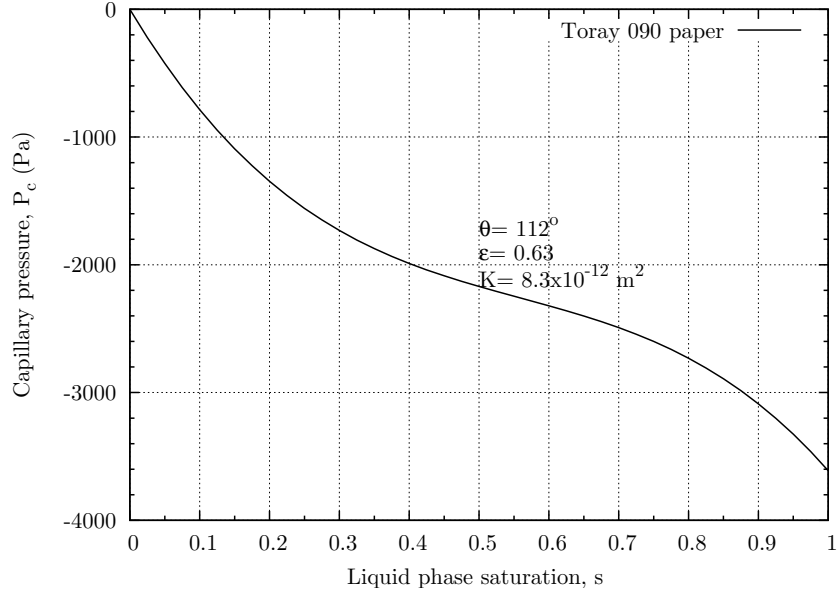


Figure 4.2: Capillary pressure curve for Toray 090 paper using Leverett function at 80 °C

The parameters d , a_1 , a_2 , c , and b are determined by curve fitting of the experimental data obtained at room temperature. Predicting the change of capillary curve experimentally at higher temperatures is still a challenge to be resolved by the researchers. Empirical correlation fitting parameters for equation (4.22) are listed in section 4.5 for the porous media including gas diffusion layer, microporous layer, and catalyst layer.

4.2.1.3 Transport of Water inside the Electrolyte

There are various solid polymer electrolytes that are capable conducting protons. While conducting positive ions within the structure, electrolytes act as a barrier for hydrogen and air and as well as electrons. Nafion[®], a common fuel cell electrolyte, has the molecular formula of $C_7HF_{13}O_5S \cdot C_2F_4$ with the chemical structure given in Figure 4.3:

There are several proposed mechanisms for the transport of positive ions (protons) within the solid polymer electrolyte. One possibility is the movement of protons through *hopping* mechanism over the SO_3^- sites. Figure 4.4 is a simplified demon-

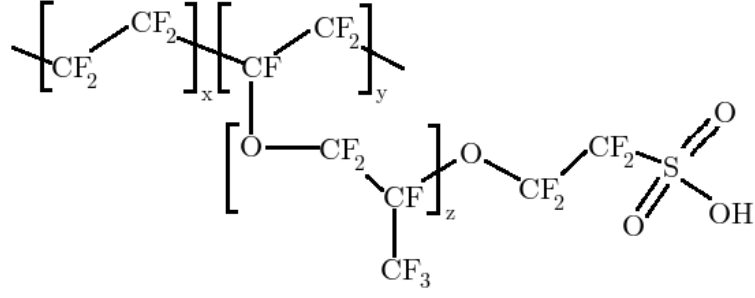


Figure 4.3: Chemical structure of Nafion[®] electrolyte

stration of the mechanism for a typical Nafion[®] 112 electrolyte.

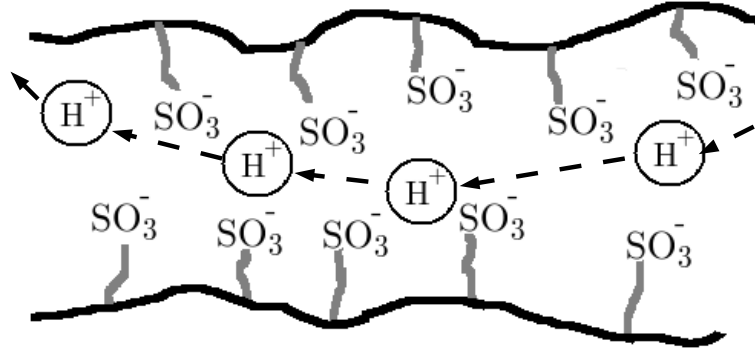


Figure 4.4: Conceptual illustration of proton transport within the Nafion[®] membrane

Generalized species transport expression within the intermediately dilute solutions can be written based on Nernst-Planck equation [117, 118]:

$$N_i^s = -\frac{z_i D_i F C_i \nabla \phi_m}{RT} - D_i \nabla C_i - D_i C_i \nabla \ln a_i + C_i u \quad (4.23)$$

Water species is free of charge and if ideal solution behavior is assumed, the transport of water inside the electrolyte may be rewritten including the flux induced by electro-osmotic drag as follows [119, 120]:

$$N_w^m = \frac{i_m}{F} n_d - D_w^m \nabla C_w^m - \frac{\rho_w K_w^m}{M_w \mu_w} \nabla P_t \quad (4.24)$$

Essentially, concentration of water in the electrolyte phase and electro-osmotic drag phenomenon within the membrane drive the water transportation inside the membrane. Therefore, omitting the net water transport due to bulk flow, water transport equation within the solid polymer electrolyte reads [55]:

$$N_w^m = \frac{i_m}{F} n_d - D_w^m \nabla C_w^m \quad (4.25)$$

Electro-osmotic drag coefficient, n_d is a measure of ability of electrolyte to transfer dissolved water per mole of proton and it is expressed as function of electrolyte water content as [21] :

$$n_d = 2.5 \frac{\lambda}{22} \quad (4.26)$$

In order to estimate the transport of water within the electrolyte, an empirical correlation is required for the diffusivity of water within the electrolyte. There are two widely accepted correlations available in the literature for the diffusion coefficient of water inside Nafion[®] membrane. Wang and Savinell [121] proposed the following piecewise function as function of water content λ from the experimental results of Springer et al. [21]:

$$D_w^m = \begin{cases} 10^{-6} e^{2416 \left(\frac{1}{303} - \frac{1}{T_s} \right)} (-3.1 + 2\lambda) & 2 < \lambda \leq 3 \\ 10^{-6} e^{2416 \left(\frac{1}{303} - \frac{1}{T_s} \right)} (6.89 - 1.33\lambda) & 3 < \lambda \leq 4 \\ 10^{-6} e^{2416 \left(\frac{1}{303} - \frac{1}{T_s} \right)} (2.563 - 0.33\lambda + 0.0264\lambda^2 - 0.000671\lambda^3) & \lambda > 4 \end{cases} \quad (4.27)$$

The following form of an empirical correlation for the diffusion coefficient of water within the electrolyte could also be used to predict transport rate of water inside the

electrolyte phase [122, 52]:

$$D_w^m = (1.76 \times 10^{-5} + \beta 1.94 \times 10^{-4} \lambda) e^{\left(-\frac{2436}{T_s}\right)} \quad (4.28)$$

Where $\beta = 2.2$ for Nafion[®] electrolyte. Equilibrium water uptake of the electrolyte is function water activity. Assuming ideal gas behavior, local water vapor activity is defined as:

$$a_w = \frac{P_{H_2O}}{P_{H_2O}^{sat}} \quad (4.29)$$

In the solid polymer electrolyte, there are several competing transport mechanisms for the movement of water from anode to cathode and from cathode to anode. At the catalyst layer membrane interface when phase saturation is zero, equilibrium water concentration in the membrane is given by the following expression:

$$\lambda^{eq} = 0.043 + 17.81 \times a_w - 39.85 \times a_w^2 + 36.0 \times a_w^3 \quad (4.30)$$

where membrane water content is related to concentration of water in the membrane as:

$$\lambda = \frac{C_w^m}{C_f} \quad (4.31)$$

A typical water uptake curve for Nafion[®] 117 electrolyte can be found in Appendix A.4. If liquid phase saturation is greater than zero, a linear variation of water content with liquid phase saturation is assumed to hold:

$$C_{H_2O}^{m,eq} = 14C_f + 2.8C_f \times s \quad (4.32)$$

Water uptake of the electrolyte may change when the electrolyte is exposed to liquid water or water vapor at equilibrium. This experimentally observed phenomena at liquid and gas phase is called *Schroeder's Paradox* [123, 124]. The following Figure 4.5 is depiction of this phenomena for a Nafion based electrolyte. Figure 4.5 clearly illustrates the change in membrane water content at activity of 1.

A better model must account for the possible variation of the water uptake with the *Schroeder's Paradox*. For simplification purposes, the present work neglects the effect of this possible change and assumes an equilibrium at electrolyte interfaces governed by the equations (4.30, 4.32).

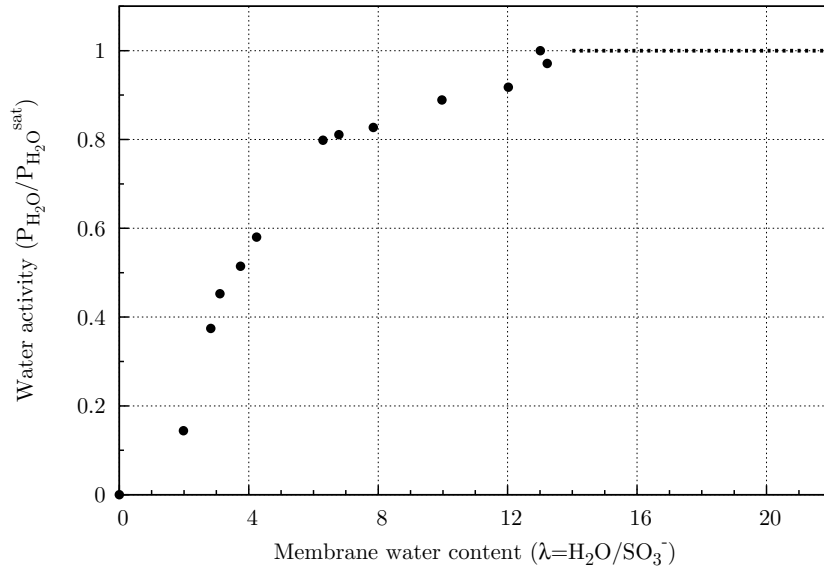


Figure 4.5: Depiction of Schroeders paradox for the solid polymer electrolyte

It is not an easy task to measure ionic conductivity of electrolytes accurately as function of relative humidity and temperature. There are some recent efforts for the proton conductivity measurements in PEM fuel cells [125]. However, still old empirical correlations are in use in the modeling era.

In 1991, Thomas Zawodzinski [126] from Los Alamos Laboratory measured the Nafion proton conductivity (see Appendix A.5) with pulsed field gradient spin echo H-NMR analysis. According to his measurements, dependence of ionic conductivity of Nafion[®]

membrane on temperature and relative humidity is given as [21]:

$$\kappa^m = \exp \left[1268 \left(\frac{1}{303} - \frac{1}{T_s^m} \right) \right] \times (0.005139\lambda - 0.00326) \quad (4.33)$$

where κ^m is the ionic conductivity of electrolyte. Water movement in the electrolyte is quite different as compared to the liquid water transport in the porous media. Therefore, special care must be taken to account for the effect of various phenomena such as dissolved water transport due to electric field, diffusion induced by concentration gradient, and hydraulic pressure gradient induced dissolved water transport.

4.2.2 Anode Electrode Kinetics

There are essentially two ways to express the reaction rate for the anode electrochemical reaction given in equation (3.1a). First and foremost methodology is the use of well known one step Butler-Volmer type reaction rate. Second, one may simplify Butler-Volmer kinetics by assuming fast reaction at the anode. Butler-Volmer reaction rate may be linearized by expanding exponential terms in series form [127]. In this dissertation, reaction mechanism based rate expressions are proposed as a third alternative to the traditional anode rate expressions.

4.2.2.1 Butler–Volmer Type HOR Rate

Conventional Butler-Volmer rate expression can be used to relate current density to overpotential at the anode. However, exponential nature of Butler-Volmer kinetics usually causes convergence problems in the solution. Grid resolution should be increased in the catalyst layer to catch the sharp changes due to exponential behavior especially at low current density region.

Considering anode electrode kinetics, general form of Butler–Volmer type reaction rate expression for the hydrogen oxidation reaction can be written as follows [128]:

$$i_a = i_{o,a}^{ref} \left(\frac{C_{H_2}}{C_{H_2}^{ref}} \right)^{1/2} \left[\exp \left(\frac{\alpha_a F}{RT} \eta_a \right) - \exp \left(-\frac{\alpha_c F}{RT} \eta_a \right) \right] \quad (4.34)$$

where i_a , $i_{o,a}^{ref}$ are the anode current density and reference exchange current density at the anode. Anode overpotential, η_a , for the hydrogen oxidation reaction is defined as:

$$\eta_a = \phi_s^a - \phi_m^a - U_{eq}^a \quad (4.35)$$

Hydrogen reversible potential, U_{eq}^a value is set to zero owing to the reference electrode definition. ϕ_s^a and ϕ_m^a are the solid phase and ionic phase potentials defined at the anode respectively.

4.2.2.2 Linearized Reaction Rate at the Anode

Anode reaction is facile and fast compared to the cathode reaction. Thus, a linear version of Butler-Volmer reaction expression may be used to analyze the anode kinetics. With the fast electrostatics approximation, linearized kinetics for the hydrogen oxidation reaction reads [129]:

$$j_a = ai_{o,a}^{ref} \left(\frac{C_{H_2}}{C_{H_2}^{ref}} \right)^{1/2} \left(\frac{\alpha_a + \alpha_c}{RT} F \eta_c \right) \quad (4.36)$$

where j_a is the volumetric anode current density for the linearized hydrogen oxidation reaction. As a first estimate, linear approximation predicts the cell performance effectively only if one uses small potential scan steps (e.g. 1mV) in the numerical solution.

4.2.2.3 Hydrogen Oxidation Reaction Mechanism

Vogel et al.[106] previously proposed the following reaction mechanism for the hydrogen oxidation reaction. Reaction for the adsorption of the hydrogen gas over the active metal surface is known as the Tafel reaction (4.37a). Tafel reaction is assumed to be

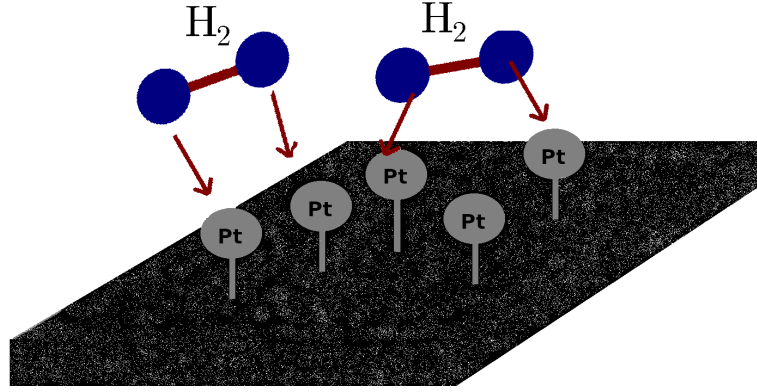


Figure 4.6: Depiction of dual site attack of hydrogen atoms onto Pt surface

the rate determining step in this reaction mechanism and electron transfer reaction (Volmer reaction, 4.37b) is considered as fast (see Appendix B.2).



Rate controlling step for hydrogen oxidation on active metal (e.g. Pt) is the dual site dissociative chemisorption of the hydrogen molecule. Figure 4.6 is an illustration of dual site attack of hydrogen atoms onto platinum surface.

Proposed reaction mechanism given in equation (4.37) are used for the derivation of electrochemical rate expression for both anode hydrogen oxidation reaction (HOR) and cathode oxygen reduction reaction (ORR). In the rate expressions θ_o denotes the equilibrium electrocatalyst surface coverage of hydrogen for the anode reaction (HOR) and electrocatalyst surface coverage of oxygen for the ORR. The following Tafel-Volmer kinetics based rate expression can be used for the anode reaction [106]:

$$k_a = \frac{i_o^a a_{Pt}^{a,agg}}{2FC_{H_2}} \left[\left(\frac{C_{H_2}}{C_{H_2o}} \right) e^{\frac{2F}{RT}\eta_a} - 1 \right] \left(\frac{1}{\theta_o + (1 - \theta_o)e^{\frac{F}{RT}\eta_a}} \right) \quad (4.38)$$

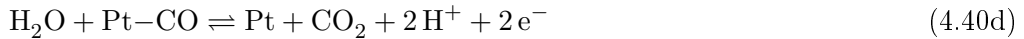
Volumetric exchange current density for the anode reaction is given as follows [112]:

$$j_{o,a}^{ref} = j_{o,a}^{ref} \Big|_{343K} \exp \left[\frac{E_a^{act}}{R} \left(\frac{1}{343} - \frac{1}{T_s} \right) \right] \quad (4.39)$$

where reference exchange current density and activation energy at anode are given as $j_{o,a}^{ref} \Big|_{343K} = 2 \times 10^2 \text{ A/cm}^3$ and $E_a^{act} = 12 \times 10^3 \text{ J/mol}$

4.2.2.4 CO Poisoning Mechanism

Considering pure hydrogen fuel at the anode, Tafel-Volmer hydrogen oxidation reaction mechanism reasonably describes electrode kinetics. However, if the fuel contains carbon monoxide, possibly coming from a reforming reaction, one must account for the possible intermediate steps to represent the anode reaction mechanism accurately. When the fuel feed contains carbon monoxide, the following proposed sequence of reactions may occur during the course of fuel cell operation [130]:



In case of the presence of CO in the fuel stream, active Pt vacant sites on the electrocatalyst surface will be attacked by both hydrogen and carbon monoxide. In other words, H_2 and CO will compete for the active surface. Unavailability of some active

surface due to adsorption of carbon monoxide onto surface is called as CO poisoning phenomena. This coverage of active sites with CO may have a dramatic effect on reaction rate at the anode. Oxidation of CO to CO₂ can only take place at high anode overpotentials [131].

4.2.3 Cathode Electrode Kinetics

4.2.3.1 Butler–Volmer Type ORR Rate

When the reaction rate at the cathode is approximated by means of Butler–Volmer type electrode kinetics, similar rate expression compared to anode electrodictics can be derived [128]:

$$i_c = i_{o,c}^{ref} \left(\frac{C_{O_2}}{C_{O_2}^{ref}} \right) \left[\exp \left(\frac{\alpha_a F}{RT} \eta_c \right) - \exp \left(-\frac{\alpha_c F}{RT} \eta_c \right) \right] \quad (4.41)$$

The overpotential in the cathode ORR rate reads:

$$\eta_c = \phi_s^c - \phi_m^c - U_{eq}^c \quad (4.42)$$

Parthasarathy et al. [132, 15, 16] have used a microelectrode technique to determine the electrode kinetics parameters of oxygen reduction reaction in the temperature range of 30–80 °C. They investigated temperature and pressure dependence of electrode kinetics for ORR. Ticianelli et al. [14] from Los Alamos Laboratory performed several electrode kinetics experiments. They presented electrode kinetics parameters for oxygen reduction reaction using various MEAs.

Berning have reported cathode exchange current density values for low temperature range and he evaluated the impact of exchange current density on fuel cell performance [133]. Ye et al. [112] previously reported a correlation for the variation of volumetric

exchange current density with temperature at the cathode:

$$j_{o,c}^{ref} = j_{o,c}^{ref} \Big|_{343K} \exp \left[\frac{E_c^{act}}{R} \left(\frac{1}{343} - \frac{1}{T_s} \right) \right] \quad (4.43)$$

where reference volumetric exchange current density and activation energy at anode are given as $j_{o,c}^{ref} \Big|_{343K} = 1 \times 10^{-2} \text{ A/cm}^3$ and $E_c^{act} = 66 \times 10^3 \text{ J/mol}$

4.2.3.2 Tafel Kinetics at the Cathode

Oxygen reduction reaction at the cathode is sluggish compared to fast anode kinetics. One can reduce Butler–Volmer rate expression to Tafel type reaction kinetics at the cathode as follows [129]:

$$j_c = -a i_{o,c}^{ref} \left(\frac{C_{O_2}}{C_{O_2}^{ref}} \right) \exp \left(-\frac{\alpha_c F}{RT} \eta_c \right) \quad (4.44)$$

In equation (4.44), exchange current density based on area is defined as follows [22, 134]:

$$i_{o,c}^{ref} = i_{o,c}^{ref} \Big|_{273K} 2^{\frac{T_s-273}{10}} \quad (4.45)$$

4.2.3.3 Oxygen Reduction Mechanism

Yeager at the Case Western Reserve University [135] has presented (Figure 4.7) some configurations for possible attachment of oxygen atoms on the surface electrocatalyst. Griffiths model [136], Pauling model [137], and Bridge model [138] depict some possible configuration between active metal nanoparticles at the electrocatalyst support surface and oxygen atoms.

Some proposed reaction mechanisms for oxygen reduction reaction were summarized in literature [107]. Mechanism including the following sequence of steps can be considered

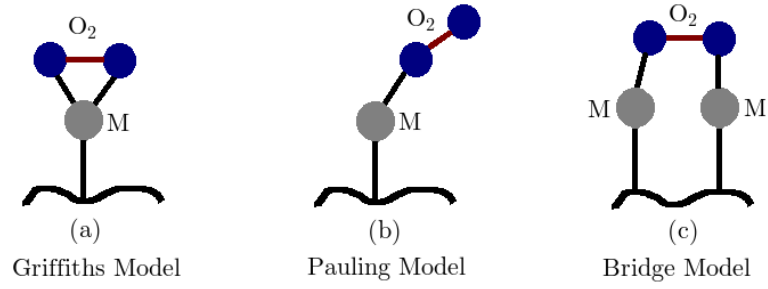


Figure 4.7: Representative models for O_2 configuration over active metals: (a) Griffiths Model, (b) Pauling Model, (c) Bridge Model

one possible route for the reduction of oxygen at the cathode side of the PEM fuel cell.



In this mechanism (4.46), oxygen molecules attack to the platinum metals from single site. Figure 4.8 exhibits single site attachment of oxygen atoms onto platinum metal.

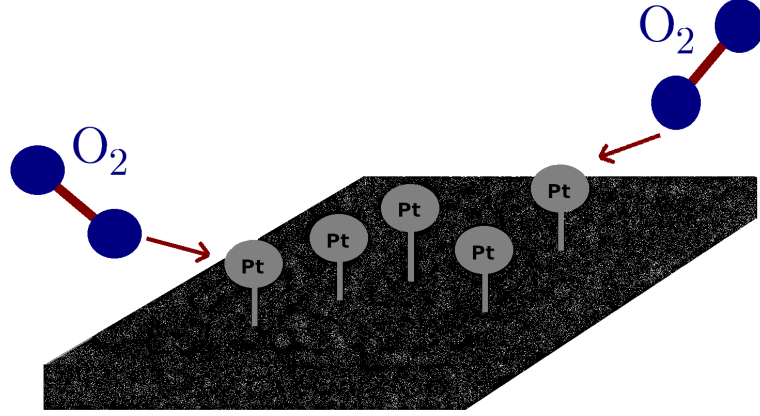


Figure 4.8: Depiction of single site attack of oxygen molecules onto Pt surface

Oxygen reduction reaction rate is derived (see Appendix B.1) for a multi-step reaction pathway [107] and the following rate expression is considered for the cathode reaction:

$$k_c = \frac{i_o^c a_{Pt}^{c,agg}}{4FC_{O_2}} \frac{\left[\left(\frac{C_{O_2}}{C_{O_2}^o} \right) \frac{\theta_o}{1-\theta_o} - 1 \right] e^{-\frac{F}{RT}\eta_c}}{\theta_o \left(\frac{1}{K} + e^{-\frac{F}{RT}\eta_c} \right)} \quad (4.47)$$

4.2.4 Thin-film and Agglomerate Approach

As a result of diffusion resistance in porous catalysts, concentration profiles will develop for reactants and products. Therefore, observed rate as compared to the reaction rate at the external surface conditions of the agglomerate will vary and decrease for positive-order reactions. This issue becomes more important for the oxygen reduction reaction in the cathode where water is produced.

Considering an idealized spherical electrocatalyst agglomerate geometry, one can define the effectiveness factor as follows [139]:

$$\xi = \frac{1}{\varphi} \left(\coth 3\varphi - \frac{1}{3\varphi} \right) \quad (4.48)$$

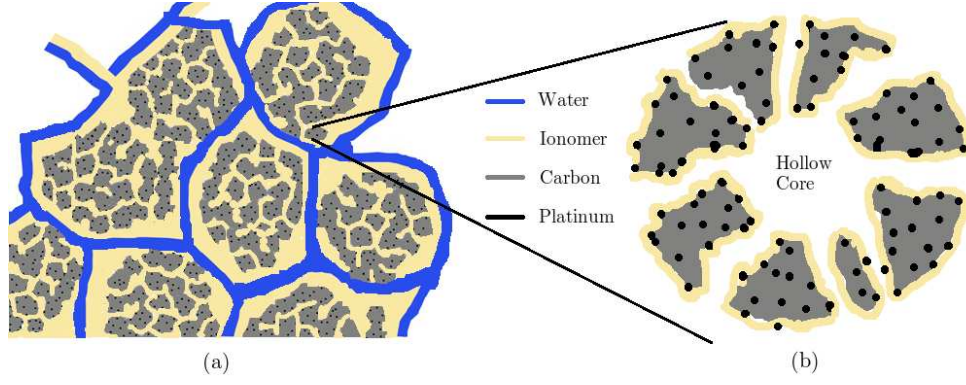


Figure 4.9: Illustration of (a) Electrocatalyst agglomerates inside the catalyst layers, (b) Hollow core mesoporous shell carbon supported Pt electrocatalyst particle coated with ionomer

where φ is known as the Thiele modulus indicating the relative importance of reaction rate to diffusion rate. A general definition for Thiele modulus reads:

$$\varphi = \frac{V_p}{A_e} \left(\frac{R_o}{D_{eff}C_{i,o}} \right)^{\frac{1}{2}} \quad (4.49)$$

In the derivation of the effectiveness factor only the interpellet diffusional effects are considered. However, in the oxygen reduction and hydrogen oxidation reactions each electrocatalyst agglomerate is expected to be surrounded by thin electrolyte film to facilitate proton transport and in fact at ternary phase points the reaction takes place.

For a constant thickness of thin electrolyte film surrounding the agglomerate, however, there is additional resistance coming from the liquid water build up around the agglomerate. This water thickness first will increase up to steady state to a certain level then probably will stay constant for a fixed current withdraw rate. Thus, the thickness is a dynamic variable and situation becomes more severe at elevated current densities or increased saturation levels.

From the secondary pores oxygen diffuses (no reaction) over the surface of the liquid water film and then dissolves and transported to the surface of ionomer via film mass convection. After dissolving in the ionomer phase reaction will proceed in a ratio of the derived effectiveness factor including the film ionomer resistance.

4.2.4.1 Thermodynamic PEM Fuel Cell Potential

Reversible cell potential, also known as thermodynamic potential, is a critical system parameter that fundamentally appears in the overpotential terms of the electrode kinetics rate expressions (e.g Butler-Volmer rate expression). To account for the changes of thermodynamic potential with temperature and pressure, one can modify Nernst equation [140] using combined laws of thermodynamics. Considering overall reaction for a H₂/O₂ PEM fuel cell, the following expression can be written [141]:

$$E_r = E^o + \frac{\Delta S}{2F}(T - T^o) - \frac{RT}{2F} \ln \frac{a_{\text{H}_2\text{O}}}{a_{\text{H}_2} a_{\text{O}_2}^{\frac{1}{2}}} \quad (4.50)$$

In equation (4.50), E^o is the cell potential defined at a standard state and its definition is given as:

$$E^o = -\frac{\Delta G^o}{nF} \quad (4.51)$$

where n is the number of electrons transferred in the overall reaction. If one selects the reference temperature as 25 °C and assumes liquid water production, the following specific reversible cell potential expression can be obtained by substituting the proper values for the variables in equation (4.50) at the reference state:

$$E_r = 1.229 - 8.5 \times 10^{-4}(T - T^o) + 4.3 \times 10^{-5} \left(\ln P_{\text{H}_2} + \frac{1}{2} P_{\text{O}_2} \right) \quad (4.52)$$

The final form of the thermodynamic cell potential expression given in equation (4.52) was used in the modeling and simulation of the polymer electrolyte fuel cells.

4.2.4.2 Dissolved Oxygen Concentration

It was assumed that electrocatalysts were surrounded with ionomer and liquid water. In this case, solubility of reactant gases within the liquid water phase and also inside

the ionomer (appearing in CL) may be an important additional external resistance affecting electrochemical reaction rates especially at the cathode. For the transport of oxygen within the liquid water and ionomer, based on the Henry's Law, following expressions are suggested to relate the gas pressure and dissolved oxygen concentration:

$$C_{O_2}^w = \frac{P_{O_2}}{H_{O_2}^w} \quad (4.53a)$$

$$C_{O_2}^m = \frac{P_{O_2}}{H_{O_2}^m} \quad (4.53b)$$

where $C_{O_2}^w$ and $C_{O_2}^m$ are the dissolved oxygen concentrations in the liquid water phase and ionomer phase respectively. These dissolved concentrations are related to the oxygen partial pressure through the following Henry's coefficients as function of temperature [134]:

$$H_{O_2}^w = 5.08 \times 10^6 e^{\frac{-498}{T_s}} \quad (4.54a)$$

$$H_{O_2}^m = 1.33 \times 10^6 e^{\frac{-666}{T_s}} \quad (4.54b)$$

where $H_{O_2}^w$ and $H_{O_2}^m$ are the Henry's coefficient correlations with temperature change for oxygen in liquid water and ionomer respectively. Since liquid and solid temperatures are assumed to be in thermal equilibrium, solid phase temperature, T_s , is used in the correlations.

In reaction rate expressions, a reference oxygen and hydrogen concentration is required to proceed with the solution. These concentrations may be assumed as dissolved oxygen and hydrogen concentrations within the ionomer. Therefore, equation (4.53b) may be used to approximate $C_{O_2}^{ref}$ and $C_{H_2}^{ref}$ with a similar expression. It is important to note that direct use of oxygen and hydrogen concentrations through ideal gas law

will be inaccurate. One must account for the dissolved gas concentrations to predict the real phenomena.

4.2.5 Two Phase Energy Balance

A convenient two-phase energy balance is being developed for the PEM fuel cells. Heat transfer is considered to occur between solid and gas phases throughout the fuel cell with various heat transfer mechanisms. Liquid water adjacent to the solid phase is assumed to have solid phase temperature, that is, a local equilibrium is assumed to hold between solid and liquid phases. For this particular model, interpellet heat transfer resistance (diffusive thermal gradient within the catalyst agglomerate) is neglected. Figure 4.10 illustrates the several competing heat transfer mechanisms within the pores of the diffusion media and catalyst layers.

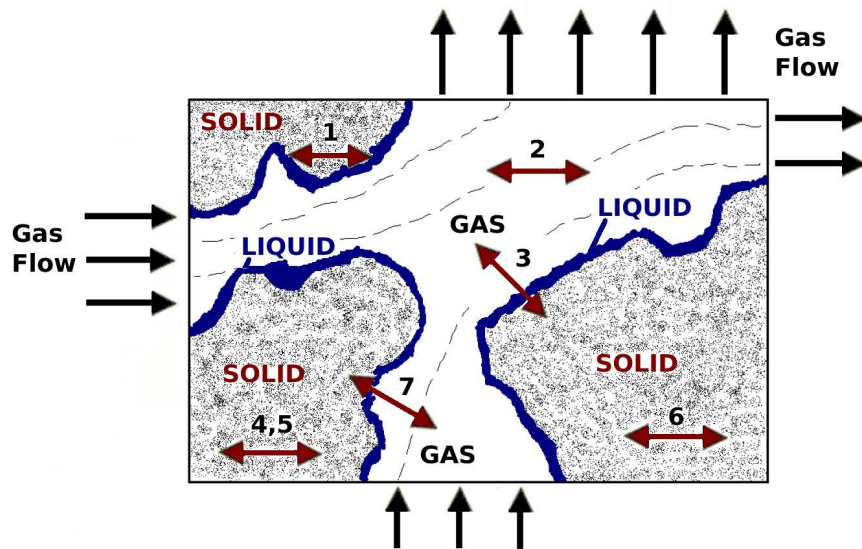


Figure 4.10: Illustration of heat transfer mechanisms inside porous diffusion media and catalyst layers: (1) Solid phase conduction, (2) Gas phase conduction and convection, (3) Gas-Solid heat exchange, (4) Irreversible heat generation by ORR or HOR, (5) Heat generation due to entropy change by ORR or HOR, (6) Joule heating in the solid and ionic phase, (7) Heat transfer due to phase change

At the steady state, considering convective and conductive heat transfer mechanisms, two-phase energy balance for the gas and solid phases can be written for the diffusion media, catalyst layers, and membrane as follows:

Gas Phase Energy Balance:

$$\rho_g \bar{C}_{p,g} \mathbf{u}_g \cdot \nabla T_g = h_{g,s} A_{g,s} (T_s - T_g) + \nabla \cdot \bar{k}_g^{eff} \nabla T_g \quad (4.55)$$

Solid Phase Energy Balance:

$$h_{g,s} A_{g,s} (T_s - T_g) = \nabla \cdot \bar{k}_s^{eff} \nabla T_s + S_s \quad (4.56)$$

where k_g^{eff} and k_s^{eff} are the effective thermal conductivity in the gas and solid phase respectively. $h_{g,s}$ is the heat transfer coefficient for the porous media between gas and solid phases. $A_{g,s}$ indicates the effective heat transfer area per volume. Heat is transferred throughout the cell by means of convection, conduction and heat exchange. Source term, S_s , in the solid phase energy balance accounts for various heat generation terms in each layer:

$$S_s = \begin{cases} |i_s|^2 \bar{R}_s^{eff} - \Delta H_{H_2O} R_{H_2O}, \text{GDL or MPL} \\ |i_s|^2 \bar{R}_s^{eff} + |i_m|^2 \bar{R}_m^{eff} + \nabla \cdot i_m \left(\eta_k + T_s \frac{\Delta S_k}{n_k F} \right) - \Delta H_{H_2O} R_{H_2O}, \text{CL} \\ |i_m|^2 \bar{R}_m^{eff}, \text{Membrane} \end{cases} \quad (4.57)$$

4.2.6 Charge Conservation

4.2.6.1 Ionic Phase Charge Conservation

Protons are produced in the anode catalyst layer and transported to the cathode catalyst layer through the electrolyte. Potential drop due to ohmic region is mainly due to the losses related to the ionic conductivity of the electrolyte. Traditional electrolytes (e.g. Nafion[®]) require humidification to serve as a good positive ion conductor at high water uptake levels. In order to understand real transport phenomena within the fuel cell, it is critical to precisely predict the ionic phase potential distribution in the

electrolyte. Protons are conserved through the following charge conservation equation in the ionic phase:

$$-\nabla \cdot i_m + S_{\phi_m} = 0 \quad (4.58)$$

where i_m is the ionic phase current density and S_{ϕ_m} is the source term due to electrode kinetics appearing in the ionic charge conservation equation. Ionic phase current density can be redefined in terms of ionic phase potential, ϕ_m , as follows:

$$i_m = -\kappa_m^{eff} \nabla \phi_m \quad (4.59)$$

Source term in equation (4.58) only appears in the anode and cathode catalyst layers due to electrochemical reactions. Here, source term represents a measure of rate of proton transfer in the catalytic regions. Using Faraday's law, the source terms can be related to global reaction rates, R_{H_2} and R_{O_2} in the anode and cathode catalyst layer as:

$$S_{\phi_m} = \begin{cases} +2FR_{H_2} & \text{anode CL} \\ -4FR_{O_2} & \text{cathode CL} \end{cases} \quad (4.60)$$

Plus and minus signs in the source terms notifies where protons are produced and depleted during the course of fuel cell operation. For every mole of hydrogen two protons are produced at the anode, whereas four protons are consumed at the cathode due to electrochemical reactions.

4.2.6.2 Solid Phase Charge Conservation

Solid matrix of the PEM fuel cell components (bipolar plate, GDL, MPL, and CL) must be highly electrically conductive to realize high performance on operating fuel

cell. Efficiency losses through electronic conduction may be detected by solving charge conservation equation in the solid phase. Electrical conductivity of the medium may change in through plane or in plane direction depending on the structure of the fuel cell component. Charge conservation in the solid phase of the physical domain reads:

$$-\nabla \cdot i_s + S_{\phi_s} = 0 \quad (4.61)$$

where i_s is the solid phase current and it is related to solid phase potential, ϕ_s , through Ohm's law. Generally, all solid matrix components are highly electrically conductive, and consequently, one would expect a very small potential drop due to electron conduction. Solid phase current, i_s , can be expressed in terms of the well known Ohm's relation as:

$$i_s = -\kappa_s^{eff} \nabla \phi_s \quad (4.62)$$

where κ_s^{eff} is the effective electronic conductivity in the direction of electron transport. Solid phase charge conservation source terms appearing only in the anode and cathode catalyst layers due to electrochemical reactions are defined as:

$$S_{\phi_s} = \begin{cases} -2FR_{H_2} & \text{anode CL} \\ +4FR_{O_2} & \text{cathode CL} \end{cases} \quad (4.63)$$

4.3 Summary of Governing Equations

There are nine variables that are required to be solved simultaneously within the computational domain, concentration of oxygen in the gas phase, $C_{O_2}^g$; concentration of hydrogen in the gas phase, $C_{H_2}^g$; concentration of water vapor in the gas phase, $C_{H_2O}^g$; ionic potential (membrane phase potential), ϕ_m ; solid phase potential (electronic phase

potential), ϕ_s ; liquid phase saturation level, s ; concentration of liquid water in the electrolyte, $C_{H_2O}^m$; temperature of the solid phase, T_s and temperature of the gas phase, T_g .

The liquid phase saturation levels are different in different fuel cell layers due to quite different nature of capillary transport mechanism. This saturation discontinuity is treated by using different variables but similar equations in the fuel cell porous media. Summary of the governing equation proposed in this chapter are given in Table 4.1 and Table 4.2. Source terms appearing in the governing equations are presented in Table 4.3.

4.4 Summary of Boundary Conditions

Initial fuel and oxidant feed inlet conditions to the PEM fuel cell can be defined by means of stoichiometric flow ratio. Stoichiometric flow ratio is defined as the amount of the reactant supplied into the chamber gas feed divided by the amount required by the electrochemical reactions [20]. For the anode and cathode stoichiometric flow ratio, ζ , is defined respectively as follows:

$$\zeta_a = y_{H_2}^o v_a^o \frac{P_a}{RT} \frac{2F}{IA} \quad (4.64a)$$

$$\zeta_c = y_{O_2}^o v_c^o \frac{P_c}{RT} \frac{4F}{IA} \quad (4.64b)$$

Adjusting initial flow rates and operating conditions, one can set the boundary conditions for each fuel cell layer of interest with the use of continuous flux approach. In cases when one or more variable is not solved in the computational domain of interest, its value is forced to zero in that region. Dirichlet and Neumann type boundary conditions are suggested considering the physical behavior of the PEM fuel cell. Appropriate boundary conditions for PEMFC anode, membrane, and cathode regions are presented in Table 4.4 and 4.5.

Table 4.1: Governing equations for anode side and membrane

Variables	Anode GDL	Anode CL	Membrane
y_{H_2}	$-\nabla \cdot N_{H_2} = 0$	$-\nabla \cdot N_{H_2} - R_{H_2} = 0$	$y_{H_2} = 0$
y_{H_2O}	$-\nabla \cdot N_{H_2O} - R_{H_2O} = 0$	$-\nabla \cdot N_{H_2O} - R_{H_2O} = 0$	$y_{H_2O} = 0$
s_G	$-\nabla \cdot N_w + R_{H_2O} = 0$	N/A	N/A
s_C	N/A	$-\nabla \cdot N_w + R_{H_2O} = 0$	N/A
P_l	$P_l = P_g - P_c$	$P_l = P_g - P_c$	$\nabla \cdot \nabla P_l = 0$
C_w^m	N/A	$-\nabla C_w^m = 0$	$-\nabla \cdot N_w^m = 0$
ϕ_m	N/A	$-\nabla \cdot i_m + 2FR_{H_2} = 0$	$-\nabla \cdot i_m = 0$
ϕ_s	$-\nabla \cdot i_s = 0$	$-\nabla \cdot i_s - 2FR_{H_2} = 0$	N/A
T_g	$\rho_g \bar{C}_{p,g} \mathbf{u}_g \cdot \nabla T_g = -\nabla \cdot q_g + Q_c$	$\rho_g \bar{C}_{p,g} \mathbf{u}_g \cdot \nabla T_g = -\nabla \cdot q_g + Q_c$	N/A
T_s	$-\nabla \cdot q_s - Q_c + S_s = 0$	$-\nabla \cdot q_s - Q_c + S_s = 0$	$-\nabla \cdot q_s + S_s = 0$

Table 4.2: Governing equations for cathode side

Variables	Cathode CL	Cathode MPL	Cathode GDL
y_{O_2}	$-\nabla \cdot N_{O_2} - R_{O_2} = 0$	$-\nabla \cdot N_{O_2} = 0$	$-\nabla \cdot N_{O_2} = 0$
y_{H_2O}	$-\nabla \cdot N_{H_2O} - R_{H_2O} = 0$	$-\nabla \cdot N_{H_2O} - R_{H_2O} = 0$	$-\nabla \cdot N_{H_2O} - R_{H_2O} = 0$
s_G	N/A	N/A	$-\nabla \cdot N_w + R_{H_2O} = 0$
s_M	N/A	$-\nabla \cdot N_w + R_{H_2O} = 0$	N/A
s_C	$-\nabla \cdot N_w + (4n_d + 2)R_{O_2} + R_{H_2O} = 0$	N/A	N/A
P_l	$P_l = P_g - P_c$	$P_l = P_g - P_c$	$P_l = P_g - P_c$
C_w^m	$-\nabla C_w^m = 0$	N/A	N/A
ϕ_m	$-\nabla \cdot i_m - 4FR_{O_2} = 0$	N/A	N/A
ϕ_s	$-\nabla \cdot i_s + 4FR_{O_2} = 0$	$-\nabla \cdot i_s = 0$	$-\nabla \cdot i_s = 0$
T_g	$\rho_g \bar{C}_{p,g} \mathbf{u}_g \cdot \nabla T_g = -\nabla \cdot q_g + Q_c$	$\rho_g \bar{C}_{p,g} \mathbf{u}_g \cdot \nabla T_g = -\nabla \cdot q_g + Q_c$	$\rho_g \bar{C}_{p,g} \mathbf{u}_g \cdot \nabla T_g = -\nabla \cdot q_g + Q_c$
T_s	$-\nabla \cdot q_s - Q_c + S_s = 0$	$-\nabla \cdot q_s - Q_c + S_s = 0$	$-\nabla \cdot q_s - Q_c + S_s = 0$

Table 4.3: Source terms for the governing equations

Source	Units
$R_{H_2O} = \gamma \frac{k_c \bar{\epsilon}_o (1-s) y_{H_2O}}{RT_s} (P_{H_2O} - P_{H_2O}^{sat}) + (1-\gamma) \frac{k_e \bar{\epsilon}_o \rho_{H_2O}}{MW_{H_2O}} (P_{H_2O} - P_{H_2O}^{sat})$	mol / cm ³ .s
$R_{H_2} = \frac{\frac{RT_s}{H_{H_2}^w}}{\frac{\delta_m}{a_r D_{H_2}^m} + \frac{\delta_w}{a_r D_{H_2}^w} \frac{H_{H_2}^w}{H_{H_2}^m} + \frac{1}{\xi_{a,k_a}}} C_{H_2}$	mol / cm ³ .s
$R_{O_2} = \frac{\frac{RT_s}{H_{O_2}^w}}{\frac{\delta_m}{a_r D_{O_2}^m} + \frac{\delta_w}{a_r D_{O_2}^w} \frac{H_{O_2}^w}{H_{O_2}^m} + \frac{1}{\xi_{c,k_c}}} C_{O_2}$	mol / cm ³ .s
$S_s = i_s ^2 \bar{R}_s^{eff} - \Delta H_{H_2O} R_{H_2O}$ where s=Diffusion Media	W / cm ³
$S_s = i_m ^2 \bar{R}_m^{eff} + i_s ^2 \bar{R}_s^{eff} + \nabla \cdot i_m \left(\eta_k + T_s \frac{\Delta S_k}{n_k F} \right) - \Delta H_{H_2O} R_{H_2O}$ where s=CL and k=anode or cathode	W / cm ³
$S_s = i_m ^2 \bar{R}_m^{eff}$ where s=Membrane	W / cm ³

Table 4.4: Boundary conditions for anode side

ANODE			
Variables	$x = 0$	GDL/CL	CL/Membrane
y_{H_2}	$y_{H_2} = y_{H_2}^{\circ}$	$N_{H_2} _{GDL} = N_{H_2} _{CL}$	$N_{H_2} _{CL} = 0$
y_{H_2O}	$y_{H_2O} = y_{H_2O}^{\circ}$	$N_{H_2O} _{GDL} = N_{H_2O} _{CL}$	$N_{H_2O} _{CL} = 0$
s_G	$P_c = 0$	$N_w _{GDL} = N_w _{CL}$	N/A
s_C	N/A	$P_c _{GDL} = P_c _{CL}$	$N_w _{CL} = N_w^m _M$
P_l	$P_l = P_g = 1 \text{ atm}$	$P_l = P_g - P_c$	$P_l = P_g - P_c$
C_w^m	N/A	$0 = N_w^m _{CL}$	$C_w^m = C_w^{m,eq}$
ϕ_m	N/A	$0 = i_m _{CL}$	$i_m _{CL} = i_m _M$
ϕ_s	$\phi_s = 0$	$i_s _{GDL} = i_s _{CL}$	$i_s _{CL} = 0$
T_g	$T_g = T_g^{\circ}$	$q_g _{GDL} = q_g _{CL}$	$q_g _{CL} = 0$
T_s	$T_s = T_s^{\circ}$	$q_s _{GDL} = q_s _{CL}$	$q_s _{CL} = q_s _M$

Table 4.5: Boundary conditions for cathode side

CATHODE				
Variables	Membrane/CL	CL/MPL	MPL/GDL	$x = L$
y_{O_2}	$0 = N_{O_2} _{CL}$	$N_{O_2} _{CL} = N_{O_2} _{MPL}$	$N_{O_2} _{MPL} = N_{O_2} _{GDL}$	$y_{O_2} = y_{O_2}^\circ$
y_{H_2O}	$0 = N_{H_2O} _{CL}$	$N_{H_2O} _{CL} = N_{H_2O} _{MPL}$	$N_{H_2O} _{MPL} = N_{H_2O} _{GDL}$	$y_{H_2O} = y_{H_2O}^\circ$
s_G	N/A	N/A	$N_w _{MPL} = N_w _{GDL}$	$P_c = 0$
s_M	N/A	$N_w _{CL} = N_w _{MPL}$	$P_c _{MPL} = P_c _{GDL}$	N/A
s_C	$N_w^m _M = N_w _{CL}$	$P_c _{CL} = P_c _{MPL}$	N/A	N/A
P_l	$P_l = P_g - P_c$	$P_l = P_g - P_c$	$P_l = P_g - P_c$	$P_l = P_g = 1\text{atm}$
C_w^m	$C_w^m = C_{w,c}^{m,eq}$	$N_w^m _{CL} = 0$	N/A	N/A
ϕ_m	$i_m _M = i_m _{CL}$	$i_m _{CL} = 0$	N/A	N/A
ϕ_s	$0 = i_s _{CL}$	$i_s _{CL} = i_s _{MPL}$	$i_s _{MPL} = i_s _{GDL}$	$\phi_s = V_{app}$
T_g	$0 = q_g _{CL}$	$q_g _{CL} = q_g _{MPL}$	$q_g _{MPL} = q_g _{GDL}$	$T_g = T_g^\circ$
T_s	$q_s _M = q_s _{CL}$	$q_s _{CL} = q_s _{MPL}$	$q_s _{MPL} = q_s _{GDL}$	$T_s = T_s^\circ$

4.5 PEM Fuel Cell Model Parameters

Estimation of electrochemical parameters and transport parameters are critical to be able to predict fuel cell behavior. Most of the predictions are due to the empirical data and correlations available. In some cases, it is possible to predict the parameter directly from experiments (e.g. exchange current density, electrochemically active area). With the use of proper correlations, dependence of the parameters on temperature and pressure was taken into account.

Experimental capillary data proposed by Lin et al. [134] and Xuhai Wang [142] are used to model liquid water effects inside the gas diffusion layer, microporous layer, and catalyst layer. The correlations proposed by Xuhai Wang are five parameter nonlinear fit of experimental data conducted by gravimetric method.

There are several mathematical model parameters used in the model simulations. Some parameters were found from literature and others were either computed or estimated by means of correlations. Table 4.6 presents the simulation parameters for the macroporous layer or gas diffusion layer (GDL).

Table 4.6: Gas diffusion layer properties used in the base case

Parameter	Value	Ref.
Bulk porosity, ε_o^{gdl}	0.6	[143]
Layer thickness, δ_{gdl}	0.025 cm	[134]
Liquid water permeability at 100 % saturation, K_o^{gdl}	1×10^{-9} cm	[134]
Coefficient in capillary pressure expression (see 4.22)		
a_1	-22.69	[142]
a_2	-16.19	[142]
b	-644.86 Pa	[142]
c	0.578	[142]
d	-7.59 Pa	[142]
Effective thermal conductivity, $k_{s,eff}^{gdl}$	0.015 W/cm K	[50]
Effective electronic conductivity (through-plane), $\kappa_{s,eff}^{gdl}$	12.5 S/cm	[143]

In the case of diffusion media with a thin microporous layer, the following base case model parameters given in Table 4.7 can be used to simulate this layer. In nature, microporous layer is similar to macroporous layer. Most of the cases, MPL is hydropho-

bized with PTFE to enhance water removal ability of the porous media by creating a pump effect.

Table 4.7: Microporous layer properties used in the base case

Parameter	Value	Ref.
Bulk porosity, ε_o^{mpl}	0.3	[144]
Layer thickness, δ_{mpl}	0.002 cm	[144]
Liquid water permeability at 100 % saturation, K_o^{mpl}	1×10^{-12} cm	[142]
Coefficient in capillary pressure expression (see 4.22)		
a_1	-30	[142]
a_2	-16	[142]
b	-9878.4 Pa	[142]
c	0.1	[142]
d	-4000 Pa	[142]
Effective thermal conductivity, $k_{s,eff}^{mpl}$	0.006 W/cm K	
Effective electronic conductivity (through-plane), $\kappa_{s,eff}^{mpl}$		

Structural catalyst layer properties are given in Table 4.8. Some parameters related to electrode kinetics and surface concentrations of fuel and oxidant are presented in Table 4.10.

Table 4.8: Catalyst layer properties used in the base case

Parameter	Value	Ref.
Bulk porosity, ε_o^{cl}	0.12	
Layer thickness, δ_{cl}	0.0015 cm	
Liquid water permeability at 100 % saturation, $K_o^{a,cl}$	1×10^{-12} cm	
Coefficient in capillary pressure expression (see 4.22)		
a_1	-45	[142]
a_2	-8	[142]
b	-5000 Pa	[142]
c	0.78	[142]
d	-1106.56 Pa	[142]
Effective thermal conductivity, $k_{s,eff}^{cl}$	0.003 W/cm K	
Effective electronic conductivity (through-plane), $\kappa_{s,eff}^{cl}$		

For the base case computation of the model, Nafion 112 is considered as the solid proton conducting polymer electrolyte. Most important parameters related to electrolyte

are the ionic conductivity and water uptake ability at the operating temperatures of interest. Table 4.9 presents some model parameters that are well suited to PFSA based membranes.

Table 4.9: Solid polymer electrolyte properties used in the base case

Parameter	Value
Layer thickness, δ_m	0.005 cm
Fixed charge site concentration, C_f	1.2×10^{-3} mol/cm ³
Effective thermal conductivity, $k_{s,eff}^m$	0.0025 W/cm K

As base case operating conditions, PEM fuel cell simulations are run at relatively operating temperatures of 60 °C and atmospheric pressures. Other parameters required for the base case operation are shown in Table 4.10.

Table 4.10: PEM fuel cell operation conditions for the base case

Parameter	Value
Gas phase temperature at the inlet, T_g	60 °C
Initial solid phase temperature, T_s	60 °C
Anode pressure, P_a	1 atm
Cathode pressure, P_c	1 atm
Oxygen mole fraction in the air inlet, $y_{O_2}^{dry}$	0.21
Anode humidity, RH_a	100 %
Cathode humidity, RH_c	10 %
Water saturation level at channel/GDL interface, s_o	0
Hydrogen reference concentration at 60 °C, $C_{H_2}^{ref}$	5.56×10^{-6} mol/cm ³
Oxygen reference concentration at 60 °C, $C_{O_2}^{ref}$	5.56×10^{-6} mol/cm ³
Anode exchange current density at 60 °C, $i_{o,a}^{ref}$	1×10^{-2} A/cm ²
Cathode exchange current density at 0 °C, $i_{o,c}^{ref}$	1×10^{-6} A/cm ²
Evaporation rate constant, k_e	100 1/atm s
Condensation rate constant, k_c	100 mol/atm cm ³ s
Anode gas phase effective thermal conductivity, $k_{a,g}^{eff}$	0.0025 W/cm K
Cathode gas phase effective thermal conductivity, $k_{c,g}^{eff}$	0.0025 W/cm K

Parameters suggested in this section are for the base case operation of a polymer electrolyte membrane fuel cell. For some test runs, different parameters were used

to analyze the effect of certain parameters on the variables of interest. In addition, for practical application purposes, PEM fuel cell is operated with air at the cathode. However, for some cases effect of pure oxygen feed was also investigated.

CHAPTER 5

NUMERICAL SIMULATION

5.1 Numerical Solution Strategy

Numerical solution of the system of the governing equations begins with the discretization of the equations for the computational domain of interest. Resulting ODE system for steady state and two point boundary value problems are being treated with the finite difference formulation. Newton's method and shooting methods are considered together to tackle the numerical difficulties arising from coupled nonlinearities. Numerical solution to these systems may well be formulated with a banded solver [145, 146] using Jacobian matrix of the linearized equations (Band J algorithm). Guess vector could be estimated with a shooting method since Newton iterations are critically dependent on the initial vector. For this purpose, a FORTRAN 90 code has been developed for the numerical simulation of the mathematical model outlined (see Appendix F).

There are some global decisions to run the numerical simulation. For instance, one need to supply or transfer the geometry to the code. Having defined the physical system, controlling subroutine of the code is recalled to teach the main program certain limitations such as the model dimensionality and operation modes (e.g. steady/transient or isothermal/nonisothermal). The major direction in the solution is due to the single phase or multiphase flow. This changes the nature of the equations and solution is much more complex for multiphase flow case.

Figure 5.1 illustrates the simplified numerical solution scheme for a steady state PEM fuel cell model. First, a global module is initiated within the FORTRAN to make some

global variables accessible to all other modules. Second, all inlet conditions together with model parameters and empirical correlations are defined with an input module. Third, an initial guess vector for all variables is set for the start of Newton's method. This step is critical to be able to direct the solution to convergence, otherwise, solution may be oscillatory. Therefore, to predict variable profiles, one must have an idea about the range and trends of the variables.

First step is to compute the transport parameters (e.g. diffusivities or thermal conductivities) of the governing equations at the operating conditions. Next step is to supply all functions in a separate module that were derived from the discretization of governing differential equations and boundary conditions with finite difference approach. Since the system of equations are nonlinear due to two-phase flow and source terms, Newton's method is used and this method requires the computation of Jacobian matrix in the following form to initiate iterations for convergence in each solution step:

$$J = \begin{bmatrix} \frac{\partial F_1}{\partial x_1} & \cdots & \frac{\partial F_1}{\partial x_n} \\ \vdots & \ddots & \vdots \\ \frac{\partial F_m}{\partial x_1} & \cdots & \frac{\partial F_m}{\partial x_n} \end{bmatrix} \quad (5.1)$$

Jacobian matrix can be computed numerically or analytically. Analytical computation of the Jacobian may be performed with the help of Mathematica[®] by symbolic differentiation and plugging the coefficients of the differentials into FORTRAN 90. The other possibility is to approximate differentials by finite differences and to find a close approximation to the governing differentials appearing in the Jacobian. In this study, Jacobian matrix is computed numerically with the use of definition of derivatives.

Once Jacobian is computed, solution proceeds for adjusted applied potential till convergence criteria is achieved. For the converged solution, variables are processed into files and average current density is computed based on molar fluxes. Then, solution is transferred into the next potential by the ramp given and all processes are repeated for the next potential till solution converges.

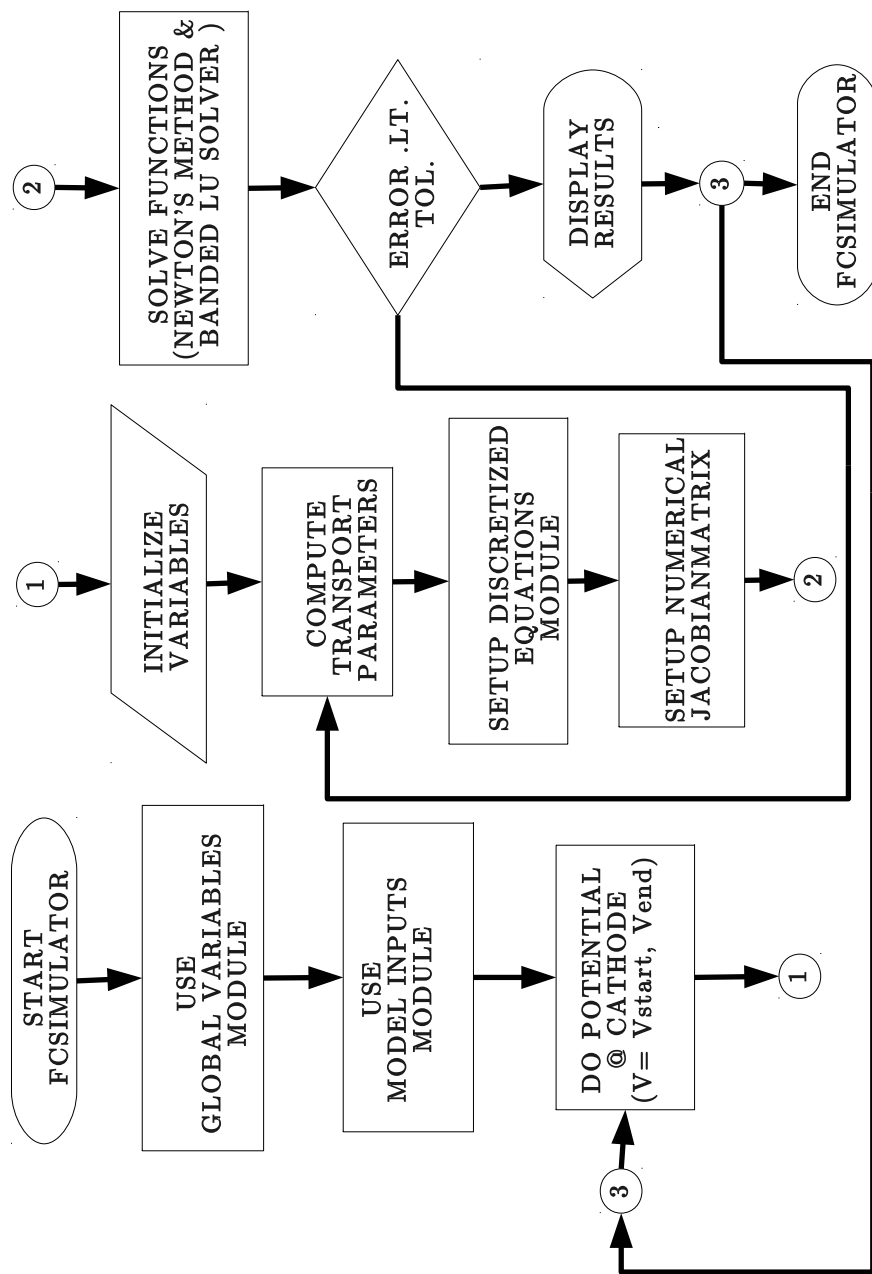
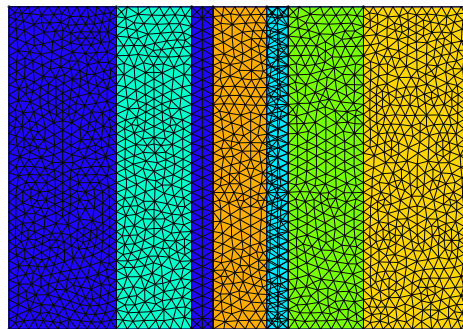


Figure 5.1: Flowchart for the numerical solution algorithm

5.2 Description of the Computational Domain

In case of two and three dimensional numerical solution, finite volume method or finite element method is well suited as the discretization scheme for the system of partial differential equations. The following Figure 5.2 is an example to the two dimensional grid generated with an adaptive mesh algorithm using Delaunay triangles as the control element. An open source GMSH software used for the production of the grid elements then the geometry definitions may be transferred to the FORTRAN 90 code. The computational grid includes all fuel cell components even the microporous layer of the diffusion media.



y
|
z x

Figure 5.2: Two dimensional adaptive PEMFC grid illustration for numerical simulation

There are several ways to generate grid with different purposes. In some portions of the computational domain, one may want to refine the grid for further resolution of the variables with increased accuracy. In this context, detection of water transport can only be understood with a refine grid in the porous region.

5.3 Finite Volume Method

For two or three dimensional problems preferred discretization scheme is based on the finite volume method [147–149]. Figure 5.3 shows a typical finite volume grid for a structured arrangement. In a staggered cell arrangement, all vectoral quantities are located at the cell faces and all other scalar variables like pressure, temperature are located at the cell centers.

One another possibility for variable arrangement in the structured grid could be the colocated variable arrangement. In that case, all variables are located at the cell centers. This arrangement is not selected due to the one nice feature of staggered arrangement. Once you obtain the solution in a staggered arrangement, you guarantee and readily conserve the mass in each cell. In the colocated arrangement, some kind interpolation is required to check the divergence or convergence of the system.

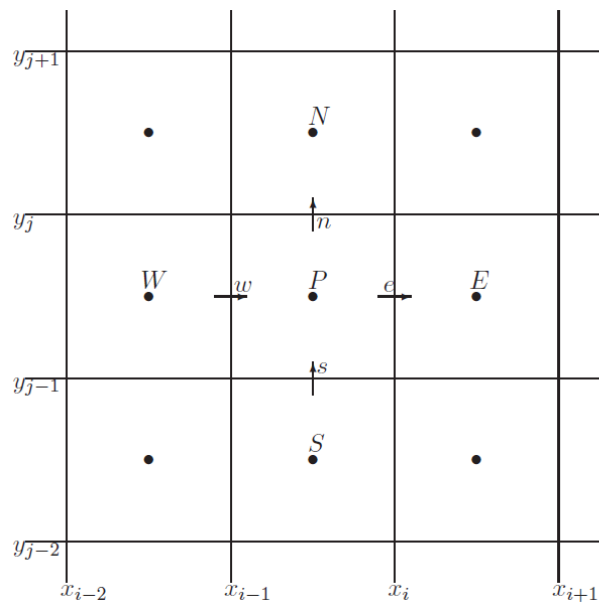


Figure 5.3: Staggered structured finite volume grid

For each and every cell governing equations are discretized and a system of linear equations are obtained. This system actually forms a sparse matrix exhibiting certain properties depending on the transport parameters and all other sources affecting the system.

5.4 Single Phase Flow

High temperature PEMFCs usually experiences single phase flow. Depending on the operating conditions or local conditions, one should also consider the possibility of liquid water formation in some regions of the fuel cell. Semi-Implicit Method for Pressure-Linked Equations (SIMPLE) numerical solution algorithm can be used for the solution of single phase flows. A simplified version of the sequence of the performed operations in a SIMPLE algorithm is given below.

- Guess the pressure field (P^*)
- Solve the momentum equations for u^* , v^* velocities in x and y directions
- Solve the pressure correction equation (P') obtained from the continuity
- Compute the pressure field by adding P' to P^*
- Calculate u , v velocities using velocity correction formulas
- Solve the discretization equation for other variables such as temperature, concentration
- Treat the corrected pressure as P as a new guessed pressure P^* and repeat all steps until a converged solution is obtained

5.5 Multiphase Flow

Considering the tight coupling of phases for PEMFCs at moderate temperatures in a multiphase flow, one should treat these coupling terms carefully to hinder the divergence of iterative solvers during the course of numerical simulation. Partially implicit treatment, Partial Elimination Algorithm (PEA) and the Simultaneous solution of Non-linearly Coupled Equations (SINCE) are the possible interphase coupling algorithms that are suitable for fuel cells [150].

Despite the increased number of computational operations, these algorithms likely to converge faster. Two common solution algorithms for sequential iterative multiphase control volume solvers are the Interphase Slip Algorithm (IPSA) and the implicit

Multifield (IMF) method. It is best to use IPSA numerical solution scheme for handling two-phase flow inside fuel cells. In a transition region from single phase to multiphase flow, it is possible to switch from one case to other to precisely track the behavior of fuel cell for different operating modes.

CHAPTER 6

EXPERIMENTAL

Experimental work was performed for electrocatalyst development and mathematical modeling purposes. First, various Pt or Pt-Pd PEM fuel cell electrocatalysts were produced, characterized and tested under fuel cell environment. Second, fuel cell diffusion media characterization studies have been conducted with Hg porosimetry and scanning electron microscopy. Microstructural information help understand and develop proper empirical correlations for the PEM fuel cell.

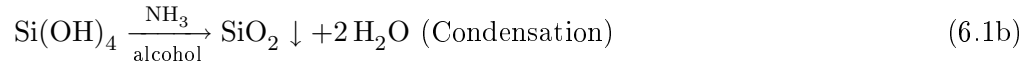
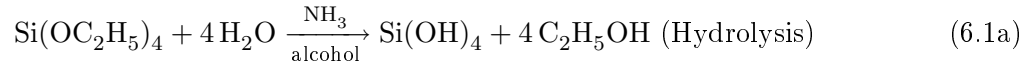
6.1 Carbon Support Development

Carbon support development for PEM fuel cell electrocatalysts was achieved by a three-step process. First, a proper silica template was synthesized by Stöber reaction to form silica spheres with desired structural properties such as porosity and average pore size. Second, a suitable carbon precursor with high carbon content was selected and incorporated into the template silica structure by template replication. Finally, removal of silica template with an etching process with HF or NaOH solution resulted in an ordered mesoporous carbon structure.

6.1.1 Solid Core Mesoporous Shell (SCMS) Silica

Uniform colloidal silica spheres can be prepared from tetraalkoxysilanes in alcohol based mixtures. Hydrolysis and condensation of the monomers are catalyzed by ammonia and alcohol and water act as co-solvents [151, 152]. The following reactions

take place during silica sphere formation:



Yu et al. [74] and Unger et al. [75] previously reported the synthesis of Solid Core Mesoporous Shell (SCMS) silica spheres with the sol-gel polymerization of Tetraethyl orthosilicate (TEOS) and Octadecyl trimethoxysilane (C18TMS). In addition, Burcu Güvenatam, a past member of our Fuel Cell Research group at METU, reported the preparation of different SCMS silica structures for various synthesis conditions in her Masters dissertation [153].

In brief, SCMS silica is synthesized with the addition of 3.5 ml of aqueous ammonia (28-30%, ACROS®) into a solution containing 74 ml of ethanol (99.8%, Riedel-de Haen®) and 10 ml of deionized water. This mixture was heated up to 303 K and then 6 ml of TEOS (98%, ACROS®) was added rapidly into the mixture as silica source under vigorous stirring and the reaction mixture was kept stirred for 1 h to yield uniform silica spheres.

A mixture containing 5 ml of TEOS and 2 ml C18TMS (tech. 90%, Aldrich®) was added drop wise over a 15 min period into the colloidal solution containing silica spheres and mixture was further reacted for 1 h. The resulting material was retrieved by centrifugation until the pH of the solution was stabilized. Nanocomposite material was dried in vacuum oven at 353 K and removal of the organic group from the octadecyltrimethoxy incorporated silica was achieved by calcination in a tubular furnace at 803 K for 6 h under the flow of oxygen.

6.1.2 Hollow Core Mesoporous Shell (HCMS) Carbon

SCMS silica is used as a template for further polymerization and carbonization steps for the synthesis of hollow core mesoporous shell (HCMS) carbon [74]. In this dissertation,

phenol/paraformaldehyde and divinylbenzene/azobis-isobutyronitrile (DVB/AIBN) (hereinafter, HCMS2) were used as carbon precursors for the preparation of HCMS1 and HCMS2 carbon supports respectively.

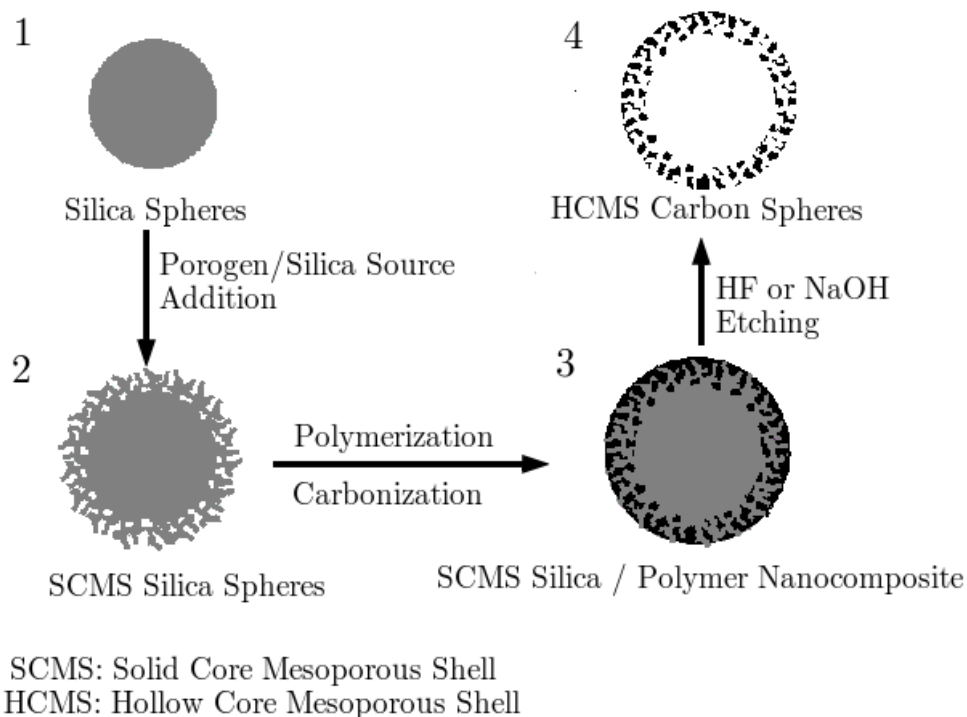


Figure 6.1: Depiction of silica template synthesis route for HCMS carbon

6.1.2.1 HCMS1 Carbon Synthesis: Phenolic Resin Route

In order to form acidic catalytic sites for phenolic resin polymerization reaction, aluminum was incorporated into the silicate framework via an impregnation method. For the impregnation of aluminum on SCMS silica, 1g of SCMS silica was added to an aqueous solution containing 0.3 g $\text{AlCl}_3 \cdot 6\text{H}_2\text{O}$ in 0.35 ml deionized water. The resulting slurry was stirred for 1h. The powder was dried in air at 353 K. Finally, the aluminum impregnated SCMS silica was calcined at 803 K for 5h in air to obtain the SCMS-aluminosilicate nanocomposite material.

For phenol/resin formation as carbon precursor over the aluminosilicate framework, 0.38 g of phenol per gram of the SCMS-aluminosilicate template was incorporated into the mesopores by heating at 373K for 12 h under vacuum. The resulting phenol-

incorporated SCMS aluminosilicate was reacted with 0.25 g paraformaldehyde under vacuum at 403K for 24 h to yield phenolic resin/HCMS-aluminosilicate nanocomposite inside the mesopores.

The phenol-resin incorporated nanocomposite material was heated with a ramp of 1Kmin^{-1} to 433K and held at that temperature for 5 h under the flowing nitrogen. The temperature was then ramped at 5Kmin^{-1} to 1103K and held at this temperature for 8 h to carbonize the phenolic resin inside the mesopores of HCMS aluminosilicate to obtain carbon/aluminosilicate nanocomposite. The aluminosilicate template was dissolved by using 48% HF solution resulted in hollow core mesoporous shell carbon (hereinafter, referred to as HCMS1 carbon) obtained from the phenolic resin route.

6.1.2.2 HCMS2 Carbon Synthesis: Divinylbenzene Route

In case of using divinylbenzene (DVB) as carbon precursor, SCMS silica was first dehydrated overnight at 473K under vacuum. After that, a carbon precursor solution containing 2 ml DVB for 1 g SCMS silica and AIBN (DVB/AIBN molar ratio is approximately 24) is added to the mesopores of SCMS silica template. The mixture is placed into a 25 ml Schlenk tube.

Prior to polymerization step, it is necessary to remove dissolved gases from the mixture. With this purpose, three freeze-pump-thaw cycles are performed to remove the dissolved oxygen. Polymerization is conducted at 343K for 18 h under nitrogen atmosphere in a drying oven. Resultant composite material is carbonized at 1103K for 8 h with a ramp of 1K min^{-1} under nitrogen flow. Etching of the silica template with 48% HF from the calcined nanocomposite material, one yields the hollow core mesoporous shell carbon (hereinafter, referred to as HCMS2).

6.2 Electrocatalyst Development

Carbon blacks are used as traditional PEMFC electrocatalyst support materials. Although carbon blacks can be produced through a relatively cost effective route, they exhibit random pore structure with low electrical conductivity. Controlling the sup-

port structure, a way of optimizing electrochemical reactions, is necessary for many specific applications. There is a need for producing suitable support materials and electrocatalysts to prepare catalyst layers that can survive in the severe reaction conditions.

Another important issue in PEM fuel cells is due to the active platinum metal. Platinum outperforms any other nanometal when it is used as electroactive material for PEM fuel cell reactions. In addition, cost and availability of platinum are the two major problems that delays the commercialization of these electrocatalysts through mass production.

In this dissertation, new Pt-Pd/HCMS bimetallic electrocatalysts were synthesized with the use of novel carbon support materials. The purpose was to prepare a functional carbon material that can serve as electrocatalyst support with superior structural, electrical, and thermal properties as compared to conventional PEM fuel cell electrocatalyst supports. Moreover, possibility of replacing the electroactive platinum metal or reducing the amount of platinum nanometal have been explored through *in situ* and *ex situ* analysis methods.

6.2.1 Synthesis of Pt/HCMS Electrocatalysts

HCMS carbons prepared by different synthesis routes (HCMS1 and HCMS2) were used as the electrocatalyst support material. Hexachloroplatinic acid (H_2PtCl_6 , ca. 40% Pt ACROS[®]) and palladium (II) chloride (PdCl_2 , 99.9% Aldrich[®]) were used as platinum and palladium precursors respectively. For the electrocatalyst preparation, a microwave oven (Akai[®], 2450 MHz, and 800W) was used to employ microwave irradiation method.

The commercial Pt (20% Pt/C, ETEK[®]) electrocatalyst was selected as base case catalyst for comparison with the novel electrocatalysts. The prepared and commercial electrocatalysts were used as either anode or cathode electrodes. Palladium content in the carbon supported bimetallic Pt-Pd catalysts were varied between 0 wt.% and 20 wt.%.

6.2.2 Synthesis of Pt-Pd/HCMS Electrocatalysts

Pt/HCMS catalysts were prepared by using microwave heating of ethylene glycol solutions of the metal precursors [86]. Briefly, 0.05M aqueous solutions of Pt and Pd precursors were prepared. A required volume of these solutions which corresponds to the desired Pt and Pd loadings were mixed with 50 ml ethylene glycol (EG) in a 100 ml beaker. Then, 0.1 g HCMS carbon was added to the solution.

After ultrasonic mixing for half an hour, the mixture was put in the center of the microwave oven and heated for 120 s by means of an 800W microwave power. The resulting suspension was cooled immediately, and then filtered off and the residue was washed with acetone and deionized water. The solid product was dried overnight at 373K in a vacuum oven.

6.2.3 Carbon Black Supported Electrocatalysts

Microwave irradiation method was used for the incorporation of the 20 wt% platinum nanoparticles into the carbon supports. Previously, effect of microwave duration on performance of Pt/Vulcan XC72 (Pt/VX) electrocatalysts was reported [154, 87] and an optimum microwave duration of 50 s at 800W was reported for Pt supported Vulcan XC72. Therefore, in the case of carbon black based electrocatalysts, microwave duration was adjusted to 50 s at 800 W.

6.3 Characterization of Carbon Supports and Electrocatalysts

In order to investigate the structural properties of the carbon support and the electrocatalyst, nitrogen adsorption analysis was carried out with a surface area analyzer (Quantachrome[®] Autosorb-1C and Micromeritics[®] Gemini V 2365). Thermogravimetric analysis (TGA) was performed with Shimadzu[®] DTG-60H under the flowing air (50 ml min⁻¹) with a heating ramp of 5 °C min⁻¹.

The crystalline phases of HCMS carbon and carbon black supported Pt electrocatalysts were identified by measuring their X-ray diffraction (XRD) patterns on a Rigaku[®] Ultima D-Max 2200 diffractometer with monochromatic Cu K α radiation source. The

scanning range of 2θ was set between 5° and 85° with a scan step size of 0.02° .

Supplementary electrocatalyst characterization was conducted with X-ray photoelectron spectroscopy (XPS, specs GMBH), scanning electron microscopy (SEM, Quanta[®] FEG), and transmission electron microscopy (TEM, JEOL[®] 2100F) analysis.

6.4 Characterization of PEM Fuel Cell Diffusion Media

PEM fuel cell diffusion media is characterized by mercury intrusion porosimetry analysis (Quantachrome[®], Poremaster 60). Bulk porosity and structural pore distribution can be obtained through this technique. Unlike nitrogen adsorption experiments, material could not be recovered due to penetration of mercury into pores. Additionally, SEM micrographs were taken for various fuel cell components including diffusion media and electrolyte. Cross section of the samples were prepared with the use of liquid nitrogen and results are presented and discussed in section 7.8 of the experimental results.

6.5 Ionic Conductivity Measurement

Proton transfer in the solid polymer electrolyte plays a critical role for the overall fuel cell performance. In order to predict the fuel cell transport mechanisms accurately by means of a mathematical model, one needs reliable experimentally measured proton conductivity data inside the membrane. For this purpose, a conductivity measurement setup given in Figure 6.2 is prepared.

The aim is to measure proton conductivity at different temperature and relative humidities. The major component of the setup is a Teflon based conductivity cell in which the membrane electrode assembly is placed (MEA). Conductivity cell has essentially two different parts; first part is the gas distribution channels on top and the second part is the saturated salt solution storage part at the bottom of the left and right components of the conductivity cell (see Figure 6.3).

A bilayer carbon based gas diffusion media (macroporous and microporous layer) is used for anode and cathode and Nafion[®] NR-212 membrane is used as the electrolyte

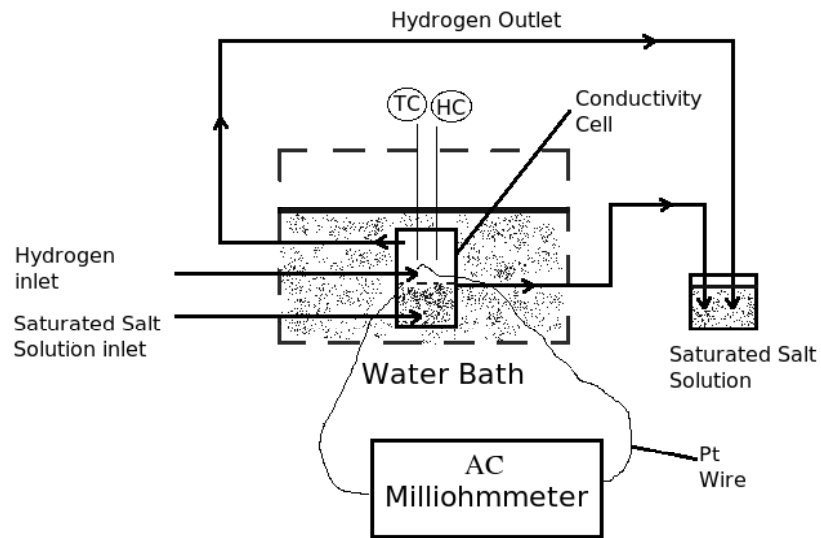


Figure 6.2: Experimental setup for ionic conductivity measurement

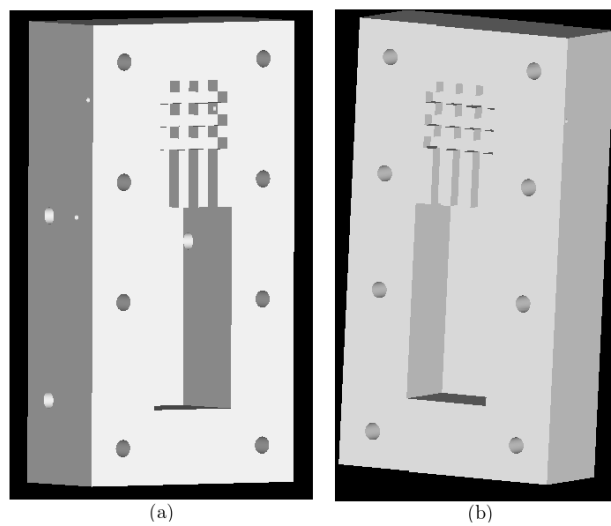


Figure 6.3: Conductivity cell for proton conductivity measurement (a) Left view, (b) Right view

in the conductivity cell. Platinum catalyst particles are uniformly distributed over the microporous layer (MPL) of the diffusion media via sputtering method. With the sputtering method [155], one can provide very uniform and controlled thickness of catalyst layer on top of the MPL.

MEA is placed, sealed and compressed to a prespecified thickness within the conductivity cell. Saturated salt solution is introduced to the cell from the bottom to a certain volume. After that, first nitrogen gas is passed through the cell slowly to remove air inside the cell and then a known pressure of hydrogen gas is fed to the electrochemical reactor.

Conductivity cell is placed inside a water bath for temperature and humidity control. Temperature of the conductivity cell is measured with thermocouple and the relative humidity is controlled by using various salt solutions [156] (e.g. NaCl). Pt wires are connected to anode and cathode for the measurement of ionic conductivity. For 25-90 °C temperature range and 0-100 % relative humidity range, ionic conductivity of the membrane can be measured with the use of an AC milliohmeter.

6.6 Capillary Transport Mechanism

In order to optimize fuel cell electrodes, one needs relation for the two phase transport properties of the materials used in the PEMFC. The following water displacement setup could be used for the measurement of capillary pressure as function of liquid phase saturation [44]. Figure 6.4 shows the simplified illustration of water displacement setup. Three major components of the setup are the sample fixture, tube connections and the horizontal tube for volume displacement measurement.

To prevent water loss to the atmosphere by evaporation, outlets were exposed to water-saturated air. Sample fixture includes two end plates, plastic at the top and stainless steel at the bottom, with a grid like channel architecture to support and provide liquid water transport. It is possible to investigate water transport characteristics for various gas diffusion layers with different wetting properties.

Filling up of water into the porous media is the first step in the measurement of capillary data. Degassed and deionized water is added to the vertical tubing (as shown

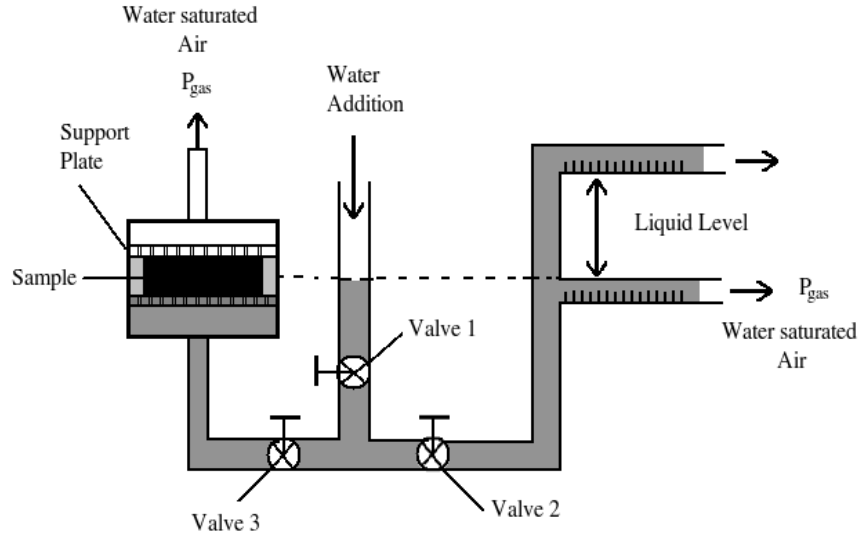


Figure 6.4: Experimental setup for capillary measurement

in Figure 6.4) by closing only valve three to fill the horizontal graduated tube with water. After that, only closing valve 2, water is supplied to the tubing until water reaches to the bottom of the sample holder.

Raising the graduated tubing with small increments (e.g. 2mm), water is introduced into the sample. Having recorded the volume displacement only after steady state, one can move to the next level in the graduated tube. The amount of water displaced is determined from the difference between the original reading and the final reading.

Liquid pressure is measured via pressure transducer. These raising the graduated tube and reading steps are repeated until a desired saturation level is reached within the sample. After the fill up cycle, first drainage curve is obtained. Consequent measurements are performed to repeat drainage and imbibition process. Multiple imbibition and drainage cycles are necessary to ensure that data are reproducible and also to check for hysteresis.

Repeating the above procedure for different samples, one can derive capillary pressure data as function of water saturation level. This experimental data is crucial for the investigation and simulation of two-phase transport in the porous diffusion media of the proton exchange membrane fuel cells (see Appendix A.3).

6.7 Electrochemical Characterization

Electrocatalytic performance of the catalysts can be tested either with half cell experiments (ex situ analysis with cyclic voltammetry tests) [157] or in a single cell PEMFC [88]. Half cell experiments are performed with rotating disk electrode (RDE). The CV analysis system is shown in Figure 6.5. It is a convenient and relatively fast method of screening electrocatalysts. Seda Şayin, a present member of our Fuel Cell Research group at METU, studied the parameters influencing long term performance and durability of PEM fuel cells with the use of cyclic voltammetry. Detailed information on cyclic voltammetry analysis can be found in her Masters dissertation [158].

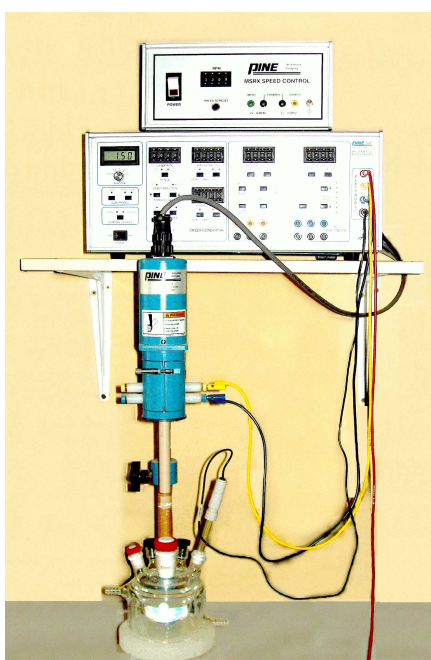


Figure 6.5: Experimental setup for cyclic voltammetry

The fuel cell test is the primary technique for the characterization of the whole fuel cell performance. PEMFC tests supply the voltage–current density relationship under fuel cell environment. The performance curve obtained also gives information about the cell losses under the fuel cell operating conditions. For a detailed characterization of the fuel cell, the effects of both system components and operating conditions have to be analyzed by performance curves. In addition, these performance curves help to determine which performance loss dominates and provide the information for a new

route to compensate the inverse effect. There are few publications in literature, which have compared the relative significance of these experimental data [159–161].

6.7.1 Cyclic Voltammetry Tests

Cyclic Voltammetry (CV) is a useful electrochemical characterization tool to measure the available electrochemically active surface area for anode and cathode reactions. Briefly, catalyst ink was prepared by mixing measured amounts of the prepared catalysts with deionized water, 1,2-Propanediol, and 15% Nafion[®] solution. The suspension was ultrasonicated for 1 h. Necessary amount of catalyst to prepare 5mm diameter glassy carbon (GC) electrode with a Pt loading of 28 $\mu\text{g Pt cm}^2$ was incorporated into the solution.

Cyclic voltammograms were recorded in a 0.1M HClO₄ electrolyte that was saturated with nitrogen for 30 min to remove the oxygen. All the experiments were performed at room temperature with a rotating disc electrode equipped with a bipotentiostat (Pine[®] AFCBP1). After 100 cycles at a scan rate of 50 mVs⁻¹, the CV curves were recorded. CV data were reported with respect to a normal hydrogen electrode [162].

6.7.2 PEM Fuel Cell Performance Tests

The prepared catalyst ink sprayed onto the gas diffusion layers and then hot pressed onto the Nafion[®] 112 membrane. After the construction of the single cell by using a commercial hardware (Electrochem[®], FC05-01 SP REF), the fuel cell tests were performed by using the home made fuel cell test station [163]. Figure 6.6 shows the flow diagram of the fuel cell test station.

PEM fuel cell performance tests were conducted at atmospheric pressure and fuel cell temperature was set to 70 °C, whereas anode and cathode humidifiers were adjusted to 70 °C. All lines prior to fuel cell were heated to maintain the uniform temperature at the inlet to the fuel cell. Pure hydrogen and oxygen gases were used as reactants and using mass flow controllers (Aalborg[®]) both of the reactants fixed flow rate were kept at 100 cm³ min⁻¹ during the experiments. The Pt loading of both anode and cathode electrodes was 0.4 mg Pt cm².

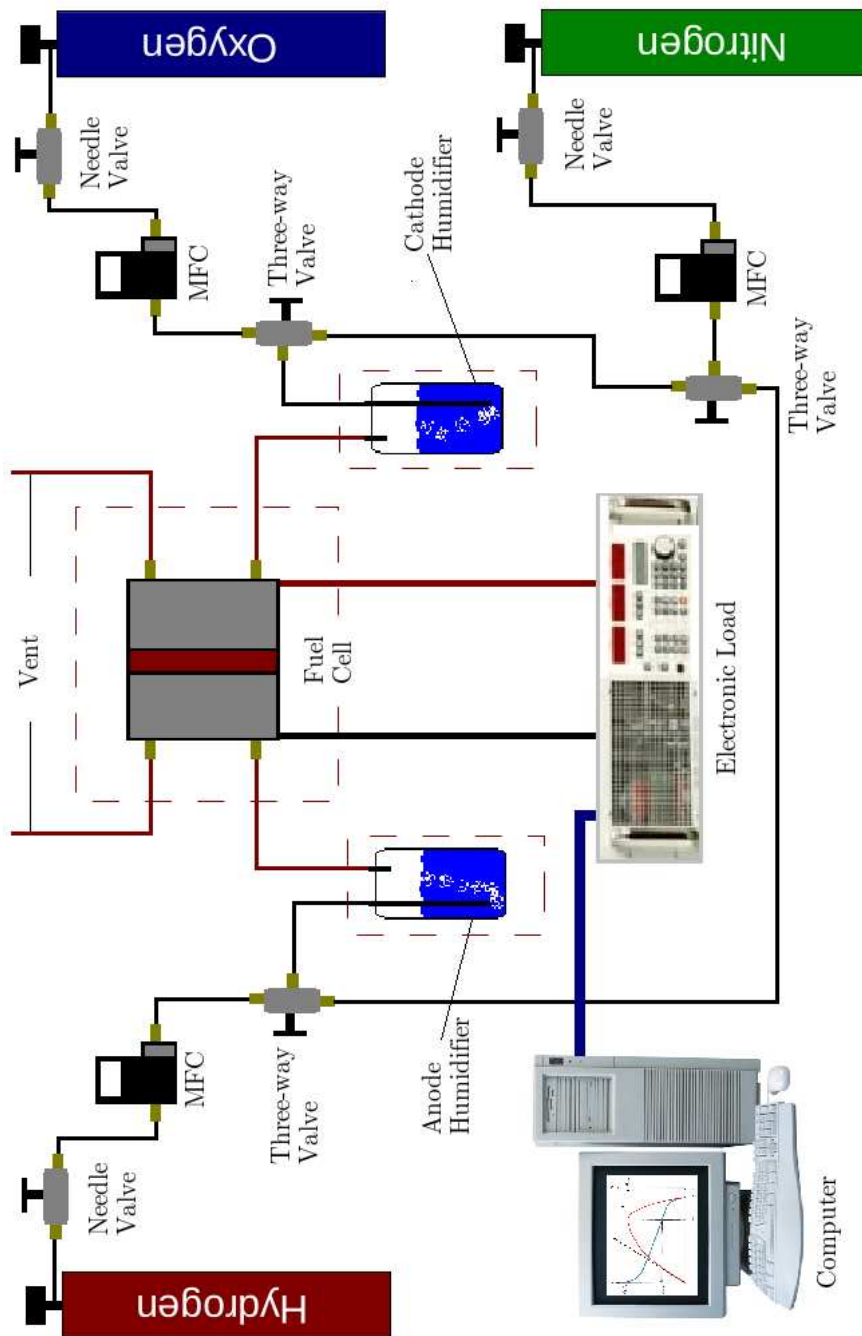


Figure 6.6: Single cell PEM Fuel Cell test station

Fuel cell was first purged with nitrogen for 30 min and then operated at 0.5 V for several hours. Potentiostatic measurements were recorded with an electronic load (TDI[®] dynaload RBL488 400W) integrated to the single fuel cell. For each data point, fuel cell was operated approximately 5 min. at the target potential to ensure steady state conditions. Following this protocol, steady state currents were measured for corresponding set potentials to derive the polarization curve. Recorded PEM fuel cell performance data for various electrocatalysts are tabulated in Appendix D.

CHAPTER 7

PEM FUEL CELL ELECTROCATALYST DEVELOPMENT

The purpose of the present research was to explore and compare the performance of Pt/C electrocatalysts supported on various carbon supports by testing their ex situ performances with cyclic voltammetry (CV) method and in situ performances in a single cell PEMFC where the catalysts are being used as cathode electrodes. The relevance of these data are compared on the electrocatalyst development and improvement for PEMFCs.

In the present work, I have prepared electrocatalysts for PEMFCs with three conventional carbon blacks (Vulcan XC72, Black Pearl 2000, and Regal 330) and a synthesized novel ordered mesoporous carbon as electrocatalyst support. High surface area HCMS carbon with a bimodal macroporous/mesoporous structure was prepared with the template replication of solid core mesoporous shell (SCMS) silica. A promising carbon nanomaterial with hollow core mesoporous shell (HCMS) structure was synthesized as PEMFC catalyst support.

Microwave synthesis method was used for the incorporation of Pt nanoparticles on carbon supports. The Pt/C electrocatalysts were characterized by N₂ adsorption analysis, X-ray diffraction (XRD), X-ray photoelectron spectroscopy (XPS), thermogravimetric analysis (TGA), scanning electron microscopy (SEM), and transmission electron microscopy (TEM). Subsequently, electrochemical activity measurements (CV tests) were conducted and single cell PEMFC performances of these electrocatalysts were investigated in the cathode electrode.

Bimetallic Pt-Pd over HCMS carbon electrocatalysts is suggested to improve oxygen reduction reaction (ORR) and hydrogen oxidation reaction (HOR). In this work, it is aimed to synthesize Pt-Pd bimetallic catalysts supported with a novel HCMS carbon by microwave irradiation. HCMS carbon spheres with periodically ordered structural properties are synthesized by two different carbon precursors with the template replication of sub micrometer-size solid core mesoporous shell (SCMS) silica spheres.

Results presented are due to the electrocatalyst development for PEM fuel cells operating at relatively low temperatures. First, ex situ characterization of Pt and Pt-Pd incorporated electrocatalysts are presented and evaluated. Second, electrochemical activity of these electrocatalysts are compared and fuel cell performance test results are concluded for the synthesized electrocatalyst.

Ordered mesoporous carbons are attractive supporting materials for use in electrocatalyst development in fuel cells. A novel mesoporous carbon nanomaterial is developed by using silica spheres as template. Platinum and Palladium metals are doped into the mesopores of the carbon supports and their electrocatalytic activity and PEM fuel cell performance experiments were conducted. In order to elucidate the effect of novel Pt/HCMS and Pt-Pd/HCMS electrocatalysts on fuel cell performance, electrocatalysts were compared with the commercial carbon black supported electrocatalysts.

7.1 Solid Core Mesoporous Shell Silica

Sub micrometer-size silica spheres exhibiting solid core mesoporous shell structure were synthesized with a molar ratio of TEOS/C18TMS = 5.3 [74, 75]. Adjusting the molar ratio of TEOS/C18TMS, one can change the core and the shell thicknesses of the silica template [164]. Scanning electron microscopy (SEM) images of SCMS silica spheres (Figure 7.1) showed that the spheres are uniformly distributed with an average particle size of 490 nm.

The transmission electron microscopy (TEM) micrograph of the solid core mesoporous shell silica is shown in Figure 7.2. TEM micrograph clearly indicates the formation of spherical silica nanoparticles with a solid core diameter of 300 nm and a mesoporous shell thickness of 95 nm respectively.

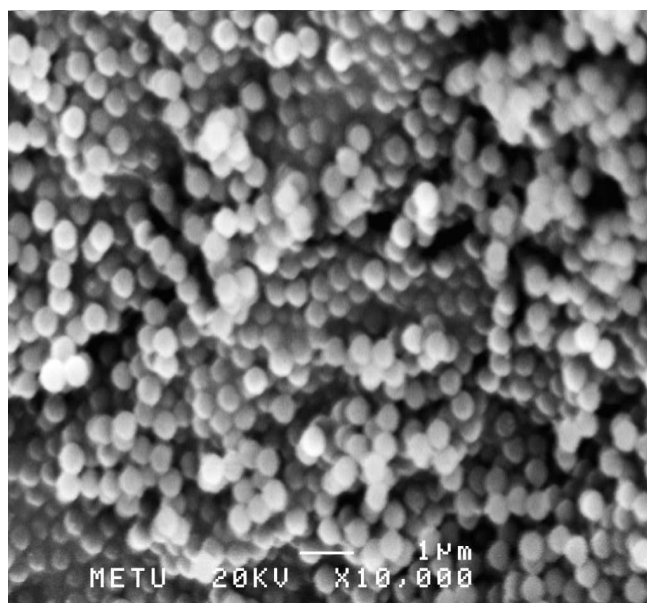


Figure 7.1: SEM micrograph of solid core mesoporous shell (SCMS) silica

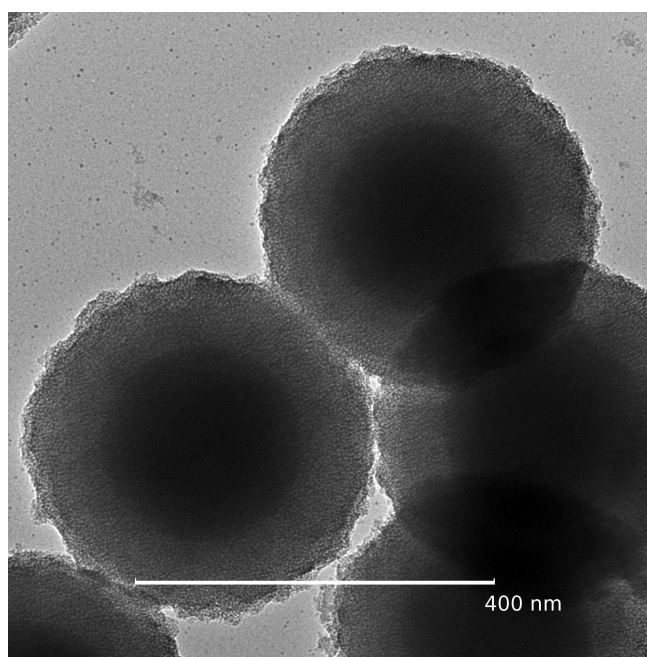


Figure 7.2: TEM micrograph of solid core mesoporous shell (SCMS) silica

Typical nitrogen adsorption/desorption isotherms and corresponding pore size distribution for SCMS silica are shown in Figure 7.3. Brauner-Emett-Teller (BET) surface area of SCMS silica was calculated as $492 \text{ m}^2 \text{ g}^{-1}$ for a total pore volume of $0.40 \text{ cm}^3 \text{ g}^{-1}$. The pore size distribution data calculated from the adsorption branches of nitrogen isotherms by the Barrett-Joyner Halenda (BJH) method indicated that the pores of the SCMS silica template are uniform and centered at 2.41 nm.

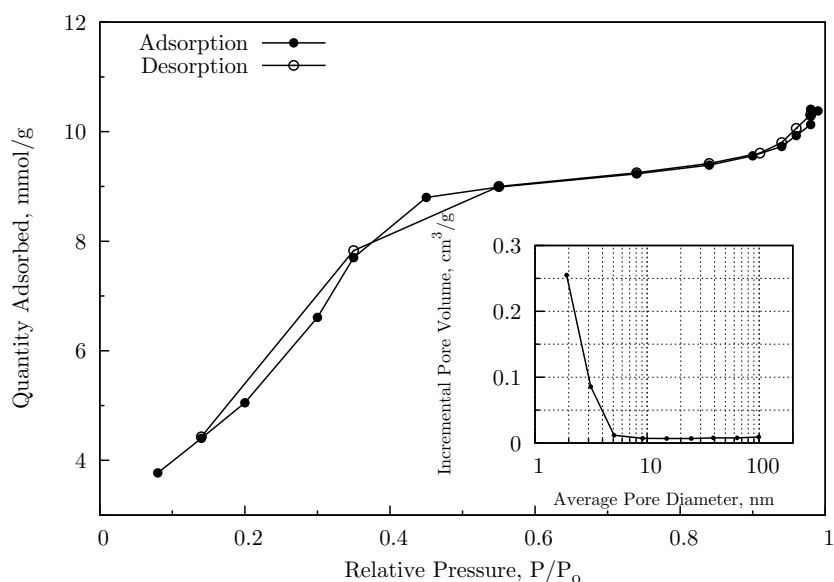
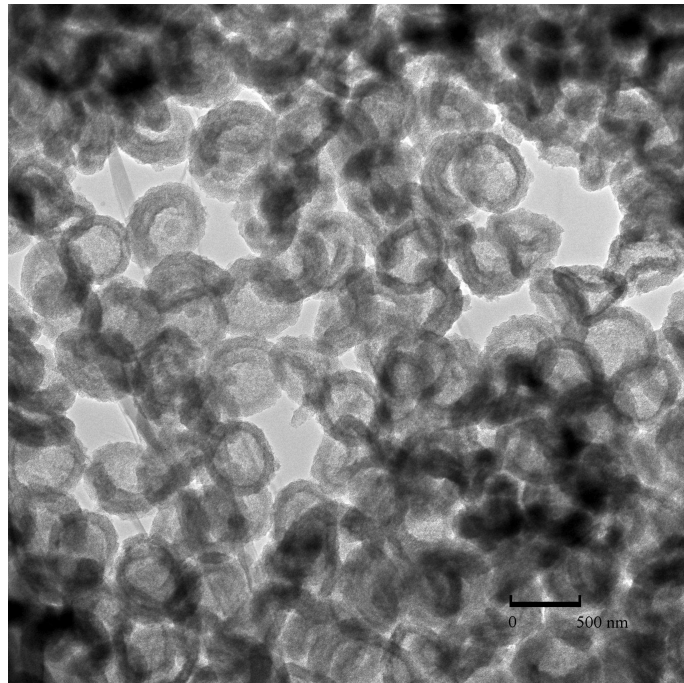


Figure 7.3: N_2 adsorption/desorption isotherms and the corresponding pore size distribution for SCMS silica

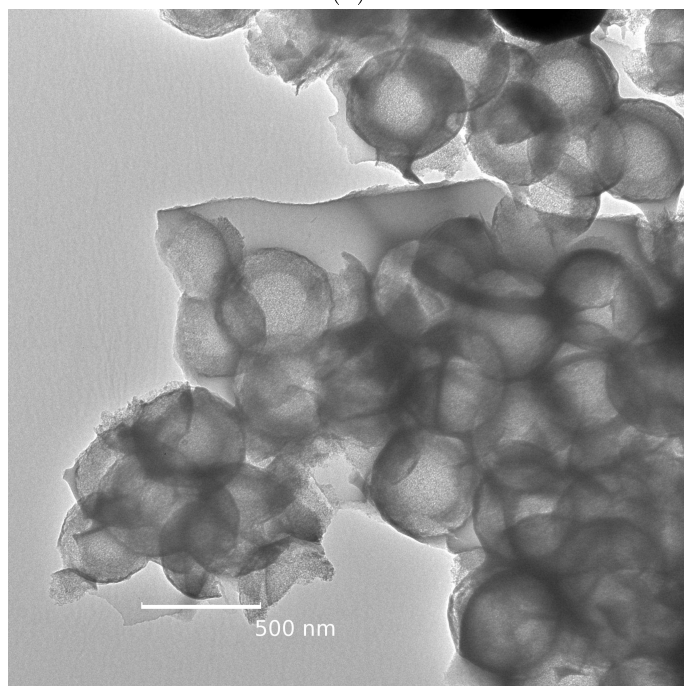
7.2 Hollow Core Mesoporous Shell Carbon

Characterization of the spherical hollow core mesoporous shell carbon structures was conducted with nitrogen adsorption, SEM, and TEM analysis. SEM micrograph of HCMS carbon (Figure 7.4a) revealed that spherical carbons were uniformly distributed with an average particle diameter of 500 nm and some carbon capsules were fragmented. TEM image (Figure 7.4b) of the HCMS2 carbon particles exhibited a uniform particle size with a core diameter of 340 nm and shell thickness of 80 nm respectively.

HCMS1 nitrogen adsorption/desorption isotherms at 77 K and corresponding pore size distributions for HCMS1 and HCMS2 are shown in Figure 7.5. The isotherm for HCMS



(a)



(b)

Figure 7.4: TEM images of (a) HCMS1 carbon and (b) HCMS2 carbon

carbon exhibited type IV with a H2 hysteresis (according to IUPAC classification). The pore size distribution of the prepared HCMS carbon spheres is uniform and the average pore diameter is 3.02 nm for HCMS1 and 3.90 nm for HCMS2 estimated from BJH analysis for the adsorption branches of the isotherm data. BET surface area of HCMS carbon was found as 1290 m² g⁻¹ for HCMS1 and 759 m² g⁻¹ for HCMS2.

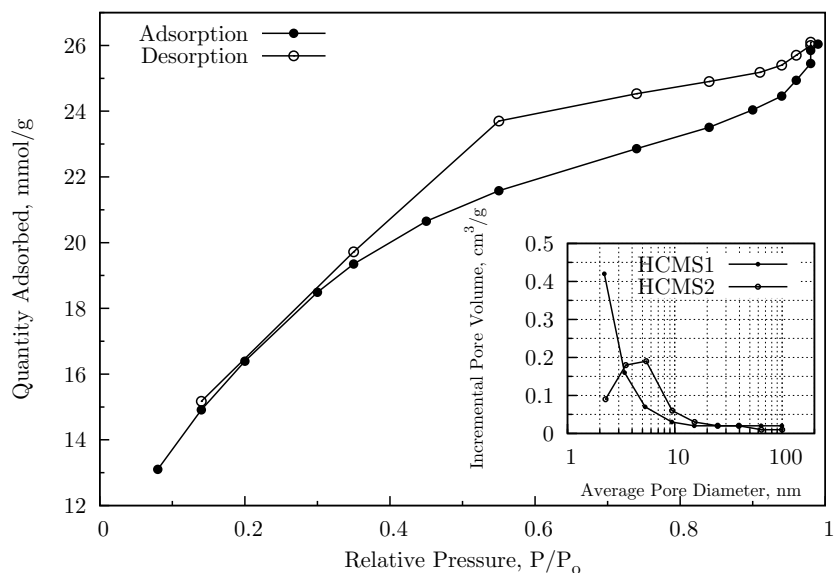


Figure 7.5: N₂ adsorption/desorption isotherms and the corresponding pore size distribution for HCMS carbon

7.3 Ex situ Characterization of the Carbon Supports and Pt/C Electrocatalysts

Nitrogen adsorption-desorption analysis of the nanomaterials was conducted at 77 K. Results of some structural parameters for both the carbon supports and the 20% Pt/C electrocatalysts are presented in Table 7.1. High surface area HCMS1 and HCMS2 nanosized spherical carbons exhibited meso/macro bimodal pore structure. BET surface area of the hollow core mesoporous shell carbons was found in the range of ca. 750-1300 m² g⁻¹. Moreover, average pore diameter of the ordered HCMS structure based carbons was calculated in the mesoporous range (ca. 3-4 nm).

On the other hand, average pore diameter of the carbon blacks with disordered struc-

tures changed approximately between 6 nm and 23 nm. In addition, BP2000 exhibited the largest BET surface area with a highly microporous structure in comparison to the other carbon blacks.

It is well known that the meso/macro structures and the porosity of the carbon support can greatly affect the electrochemical properties of the catalyst in the fuel cell environment [165, 166]. Therefore, it is critical to obtain a suitable pore structure for both high metal dispersion and high gas flow.

Table 7.1: Structural properties of the carbon supports and the electrocatalysts

Carbon support	BET surface area (m^2g^{-1})	Total pore volume (cm^3g^{-1})	Average pore diameter (nm)
HCMS1	1290	0.80	3.0
HCMS2	759	0.99	3.9
BP2000	1579	4.77	5.9
Regal	83	0.55	23.1
VX	211	0.34	8.8
Electrocatalyst			
Pt/HCMS1	1054	0.72	3.2
Pt/HCMS2	276	0.33	3.4
Pt/BP2000	987	0.90	5.8
Pt/Regal	75	0.39	17.9
Pt/VX	140	0.31	9.8

As the Pt nanoparticles were incorporated into the carbon supports, BET surface areas of the electrocatalysts were found to change between $75 \text{ m}^2 \text{ g}^{-1}$ (Pt/Regal) and $1054 \text{ m}^2 \text{ g}^{-1}$ (Pt/HCMS1). It has to be remarked that introducing the platinum nanoparticles into the HCMS2 carbon support structure lowered the BET surface area of the electrocatalyst sharply, which might indicate the uniform dispersion of Pt particles in the mesopores of the HCMS2 carbon structure. However, due to the slight decrease in BET surface area of Pt/HCMS1 electrocatalyst (Table 7.1), one can conclude that the smaller pore size of the HCMS1 carbon ($\approx 3.0 \text{ nm}$) hindered the incorporation of the larger Pt nanoparticles into the HCMS1 carbon structure.

Pore size distribution data were calculated from the adsorption branches of nitrogen isotherms by the Barrett-Joyner-Halenda (BJH) method. Typical pore size distribution for the carbon supports and Pt/C electrocatalysts is shown in Figure 7.6 and 7.7.

HCMS based carbons present a different morphology and pore texture both at the nanoscopic level and at the macroscopic level.

As can be seen from Figure 7.6, pore size distribution of the prepared HCMS carbon spheres is uniform and the average pore diameter is centered at around 3.0 nm in the mesoporous region. On the other hand, Vulcan XC72 and Regal have random pores and indicate a pore size distribution both in the mesoporous and macroporous regions (Figure 7.6).

Inset curve in Figure 7.6 shows the pore size distribution of Black Pearl 2000 (BP2000) carbon support. BP2000 exhibited a uniform pore size distribution in the highly microporous region leading to a higher Brauner-Emett-Teller (BET) surface area. Conversely, Regal carbon support showed a pore size distribution mostly in the meso/macro range with larger pores and smaller BET surface area (Table 7.1).

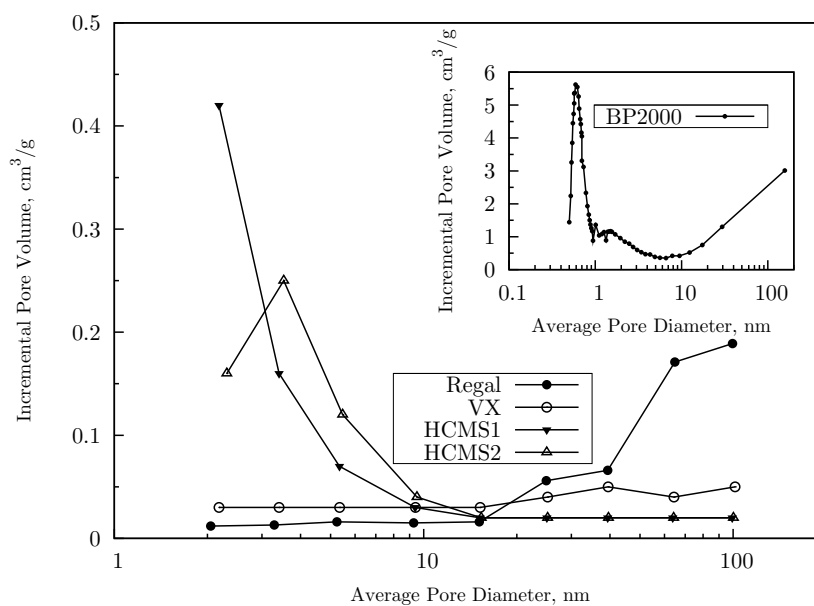


Figure 7.6: Pore size distribution of the carbon supports

Figure 7.7 shows the pore size distribution of the Pt/C electrocatalysts. Inset curve for Pt/HCMS1 electrocatalyst shows a sharp pore size distribution centered at ca. 3.5 nm, whereas Pt/HCMS2 electrocatalyst signifies a broadened peak at ca. 3.0 nm that is mostly spread in the mesoporous region with larger mesopores. Modification in the pore structure with the use of different carbon precursor might be responsible for the

better transfer of reactants and products inside the catalyst layer.

As compared to HCMS carbon based electrocatalysts, pore size distribution curves for Vulcan XC72 carbon based Pt/VX and Pt/C (ETEK[®]) catalysts exhibited a lower total pore volume and micropore fraction. Large portion of the pores of Pt/VX and Pt/C (ETEK[®]) electrocatalysts were detected in the mesoporous and macroporous regions with significantly larger pores compared to the HCMS carbon based electrocatalysts.

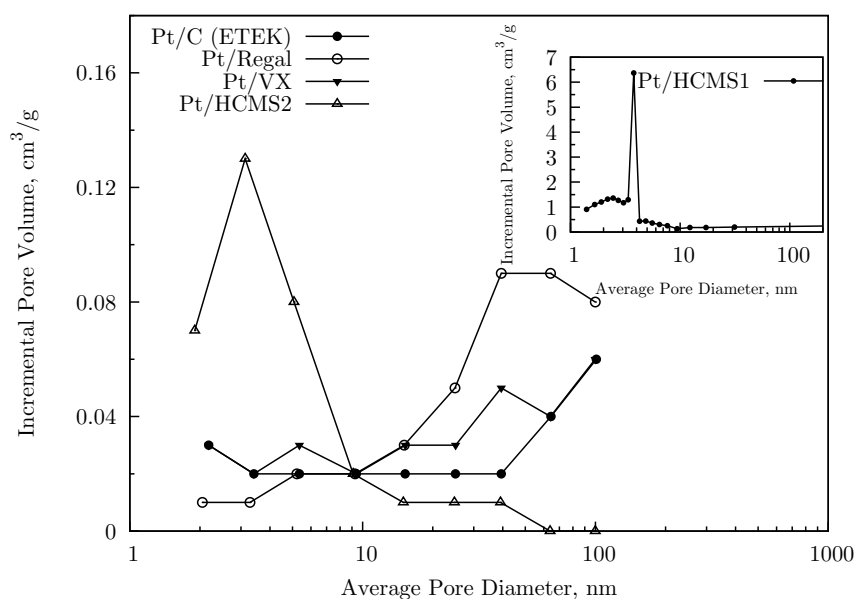


Figure 7.7: Pore size distribution of the 20% Pt/C electrocatalysts

Typical XRD patterns for both HCMS carbon based electrocatalysts and commercial carbon based electrocatalysts are shown in Figure 7.8. It was observed that all the XRD patterns of the Pt/C electrocatalysts exhibit the main characteristic peaks of FCC crystalline Pt with the planes of (111), (200), (220) and (311). The particle sizes of the catalysts were calculated by using Scherrer equation and given in Table 7.3. Incorporation of Pt particles by microwave synthesis resulted in smaller catalyst particles. Particle size diameters were computed in a range of 3.3-4.0 nm.

During the catalyst preparation, as the microwave duration increases the temperature of the solution increases that may cause the growth of the Pt particle size. Effect of

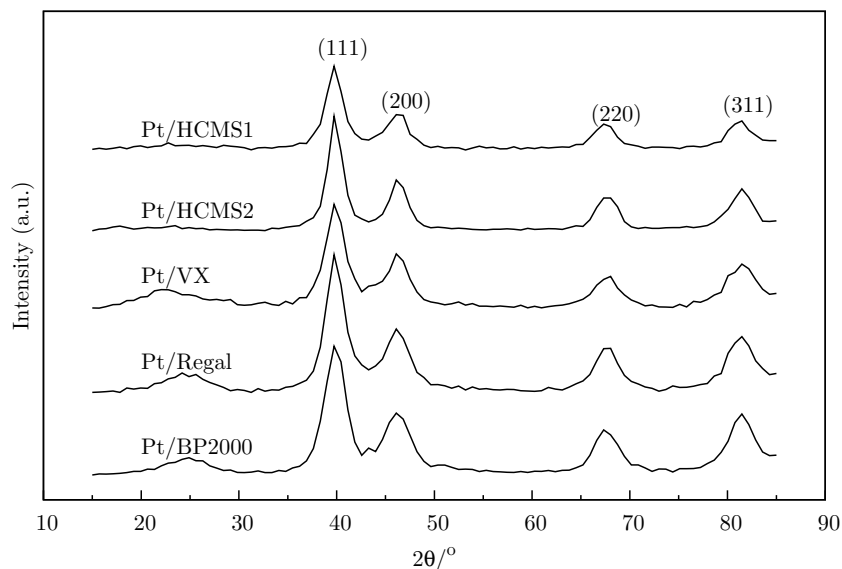


Figure 7.8: The XRD patterns of 20% Pt/C electrocatalysts

microwave duration on average catalyst particle size was previously reported for Pt/VX electrocatalysts [87]. Optimum microwave duration was found as 50 s for VX based catalysts. When the microwave duration was increased up to 120 s, relatively larger catalyst particles of 5.7 nm were obtained for Pt/VX catalysts. It may be concluded that both the carbon structure and the microwave duration affect the catalyst average particle size and therefore it is essential to optimize microwave duration to meet the desired catalyst particle size.

For HCMS carbon based Pt/C electrocatalyst synthesis, microwave duration was optimized and set to 120 s, whereas microwave duration for the carbon black based Pt/C electrocatalysts was adjusted to 50 s (Table 7.3).

Oxygen reduction reaction of PEM fuel cells is highly dependent on the oxidation states of the Pt crystallites on the surface of the electrocatalyst. Pt oxidation state and the interaction between carbon support and platinum metal were determined by XPS. Figure 7.9 shows the Pt 4f core level spectra of 20% Pt/C electrocatalysts for high and low energy bands.

Table 7.2 presents the XPS data for the Pt/C electrocatalysts. Intensive doublet

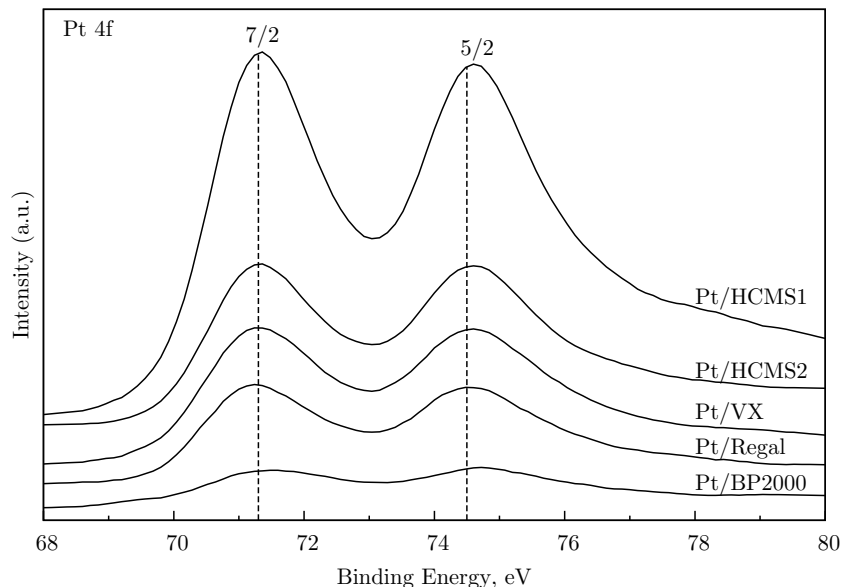


Figure 7.9: Pt 4f XPS spectra for 20% Pt/C electrocatalysts

at ca. 71.3 and 74.5 eV indicates the existence of metallic platinum for all Pt/C electrocatalysts. The observed slight shift of the doublet to the higher binding energies might be a signal of stronger carbon support/platinum interaction. Pt 4f_{7/2} core level spectra shifted from the probable 70.9 eV to 71.3 eV for Pt/HCMS1 and Pt/HCMS2 electrocatalysts and in the case of carbon black based electrocatalysts Pt 4f_{7/2} peak shifted slightly to higher binding energies for the carbon blacks (Table 7.2). This small shift of Pt 4f_{7/2} peak can signify the oxidation of platinum [165, 167].

Table 7.2: XPS data of carbon supported platinum electrocatalysts

Electrocatalyst	Binding energy (eV)			
	Pt 4f _{7/2}	Pt 4f _{5/2}	C 1s	O 1s
Pt/HCMS1	71.3	74.6	284.4	532.8
Pt/HCMS2	71.3	74.5	284.4	532.4
Pt/BP2000	71.5	74.8	284.8	532.8
Pt/Regal	71.2	74.5	284.4	532.4
Pt/VX	71.2	74.4	284.4	532.4

Figure 7.10 shows the XPS survey spectra of HCMS carbon based and carbon black based electrocatalysts. As can be seen from the figure, XPS spectra were dominated by Pt and C signals. C 1s and O 1s peaks were detected at the binding energy ranges

of 284.4-284.8 eV and 532.4-532.8 eV respectively (Table 7.2). A slight shift of C 1s and O 1s peaks was observed for Pt/BP2000 electrocatalyst, small shift of O 1s peak to higher values might indicate a higher content of surface oxides on the BP2000 carbon support surface due to electrochemical oxidation [166].

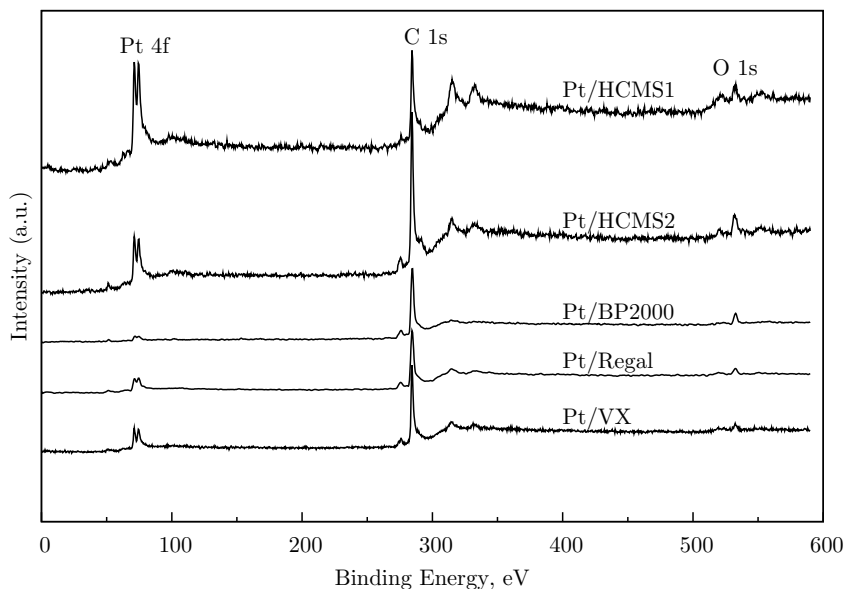


Figure 7.10: XPS survey spectra for 20% Pt/C electrocatalysts

As a result of surface elemental composition analysis by XPS, some small amounts of chlorine and fluorine anions were found in the HCMS carbon based catalyst structure. In addition, some chlorine anion was also measured in carbon black based electrocatalysts. It is noteworthy that no harmful effect of anions like Cl^- and F^- was detected on single cell polymer electrolyte membrane fuel cell performance.

Thermogravimetric analysis results of 20% Pt/C electrocatalysts are shown in Figure 7.11. TGA experiments were performed under the flowing air to roughly estimate the Pt content and detect the thermal decomposition of the electrocatalysts [168]. Incorporation of platinum into the carbon support accelerated the oxidation of carbon supports. Each electrocatalyst follows a different thermal history, which might be a consequence of surface functional groups.

It was found that the Pt content of the Pt/C electrocatalysts was close to the 20 wt% target Pt loading (Table 7.3). It can be concluded that the thermal stability of

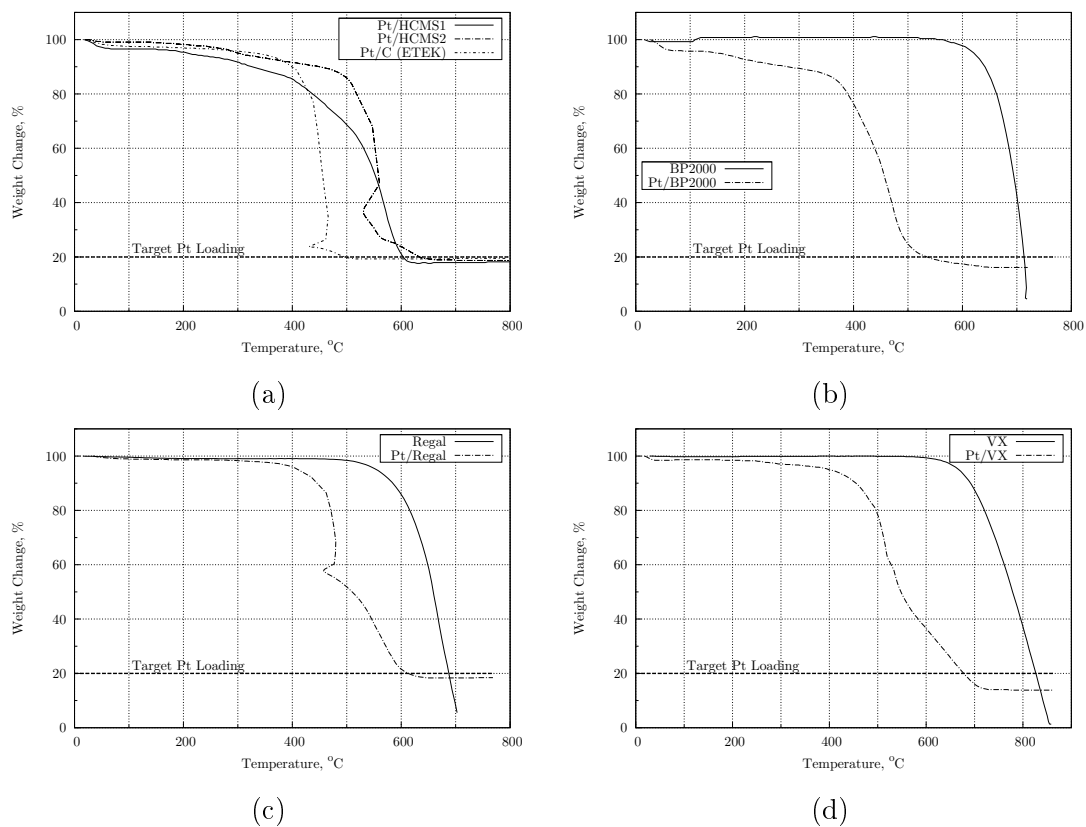


Figure 7.11: TGA data of (a) 20% Pt/HCMS1, 20% Pt/HCMS2 and 20% Pt/C (ETEK[®]), (b) BP2000 and 20% Pt/BP2000, (c) Regal and 20% Pt/Regal, (d) VX and 20% Pt/VX

the HCMS2 supported catalyst was increased considerably with respect to HCMS1 supported catalyst (Figure 7.11a). Furthermore, both BP2000 and Regal started to decompose at around 600 °C (Figure 7.11b and 7.11c). However, Pt/BP2000 electrocatalyst exhibits much less thermal stability compared to the other electrocatalysts for the reported temperature ranges. On the other hand, VX and Pt/VX (Figure 7.11d) exhibited a higher thermal stability compared to the other nanomaterials.

7.4 Electrochemical Characterization of Pt/C Electrocatalysts

Cyclic voltammograms for the HCMS carbon based catalysts, commercial catalyst, and for the commercial carbon black based catalysts are given in Figure 7.12 and 7.13, respectively. Analyzing the electrochemical activity of the electrocatalysts, hydrogen adsorption/desorption peaks were observed between 0 and 0.4 V both for the anodic and the cathodic regions, whereas Pt oxide formation was observed at ≈ 0.75 V for anodic region and the Pt reduction was observed at ≈ 0.65 V for the cathodic region.

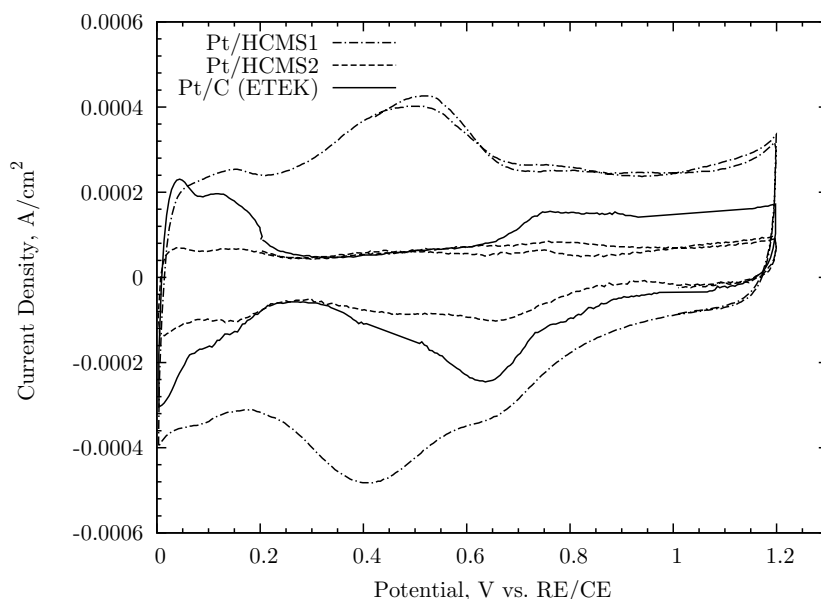


Figure 7.12: Cyclic voltammograms for the catalysts prepared with the synthesized carbon supports and commercial catalyst (Pt/C ETEK[®]) in 0.1M HClO₄ in N₂ atmosphere at a scan rate of 50 mVs⁻¹

The CV curves for Pt/HCMS1 and Pt/BP2000 electrocatalysts were investigated. There were distinguished peaks in the anodic and cathodic reduction regions at ≈ 0.52

and 0.45 V which resulted from the oxidation/reduction of the oxygen containing surface groups on HCMS1 and BP2000.

Wang et al. [166] investigated the corrosion of BP2000 and Vulcan XC72 by applying a fixed potential of 1.2 V and they observed surface oxide formation due to the hydroquinone–quinone (HQ–Q) redox couple on the carbon black support. They found that the increased amount of HQ–Q redox couple (the current peaks resulted from the surface oxide formation due to this redox reaction) on BP2000 was about 1.5 times that on Vulcan XC72 if referred to the electrochemical active area. Also, the higher surface areas of the BP2000 and HCMS1 carbon supports may increase the tendency of carbon support oxidation.

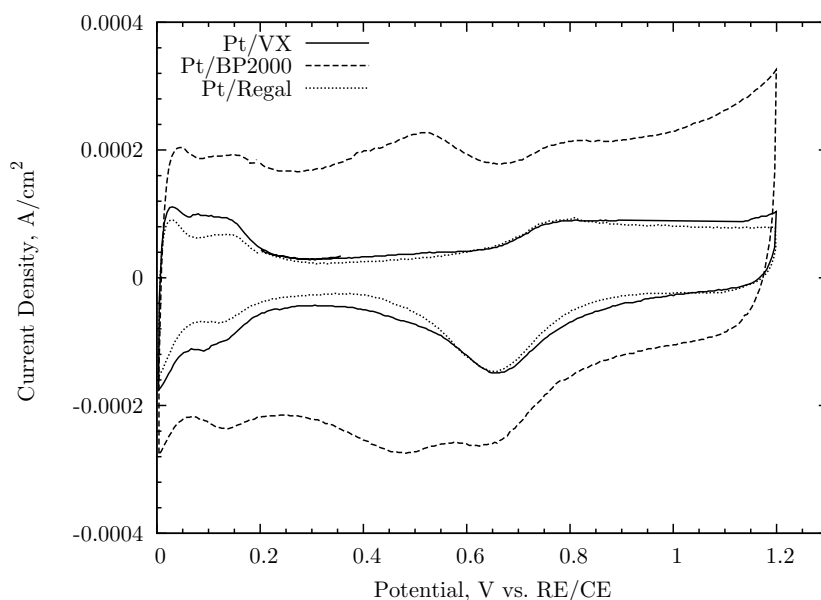


Figure 7.13: Cyclic voltammograms for the catalysts prepared with the carbon black supports in 0.1M HClO₄ in N₂ atmosphere at a scan rate of 50 mVs⁻¹

The calculated electrochemical and total surface area of the prepared and commercial catalysts from the XRD and CV data are given in Table 7.3. Electrochemical surface areas were calculated by taking into account both hydrogen adsorption and desorption regions. The maximum electrochemical surface area and Pt utilization were obtained for the commercial catalyst, which has the smallest particle size.

From Figure 7.12 and 7.13, it was observed that the double layer capacitance of the catalysts increased with the increasing carbon support surface area. Cyclic voltam-

metry results showed that even if the particle size of the Pt/HCMS2 catalyst is the highest among the other prepared catalysts, the Pt utilization was similar to the other electrocatalysts, such as Pt/Regal and Pt/VX. Considering the mesoporous structure of the carbon support, improvement in the metal and electrolyte contact probably enhanced the Pt utilization.

Table 7.3: Electrochemical and total surface area of the synthesized electrocatalysts

Catalyst	Microwave time (s)	Pt ^a (%)	d ^b (nm)	SA _{Pt} (m ² g ⁻¹)	ESA _{Pt} (m ² g ⁻¹)	Pt utilization ^c (%)
Pt/HCMS1	120	18.7	3.6	78	5	6
Pt/HCMS2	120	18.7	4.0	70	14	20
Pt/BP2000	50	17.5	3.7	77	6	8
Pt/Regal	50	18.3	3.4	82	16	20
Pt/VX	50	17.1	3.3	85	20	23
Pt/C (E TEK [®])	50	19.6	2.7	104	41	39

^a Thermogravimetric analysis data

^b X-ray Diffraction data

^c Cyclic voltammetry analysis, Pt utilization (%) = $ESA_{Pt} / SA_{Pt} \times 100$

In comparison to Pt/HCMS2 electrocatalyst, Pt/HCMS1 electrocatalyst exhibited a higher surface area and lower average pore diameter. Consequently, the Pt utilization of Pt/HCMS1 was about one third of the Pt/HCMS2. Figure 7.13 shows the CV curve for the catalysts prepared with different commercial carbon supports. Similarly, it was seen that the double layer capacitance increased with the increase in the carbon support surface area.

The lowest Pt utilization was observed for Pt/BP2000 catalyst. It can be concluded that one possible reason for low Pt utilization of Pt/BP2000 electrocatalyst might be due to the fact that approximately one third of the BP2000 carbon support structure includes micropores. There was a carbon support oxidation tendency for both Pt/HCMS1 and Pt/BP2000 catalysts which may also resulted in a decrease in the electrochemical activity and low Pt utilization.

7.5 PEMFC Performance Tests for Pt/C Electrocatalysts

For the achievement of improved PEM fuel cell performance, microwave synthesis conditions were optimized. For this purpose, microwave duration in the synthesis conditions was changed in a range of 50–150 s for HCMS1 carbon based catalysts.

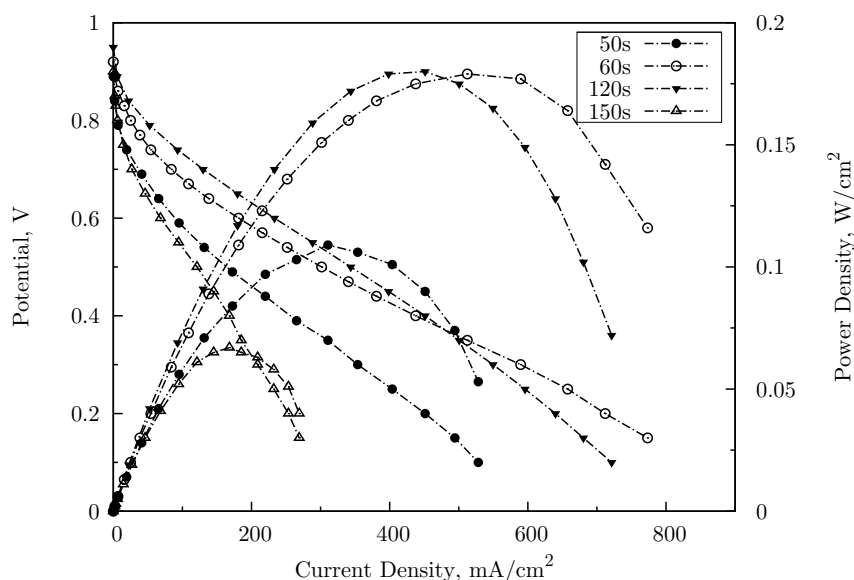


Figure 7.14: PEMFC polarization curves for Pt/HCMS1 cathode catalysts synthesized with different microwave durations (anode catalyst is 20% Pt/C, ETEK[®])

Figure 7.14 shows the effect of microwave duration on PEM fuel cell performance for Pt/HCMS1 catalysts. As the microwave duration was increased from 50 to 150 s, fuel cell performance was improved up to 120 s; however, further increase in the microwave duration decreased the fuel cell performance. It should be emphasized that the best fuel cell performance was obtained with microwave duration of 120 s.

For the optimized (microwave duration is 120 s) synthesis conditions, single cell tests showed that 233 mA/cm² current density and 0.14 W/cm² power density can be drawn for the fixed potential of 0.6 V for Pt/HCMS1 electrocatalyst. Moreover, it is also clearly seen from the figure that the current density and power density values were approximately doubled as the microwave synthesis duration was increased from 50 to 120 s.

Similar results were obtained for Vulcan XC72 carbon support based Pt/C catalysts

[87]. As the microwave duration was increased from 50 to 60 s catalyst particle growth was observed and the particle diameter increased from 3.3 nm to 4.6 nm. It was also reported that in comparison to a microwave synthesis duration of 120 s, fuel cell performance of Pt/VX catalysts was improved for the microwave duration of 60 s at relatively higher current densities ($>400 \text{ mA/cm}^2$). This may indicate a better control of mass transfer issues (e.g. water management) by optimizing the synthesis conditions.

Current and power densities of the HCMS carbon based and the carbon black based 20% Pt/C electrocatalysts at 0.6 V and 0.4 V are presented in Table 7.4. It should be noted that with the slight modification of the pore structure of the HCMS2 carbon, Pt utilization of the electrocatalyst was increased sharply compared to the HCMS1 carbon based catalysts (Table 7.3). Promising single cell fuel cell performance results were measured with respect to the commercial Pt/C (20%, ETEK[®]) electrocatalyst. Catalysts synthesized with HCMS2 carbon exhibit significant PEMFC performance and have a potential to be a promising cathode electrode.

Table 7.4: PEMFC performance of the platinum based electrocatalysts for various carbon supports

Electrocatalyst	@ 0.6 V		@ 0.4 V	
	i (mA/cm ²)	P (W/cm ²)	i (mA/cm ²)	P (W/cm ²)
Pt/HCMS1	233	0.14	451	0.18
Pt/HCMS2	329	0.20	560	0.22
Pt/BP2000	100	0.06	310	0.12
Pt/Regal	200	0.12	606	0.24
Pt/VX	474	0.28	836	0.33
Pt/C (ETEK [®] , [87])	524	0.31	808	0.32

With the use of two different carbon precursors, carbon supports exhibiting different pore textures were obtained (HCMS1 and HCMS2). For HCMS carbon based catalysts, effect of structural changes on the fuel cell performance is shown in Figure 7.15. Slight enhancement of average pore diameter of carbon supports from 3.0 nm to 3.9 nm showed a significant increase on the fuel cell performance of Pt/HCMS electrocatalysts.

Single cell performance tests showed that Pt/HCMS1 electrocatalyst exhibited 233 mA/cm² current density and 0.14 W/cm² power density at 0.6 V, whereas Pt/HCMS2

electrocatalyst exhibited a current density of 329 mA/cm² and a power density of 0.2 W/cm² at 0.6 V (Table 7.4).

These results indicate that tailoring the pore texture (e.g. mesopores) and form (well developed ordered microspheres) of the carbon support enhances the fuel cell performance. This enhancement shows the fact that simple modifications in the structure of the supporting material may improve the activity of the catalyst and this may allow a better control of incorporation of the platinum metals over the surface of the catalyst support. Figure 7.15 also illustrates the effect of the commercial carbon black supports on the PEMFC performance. Single cell test showed that the best performance was obtained with Pt/VX electrocatalyst.

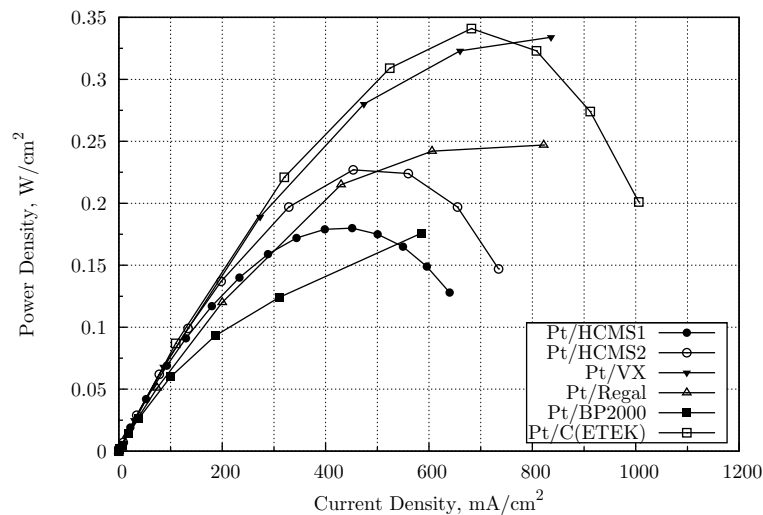
During the course of operation, using Pt/VX cathode catalyst exhibited a current density of 474 mA/cm² and a power density of 0.28 W/cm² at 0.6 V fixed potential. BP2000 carbon supported Pt electrocatalyst showed relatively poor fuel cell performance (100 mA/cm² and 0.06 W/cm² at 0.6 V), which may be due to the high micro porosity of the nanomaterial. Inefficient loading of the platinum metals into the structure and possible clogging of the pores with Nafion[®] solution may lower the fuel cell performance for Pt/BP2000 electrocatalyst.

Structural properties of the carbon supports and the functional groups formed on the support surface play an important role on the electrochemical activity of the catalysts. In order to provide a better contact between the electrolyte and the Pt metal, uniform dispersion of the platinum metal on the carbon support (particle size effect) and also the accessibility of the metal on the supporting material are very crucial in proton exchange membrane fuel cells.

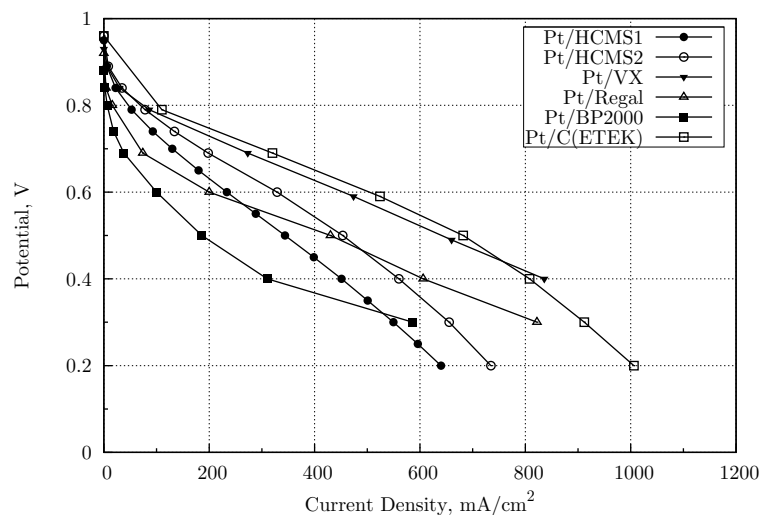
7.6 Ex situ Characterization of the Pt-Pd/HCMS Electro catalysts

BET surface areas for the prepared Pt-Pd/HCMS2 catalysts are given in Table 7.5. BET surface area for the HCMS2 carbon supported Pt-Pd electro catalysts were almost on the same order of magnitude. Insufficient Pd nanometal incorporation into the mesopores resulted in the highest BET surface area for Pd/HCMS2 electro catalyst.

Figure 7.16 shows SEM and TEM images of Pt/HCMS2 electro catalyst. It is clearly



(a)



(b)

Figure 7.15: PEMFC performance test for Pt/C cathode electrocatalysts (anode catalyst is 20% Pt/C, ETEK[®])

Table 7.5: Structural properties of the Pt-Pd/HCMS2 electrocatalysts

Catalyst	Pt (%)	Pd (%)	Microwave time (s)	BET area (m ² g ⁻¹)	Pore volume (cm ³ g ⁻¹)	Avg. particle size (nm)
Pt/HCMS2	20	0	120	277	0.33	4
PtPd/HCMS2	15	5	120	325	0.41	5
PtPd/HCMS2	10	10	120	262	0.34	8
PtPd/HCMS2	5	15	120	319	0.39	6
Pd/HCMS2	0	20	120	335	0.41	16

seen from the TEM image that Pt nanoparticles were uniformly distributed over carbon support. However, some of the spheres were corrupted and particle growth for some specific regions was observed. It was aimed to distribute Pt and Pd nanoparticles into the mesoporous structure of the bimodal carbon structure. Some of the relatively larger Pt particles was over the surface of the carbon spheres. This was also revealed by surface composition analysis.

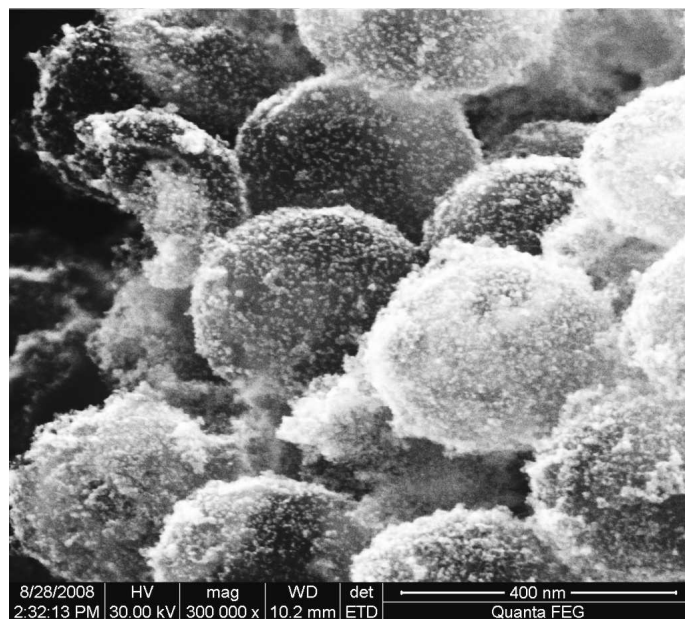
Figure 7.17 shows TEM images of HCMS2 based electrocatalysts for different Pt/Pd weight percentages. It is clearly seen from the TEM micrographs that as the Pd content was increased particle size growth was observed and more of the Pd particles are over the surface of the catalyst but not in the mesopores. The placement of the Pd metal into the mesopores with 1-3 nm in size is critical to enhance electrode kinetics.

TEM micrographs indicate that platinum dispersion over the electrocatalyst is uniform but still particle size reduction is required. It is concluded that agglomeration and particle growth can be controlled and hindered by modifying surface functional groups over carbon spheres and altering microwave synthesis conditions.

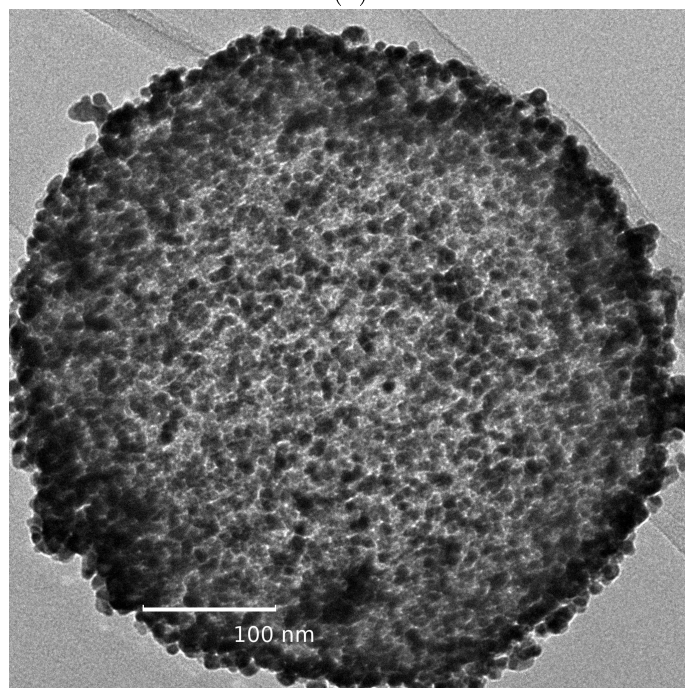
Figure 7.18 shows the XRD patterns of the SCMS silica template and HCMS2 carbon and Figure 7.19 shows the typical XRD patterns of Pt-Pd/HCMS2 for different Pt/Pd percent weight ratios on carbon support. The XRD pattern for the SCMS silica particles as shown in Figure 7.18, indicated a strong primary (100) diffraction peak centered at $2\theta = 2.10^\circ$. A slight shift to lower angles was detected related to the alkyl chain length of the surfactant [169]. The XRD pattern of the HCMS2 carbon spheres revealed a strong (002) diffraction peak centered at $2\theta = 18^\circ$, demonstrating the amorphous character of the carbon [164].

From Figure 7.19, it is observed that all the XRD patterns of the Pt-Pd/HCMS2 catalysts exhibit the main characteristic peaks of fcc crystalline Pt and Pd with the planes of (111), (200), (220), and (311). The particle sizes of the catalysts were calculated by using Scherrer equation for the half-full-width at half maximum of the (220) inflection and given in Table 7.5. As can be seen from the table, for the Pt/HCMS2 catalyst the particle size was calculated as 4 nm.

With the addition of the second metal of Pd, the particle size of the bimetallic elec-



(a)



(b)

Figure 7.16: SEM (a) and TEM (b) micrograph of 20% Pt/HCMS2 electrocatalyst

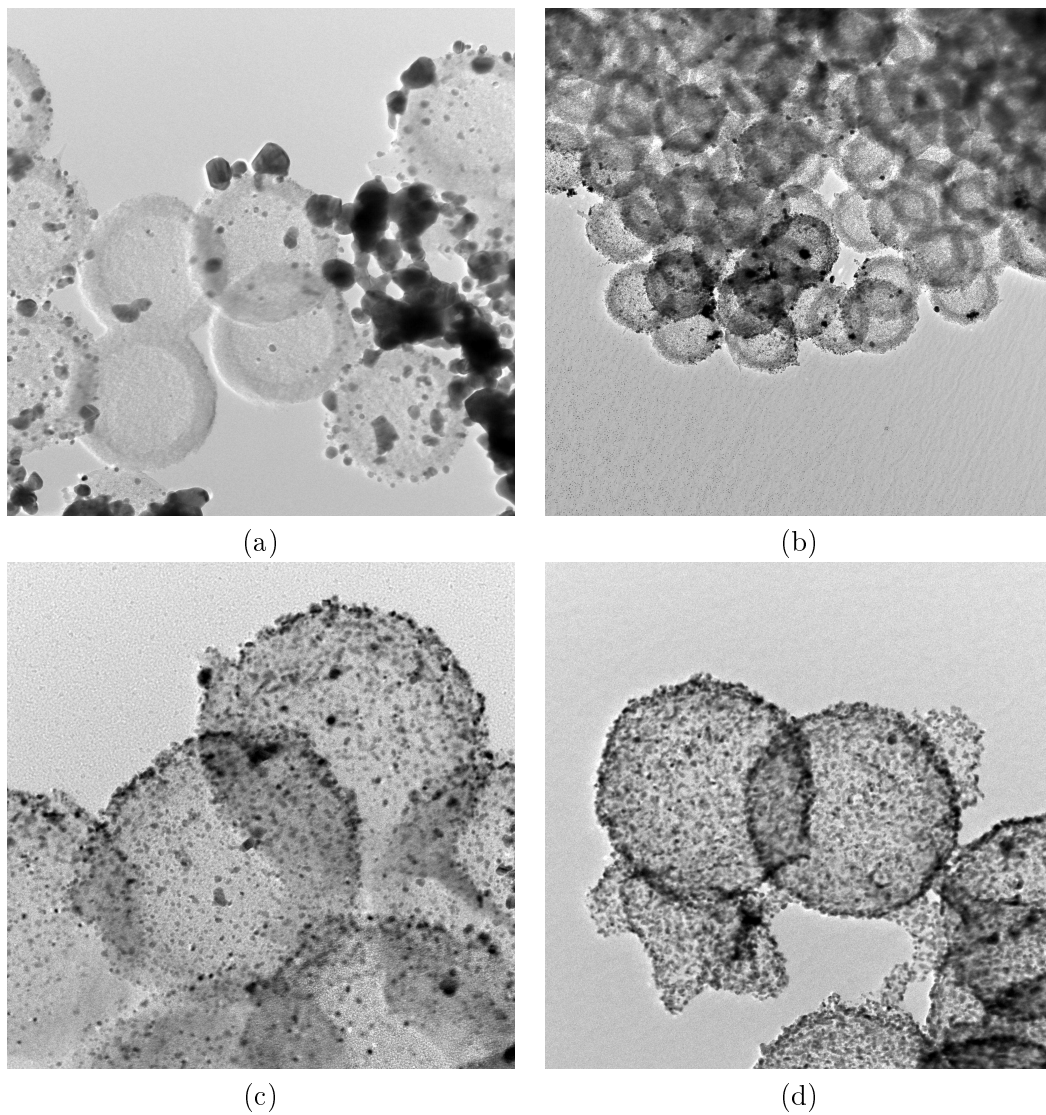


Figure 7.17: TEM micrographs of (a) Pd/HCMS2 (20), (b) PdPt/HCMS2 (15:5), (c) PdPt/HCMS2 (10:10), (d) PdPt/HCMS2 (5:15)

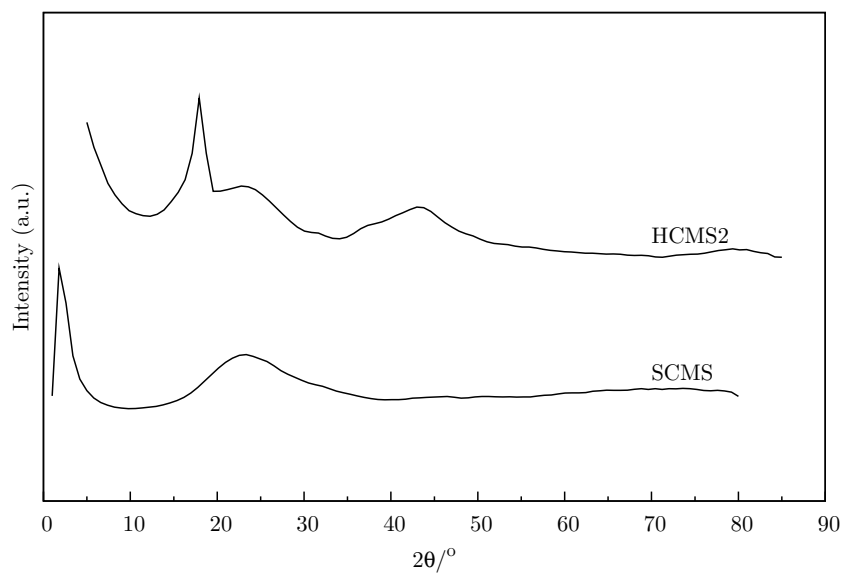


Figure 7.18: The XRD patterns of as-synthesized SCMS silica and HCMS2 carbon

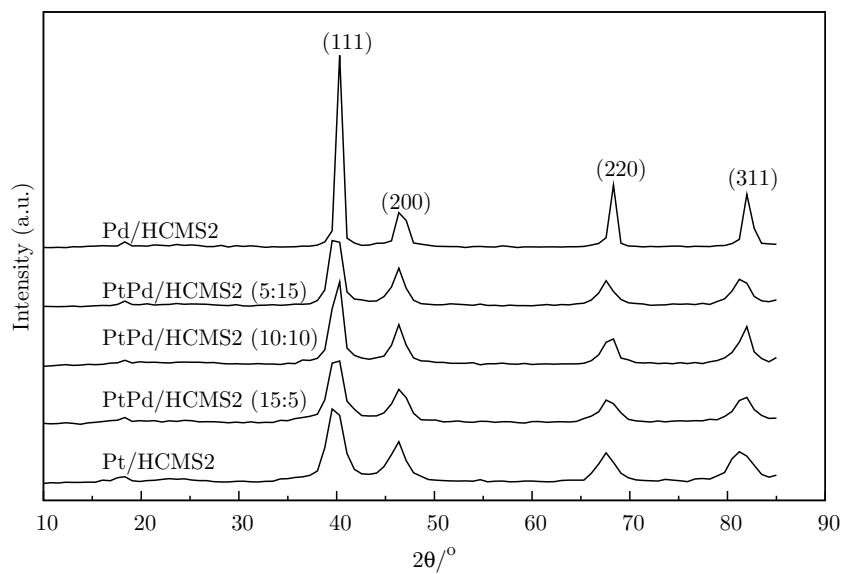


Figure 7.19: The XRD patterns of Pt-Pd/HCMS2 electrocatalysts

trocatalysts increased. The diffraction peaks were slightly shifted to higher 2θ values for the bimetallic and also for Pd/HCMS2 catalysts when compared to Pt/HCMS2 catalyst. Figure 7.20 shows the XPS spectra for Pt 4f core level spectra. The two doublets for high and low energy bands are seen at around 71.3 eV and 74.5 eV which correspond to Pt 4f_{7/2} and Pt 4f_{5/2}, respectively, indicating the existence of Pt metal.

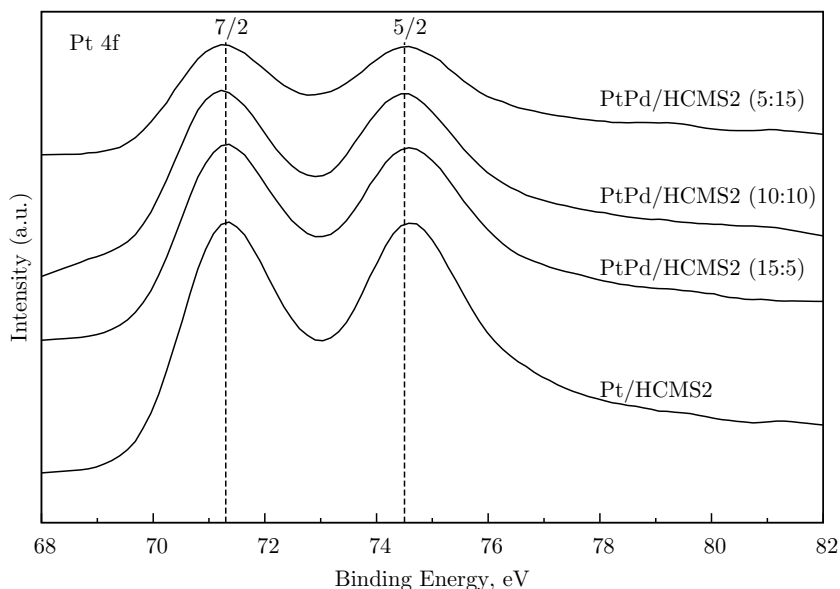


Figure 7.20: Pt 4f XPS spectra for HCMS2 based electrocatalysts

Also the Pd 3d core level spectrum is given in Figure 7.21. The two doublets corresponding to Pd 3d were seen at around 335.3 eV and 340.5 eV which correspond to Pd 3d_{5/2} and Pd 3d_{3/2}, respectively, indicating the existence of Pd metal. The shift of the peaks is shown with dashed lines in the figures which might be resulted from the alloy formation and the electronic interaction between Pt and Pd atomic orbit [167].

The survey spectra for Pt/HCMS2, PtPd/HCMS2 (10:10) and Pd/HCMS2 are given in Figure 7.22. As can be seen from the figure carbon and oxygen peaks exist for all catalysts. C 1s peak was observed at a binding energy of 284.4 eV, whereas O 1s binding energy values were centered at 532.0–532.8 eV. The oxidation states information of the elements composed of Pt-Pd/HCMS2 materials was obtained by XPS studies.

Amount of oxygenated groups on the carbon support affects the platinum and palladium surface areas. Interaction of platinum with the carbon support shifts the peak

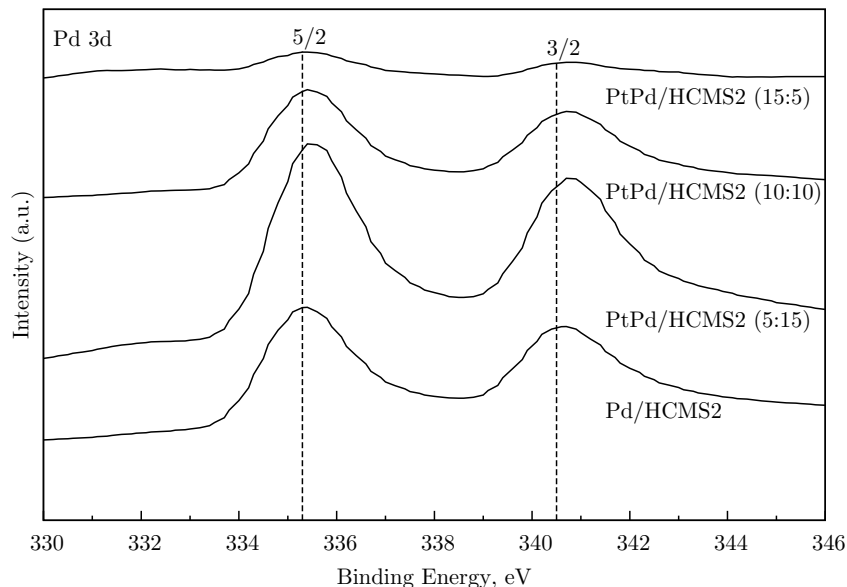


Figure 7.21: Pd 3d XPS spectra for HCMS2 based electrocatalysts

maxima from the expected 70.9 eV value to the higher values of 71.3 eV and 71.2 eV for the catalysts Pt/HCMS2 and Pt-Pd/HCMS2 (10:10), respectively. Shift of Pt 4f_{7/2} core level spectra can be considered as a measurement of oxidized platinum [165].

Palladium surface oxidation is characterized by Pd 3d_{5/2} peaks at 334.9 eV, 335.5 eV, and 336.3 eV, which corresponds to the bulk Pd atoms and Pd atoms with two and four O neighbors, respectively. XPS survey spectra given in Figure 7.22, indicates Pd 3d_{5/2} peaks centered at 335.2 eV. This slight shift might signify the oxidation of Pd atoms with two O neighbors [170].

Surface elemental composition was obtained by XPS analysis. Despite the presence of contaminants in the electrocatalysts, the XPS spectra were all dominated by palladium, platinum, and carbon signals. During the synthesis, extraneous anions like F⁻ and Cl⁻ were detected due to the use of HF in the etching process and metal precursors (H₂PtCl₆, PdCl₂) to incorporate palladium and platinum, respectively. Even though the presence of extraneous anions in small amounts in the electrocatalysts, no detrimental effect on fuel cell performance was observed.

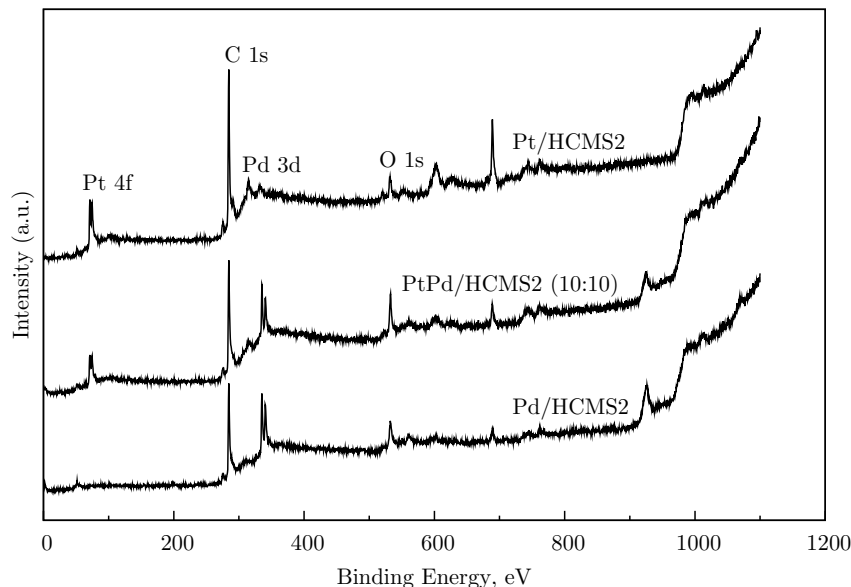


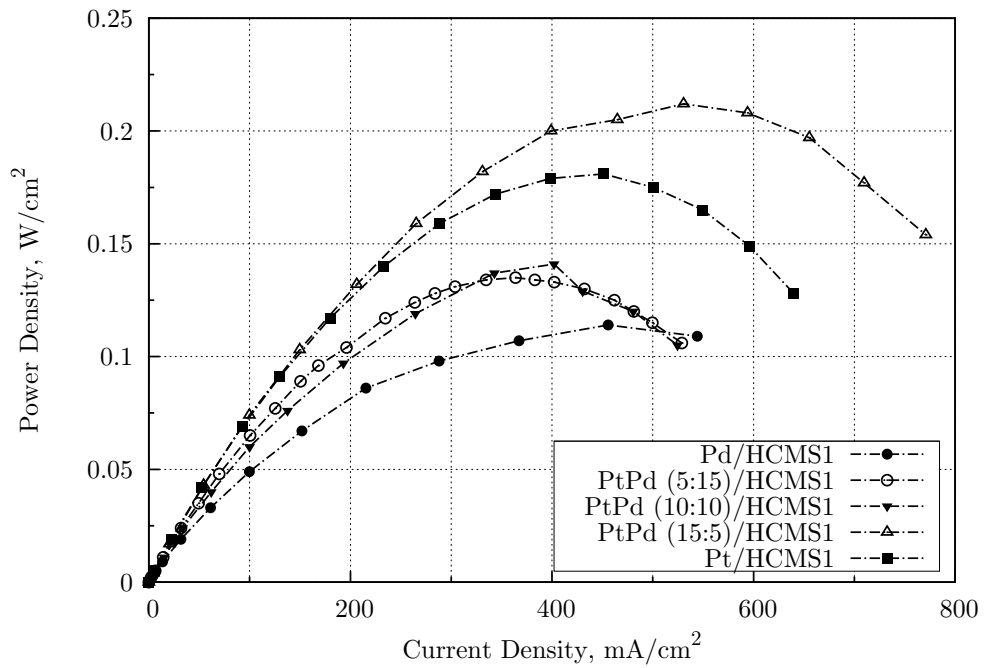
Figure 7.22: XPS survey spectra for Pt/HCMS2, PtPd/HCMS2 (10:10) and Pd/HCMS2 electrocatalysts

7.7 PEMFC Performance Tests for Pt-Pd/HCMS Electro-catalysts

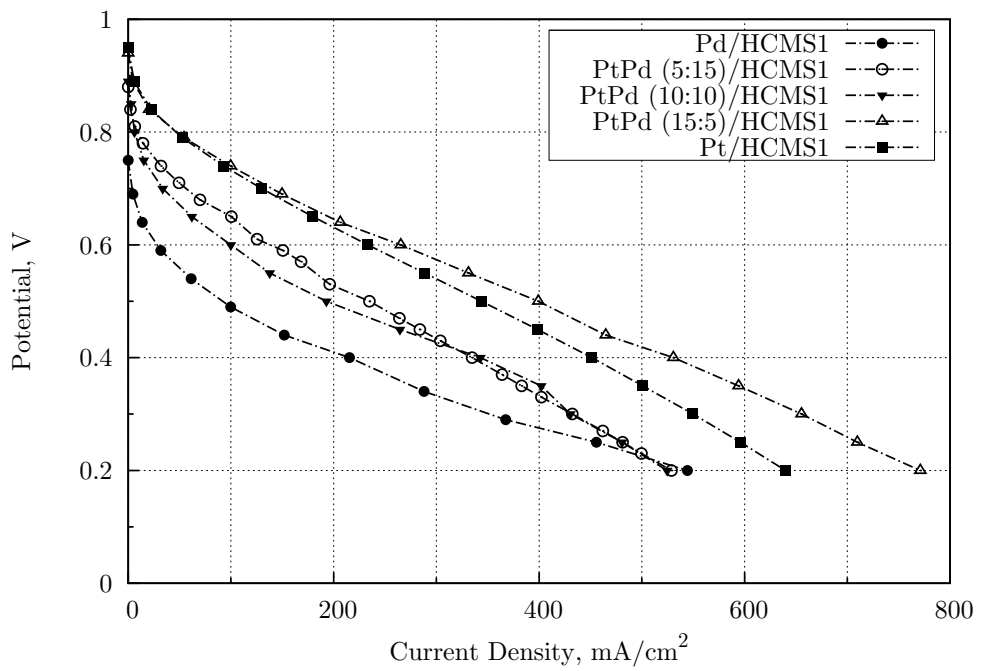
Fig. 7.23 shows the PEMFC polarization curve of the HCMS1 based catalysts. The curve shows that only the addition of 5% Pd into Pt/HCMS1 catalyst increased the performance of the PEMFC. The best fuel cell performance was observed for Pd-Pt/HCMS1 containing 5% Pd and 15% Pt. Additional increase of palladium content lowered the fuel cell performance when HCMS1 was used as catalyst support. At high current densities ($>300 \text{ mA/cm}^2$) the difference between the fuel cell performances of Pt-Pd/HCMS1 (5:15) and PtPd/HCMS1 (10:10) catalysts decreased and similar results were obtained. The current and power densities of the catalysts at 0.6V and 0.4V potentials are given in Table 7.6.

These results are also compared with the performance of commercial Pt/C (20%, ETEK[®]) catalyst [20]. It should be emphasized that 5% Pd metal containing electro-catalyst has a potential to be used as cathode catalyst in further studies.

Figure 7.24 exhibits the PEMFC performance curves of the HCMS2 based catalysts when the catalyst is used as the cathode electrode. In case of HCMS2, the best fuel cell performance was obtained with 20% Pt over HCMS2 catalyst. When compared with



(a)



(b)

Figure 7.23: PEMFC performance test for Pt-Pd/HCMS1 cathode electrocatalysts (anode catalyst is 20% Pt/C, ETEK[®])

Table 7.6: PEMFC performance of the synthesized cathode electrocatalysts at 0.6 V and 0.4 V

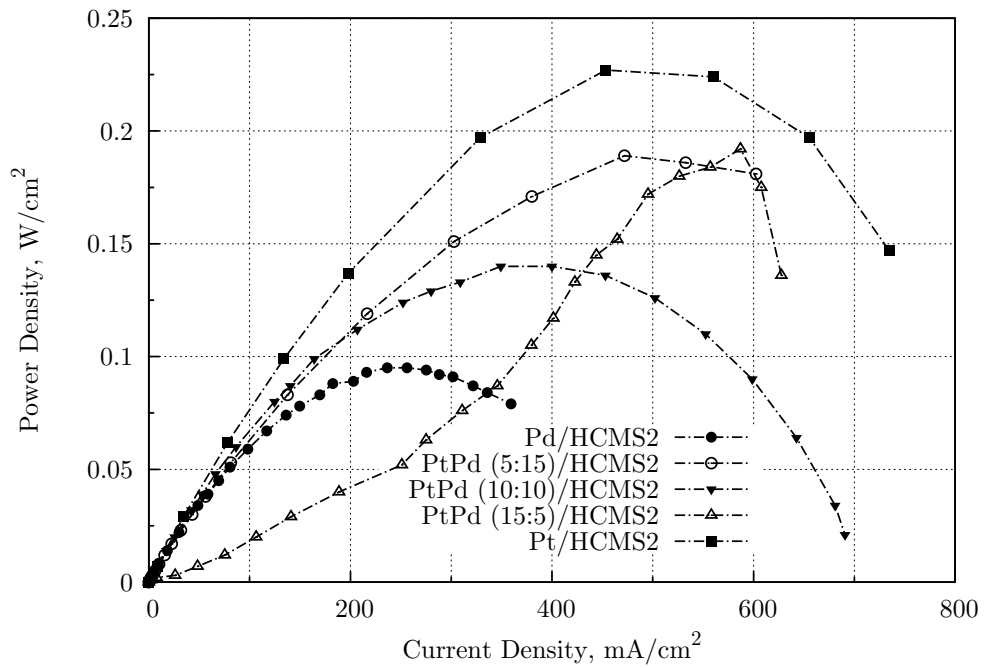
Electrocatalyst	@ 0.6 V		@ 0.4 V	
	<i>i</i> (mA/cm ²)	<i>P</i> (W/cm ²)	<i>i</i> (mA/cm ²)	<i>P</i> (W/cm ²)
Pt/HCMS1	233	0.14	451	0.18
PtPd/HCMS1 (15:5)	265	0.16	531	0.21
PtPd/HCMS1 (10:10)	100	0.06	343	0.14
PtPd/HCMS1 (5:15)	143	0.08	335	0.13
Pd/HCMS1	28	0.02	215	0.09
Pt/HCMS2	329	0.20	560	0.22
PtPd/HCMS2 (15:5)	250	0.15	480	0.19
PtPd/HCMS2 (10:10)	164	0.10	349	0.14
PtPd/HCMS2 (5:15)	138	0.08	472	0.19
Pd/HCMS2	98	0.06	237	0.10

20% Pt/HCMS2 catalyst, it was seen that the fuel cell performance for 5% palladium containing catalyst exhibited very close behavior to the Pt/HCMS2 electrocatalyst. Relatively lower fuel cell performances were obtained as the palladium amount was increased in the catalyst. It should be noted that Pd particle size increases with increasing Pd content. This result may indicate that Pd particle size is a critical parameter affecting the fuel cell performance.

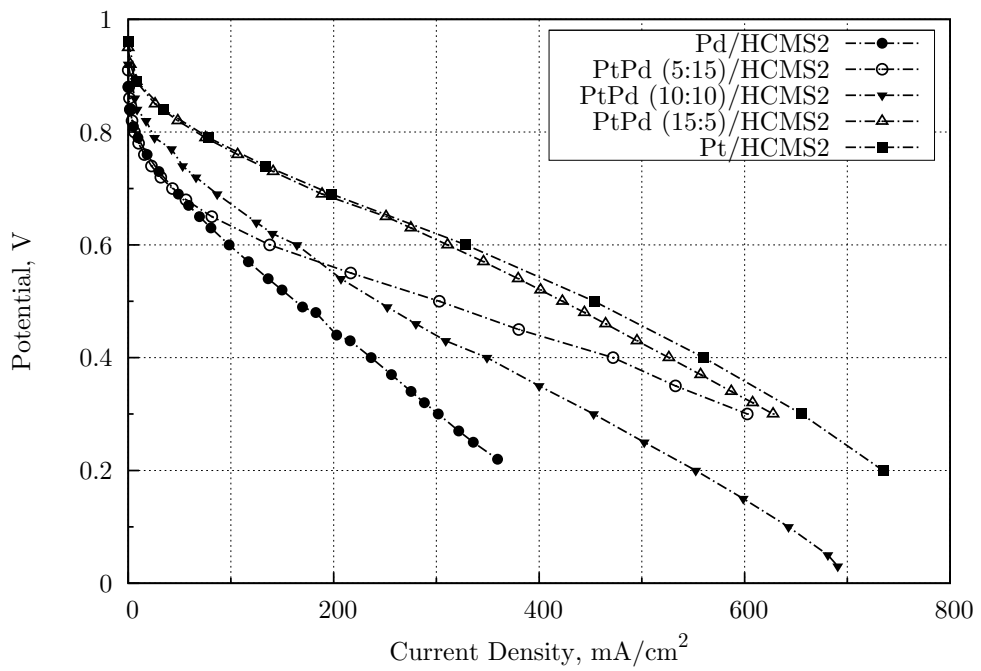
Figure 7.25 shows overall PEM fuel cell performance of the HCMS2 carbon based anode electrocatalysts. Utilization of Pd as an anode catalyst enhanced the hydrogen oxidation reaction. As the palladium content of the electrocatalyst was increased from 5% to 15%, fuel cell performance was decreased slightly.

The comparison of the current and power densities of the HCMS2 based catalysts for anode and cathode electrode at 0.6V is given in Table 7.7. From the tabulated data, it is clear that when the Pd doped Pt catalysts are used as anode electrode the current density is approximately doubled. Pt-Pd/HCMS2 alloy catalysts exhibited good anode electrocatalysis compared to the cathode electrocatalysis.

HCMS2 based electrocatalysts performed better than the HCMS1 based electrocatalysts. At relatively high current densities, transport of the reactants and the products was facilitated by increasing the average pore diameter of the hollow core mesoporous shell carbon from 3.02nm to 3.90 nm. A further increase of average pore diameter by



(a)



(b)

Figure 7.24: PEMFC performance test for Pt-Pd/HCMS2 cathode electrocatalysts (anode catalyst is 20% Pt/C, ETEK[®])

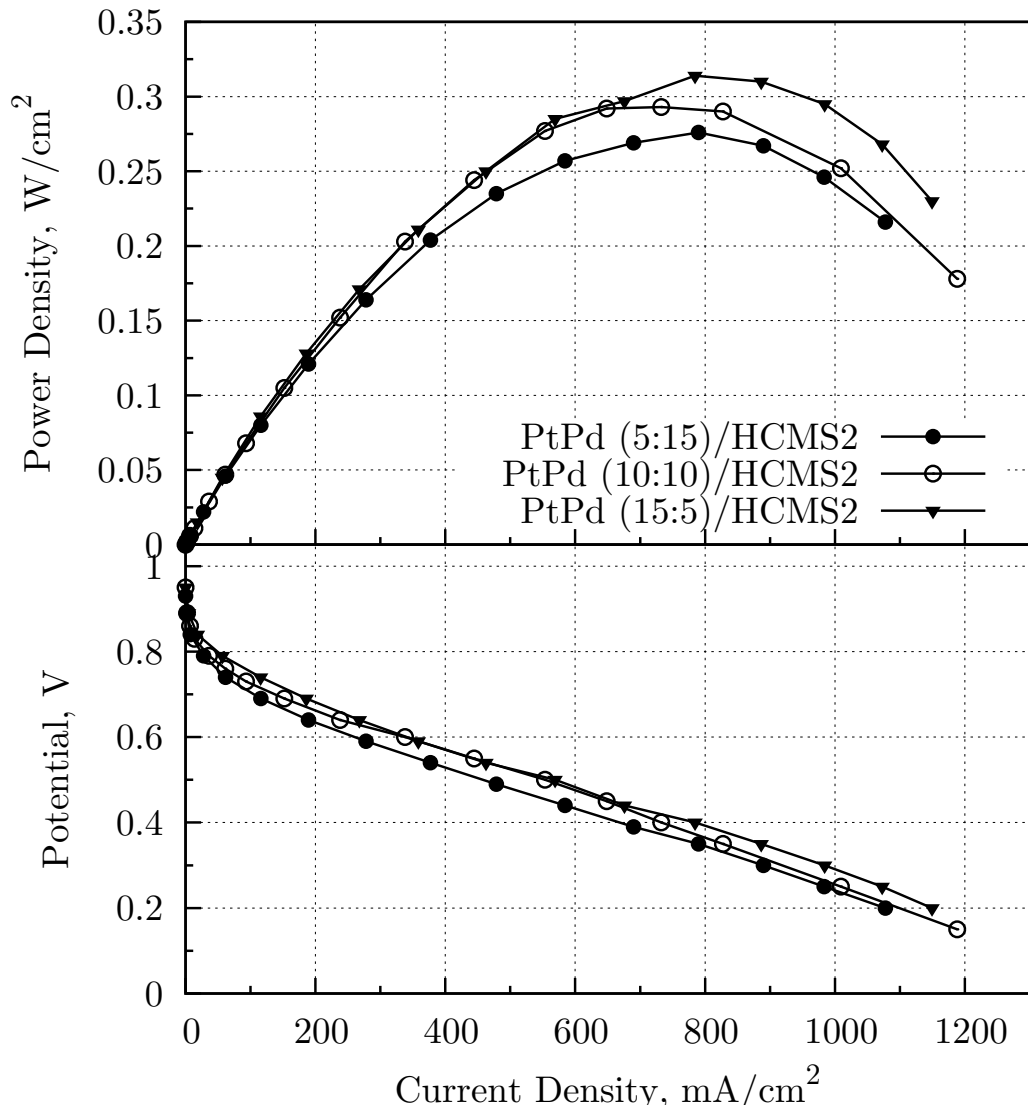


Figure 7.25: PEMFC polarization curve of the HCMS2 based anode catalysts (cathode catalyst is 20% Pt/C, ETEK[®])

Table 7.7: Fuel cell performance comparison of the anode and cathode HCMS2 carbon supported electrocatalysts at 0.6 V

Electrocatalyst	@ 0.6 V (Cathode)		@ 0.6 V (Anode)	
	i (mA/cm ²)	P (W/cm ²)	i (mA/cm ²)	P (W/cm ²)
PtPd/HCMS2 (15:5)	250	0.15	340	0.20
PtPd/HCMS2 (10:10)	164	0.10	338	0.20
PtPd/HCMS2 (5:15)	138	0.08	260	0.15

changing the carbon precursor or silica template structure will probably increase the fuel cell performance.

7.8 Characterization of Fuel Cell Components

Focusing to the MEA part of the fuel cell, the effort is given to the understanding of solid polymer electrolyte, diffusion media, and catalyst layers. Table 7.8 and 7.9 tabulate typical properties for some particular diffusion media available in the market. Among these alternatives, SGL Sigracet[®] GDL 30BC was used for all experiments throughout the PhD study.

Table 7.8: Structural properties of SGL carbon papers

Material ^{a,b}	Thickness (μm)	Areal Weight (g/m^2)	Porosity	MPL ^c	Electrical Resistance ($\text{m}\Omega \text{ cm}^2$)
GDL 10 BA	400	85	0.88	No	< 12
GDL 10 BC	420	135	0.84	Yes	< 16
GDL 25 BA	190	40	0.88	No	< 10
GDL 25 BC	235	86	0.80	Yes	< 12
GDL 30 BA	310	95	0.81	No	< 10
GDL 30 BC	330	140	0.77	Yes	< 15
GDL 35 BC	325	110	0.80	Yes	< 15

^a Properties are adapted from SGL Sigracet[®] specification sheet

^b AA=plain, BA=5/0 wt % substrate/MPL, BC=5/23 wt % substrate/MPL

^c Standard microporous layer on one side

SGL[®] 30BC diffusion media exhibits a total thickness of 330 microns. This type of diffusion media includes both a 310 microns macroporous layer with 5 wt% PTFE and a 20 microns standard microporous layer with 23% PTFE. This material has a bulk porosity of around 0.77. On the other hand, SGL[®] 35BC has very similar structural properties as compared to SGL[®] 30BC. The only difference is due to the thickness of microporous layer, which is about 15 microns for SGL 35 BC. Thickness of microporous layer may be very significant at high current density region, where more water is produced and water removal strategies become very important.

Table 7.9 presents the structural properties of Toray[®] diffusion media. Toray[®] carbon papers are another type of diffusion media widely used in research studies as well as

in the fuel cell market. Thickness of the materials are changing from 110 microns to 370 microns. These carbon papers may be hydrophobized with PTFE upon request. Similar to SGL diffusion media, Toray carbon papers exhibit bulk porosity of ca. 0.80.

Table 7.9: Structural properties of Toray carbon papers

Properties ^a	TGPH030	TGPH060	TGPH090	TGPH120
Thickness, μm	110	190	280	370
Bulk Density, g/cm^3	0.40	0.44	0.44	0.45
Porosity	0.80	0.78	0.78	0.78
Electrical Resistivity				
through plane, $\text{m}\Omega\text{ cm}$	80	80	80	80
in plane, $\text{m}\Omega\text{ cm}$	-	5.8	5.6	4.7
Thermal Conductivity				
through plane (25 °C), $\text{W}/\text{cm K}$	-	0.017	0.017	0.017
in plane (25 °C), $\text{W}/\text{cm K}$	-	0.21	0.21	0.21
in plane (100 °C), $\text{W}/\text{cm K}$	-	0.23	0.23	0.23

^a Properties are adapted from Toray[®] specification sheet

Transport properties of the porous diffusion media are critical to have control over water and thermal management issues. SGL[®] 31 BA, SGL[®] 30BC, and a typical SGL[®] carbon cloth porous diffusion media were characterized by mercury intrusion porosimetry. Figure 7.26 shows the pore size distribution of various diffusion media components for proton exchange membrane fuel cells.

Since SGL[®] 31BA only includes a macroporous layer, it exhibits a pore size distribution with substantially macro pores. This type of material is well suited for anode side to create a back pressure gradient from cathode to anode by excluding the microporous layer. As can be seen from Figure 7.26, carbon cloth material exhibits a uniform macroporous structure with an average pore diameter of $\approx 0.08\ \mu\text{m}$.

Depending on the operating conditions, carbon cloth material could be used at both anode and cathode compartments with proper loading of hydrophobic material (e.g. PTFE) to control water distribution throughout the fuel cell. A bimodal pore structure was observed for SGL[®] 30BC diffusion media (Figure 7.26). This pore size distribution is due to the inclusion of both microporous and macroporous layer in the structure of the diffusion media. This type of material is appropriate for cathode diffusion media, where one can increase liquid phase saturation level at the cathode catalyst layer to

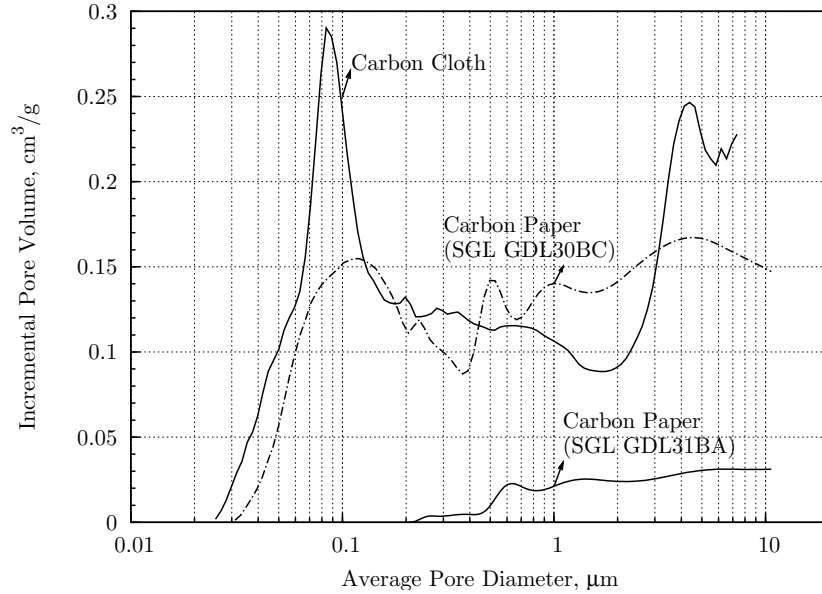


Figure 7.26: Pore size distribution for various diffusion media components for PEM fuel cells

enhance liquid water transport.

Figure 7.27 shows SEM images of the SGL[®] 30 BC diffusion media used in all experimental runs. Figure 7.27a is depicting SEM micrograph of gas diffusion layer with 310 microns thickness, whereas Figure 7.27b exhibits microporous layer of the same diffusion media and it has a thickness of 20 microns. For SGL[®] 30BC material gas diffusion layer side is hydrophobized with 5 wt.% PTFE and the diffusion media includes an additional standard microporous layer with 23 wt.% PTFE on one side.

Figure 7.28 exhibit SEM image of cross section view of membrane electrode assembly. Cross section was obtained through cracking with liquid nitrogen treatment. The SEM image of the MEA was taken after the operation in a single cell test system (approximately after 24 h of operation). Some variations in the thickness of the MEA is observed. Probably, this anisotropic structure results from the MEA preparation (hot press stage) and compressional forces over the MEA when assembled into the single cell test system.

It is also interesting to note that cathode compartment of the membrane electrode assembly is more distorted as compared to the anode compartment. This might occur

due to the electro-osmotic drag and water production and removal from the cathode side of the electrode.

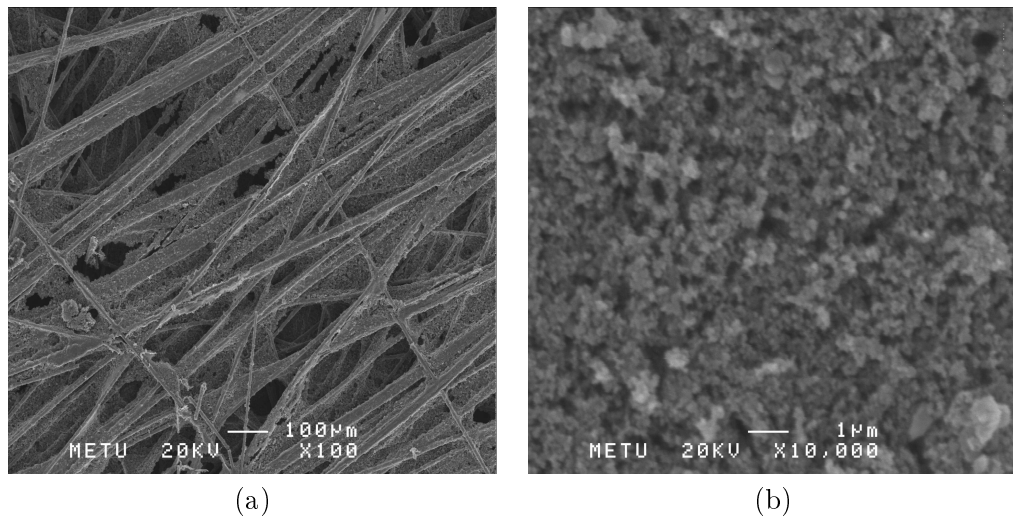


Figure 7.27: SEM micrograph of SGL 30BC (a) Gas diffusion layer (b) Microporous Layer

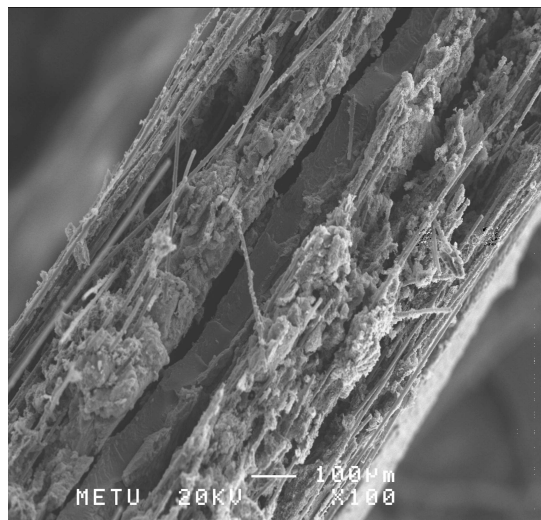


Figure 7.28: SEM micrograph of a used membrane electrode assembly (Diffusion Media: SGL 30BC, Membrane: Nafion 112, Anode Catalyst Layer: 20% Pt/C, ETEK[®], and Cathode Catalyst Layer: 20% Pt/HCMS2)

CHAPTER 8

PEM FUEL CELL MODEL PREDICTIONS

Numerical simulation for the proposed mathematical model are given for various runs at different operating conditions and transport parameters. Both isothermal and non-isothermal fuel cell performances are compared at steady state for different cases. Focus is given to the detailed electrode kinetics and two-phase energy balance approach. Effect of these modeling approach on water and thermal management are discussed.

8.1 0-D Model Predictions of PEM Fuel Cells

In order to estimate fundamental electrochemical parameters, a minimization algorithm was used to fit the experimental data to a 0-D model. Equation (3.6) was used as the 0-D model and efficient Levenberg-Marquardt algorithm is used for the nonlinear regression of the experimental data. Each variable is minimized according to the given model. Table 8.1 shows the zero dimensional model prediction results for Pt/C based electrocatalysts.

Table 8.1: 0-D Model nonlinear fit parameters for Pt/C electrocatalysts

Electrocatalyst	α	$i_o \times 10^8$ (A/cm ²)	R_{ohm} (Ω cm ²)	i_L (A/cm ²)	χ_r
Pt/HCMS1	1.06	1.99	0.67	0.70	0.00013
Pt/HCMS2	1.03	51.61	0.70	0.82	0.00023
Pt/BP2000	1.11	1.09	0.90	0.66	0.02323
Pt/Regal	1.05	1.14	0.38	0.93	0.00466
Pt/VX	1.30	0.41	0.35	1.50	0.00239
Pt/C (ETEK [®])	1.00	24.10	0.35	1.14	0.00239

With the use of the mathematical model fit parameters tabulated in Table 8.1, one can compare the lumped model predictions with the experimental data. For example, Figure 8.1 shows PEM fuel cell polarization curves for the zero dimensional model (see equation (3.6)) and experimental data for 20 % Pt/HCMS2 cathode electrocatalyst. Anode electrocatalyst was commercial 20 % Pt/C (E TEK[®]) electrocatalyst. Experiments for the novel carbon supported electrocatalysts were performed at 70 °C and atmospheric pressures.

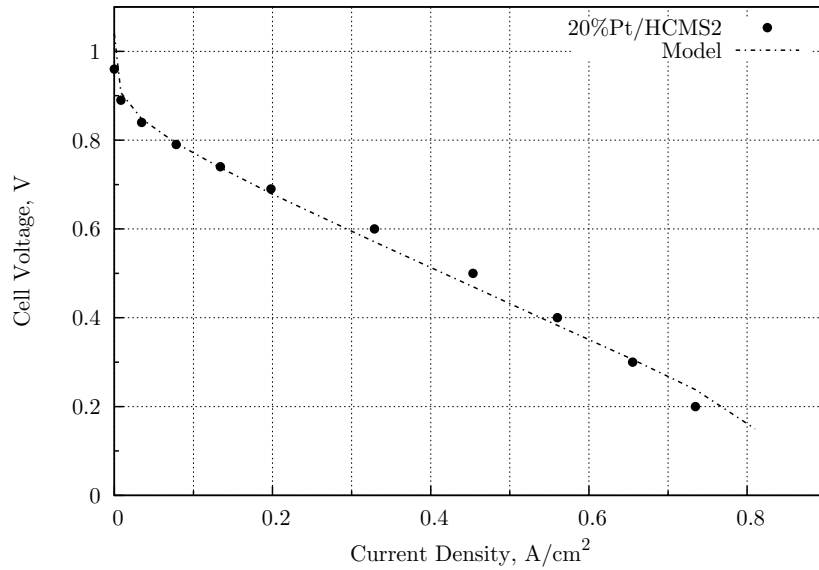


Figure 8.1: Zero dimensional model validation for PEMFC with 20% Pt/HCMS2 cathode electrocatalyst ($T=70$ °C, $P_a=1$ atm, $P_c=1$ atm, Anode RH= 100 %, Cathode RH= 100 %)

It is clearly seen from Figure 8.1 that lumped model prediction is in good agreement with the steady state polarization curve of Pt/HCMS2 cathode electrocatalyst based PEM fuel cell results. One may use the lumped modeling approach to get an idea about the overall system parameters. For instance, lumped model results estimate a total cell resistance, R_{ohm} , of $0.70 \Omega \text{ cm}^2$ for 20% Pt/HCMS2 electrocatalyst based PEM fuel cell, which is mostly due to the ionic resistance developing with the operation of fuel cell. this rough predictions may give an insight for the decision in material selection.

Although zero dimensional models are quick and easy to implement with reasonable agreement, one can not gain understanding for the transport and electrochemical pro-

cesses occurring within the fuel cell. In order to improve fuel cell performance through system design and optimization, it is necessary to take the advantage of higher dimensional models. Furthermore, in addition to higher dimensional models, transient models are useful dynamic models to capture degradation issues.

8.2 PEM Fuel Cell Performance

As described in chapter 3, the first and foremost characterization tool for PEM fuel cells is the polarization curve. Polarization curve and corresponding power density curve are ways of analyzing the overall PEM fuel cell system performance under a variety of operating conditions and parameters. One can notice most of the performance failure mechanisms by following the behavior of these curves at different current density regions. Further analysis to understand the underlying phenomena can be achieved through the observation of variable profiles within the fuel cell.

To begin with, adjusting the fuel cell operating temperature to 60 °C with the other base case parameters presented in chapter 4, model predictions of polarization and power curves are presented in Figure 8.2 for isothermal and steady state operations. Maximum power observed was around 0.25 W/cm² at 0.5 V for the isothermal operation.

Another important observation from Figure 8.2 is that the flooding of the cell was seen at high current density region. In other words, reactant starvation is detected due to mass transfer limitations. This situation will be clarified when we analyze the effect of cathode humidification on system efficiency in subsections.

Simulating the fuel cell with fully humidified streams at the operating temperature and relatively lower cell temperature exhibited a poor overall fuel cell performance. Generally, choice of operating conditions is critically dependent on the fuel cell application. However, it is customary to use much lower cathode humidification (ca. 10% or none) with elevated cell temperatures of around 70 °C for optimal efficiency.

On the other hand, as a result of electro-osmotic drag phenomena, water molecules are carried away from anode to cathode. Therefore, in many cases, it is necessary to humidify anode stream to avoid severe dehydration at anode/membrane interface.

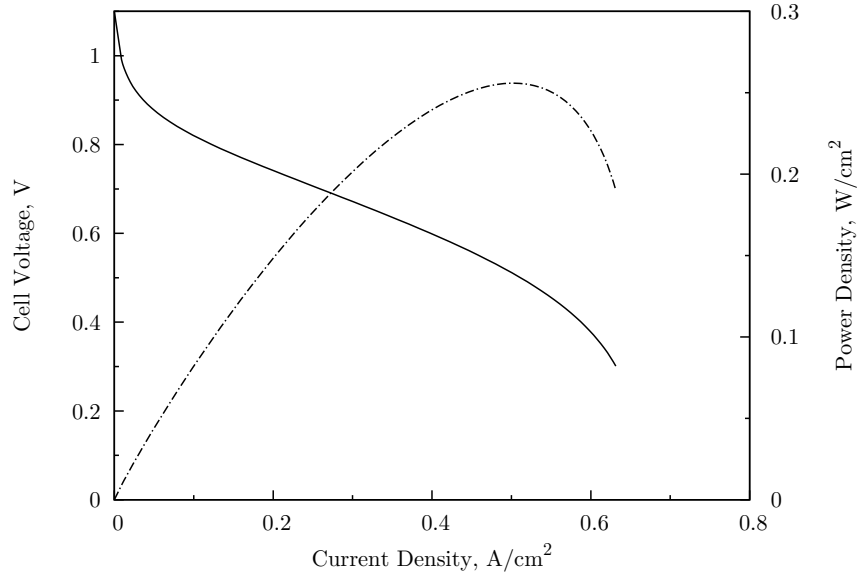


Figure 8.2: Steady state isothermal polarization and power curve for H_2/Air PEMFC ($T=60\text{ }^\circ\text{C}$, $P_a=1\text{ atm}$, $P_c=1\text{ atm}$, Anode RH= 100 %, Cathode RH= 100 %)

Figure 8.3 depicts PEM fuel cell performance at $70\text{ }^\circ\text{C}$. Only increasing fuel cell temperature by $10\text{ }^\circ\text{C}$ resulted in a slightly increase in PEM fuel cell performance. When system cell temperature is kept at $70\text{ }^\circ\text{C}$, maximum power density was computed as 0.29 W/cm^2 at a cell potential of 0.53 V for the isothermal steady state operation. Fuel cell starts to die out at a current density of ca. 0.6 A/cm^2 , which is a very low value for a typical PEM fuel cell.

Since electrode kinetic parameters and diffusion coefficients are directly correlated with temperature, one would expect a higher overall efficiency with the temperature elevation. Considering local temperature and pressure, one reasonable explanation for relatively small enhancement in the fuel cell performance is related to the condensation of water vapor. Produced water condenses at the capillaries of the cathode catalyst layer and diffusion media and decreases the oxidant, if not hinders, transfer rate to the electroactive sites. One possible way to enhance fuel cell performance is to lower cathode inlet humidification level.

Figure 8.4 presents a comparison between H_2/Air and H_2/O_2 PEM fuel cells. A simulation test case run was performed at a cell operating temperature of $70\text{ }^\circ\text{C}$ for isothermal and steady state conditions. When the current density is around 0.53

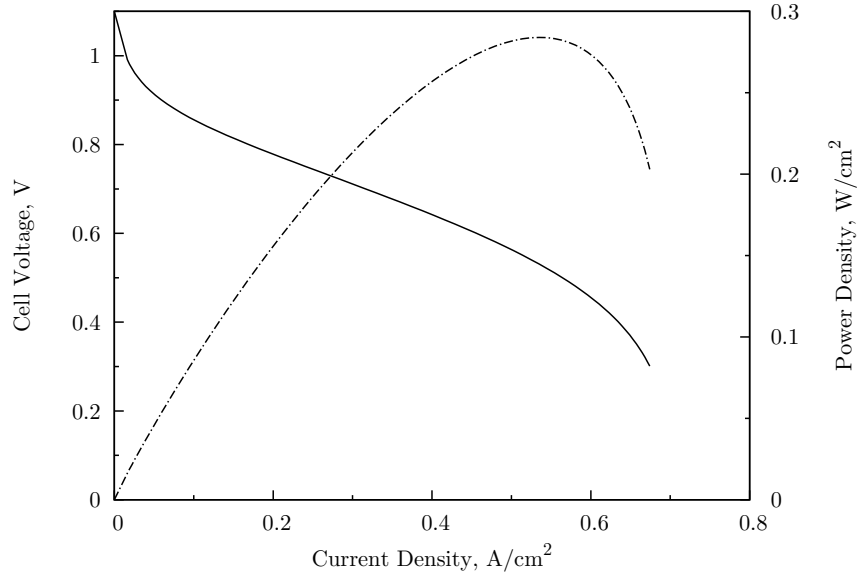


Figure 8.3: Steady state isothermal polarization and power curve for H_2/Air PEMFC ($T=70\text{ }^\circ\text{C}$, $P_a=1\text{ atm}$, $P_c=1\text{ atm}$, Anode RH= 100 %, Cathode RH= 100 %)

A/cm^2 , a maximum power of $0.28\text{ W}/\text{cm}^2$ was observed for air fed fuel cell. For oxygen fed fuel cells, maximum power shifts to a higher current density ($0.48\text{ A}/\text{cm}^2$) with a value of $0.45\text{ W}/\text{cm}^2$ almost 1.5 times larger compared air-based systems.

In the case of using pure oxygen as oxidant feed, fuel cell performance exceeds the overall performance of H_2/Air fuel cell at the moderate and high current density region. At low current density region, two fuel cells exhibit similar performance, where less water is produced and mass transfer limitation is not significant. Presence of an inert nitrogen species and liquid water affects the fuel cell system at elevated current draw rates. It is practical to work with air fed PEM fuel cells to reflect the phenomena of real systems. Therefore, all simulations considered are based on H_2/Air PEM fuel cells, unless otherwise stated.

8.3 Single Phase and Two-phase Flow Model Predictions

There are several competing mechanisms for the transport of liquid water from catalyst layers to the flow channels. Evaporation, diffusion in the gas phase, and capillary flow in the porous media are the basic transport phenomena for the water species. These

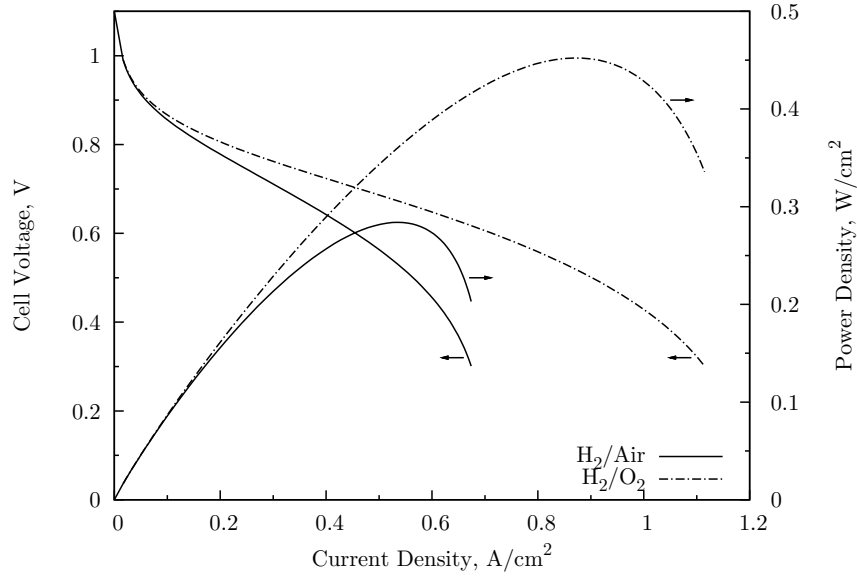


Figure 8.4: Steady state isothermal polarization and power curve comparison for different oxidant feeds ($T=70\text{ }^{\circ}\text{C}$, $P_a=1\text{ atm}$, $P_c=1\text{ atm}$, Anode RH= 100 %, Cathode RH= 100 %)

processes are interrelated with the local temperature such that mass transfer gradient occurs along with the temperature gradient. This overall mechanism acts as a pump and water is pumped from the catalyst layer to the flow channels.

In order to differentiate the effect of single phase (all water is assumed to be in gas phase) and two-phase flow on fuel cell performance, a computational experiment was conducted at $70\text{ }^{\circ}\text{C}$. This time cathode inlet humidity is lowered to 10% to decrease the effect of flooding issue. Figure 8.5 reflects the two fuel cell performance curves for single phase and two-phase flow. This computational run can be considered as a comparison of the fuel cell performance for the cases with and without liquid water effect. In order to alleviate or remove the effect of liquid water, one may supply higher liquid permeability values in the catalyst and backing layers or may exclude the solution of liquid phase saturation by assuming only gas phase present.

It can be seen from Figure 8.5 that the single phase flow outperforms the two-phase flow at the high current density region. At low current density region, diffusion of oxidant and fuel is rapid as compared to electrochemical reaction rates at the anode and cathode. Thus, reactants can access to the active reaction sites in same proportions

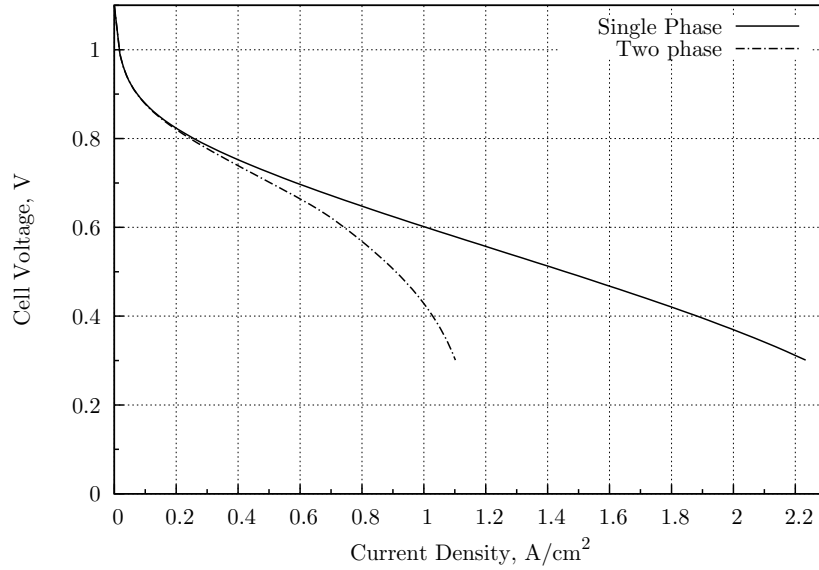


Figure 8.5: PEM fuel cell performance comparison for single phase and two-phase flow at isothermal and steady state conditions ($T=70\text{ }^{\circ}\text{C}$, $P_a=1\text{ atm}$, $P_c=1\text{ atm}$, Anode RH= 100 %, Cathode RH= 10 %)

for both single phase and two-phase flow cases.

As the reaction proceeds, produced liquid water will likely to build up in the cathode catalyst layer and diffusion layers. However, liquid water does not act as a barrier for the passage of fuel and oxidant at the low current density region. For this reason, fuel cell performance curves (see Figure 8.5) overlap almost up to 0.4 A/cm^2 . In the $0\text{--}0.4\text{ A/cm}^2$ current density range, activation losses due to reactions and ohmic potential drops are same for the two cases.

8.4 Effect of Temperature on PEM Fuel Cell Performance

There is a direct impact of cell operating temperature on overall fuel cell performance. Effect of temperature was analyzed and evaluated through numerical simulation in the temperature range of $40\text{--}80\text{ }^{\circ}\text{C}$. Figure 8.6 illustrates the fuel cell polarization curves for different cell operating temperatures. As the fuel cell operating temperature was increased from $40\text{ }^{\circ}\text{C}$ to $80\text{ }^{\circ}\text{C}$, polarization curve shifted to the higher current densities at the same cell voltages.

As the fuel cell is operated at an elevated temperature, diffusion rates of reactants to the active catalytic sites are improved. In addition, increase in cell temperature also enhances the electrochemical activity of the fuel cell due to higher electrode kinetics at the three-phase boundary. Moreover, water removal capability of the fuel cell is also enhanced tremendously owing to the phase change (evaporation).

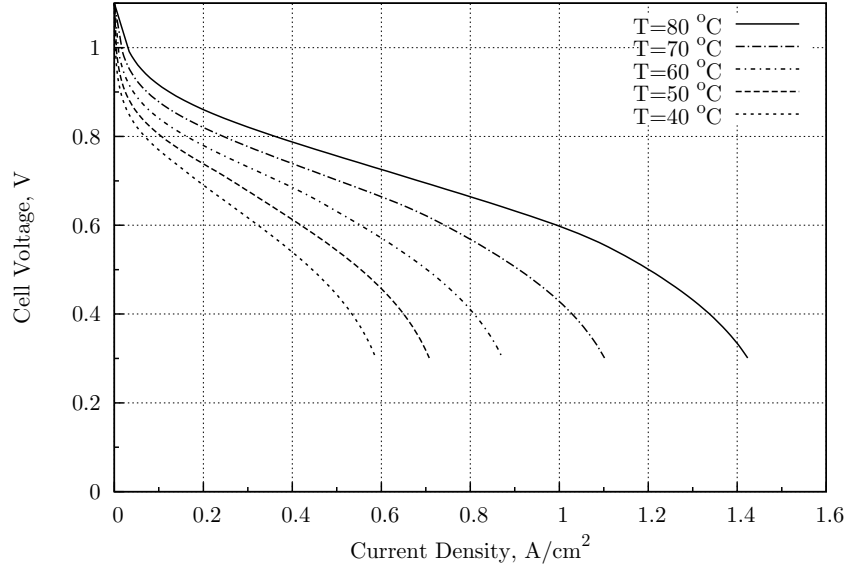


Figure 8.6: Effect of cell temperature on PEM fuel cell performance for isothermal and steady state operation ($P_a=1$ atm, $P_c=1$ atm, Anode RH= 100 %, Cathode RH= 10 %)

In all functional cases, depending on the operating conditions, evaporation decreases or eliminates the possibility of flooding. As shown in Figure 8.6, generally, higher operating temperature will help reduce the adverse effects (e.g. flooding or slow kinetics) and will improve the PEM fuel cell performance as observed experimentally.

In an experimental context, operating temperature has an upper limit due to practical issues related to the electrolyte or ionomer in the catalyst layer. Nevertheless, inlet humidity levels at the anode and cathode may play a significant role at higher temperatures. For example, in cases of low inlet cathode humidity levels at elevated temperatures may result in performance loss due to dehydration in the electrolyte or within the catalyst layers.

8.5 Effect of Pressure on PEM Fuel Cell Performance

There is a straightforward effect of fuel cell operating pressure, when the liquid water effects are discarded. Figure 8.7 demonstrates the fuel cell performance with increasing pressure for a single phase flow case at 70 °C . As the cathode pressure was increased from 1 atm to 2 atm, considerable improvement in polarization curve was observed at moderate and higher current density regions.

Further increase in pressure, say to 3 atm, has a positive effect on fuel cell performance. However, in practical applications, pressure is kept at conditions close to atmospheric pressures to avoid complex system design required for the supply of higher pressures. Therefore, increasing inlet pressure for the sake of improved performance is a critical system design criteria necessitates optimization.

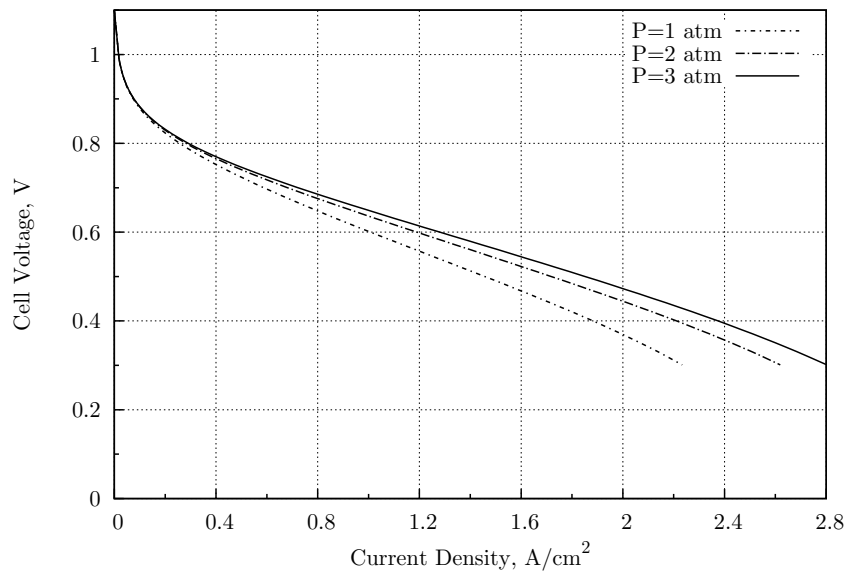


Figure 8.7: Effect of cathode feed pressure on PEM fuel cell performance for single phase flow at isothermal and steady state operating conditions ($T=70$ °C, $P_a=1$ atm, Anode RH= 100 %, Cathode RH= 10 %)

Effect of pressure becomes more complicated in real situations like in the case of two-phase flow. Figure 8.8 exhibits the effect of pressure on overall fuel cell polarization curve for two-phase flow. As the fuel cell was simulated at a higher pressure, say 2 atm, a decrease in total fuel cell efficiency was observed. Increasing the pressure beyond 2

atm even worsen the fuel cell performance at practical operating conditions.

Liquid water is produced at the cathode catalyst layer due to oxygen reduction reaction. Additionally, protons drag the water molecules from anode to cathode. At higher current densities, there is a significant liquid water accumulation in the cathode catalyst layer and porous transport layers. Considering saturation pressure of water at the operating temperature, further increase in pressure will decrease the water removal ability by evaporation due to increased partial pressures of water. Consequently, water condenses along the temperature gradient and fills the pores available for gas flow and hinders the transport of oxidant.

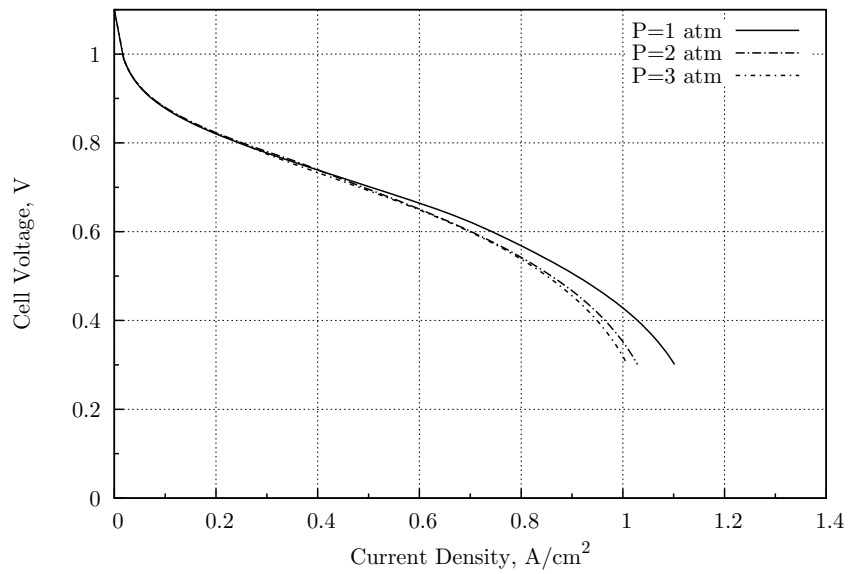


Figure 8.8: Effect of cathode feed pressure on PEM fuel cell performance for two phase flow at isothermal and steady state operating conditions ($T=70\text{ }^{\circ}\text{C}$, $P_a=1\text{ atm}$, Anode RH= 100 %, Cathode RH= 10 %)

In some cases, a small positive pressure gradient is useful to create back flow from cathode to anode. This hydraulic pressure effect on two sides of the electrolyte helps improve water discharge capacity of the fuel cell as well as provides humidification at the anode. This effect is similar to use of a microporous layer at the cathode side to push and pump water back to the anode.

Effective water management strategies require the optimal adjustment of operating conditions with the use of proper fuel cell components (e.g. inclusion of a microporous

layer at the cathode). Another important point to mention related to higher operating pressures is the possibility of cross-over and pin hole formation in the electrolyte due to thinness of the proton conducting layer (approximately 2 mils).

Hydrogen and oxygen may cross over to the cathode and anode side respectively with increasing pressure. This shorts the fuel cell and it is extremely undesired condition during the course of operation. However, in the case of using interdigitated flow field architecture (see chapter 1), a higher pressure is a must to force the flow of fuel and oxidant. In this case, a small excess pressure should be provided to get the best performance out of the fuel cell.

8.6 Effect of Cathode Humidity on PEM Fuel Cell Performance

To achieve optimal cell performance, a delicate balance between membrane dehydration and cathode flooding must be provided. One way to reach this target is to dynamically control the inlet humidity levels at the anode and cathode. In PEM fuel cells, a higher humidification is required at anode and usually very low cathode inlet humidity is sufficient to maximize fuel cell performance. As described in the introduction part, conventional humidification method is not suitable to supply humidity levels under saturation pressure. Liquid or vapor injection methods are preferred to control the power output from the fuel cell system.

Oxidant and fuel inlet relative humidity has an impact on the partial pressure of oxygen and hydrogen respectively. Vapor content in the gas streams at anode and cathode is one way to control the ability of the gas streams to eject water through backing layers. In this case simulation, keeping anode relative humidity at fully humidified conditions, effect of cathode relative humidity on fuel cell performance has been investigated.

Figure 8.9 shows the variation of PEM fuel cell overall performance with cathode relative humidity at 60 °C . As it can be seen from the graph, increase in cathode relative humidity resulted in a poor fuel cell performance. As the water vapor content of the cathode gas stream was increased, more water is likely to be in the liquid phase. This will disable or diminish water discharge capability of gas mixture by evaporation with the phase change.

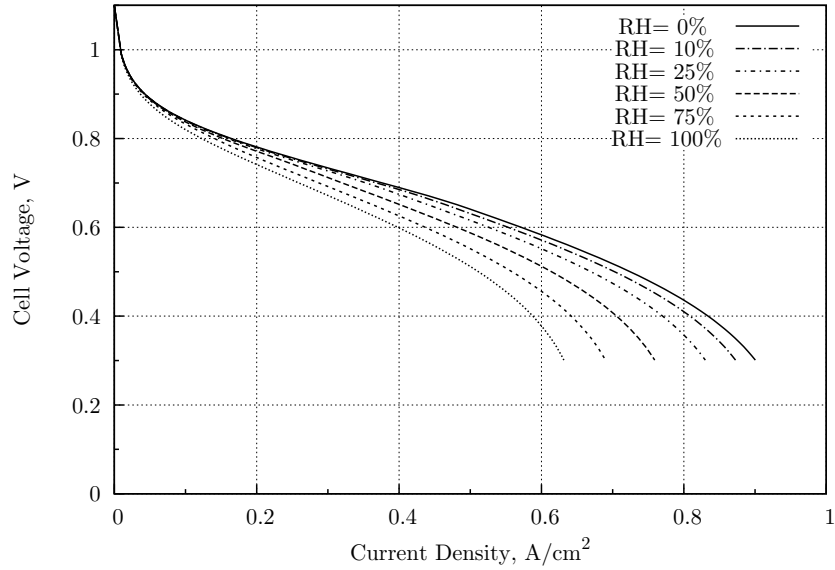


Figure 8.9: Variation of PEM fuel cell performance with cathode relative humidity ($T=60\text{ }^{\circ}\text{C}$, $P_a=1\text{ atm}$, Anode RH= 100 %)

It is important to notice the differentiation of curves in Figure 8.9 at high current density region, where more water is produced owing to electrochemical reaction. Liquid phase saturation levels together with thermal gradients play a significant role in the water evolution within the fuel cell.

In practical operating conditions, PEM fuel cells probably will not be operated below 0.4 volts. In that case, the difference between the fuel cell performance curves is small. However, cathode humidity level has a considerable impact on degradation mechanisms, especially in the electrolyte. Thus, effective and dynamic control of inlet humidity is necessary.

In order to see the effect of air inlet relative humidity at an elevated temperature, simulation were run at $70\text{ }^{\circ}\text{C}$ for the same case. Figure 8.10 presents the variation of cell efficiency with inlet cathode humidity. It is clearly seen from the figure that, span between curves become extended as compared to previous case at high current density. This is due to the exponential nature of water vapor saturation pressure with temperature. Water removal efficiency of the cathode gas stream by evaporation can be enhanced greatly by adjusting cathode inlet humidity level to a value of around 10%.

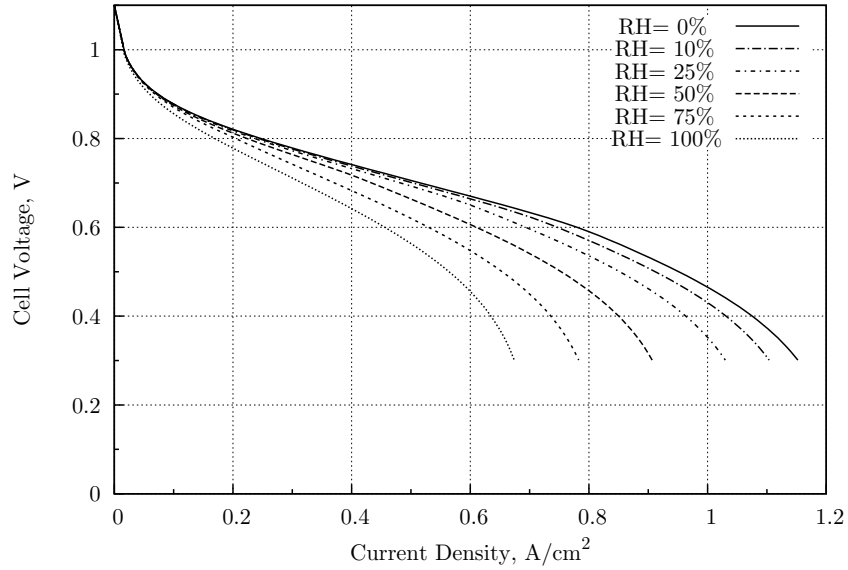


Figure 8.10: Variation of PEM fuel cell performance with cathode relative humidity ($T=70\text{ }^{\circ}\text{C}$, $P_a=1\text{ atm}$, Anode RH= 100 %)

Humidity effect becomes very dominant and critical especially at high operating temperatures. For this purpose, humidity may be set in real time according to the current withdraw rate for optimized operation.

8.7 Ionic Phase Potential Distribution at PEM Fuel Cell Cathode

Ionic phase potential (potential in the electrolyte) distribution occurs within the electrolyte as well as in the catalyst layers due to the ionomer content of the electrocatalysts. Note that ionic phase potential loss dominantly signifies the performance loss within the ohmic region of a typical polarization curve. To elucidate the difference in ionic phase distribution, computational run was conducted at $60\text{ }^{\circ}\text{C}$ for different applied solid phase (electronic phase) cell potentials.

Figure 8.11 reflects the variation of ionic phase potential at the cathode catalyst layer and membrane with applied potential. A linear change in ionic potential was observed within the electrolyte, whereas a nonlinear variation was detected for ionic phase potential within the ionomer portions of the cathode catalyst layer. As more current drawn from the fuel cell, sharp span of ionic phase potential was seen.

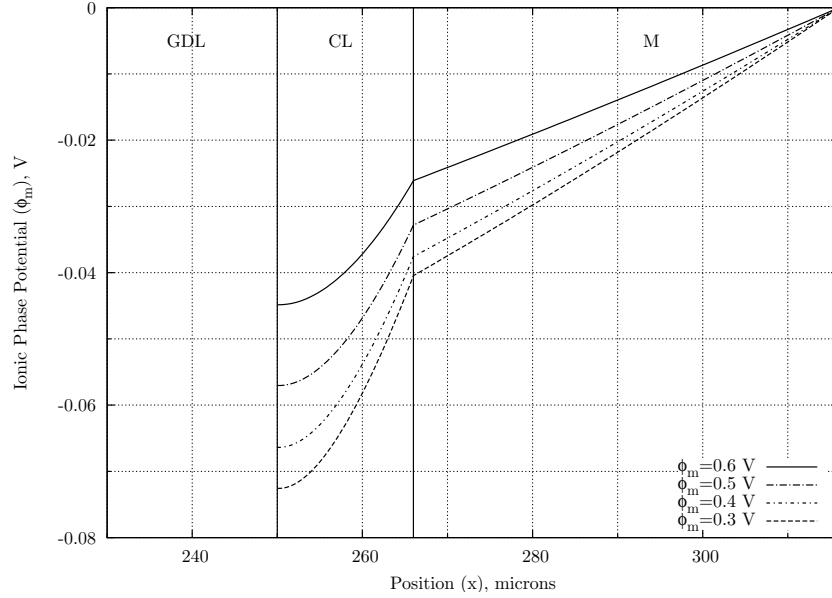


Figure 8.11: Ionic phase potential distribution at cathode for the base case ($T=60\text{ }^{\circ}\text{C}$, $P_a=1\text{ atm}$, Anode RH= 100 %, Cathode RH= 10 %)

To minimize the ionic phase potential change, one may keep the electrolyte humidified at all times to enhance the protonic conductivity inside the electrolyte. Nonlinear nature of the potential distribution at the cathode catalyst layer is probably due to the coupled species consumption (proton, oxygen) at the catalytic regions. A thinner electrolyte with superior proton conduction will be one of the best solutions to suppress the effects of ionic potential drop.

8.8 Liquid Water Transport in PEM Fuel Cells

Besides some experimental techniques, water distribution within the fuel cell is an important diagnostic tool that may be monitored through the numerical simulation of the PEM fuel cell model. For optimum removal of liquid water from the porous regions, liquid phase saturation levels throughout the fuel cell needs to be investigated. Capillary transport mechanism is the fundamental water transport mechanism within the porous media. Effects of relative humidity, pressure, and temperature on liquid phase saturation distribution have been explored through numerical simulations.

8.8.1 Humidity Effect on Liquid Water Transport

For optimal fuel cell operation, one critical parameter is the liquid phase saturation, s , inside the porous diffusion media. Figure 8.12 presents the effect of inlet cathode relative humidity on overall cell efficiency at 60 °C. Saturation levels strictly change with the structural characteristics of the porous media such as wetting properties, hydrophobicity content (e.g. PTFE or FEP content), porosity, and tortuosity. Depending on the fuel cell application a proper selection of diffusion media material is vital for optimum performance.

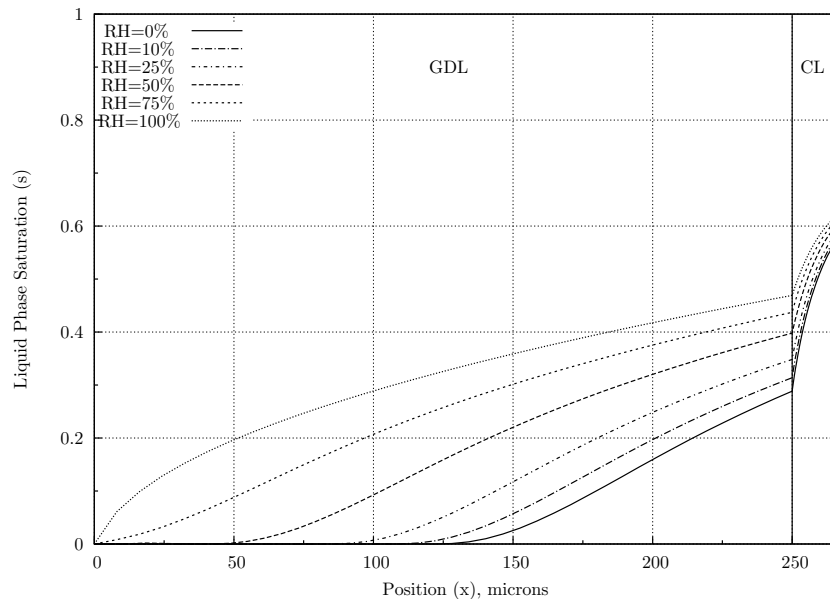
Figure 8.12 illustrates the effect of different phase saturations at the cathode gas diffusion layer and catalyst layer. Oxygen reduction reaction solely takes place at the cathode catalyst layer. Therefore, cathode catalyst layer is saturated over the whole catalytic region, whereas gas phase in the diffusion media is partially saturated with the water vapor.

Water is produced at the cathode catalyst layer as well as it is transported from anode to cathode by electro-osmosis. Water can be removed from the diffusion media and catalyst layer pores by capillary transport, phase change (evaporation) and diffusion in the gas phase. Capillary transport mechanism is slow as compared to evaporation. First, gas phase becomes saturated and then the remaining water is transported by capillary flow in the tortuous path.

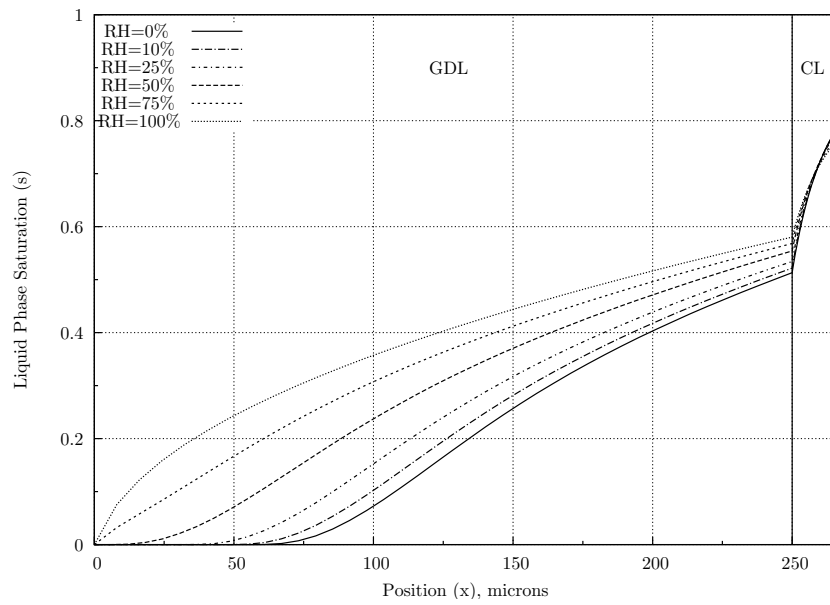
As the current draw rate is increased (Figure 8.12b), the gas diffusion media becomes more saturated with the liquid water and the transport of reactants to the active sites turn out be a major issue. Thickness of the diffusion layer may be reduced further to sweep liquid water to the flow channels. Alternatively, hydrophobicity, porosity of the medium may be redesigned to alleviate the problems associated with the liquid water transport.

8.8.2 Pressure Effect on Liquid Water Transport

Pressure effect, as a design parameter, on liquid water transport can be considered as an interplay between enhanced reactant transport and cathode flooding. Figure



(a)



(b)

Figure 8.12: Variation of liquid phase saturation with cathode relative humidity at a cell potential of (a) 0.6 V (b) 0.4 V ($T=60\text{ }^{\circ}\text{C}$, $P_a=1\text{ atm}$, Anode RH= 100 %)

8.13 shows the variation of liquid phase saturation profile with different cathode inlet pressures.

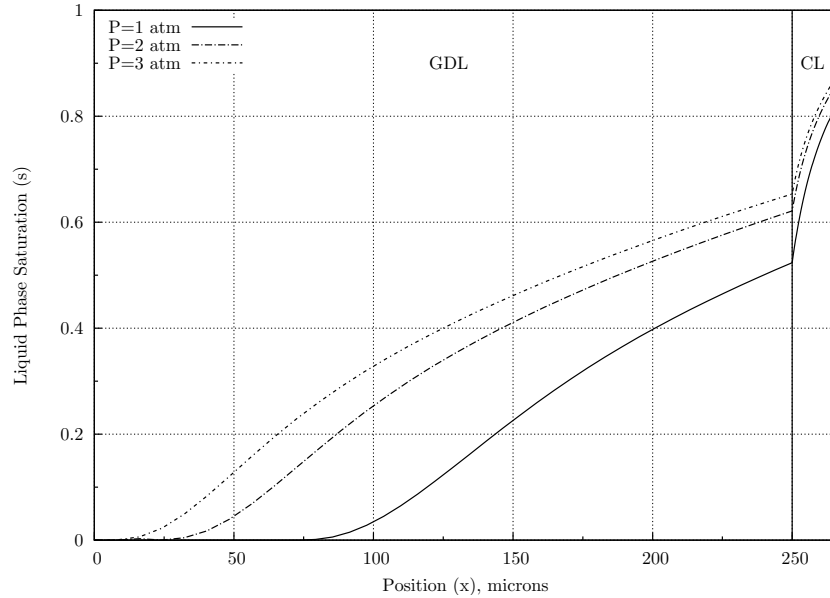


Figure 8.13: Variation of liquid phase saturation with cathode pressure at a cell potential of 0.3 V ($T=70\text{ }^{\circ}\text{C}$, $P_a=1\text{ atm}$, Anode RH= 100 %, Cathode RH= 10 %)

Increasing fuel cell inlet pressure may force the flow of reactants to the active catalytic regions. However, high pressure leads to the rapid saturation of the diffusion media with liquid water. Most flow field architecture require a slightly higher inlet pressure than the atmospheric pressure to compensate the pressure drop related to channel flow. Additionally, higher pressure necessitates more compressor work, which decreases overall system efficiency. For example, in the case of using an interdigitated flow geometry, a slightly higher inlet pressure (e.g 1.2 atm or 1.3 atm) may be sufficient to provide optimal operation of PEM fuel cell.

8.8.3 Temperature Effect on Liquid Water Transport

Effect of operating temperature on liquid water transport was simulated for cathode side at $60\text{ }^{\circ}\text{C}$ and $80\text{ }^{\circ}\text{C}$ respectively. Figure 8.14 shows the liquid water distribution at the cathode for an isothermal and steady state PEM fuel cell operating at $60\text{ }^{\circ}\text{C}$. Owing to the relatively low cell temperature, ability of movement of liquid water by evaporation is reduced. As a result, water first builds up at the cathode, and

consequently, high saturation distribution was seen at the diffusion media.

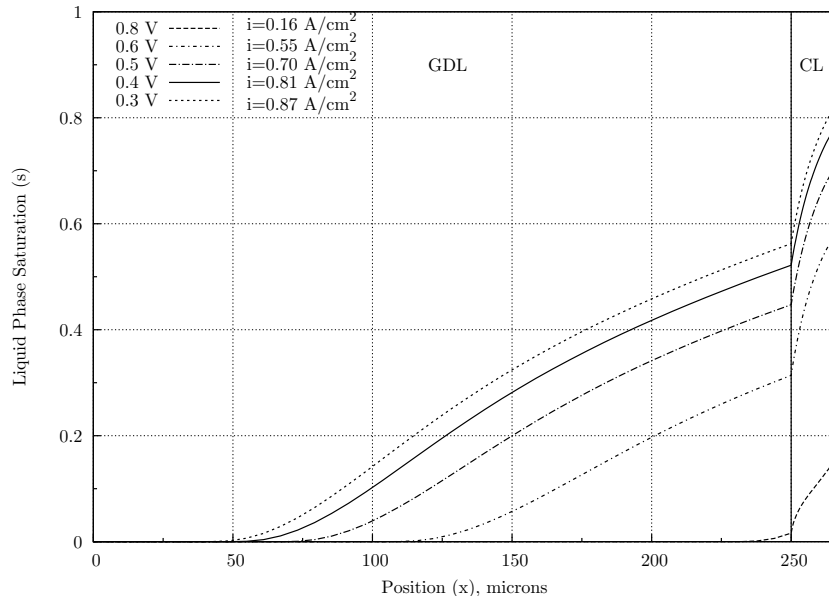


Figure 8.14: Liquid phase saturation distribution for different cell potentials ($T=60$ °C, $P_a=1$ atm, $P_c=1$ atm, Anode RH= 100 %, Cathode RH= 10 %)

When the fuel cell was run with the same conditions at a higher operating temperature of 80 °C, simulation results in Figure 8.15 showed that most of the liquid water was removed by evaporation and lower values of phase saturation was seen at the cell entrance. In addition, cathode catalyst layer was not flooded by water and there seems to form a sharp capillary gradient for water transport.

It is known that experimental results exhibit a more severe situation (possibility of flooding and reactant starvation) as compared to the simulation findings at 80 °C. In order to elucidate and understand this water evolution mechanism, this time simulation test run was performed with the same base case parameters for nonisothermal condition.

Figure 8.16 illustrates the major difference between an isothermal and nonisothermal operation. Depending on the local temperature distribution within the fuel cell components, especially at higher currents fuel cell performance is affected by non-isothermal operation considering phase change followed by temperature gradient [50]. This is a balance between water and thermal management and better performance is strictly controlled by this phase change effect as a result of temperature increase due

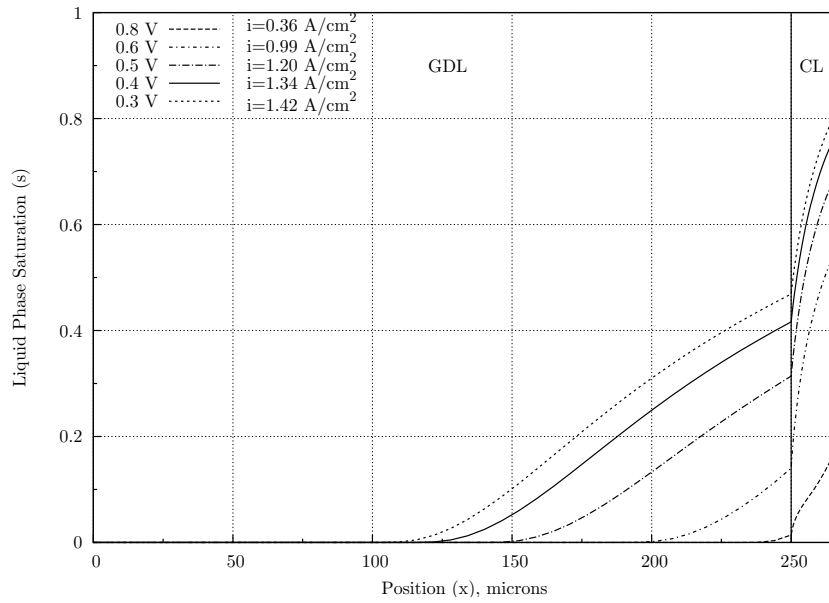


Figure 8.15: Isothermal liquid phase saturation distribution for different cell potentials ($T=80\text{ }^{\circ}\text{C}$, $P_a=1\text{ atm}$, $P_c=1\text{ atm}$, Anode RH= 100 %, Cathode RH= 10 %)

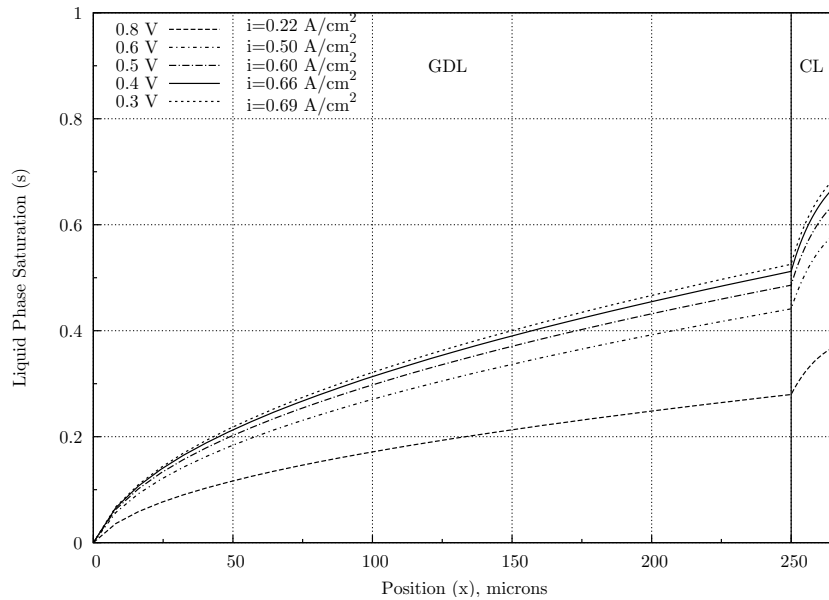


Figure 8.16: Nonisothermal liquid phase saturation distribution for different cell potentials ($T=80\text{ }^{\circ}\text{C}$, $P_a=1\text{ atm}$, $P_c=1\text{ atm}$, Anode RH= 100 %, Cathode RH= 10 %)

to reaction and other heat generation mechanisms.

Water condenses with the temperature gradient and higher liquid phase saturation distributions are realized within the PEM fuel cell. Up to date, there have been little effort on thermal modeling of PEM fuel cells. Most of the thermal models presented in the literature assumes a local lumped temperature for PEMFC and treats the heat removal at the boundaries of the cell.

Due to exponential nature of the water vapor saturation pressure, even a small temperature gradient within the fuel cell sandwich results in rapid and sharp changes. Coupled thermal and water phenomena can only be understood by solving the coupled two-phase flow and energy balance. In other words, saturation distribution can be related to temperature distribution for a particular case. This will help adjust the operating conditions properly during the operation of the PEM fuel cell.

8.9 Thermal Effects in PEM Fuel Cells

In order to gain an understanding related to cold start characteristics of a PEM fuel cell, two phase energy balance approach was suggested. Figure 8.17 shows the steady state isothermal and nonisothermal polarization and power curve for H₂/Air PEMFC operating at 80 °C and atmospheric pressure. Fuel cell simulation conditions were kept at fully humidified conditions for anode and cathode.

Maximum power observed was around 0.30 W/cm² at 0.6 V for both isothermal and nonisothermal operation. Polarization curves coincide for the two modes of operation upto mass transfer regions. At high current region, isothermal operation exhibits slightly higher performance. When a pure oxygen feed is used as oxidant, overall performance of the polarization and power curves increases as shown in Figure 8.18

Similar to isothermal case, a test run was performed to analyze the effect of cell temperature on fuel cell performance. Figure 8.19 shows the variation of polarization curves for different temperatures for air fed PEM fuel cells. As compared to isothermal case, nonisothermal solution of the model predicts lower cell performance owing to phase change induced condensation phenomena. To catch up real cell behavior, one must account for the thermal effects in the cell.

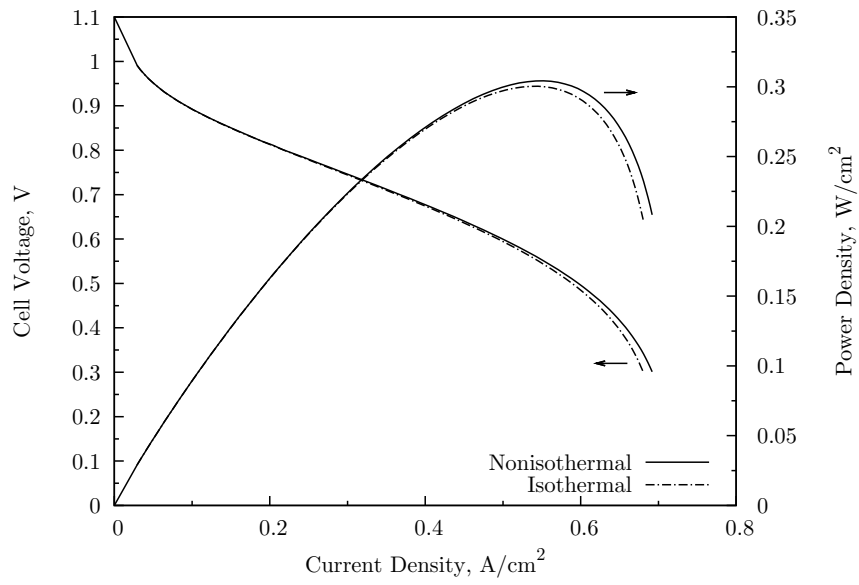


Figure 8.17: Steady state isothermal and nonisothermal polarization and power curve for H_2 /Air PEMFC ($T=80\text{ }^\circ\text{C}$, $P_a=1\text{ atm}$, $P_c=1\text{ atm}$, Anode RH= 100 %, Cathode RH= 100 %)

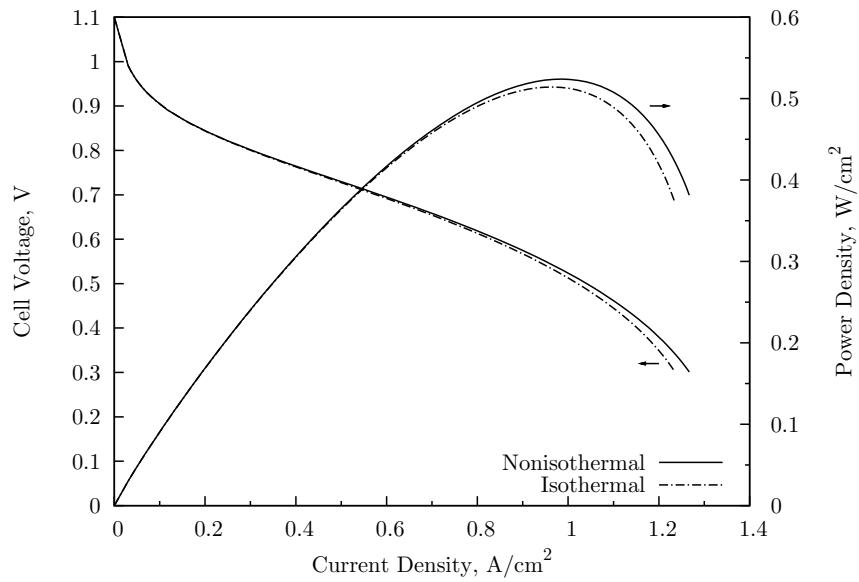


Figure 8.18: Steady state isothermal and nonisothermal polarization and power curve for H_2 / O_2 PEMFC ($T=80\text{ }^\circ\text{C}$, $P_a=1\text{ atm}$, $P_c=1\text{ atm}$, Anode RH= 100 %, Cathode RH= 100 %)

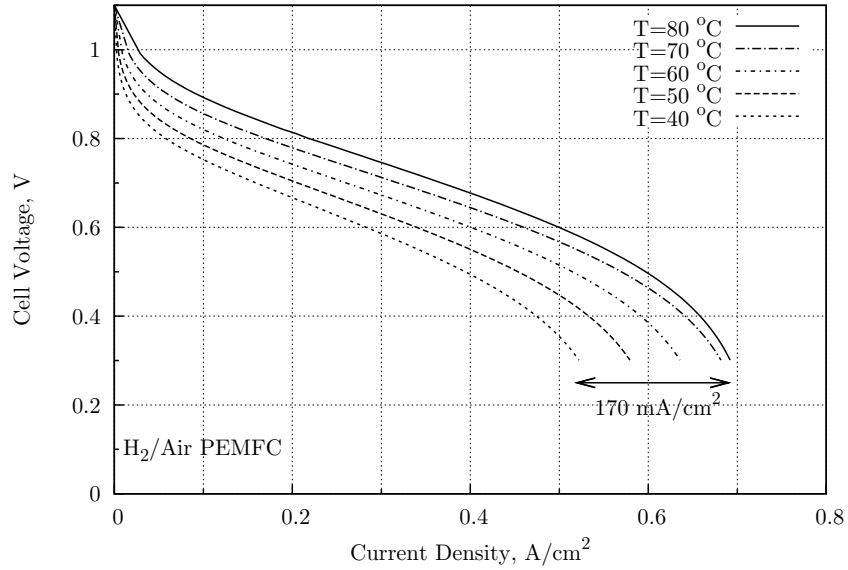


Figure 8.19: Effect of cell temperature on PEM fuel cell performance for nonisothermal and steady state operation ($P_a=1$ atm, $P_c=1$ atm, Anode RH= 100 %, Cathode RH= 100 %)

Figure 8.20 presents the nonisothermal steady state temperature profile in the cathode PEM fuel cell for different cell potentials at 50 °C. A maximum temperature difference of around 0.7 °C was observed. Even with a small change in temperature, considerably high amount of liquid water condensation was detected.

Figure 8.21 presents the nonisothermal steady state temperature profile in the cathode PEM fuel cell for different cell potentials. A maximum temperature difference of 0.82 °C was observed between 0.8 V and 0.3 V. The mathematical model presented here assumes a local thermal equilibrium between liquid phase and solid phase. However, there may be significant heat transfer between the solid and gas phases.

Based on the feed temperatures and operating conditions, heat is exchanged between the two phases. Heat transfer coefficient is an important design parameter for the optimum operation of the PEM fuel cell. If the heat transfer rate is poor between the two phases (ca. $h=0.001$ W/m²K), there will be two different temperature profiles for solid and gas phases and improvement of fuel cell performance will strictly be dependent on the control of heat transfer rate between phases.

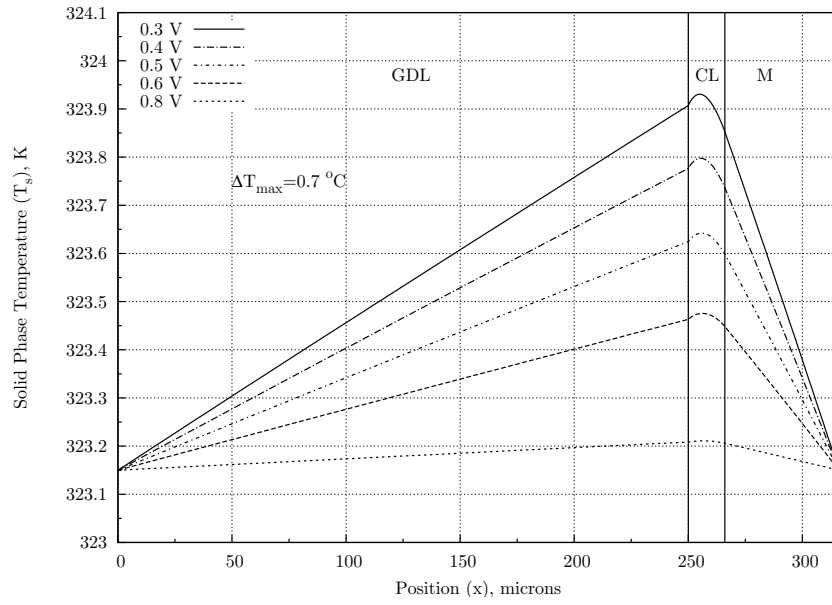


Figure 8.20: Nonisothermal steady state temperature profile in the cathode PEM fuel cell ($T=50\text{ }^{\circ}\text{C}$, $P_a=1\text{ atm}$, $P_c=1\text{ atm}$, Anode RH= 100 %, Cathode RH= 100 %)

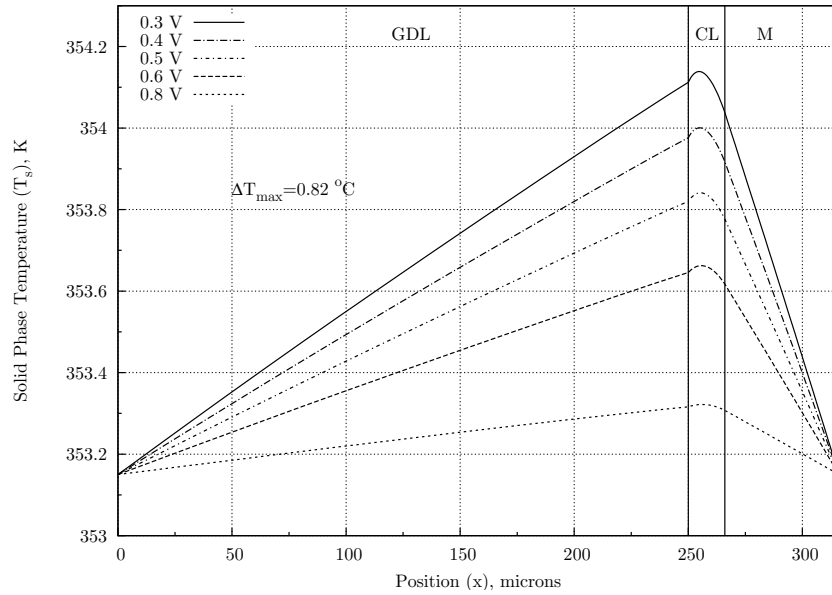


Figure 8.21: Nonisothermal steady state temperature profile in the cathode PEM fuel cell ($T=80\text{ }^{\circ}\text{C}$, $P_a=1\text{ atm}$, $P_c=1\text{ atm}$, Anode RH= 100 %, Cathode RH= 100 %)

Engineering of new materials for enhanced thermal management is essential for PEM fuel cells. If the heat exchange is sufficiently high between the two phases (ca. $h = 2.5 \text{ W/m}^2\text{K}$), solid and gas phase temperature profiles will coincide. In this case, liquid, solid, and gas phases are assumed to be in thermal equilibrium. Indeed, most of the studies reported in the literature neglect the two phase energy balance approach. This phenomenon could have very dramatic effects on fuel cell performance under cold start up conditions.

CHAPTER 9

CONCLUSIONS AND RECOMMENDATIONS

A two-phase, nonisothermal mathematical model was developed for the investigation of water and heat transport through the membrane electrode assembly (MEA) of the PEMFC. A FORTRAN 90 code was written for the numerical simulation of the mathematical model. In addition, novel carbon supported PEM fuel cell electrocatalysts exhibiting different structural properties were designed and synthesized. Ex situ and in situ characterization of Pt/C and Pt-Pd/C electrocatalysts were conducted with various morphological and electrochemical methods. As a result of the experimental studies and mathematical model simulations, concluding remarks observed are as follows:

1. In the theoretical part of the work, emphasis is given to the modeling of anode and cathode catalyst layers, where different reaction mechanisms are considered for anode and cathode. This mechanistic approach will help to evaluate how the different mechanisms will impact the fuel cell performance.
2. Dual site adsorption of hydrogen and single site adsorption of oxygen onto active platinum sites are considered to be the rate determining steps for hydrogen oxidation and oxygen reduction reactions respectively. Langmuir-Butler-Volmer type rate expressions were proposed for the first time for PEM fuel cell modeling and these rate expressions were coupled with agglomerate and thin film approach to investigate electrode kinetics in detail. Highly coupled and nonlinear nature of Langmuir-Butler-Volmer type reaction rates with temperature was examined to understand the effect of different phase temperatures on electrode kinetic parameters.

3. Fundamentally, overall fuel cell performance can be considered as interplay between water and thermal management. In order to capture different heat transfer effects throughout the fuel cell, a two-phase energy balance between gas and solid phase was suggested to capture the phenomena for the cases such as cold-start up or when there is a significant temperature difference between the fuel cell temperature and the reactant feeds temperatures. This will help predict more accurately the phenomena occurring during cold start-up like the location of ice formation. If the temperatures of the two phases are equal, then ice will form in or near the flow channels. Otherwise, ice will form where the gas phase temperature reaches the freezing point. This may occur in the microporous layer or catalyst layer as observed experimentally.
4. Model results will help guide the development of experimental measurements needed to validate the model. The mathematical model may serve as a useful tool to evaluate the performance of various electrocatalysts. In order to understand cold start case in depth for proton exchange membrane fuel cells, mathematical model may further be improved for the transient case. Agglomerate and thin film approach is a better representation of the catalytic regions of PEM fuel cell. Additionally, further improvement of the model in terms of anode and cathode reaction mechanisms will help elucidate and understand the relative effects of several electrode kinetic parameters on PEM fuel cell performance. Much more work has to be done on mathematical modeling and simulation on multiple length and time scale to gain qualitative and quantitative insight for material development suited for PEM fuel cell applications.
5. This dissertation study has demonstrated that hollow core mesoporous shell carbon supported Pt electrocatalysts have a promising potential to be used as PEMFC cathode catalysts. Nanosized spherical carbon supports (HCMS1, HCMS2) with hollow core mesoporous shell structure were prepared by using silica spheres as template. Microwave irradiation method has been verified to be a successful and fast technique for the preparation of Pt/C electrocatalysts for PEMFCs. In order to control the catalyst particle size and provide a better Pt utilization, it is critical to optimize the microwave duration at 800 W.
6. Not only the high surface area but also meso/macro bimodal pore structure of the

carbon support might be functional for the improvement of electrode kinetics as compared to microporous support structure in terms of homogeneous dispersion of active metal nanoparticles, prevention of possible pore clogging, and reduced mass transfer resistance.

7. Compared to Pt/VX and ETEK[®] electrocatalysts, HCMS carbon based electrocatalysts showed encouraging cathode electrochemical performance results in the fuel cell environment. Pt/HCMS2 electrocatalysts showed higher ORR activity than Pt/HCMS1. This improved electrochemical performance might result from the tailored pore texture of the HCMS2 carbon support. Results of CV tests showed that Pt/HCMS2 electrocatalysts provided the proximate Pt utilization value as compared to the commercial ETEK[®] catalyst. In addition, polarization curves obtained from PEMFC performance tests were in well agreement with Pt utilization values estimated from CV analysis. It might be concluded that Pt utilization and ORR activity increase with the better control of the pore structure of the carbon supports.
8. Hollow core mesoporous shell carbon was synthesized using two carbon precursors and Pt-Pd alloy catalysts over carbon supports (HCMS1 and HCMS2) were prepared by microwave irradiation method. It was concluded that as the pore size of the carbon was increased by changing the type of the carbon precursor, fuel cell performances of the HCMS2 based catalysts were improved significantly.
9. Pt-Pd/HCMS electrocatalysts are promising anode and cathode PEMFC catalysts. Fuel cell tests showed that Pt-Pd/HCMS2 catalysts were more active when the catalysts were used as anode electrode and the fuel cell performance was doubled. Considering the high cost and lack of reserves of platinum, palladium seems to be a promising electrocatalyst for PEMFCs.
10. Bimetallic catalysts exhibited a considerable activity for low Pd content Pt-Pd/HCMS catalysts. Adding Pd in small amounts might increase the stability of the electrocatalyst and can help to the reconfiguration of Pt-C interaction. An increase in the particle size of the Pt-Pd bimetallic catalysts was observed as the Pd loading was increased. Decreasing Pt-Pd alloy particle size by controlling synthesis conditions, one will probably increase the dispersion and prevent the

possible agglomeration and consequently particle growth might be controlled during the course of fuel cell operation.

11. For optimal fuel cell operation, novel electrocatalyst support materials are still required to facilitate the transport of fuel, oxidant, and water through the porous matrix. The support structure must exhibit an ordered pore texture with larger mesopores ($\approx 10\text{-}20$ nm). Controlling the structure by pore tailoring and achieving high electronic conductivity at the same time is a difficult task. This challenging issue needs to be resolved with the design of novel electrocatalyst supports with desired characteristics.

REFERENCES

- [1] J.H. Hirschenhofer, D.B. Stauffer, R.R. Engleman, and M.G. Klett. *Fuel cell handbook*. US Department of Energy, Morgantown, WV, 7th edition, 2004.
- [2] S. Thomas and M. Zalbowitz. *Fuel cells: Green power*. Los Alamos National Laboratory, 1999.
- [3] F. Barbir and T. Gomez. Efficiency and economics of proton exchange membrane (PEM) fuel cells. *International Journal of Hydrogen Energy*, 22(10-11):1027–1037, 1997.
- [4] T.V. Nguyen. A Gas Distributor Design for Proton-Exchange-Membrane Fuel Cells. *Journal of the Electrochemical Society*, 143(5):L103–L105, 1996.
- [5] T.V. Nguyen. Water Management by Material Design and Engineering for PEM Fuel Cells. *ECS Transactions*, 3(1):1171–1180, 2006.
- [6] J.T. Gostick, M.A. Ioannidis, M.W. Fowler, and M.D. Pritzker. On the role of the microporous layer in PEMFC operation. *Electrochemistry Communications*, 11(3):576–579, 2009.
- [7] R. Friedmann and T.V. Nguyen. Optimization of the Microstructure of the Cathode Catalyst Layer of a PEMFC for Two-Phase Flow. *Journal of the Electrochemical Society*, 157(2):B260–B265, 2010.
- [8] Z. Liu, X.Y. Ling, X. Su, and J.Y. Lee. Carbon-supported Pt and PtRu nanoparticles as catalysts for a direct methanol fuel cell. *The Journal of Physical Chemistry B*, 108(24):8234–8240, 2004.
- [9] R. Friedmann and T.V. Nguyen. Optimization of the cathode catalyst layer composition using a novel 2-step preparation method. *ECS Transactions*, 16(2):2021, 2008.

- [10] J. Giner and C. Hunter. The Mechanism of Operation of the Teflon-Bonded Gas Diffusion Electrode: A Mathematical Model. *Journal of The Electrochemical Society*, 116(8):1124–1130, 1969.
- [11] MB Cutlip. An approximate model for mass transfer with reaction in porous gas diffusion electrodes. *Electrochimica Acta*, 20(10):767–773, 1975.
- [12] R.P. Iczkowski and M.B. Cutlip. Voltage losses in fuel cell cathodes. *Journal of The Electrochemical Society*, 127(7):1433–1440, 1980.
- [13] M.B. Cutlip, S.C. Yang, and P. Stonehart. Simulation and optimization of porous gas-diffusion electrodes used in hydrogen oxygen phosphoric acid fuel cells—II development of a detailed anode model. *Electrochimica Acta*, 36(3-4):547–553, 1991.
- [14] E.A. Ticianelli, C.R. Derouin, A. Redondo, and S. Srinivasan. Methods to advance technology of proton exchange membrane fuel cells. *Journal of the Electrochemical Society*, 135:2209–2214, 1988.
- [15] A. Parthasarathy, S. Srinivasan, A.J. Appleby, and C.R. Martin. Temperature dependence of the electrode kinetics of oxygen reduction at the platinum/naion interface—a microelectrode investigation. *Journal of the Electrochemical Society*, 139(10):2530–2537, 1992.
- [16] A. Parthasarathy, S. Srinivasan, A.J. Appleby, and C.R. Martin. Pressure dependence of the oxygen reduction reaction at the platinum microelectrode/naion interface: electrode kinetics and mass transport. *Journal of the Electrochemical Society*, 139(10):2856–2862, 1992.
- [17] J. Kim, S.M. Lee, S. Srinivasan, and C.E. Chamberlin. Modeling of proton exchange membrane fuel cell performance with an empirical equation. *Journal of the Electrochemical Society*, 142(8):2670–2674, 1995.
- [18] V.A. Paganin, E.A. Ticianelli, and E.R. Gonzalez. Development and electrochemical studies of gas diffusion electrodes for polymer electrolyte fuel cells. *Journal of Applied Electrochemistry*, 26(3):297–304, 1996.

- [19] D.M. Bernardi and M.W. Verbrugge. Mathematical model of a gas diffusion electrode bonded to a polymer electrolyte. *AIChE Journal*, 37(8):1151–1163, 1991.
- [20] D.M. Bernardi and M.W. Verbrugge. A Mathematical Model of the Solid-Polymer-Electrolyte Fuel Cell. *Journal of the Electrochemical Society*, 139(9):2477–2491, 1992.
- [21] T.E. Springer, T.A. Zawodzinski, and S. Gottesfeld. Polymer electrolyte fuel cell model. *Journal of the Electrochemical Society*, 138:2334–2342, 1991.
- [22] D. Natarajan and T.V. Nguyen. Three-dimensional effects of liquid water flooding in the cathode of a PEM fuel cell. *Journal of Power Sources*, 115(1):66–80, 2003.
- [23] Y. Wang, K.S. Chen, J. Mishler, S.C. Cho, and X.C. Adroher. A review of polymer electrolyte membrane fuel cells: Technology, applications, and needs on fundamental research. *Applied Energy*, 88:981–1007, 2011.
- [24] M. Eikerling. Water management in cathode catalyst layers of PEM fuel cells. *Journal of the Electrochemical Society*, 153(3):E58–E70, 2006.
- [25] R. Borup, J. Meyers, B. Pivovar, Y.S. Kim, R. Mukundan, N. Garland, D. Myers, M. Wilson, F. Garzon, D. Wood, et al. Scientific aspects of polymer electrolyte fuel cell durability and degradation. *Chemical Reviews*, 107(10):3904–3951, 2007.
- [26] V. Gurau and J.A. Mann Jr. A Critical Overview of Computational Fluid Dynamics Multiphase Models for Proton Exchange Membrane Fuel Cells. *SIAM Journal on Applied Mathematics*, 70:410–454, 2009.
- [27] R.J. Bellows, M.Y. Lin, M. Arif, A.K. Thompson, and D. Jacobson. Neutron imaging technique for in situ measurement of water transport gradients within Nafion in polymer electrolyte fuel cells. *Journal of the Electrochemical Society*, 146(3):1099–1103, 1999.
- [28] R. Satija, D.L. Jacobson, M. Arif, and S.A. Werner. In situ neutron imaging technique for evaluation of water management systems in operating PEM fuel cells. *Journal of Power Sources*, 129(2):238–245, 2004.

- [29] I. Manke, C. Hartnig, M. Grünerbel, W. Lehnert, N. Kardjilov, A. Haibel, A. Hilger, J. Banhart, and H. Rieseemeier. Investigation of water evolution and transport in fuel cells with high resolution synchrotron x-ray radiography. *Applied Physics Letters*, 90:174105–1–3, 2007.
- [30] C. Hartnig, I. Manke, R. Kuhn, N. Kardjilov, J. Banhart, and W. Lehnert. Cross-sectional insight in the water evolution and transport in polymer electrolyte fuel cells. *Applied Physics Letters*, 92:134106–1–3, 2008.
- [31] M.C. Leverett. Capillary behavior in porous solids. *AIME Transactions*, 142(152):152–169, 1941.
- [32] K.S. Udell. Heat transfer in porous media considering phase change and capillarity—the heat pipe effect. *International Journal of Heat and Mass Transfer*, 28(2):485–495, 1985.
- [33] U. Pasaogullari and C.Y. Wang. Liquid water transport in gas diffusion layer of polymer electrolyte fuel cells. *Journal of the Electrochemical Society*, 151(3):A399–A406, 2004.
- [34] J.H. Nam and M. Kaviany. Effective Diffusivity and Water-saturation Distribution in Single and Two Layer PEMFC Diffusion Medium. *International Journal of Heat and Mass Transfer*, 46(24):4595–4611, 2003.
- [35] M.V. Williams, E. Begg, L. Bonville, H.R. Kunz, and J.M. Fenton. Characterization of gas diffusion layers for PEMFC. *Journal of the Electrochemical Society*, 151(8):A1173–A1180, 2004.
- [36] H.K. Lee, J.H. Park, D.Y. Kim, and T.H. Lee. A study on the characteristics of the diffusion layer thickness and porosity of the PEMFC. *Journal of Power Sources*, 131(1-2):200–206, 2004.
- [37] M. Prasanna, HY Ha, EA Cho, S.A. Hong, and I.H. Oh. Influence of cathode gas diffusion media on the performance of the PEMFCs. *Journal of Power Sources*, 131(1-2):147–154, 2004.
- [38] J.H. Jang, W.M. Yan, and C.C. Shih. Effects of the gas diffusion-layer parameters on cell performance of PEM fuel cells. *Journal of Power Sources*, 161(1):323–332, 2006.

- [39] S. Escribano, J.F. Blachot, J. Etheve, A. Morin, and R. Mosdale. Characterization of PEMFCs gas diffusion layers properties. *Journal of Power Sources*, 156(1):8–13, 2006.
- [40] J.T. Gostick, M.W. Fowler, M.A. Ioannidis, M.D. Pritzker, YM Volkovich, and A. Sakars. Capillary pressure and hydrophilic porosity in gas diffusion layers for polymer electrolyte fuel cells. *Journal of Power Sources*, 156(2):375–387, 2006.
- [41] E.C. Kumbur, K.V. Sharp, and M.M. Mench. Validated Leverett approach for multiphase flow in PEFC diffusion media I. Hydrophobicity effect. *Journal of the Electrochemical Society*, 154(12):B1295–B1304, 2007.
- [42] E.C. Kumbur, K.V. Sharp, and M.M. Mench. Validated Leverett approach for multiphase flow in PEFC diffusion media II. Compression effect. *Journal of the Electrochemical Society*, 154(12):B1305–B1314, 2007.
- [43] E.C. Kumbur, K.V. Sharp, and M.M. Mench. Validated Leverett approach for multiphase flow in PEFC diffusion media III. Temperature effect and unified approach. *Journal of the Electrochemical Society*, 154(12):B1315–B1324, 2007.
- [44] T.V. Nguyen, G. Lin, H. Ohn, and X. Wang. Measurement of Capillary Pressure Property of Gas Diffusion Media Used in Proton Exchange Membrane Fuel Cells. *Electrochemical and Solid-State Letters*, 11(8):B127–B131, 2008.
- [45] A. Bazylak. Liquid water visualization in PEM fuel cells: A review. *International Journal of Hydrogen Energy*, 34(9):3845–3857, 2009.
- [46] S. Tsushima, K. Teranishi, and S. Hirai. Magnetic resonance imaging of the water distribution within a polymer electrolyte membrane in fuel cells. *Electrochemical and Solid-State Letters*, 7:A269–A272, 2004.
- [47] S.J. Lee, N.Y. Lim, S. Kim, G.G. Park, and C.S. Kim. X-ray imaging of water distribution in a polymer electrolyte fuel cell. *Journal of Power Sources*, 185(2):867–870, 2008.
- [48] V. Gurau, M.J. Bluemle, E.S. De Castro, Y.M. Tsou, J.A. Mann, et al. Characterization of transport properties in gas diffusion layers for proton exchange membrane fuel cells:: 1. Wettability (internal contact angle to water and surface energy of GDL fibers). *Journal of Power Sources*, 160(2):1156–1162, 2006.

- [49] S. Litster, D. Sinton, and N. Djilali. Ex situ visualization of liquid water transport in PEM fuel cell gas diffusion layers. *Journal of Power Sources*, 154(1):95–105, 2006.
- [50] A.Z. Weber and J. Newman. Coupled thermal and water management in polymer electrolyte fuel cells. *Journal of the Electrochemical Society*, 153(12):A2205–A2214, 2006.
- [51] T.F. Fuller and J. Newman. Water and Thermal Management in Solid-Polymer-Electrolyte Fuel Cells. *Journal of the Electrochemical Society*, 140(5):1218–1225, 1993.
- [52] T.V. Nguyen and R.E. White. A Water and Heat Management Model for Proton-Exchange-Membrane Fuel Cells. *Journal of the Electrochemical Society*, 140(8):2178–2186, 1993.
- [53] L. Mao and C.Y. Wang. Analysis of cold start in polymer electrolyte fuel cells. *Journal of the Electrochemical Society*, 154(2):B139–B146, 2007.
- [54] A. Nandy, F. Jiang, S. Ge, C.Y. Wang, and K.S. Chen. Effect of Cathode Pore Volume on PEM Fuel Cell Cold Start. *Journal of The Electrochemical Society*, 157(5):B726–B736, 2010.
- [55] B. Fıçıcılar, İ. Eroğlu, and T.V. Nguyen. A Five Layer One-Dimensional PEMFC Model with Detailed Electrode Kinetics. *ECS Transactions*, 33(1):1515–1527, 2010.
- [56] E. Antolini. Formation, microstructural characteristics and stability of carbon supported platinum catalysts for low temperature fuel cells. *Journal of Materials Science*, 38(14):2995–3005, 2003.
- [57] T.V. Nguyen, S. Wiley, and M.V. Nguyen. Effect of catalyst support particle size on pem fuel cell performance. In *Membrane and Electrode Assemblies Session, Fuel Cell Technology: Opportunities and Challenges, Paper No. 83c, AIChE Spring Annual Meeting, New Orleans, Louisiana, USA*, 2002.
- [58] F. Rodriguez-Reinoso. The role of carbon materials in heterogeneous catalysis. *Carbon*, 36(3):159–175, 1998.

- [59] E. Antolini. Formation of carbon-supported PtM alloys for low temperature fuel cells: a review. *Materials Chemistry and Physics*, 78(3):563–573, 2003.
- [60] A.L. Dicks. The role of carbon in fuel cells. *Journal of Power Sources*, 156(2):128–141, 2006.
- [61] T.R. Ralph and M.P. Hogarth. Catalysis for low temperature fuel cells Part I: the cathode challenges. *Platinum Metals Review*, 46(1):3–14, 2002.
- [62] T.R. Ralph and M.P. Hogarth. Catalysis for low temperature fuel cells Part II: the anode challenges. *Platinum Metals Review*, 46(3):117–135, 2002.
- [63] E. Antolini. Carbon supports for low-temperature fuel cell catalysts. *Applied Catalysis B: Environmental*, 88(1-2):1–24, 2009.
- [64] D.J. Guo and H.L. Li. Electrocatalytic oxidation of methanol on Pt modified single-walled carbon nanotubes. *Journal of Power Sources*, 160(1):44–49, 2006.
- [65] J. Lee, J. Kim, and T. Hyeon. Recent progress in the synthesis of porous carbon materials. *Advanced Materials*, 18(16):2073–2094, 2006.
- [66] S.H. Joo, H.I. Lee, D.J. You, K. Kwon, J.H. Kim, Y.S. Choi, M. Kang, J.M. Kim, C. Pak, H. Chang, et al. Ordered mesoporous carbons with controlled particle sizes as catalyst supports for direct methanol fuel cell cathodes. *Carbon*, 46(15):2034–2045, 2008.
- [67] C. Moreno-Castilla and F.J. Maldonado-Hódar. Carbon aerogels for catalysis applications: An overview. *Carbon*, 43(3):455–465, 2005.
- [68] N.M. Rodriguez, A. Chambers, and R.T.K. Baker. Catalytic engineering of carbon nanostructures. *Langmuir*, 11(10):3862–3866, 1995.
- [69] N. Sano and S. Ukita. One-step synthesis of Pt-supported carbon nanohorns for fuel cell electrode by arc plasma in liquid nitrogen. *Materials Chemistry and Physics*, 99(2-3):447–450, 2006.
- [70] M. Sevilla, G. Lota, and A.B. Fuertes. Saccharide-based graphitic carbon nanocoils as supports for PtRu nanoparticles for methanol electrooxidation. *Journal of Power Sources*, 171(2):546–551, 2007.

- [71] Q. Chen, M.C. Granger, T.E. Lister, and G.M. Swain. Morphological and Microstructural Stability of Boron-Doped Diamond Thin Film Electrodes in an Acidic Chloride Medium at High Anodic Current Densities. *Journal of the Electrochemical Society*, 144(11):3806–3812, 1997.
- [72] J. Xu, M.C. Granger, Q. Chen, J.W. Strojek, T.E. Lister, G.M. Swain, and M. Swain. Boron-doped diamond thin-film electrodes. *Analytical Chemistry-Columbus*, 69(19):591–597, 1997.
- [73] P. Gallezot, S. Chaumet, A. Perrard, and P. Isnard. Catalytic Wet Air Oxidation of Acetic Acid on Carbon-Supported Ruthenium Catalysts. *Journal of Catalysis*, 168(1):104–109, 1997.
- [74] S.B. Yoon, K. Sohn, J.Y. Kim, C.H. Shin, J.S. Yu, and T. Hyeon. Fabrication of carbon capsules with hollow macroporous core/mesoporous shell structures. *Advanced Materials*, 14(1):19–21, 2002.
- [75] G. Büchel, K.K. Unger, A. Matsumoto, and K. Tsutsumi. A novel pathway for synthesis of submicrometer-size solid core/mesoporous shell silica spheres. *Advanced Materials*, 10(13):1036–1038, 1998.
- [76] J.S. Yu, G.S. Chai, and S.B. Yoon. HCMS carbon capsule, electrocatalysts for fuel cell supported by HCMS carbon capsule, and method of preparing the same, 2007. US Patent 7,157,402 B2.
- [77] G. Chai, S.B. Yoon, S. Kang, J.H. Choi, Y.E. Sung, Y.S. Ahn, H.S. Kim, and J.S. Yu. Ordered uniform porous carbons as a catalyst support in a direct methanol fuel cell. *Electrochimica Acta*, 50(2-3):823–826, 2004.
- [78] JK Nørskov, J. Rossmeisl, A. Logadottir, L. Lindqvist, J.R. Kitchin, T. Bligaard, and H. Jonsson. Origin of the overpotential for oxygen reduction at a fuel-cell cathode. *J. Phys. Chem. B*, 108(46):17886–17892, 2004.
- [79] MH Shao, T. Huang, P. Liu, J. Zhang, K. Sasaki, MB Vukmirovic, and R.R. Adzic. Palladium Monolayer and Palladium Alloy Electrocatalysts for Oxygen Reduction. *Langmuir*, 22(25):10409–10415, 2006.
- [80] K. Lee, O. Savadogo, A. Ishihara, S. Mitsushima, N. Kamiya, and K. Ota. Methanol-tolerant oxygen reduction electrocatalysts based on Pd-3D transition

metal alloys for direct methanol fuel cells. *Journal of the Electrochemical Society*, 153:A20, 2006.

- [81] K. Kinoshita. Particle size effects for oxygen reduction on highly dispersed platinum in acid electrolytes. *Journal of the Electrochemical Society*, 137(3):845–848, 1990.
- [82] F.J. Nores-Pondal, I.M.J. Vilella, H. Troiani, M. Granada, S.R. de Miguel, O.A. Scelza, and H.R. Corti. Catalytic activity vs. size correlation in platinum catalysts of PEM fuel cells prepared on carbon black by different methods. *International Journal of Hydrogen Energy*, 34(19):8193–8203, 2009.
- [83] M. Kim, J.N. Park, H. Kim, S. Song, and W.H. Lee. The preparation of Pt/C catalysts using various carbon materials for the cathode of PEMFC. *Journal of Power Sources*, 163(1):93–97, 2006.
- [84] C.O. Kappe. Controlled microwave heating in modern organic synthesis. *Angewandte Chemie International Edition*, 43(46):6250–6284, 2004.
- [85] Z. Liu, J.Y. Lee, W. Chen, M. Han, and L.M. Gan. Physical and electrochemical characterizations of microwave-assisted polyol preparation of carbon-supported PtRu nanoparticles. *Langmuir*, 20(1):181–187, 2004.
- [86] Y. Liang, H. Zhang, H. Zhong, X. Zhu, Z. Tian, D. Xu, and B. Yi. Preparation and characterization of carbon-supported PtRuIr catalyst with excellent CO-tolerant performance for proton-exchange membrane fuel cells. *Journal of Catalysis*, 238(2):468–476, 2006.
- [87] A. Bayrakçeken, L. Türker, and İ. Eroğlu. Improvement of carbon dioxide tolerance of PEMFC electrocatalyst by using microwave irradiation technique. *International Journal of Hydrogen Energy*, 33(24):7527–7537, 2008.
- [88] B. Fıçıcılar, A. Bayrakçeken, and İ. Eroğlu. Effect of Pd loading in Pd-Pt bimetallic catalysts doped into hollow core mesoporous shell carbon on performance of proton exchange membrane fuel cells. *Journal of Power Sources*, 193(1):17–23, 2009.

- [89] E. Antolini, L. Giorgi, F. Cardellini, and E. Passalacqua. Physical and morphological characteristics and electrochemical behaviour in PEM fuel cells of PtRu/C catalysts. *Journal of Solid State Electrochemistry*, 5(2):131–140, 2001.
- [90] P. Yu, M. Pemberton, and P. Plasse. PtCo/C cathode catalyst for improved durability in PEMFCs. *Journal of Power Sources*, 144(1):11–20, 2005.
- [91] H.A. Gasteiger, S.S. Kocha, B. Sompalli, and F.T. Wagner. Activity benchmarks and requirements for Pt, Pt-alloy, and non-Pt oxygen reduction catalysts for PEMFCs. *Applied Catalysis B: Environmental*, 56(1-2):9–35, 2005.
- [92] A. Faghri and Y. Zhang. *Transport phenomena in multiphase systems*. Academic Press, 2006.
- [93] V. Gurau, R.V. Edwards, J.A. Mann Jr, and T.A. Zawodzinski. A Look at the Multiphase Mixture Model for PEM Fuel Cell Simulations. *Electrochemical and Solid-State Letters*, 11:B132, 2008.
- [94] C.Y. Wang. Comment on A Look at the Multiphase Mixture Model for PEM Fuel Cell Simulations [Electrochem. Solid-State Lett.,[bold 11], B132 (2008)]. *Electrochemical and Solid-State Letters*, 12:S2, 2009.
- [95] V. Gurau. Response to Comment on A Look at the Multiphase Mixture Model for PEM Fuel Cell Simulations [Electrochem. Solid-State Lett.,[bold 11], B132 (2008)]. *Electrochemical and Solid-State Letters*, 12:S4, 2009.
- [96] C.Y. Wang and P. Cheng. Multiphase flow and heat transfer in porous media. *Advances in Heat Transfer*, 30:93–182, 1997.
- [97] Z.H. Wang, C.Y. Wang, and K.S. Chen. Two-phase flow and transport in the air cathode of proton exchange membrane fuel cells. *Journal of Power Sources*, 94(1):40–50, 2001.
- [98] W. He, J.S. Yi, and T.V. Nguyen. Two-phase flow model of the cathode of PEM fuel cells using interdigitated flow fields. *AIChE Journal*, 46(10):2053–2064, 2000.
- [99] S. Whitaker. *The method of volume averaging*. Kluwer academic publishers, 1999.

- [100] F. Barbir. *PEM fuel cells: Theory and practice*. Academic Press, 2005.
- [101] K.R. Cooper, V. Ramani, J.M. Fenton, and H.R. Kunz. *Experimental methods and data analyses for polymer electrolyte fuel cells*. Scribner Associates Inc., 2005.
- [102] E. Gileadi. *Electrode kinetics for chemists, chemical engineers and materials scientists*. Wiley-VCH, 1993.
- [103] A.J. Bard and L.R. Faulkner. *Electrochemical methods: fundamentals and applications*. John Wiley & Sons, New York, 2001.
- [104] F. Gloaguen, J.M. Leger, and C. Lamy. Electrocatalytic oxidation of methanol on platinum nanoparticles electrodeposited onto porous carbon substrates. *Journal of Applied Electrochemistry*, 27(9):1052–1060, 1997.
- [105] T.R. Ralph, G.A. Hards, J.E. Keating, S.A. Campbell, D.P. Wilkinson, M. Davis, J. St-Pierre, and M.C. Johnson. Low cost electrodes for proton exchange membrane fuel cells. *Journal of the Electrochemical Society*, 144:3845–3857, 1997.
- [106] W. Vogel, L. Lundquist, P. Ross, and P. Stonehart. Reaction pathways and poisons II: The rate controlling step for electrochemical oxidation of hydrogen on Pt in acid and poisoning of the reaction by CO. *Electrochimica Acta*, 20(1):79–93, 1975.
- [107] R. Adžić. Recent advances in the kinetics of oxygen reduction. In J. Lipkowski and P.N. Ross, editors, *Electrocatalysis*, chapter 5, pages 197–242. Vch Verlagsgesellschaft Mbh, 1998.
- [108] R.B. Bird, W.E. Stewart, and E.N. Lightfoot. *Transport phenomena*. John Wiley, 1960.
- [109] R. Taylor and R. Krishna. *Multicomponent mass transfer*. Wiley-Interscience, 1993.
- [110] J.C. Slattery and R.B. Bird. Calculation of the diffusion coefficient of dilute gases and of the self-diffusion coefficient of dense gases. *AIChE Journal*, 4(2):137–142, 1958.

- [111] DAG Bruggeman. Berechnung verschiedener physikalischer Konstanten von heterogenen Substanzen. I. Dielektrizitätskonstanten und Leitfähigkeiten der Mischkörper aus isotropen Substanzen. *Annalen der Physik*, 416(7):636–664, 1935.
- [112] Q. Ye and T.V. Nguyen. Three-dimensional simulation of liquid water distribution in a PEMFC with experimentally measured capillary functions. *Journal of the Electrochemical Society*, 154(12):B1242–B1251, 2007.
- [113] P.K. Sinha, C.Y. Wang, and E.E. Center. Probing Effects of GDL Microstructure on Liquid Water Transport by Pore Network Modeling. *ECS Transactions*, 3:387–396, 2006.
- [114] U. Pasaogullari and C.Y. Wang. Two-phase transport and the role of microporous layer in polymer electrolyte fuel cells. *Electrochimica Acta*, 49(25):4359–4369, 2004.
- [115] U. Paşaoğulları. *Two-phase transport and prediction of flooding in polymer electrolyte fuel cells*. PhD thesis, The Pennsylvania State University, 2005.
- [116] Ç. Kumbur. *Fundamental characterization of multi-phase transport in thin-film fuel cell diffusion media*. PhD thesis, The Pennsylvania State University, 2007.
- [117] J.S. Newman and K.E. Thomas-Alyea. *Electrochemical systems*. Wiley-Interscience, 2004.
- [118] A.Z. Weber. *Modeling water management in polymer-electrolyte fuel cells*. PhD thesis, University of California, Berkeley, 2004.
- [119] L. You and H. Liu. A two-phase flow and transport model for PEM fuel cells. *Journal of Power Sources*, 155(2):219–230, 2006.
- [120] X. Wang and T.V. Nguyen. Modeling the Effects of the Microporous Layer on the Net Water Transport Rate Across the Membrane in a PEM Fuel Cell. *Journal of the Electrochemical Society*, 157(4):B496–B505, 2010.
- [121] J.T. Wang and R.F. Savinell. Simulation studies on the fuel electrode of a H₂—O₂ polymer electrolyte fuel cell. *Electrochimica Acta*, 37(15):2737–2745, 1992.
- [122] S. Motupally, A.J. Becker, and J.W. Weidner. Diffusion of water in Nafion 115 membranes. *Journal of the Electrochemical Society*, 147(9):3171–3177, 2000.

- [123] S.J. Paddison and K.S. Promislow. *Device and materials modeling in PEM fuel cells*. Springer, 2009.
- [124] A.Z. Weber and J. Newman. Transport in polymer-electrolyte membranes I. Physical model. *Journal of the Electrochemical Society*, 150(7):A1008–A1015, 2003.
- [125] D. Spornjak. *Experimental characterization of water transport in polymer electrolyte membrane fuel cells*. PhD thesis, University of Delaware, 2010.
- [126] T.A. Zawodzinski Jr, M. Neeman, L.O. Sillerud, and S. Gottesfeld. Determination of water diffusion coefficients in perfluorosulfonate ionomeric membranes. *The Journal of Physical Chemistry*, 95(15):6040–6044, 1991.
- [127] R.F. Mann, J.C. Amphlett, B.A. Peppley, and C.P. Thurgood. Application of Butler-Volmer equations in the modelling of activation polarization for PEM fuel cells. *Journal of Power Sources*, 161(2):775–781, 2006.
- [128] T. Berning and N. Djilali. Three Dimensional Numerical Analysis of Fluid Flow, Heat and Mass Transfer in Fuel Cells. *Journal of Power Sources*, 106:284–294, 2002.
- [129] H. Ju, C.Y. Wang, S. Cleghorn, and U. Beuscher. Nonisothermal Modeling of Polymer Electrolyte Fuel Cells I. Experimental Validation. *Journal of The Electrochemical Society*, 152(8):A1645–A1653, 2005.
- [130] T. Zhou and H. Liu. A 3D model for PEM fuel cells operated on reformat. *Journal of Power Sources*, 138(1-2):101–110, 2004.
- [131] T.E. Springer, T. Rockward, T.A. Zawodzinski, and S. Gottesfeld. Model for Polymer Electrolyte Fuel Cell Operation on Reformate Feed: Effects of CO, H Dilution, and High Fuel Utilization. *Journal of The Electrochemical Society*, 148:A11–A23, 2001.
- [132] A. Parthasarathy, B. Davé, S. Srinivasan, A.J. Appleby, and C.R. Martin. The platinum microelectrode/Nafion interface: an electrochemical impedance spectroscopic analysis of oxygen reduction kinetics and Nafion characteristics. *Journal of the Electrochemical Society*, 139(6):1634–1641, 1992.

- [133] T. Berning. *Three-dimensional computational analysis of transport phenomena in a PEM fuel cell*. PhD thesis, University of Victoria, 2002.
- [134] G. Lin, W. He, and T.V. Nguyen. Modeling liquid water effects in the gas diffusion and catalyst layers of the cathode of a PEM fuel cell. *Journal of the Electrochemical Society*, 151(12):A1999–A2006, 2004.
- [135] E. Yeager. Electrocatalysts for O₂ reduction. *Electrochimica Acta*, 29(11):1527–1537, 1984.
- [136] J.S. Griffith. On the magnetic properties of some haemoglobin complexes. *Proceedings of the Royal Society of London. Series A. Mathematical and Physical Sciences*, 235(1200):23, 1956.
- [137] MR Tarasevich, A. Sadkowski, and E. Yeager. Comprehensive treatise of electrochemistry. *Plenum Press, New York*, 7:301, 1983.
- [138] H. Li, G. Sun, N. Li, S. Sun, D. Su, and Q. Xin. Design and preparation of highly active Pt-Pd/C catalyst for the oxygen reduction reaction. *The Journal of Physical Chemistry C*, 111(15):5605–5617, 2007.
- [139] G. Doğu. Diffusion limitations for reactions in porous catalysts. In N.P. Cheremisinoff, editor, *Handbook of Heat and Mass Transfer Volume:2 Mass Transfer and Reactor Design*, chapter 8, pages 433–484. Gulf Publishing, 1986.
- [140] J.O.M. Bockris and A.K.N. Reddy. *Modern electrochemistry*. Springer Us, 2000.
- [141] J.J. Baschuk and X. Li. Modelling of polymer electrolyte membrane fuel cells with variable degrees of water flooding. *Journal of Power Sources*, 86(1-2):181–196, 2000.
- [142] X. Wang. *Experimental and Modeling Studies of Two-Phase Flow in Porous Media and Its Effects on the Performance of a PEM Fuel Cell*. PhD thesis, University of Kansas, 2010.
- [143] G. Lin and T.V. Nguyen. A two-dimensional two-phase model of a PEM fuel cell. *Journal of the Electrochemical Society*, 153(2):A372–A382, 2006.

- [144] X. Wang and T.V. Nguyen. Modeling the Effects of Capillary Property of Porous Media on the Performance of the Cathode of a PEMFC. *Journal of the Electrochemical Society*, 155(11):B1085–B1092, 2008.
- [145] R.E. White. On Newman’s numerical technique for solving boundary value problems. *Industrial & Engineering Chemistry Fundamentals*, 17(4):367–369, 1978.
- [146] T.V. Nguyen and R.E. White. A finite difference procedure for solving coupled, nonlinear elliptic partial differential equations. *Computers & Chemical Engineering*, 11(5):543–546, 1987.
- [147] S.V. Patankar. *Numerical heat transfer and fluid flow*. Hemisphere Pub, 1980.
- [148] J.H. Ferziger and M. Perić. *Computational methods for fluid dynamics*. Springer-Verlag, 2002.
- [149] H.K. Versteeg and W. Malalasekera. *An introduction to computational fluid dynamics: the finite volume method*. Prentice Hall, 2007.
- [150] H. Karema and S. Lo. Efficiency of interphase coupling algorithms in fluidized bed conditions. *Computers & Fluids*, 28(3):323–360, 1999.
- [151] W. Stöber, A. Fink, and E. Bohn. Controlled growth of monodisperse silica spheres in the micron size range. *Journal of Colloid and Interface Science*, 26(1):62–69, 1968.
- [152] A. Van Blaaderen, J. Van Geest, and A. Vrij. Monodisperse colloidal silica spheres from tetraalkoxysilanes: particle formation and growth mechanism. *Journal of Colloid and Interface Science*, 154(2):481–501, 1992.
- [153] B. Güvenatam. Development of different carbon supports for proton exchange membrane fuel cell electrocatalysts. Master’s thesis, Middle East Technical University, Ankara, Turkey, 2010.
- [154] A. Bayrakçeken. *Platinum and platinum–ruthenium based catalysts on various carbon supports prepared by different methods for PEM fuel cell applications*. PhD thesis, Middle East Technical University, Ankara, Turkey, 2008.

- [155] P. Brault, A. Caillard, AL Thomann, J. Mathias, C. Charles, RW Boswell, S. Escibano, J. Durand, and T. Sauvage. Plasma sputtering deposition of platinum into porous fuel cell electrodes. *Journal of Physics D Applied Physics*, 37(24):3419–3423, 2004.
- [156] F.E.M. O'brien. The control of humidity by saturated salt solutions. *Journal of Scientific Instruments*, 25:73–76, 1948.
- [157] A. Bayrakçeken, A. Smirnova, U. Kitkamthorn, M. Aindow, L. Türker, İ. Eroğlu, and C. Erkey. Vulcan-Supported Pt Electrocatalysts for PEMFCs Prepared using Supercritical Carbon Dioxide Deposition. *Chemical Engineering Communications*, 196(1):194–203, 2009.
- [158] E.S. Şayin. Parameters influencing long term performance and durability of PEM fuel cells. Master's thesis, Middle East Technical University, Ankara, Turkey, 2011.
- [159] N. Rajalakshmi, H. Ryu, M.M. Shaijumon, and S. Ramaprabhu. Performance of polymer electrolyte membrane fuel cells with carbon nanotubes as oxygen reduction catalyst support material. *Journal of Power Sources*, 140(2):250–257, 2005.
- [160] J. Zhang, Z. Xie, J. Zhang, Y. Tang, C. Song, T. Navessin, Z. Shi, D. Song, H. Wang, D.P. Wilkinson, et al. High temperature PEM fuel cells. *Journal of power sources*, 160(2):872–891, 2006.
- [161] J. Jiang, T.D. Hall, L. Tsagalas, D.A. Hill, and A.E. Miller. Photographic production of metal nano-particles for fuel cell electrodes. *Journal of Power Sources*, 162(2):977–984, 2006.
- [162] A. Bayrakçeken, A. Smirnova, U. Kitkamthorn, M. Aindow, L. Türker, İ. Eroğlu, and C. Erkey. Pt-based electrocatalysts for polymer electrolyte membrane fuel cells prepared by supercritical deposition technique. *Journal of Power Sources*, 179(2):532–540, 2008.
- [163] A. Bayrakçeken, S. Erkan, L. Türker, and İ. Eroğlu. Effects of membrane electrode assembly components on proton exchange membrane fuel cell performance. *International Journal of Hydrogen Energy*, 33(1):165–170, 2008.

- [164] M. Kim, S.B. Yoon, K. Sohn, J.Y. Kim, C.H. Shin, T. Hyeon, and J.S. Yu. Synthesis and characterization of spherical carbon and polymer capsules with hollow macroporous core and mesoporous shell structures. *Microporous and Mesoporous Materials*, 63(1-3):1–9, 2003.
- [165] P.L. Antonucci, V. Alderucci, N. Giordano, D.L. Cocco, and H. Kim. On the role of surface functional groups in Pt carbon interaction. *Journal of Applied Electrochemistry*, 24(1):58–65, 1994.
- [166] J. Wang, G. Yin, Y. Shao, S. Zhang, Z. Wang, and Y. Gao. Effect of carbon black support corrosion on the durability of Pt/C catalyst. *Journal of Power Sources*, 171(2):331–339, 2007.
- [167] Y. Xu and X. Lin. Facile fabrication and electrocatalytic activity of Pt_{0.9}Pd_{0.1} alloy film catalysts. *Journal of Power Sources*, 170(1):13–19, 2007.
- [168] O.A. Baturina, S.R. Aubuchon, and K.J. Wynne. Thermal stability in air of Pt/C catalysts and PEM fuel cell catalyst layers. *Chem. Mater*, 18(6):1498–1504, 2006.
- [169] S.B. Yoon, J.Y. Kim, J.H. Kim, Y.J. Park, K.R. Yoon, S.K. Park, and J.S. Yu. Synthesis of monodisperse spherical silica particles with solid core and mesoporous shell: mesopore channels perpendicular to the surface. *Journal of Materials Chemistry*, 17(18):1758–1761, 2007.
- [170] G. Ketteler, D.F. Ogletree, H. Bluhm, H. Liu, E.L.D. Hebenstreit, and M. Salmeron. In situ spectroscopic study of the oxidation and reduction of Pd (111). *The Journal of the American Chemical Society*, 127(51):18269–18273, 2005.
- [171] D.P. DeWitt and F.P. Incropera. *Fundamentals of heat and mass transfer*. John Wiley and Sons, 2002.
- [172] R.H. Perry and D.W. Green. *Perry's chemical engineers' handbook*. McGraw-Hill Professional, 2007.
- [173] K. Levenberg. A method for the solution of certain nonlinear problems in least squares. *Quarterly of Applied Mathematics*, 2(2):164–168, 1944.

- [174] D.W. Marquardt. An algorithm for least-squares estimation of nonlinear parameters. *Journal of the Society for Industrial and Applied Mathematics*, 11(2):431–441, 1963.
- [175] T.A. Zawodzinski Jr, C. Derouin, S. Radzinski, R.J. Sherman, V.T. Smith, T.E. Springer, and S. Gottesfeld. Water uptake by and transport through Nafion 117 membranes. *Journal of the Electrochemical Society*, 140(4):1041–1047, 1993.
- [176] B. Fıçıcılar. Carbon dioxide removal in steam reforming: Adsorption of CO₂ onto hydrotalcite and activated soda. Master’s thesis, Middle East Technical University, Ankara, Turkey, 2004.
- [177] B. Fıçıcılar, A. Bayrakçeken, and İ. Eroğlu. Pt incorporated hollow core mesoporous shell carbon nanocomposite catalyst for proton exchange membrane fuel cells. *International Journal of Hydrogen Energy*, 35(18):9924–9933, 2010.

APPENDIX A

PROPERTIES AND CORRELATIONS FOR THE PEMFC MODEL

A.1 Physical Properties of Water

At moderate temperatures of operation, it is assumed that liquid water is produced at the cathode catalyst layer. For the estimation of capillary transport mechanism of liquid water throughout the fuel cell system, the following correlations were used for surface tension, density, and viscosity of water as function of temperature. The pressure dependence is not considered significant for the range of operating conditions [171].

Table A.1: Physical properties of water

Property	Symbol	Correlation ^a	Units
Water surface tension	σ_w	$0.12398 - 1.7393 \times 10^{-3} \times T_s$	N/m
Water density	ρ_w	$1.1603 - 5.371 \times 10^{-3} \times T_s$	g/cm ³
Water viscosity	μ_w	$1 \times 10^{-11} (2695.3 - 6.6T_s)$	bar s

^a Solid phase temperature, T_s , is in Kelvin

A.2 Water Vapor Saturation Pressure

An empirical equation (4.11) was fit from the experimental data shown in Figure A.1 for the formulation of temperature dependence of water saturation pressure. For this purpose, a large set of experimental data was used for the fit from an engineering handbook [172]. Equation fit was performed with the open source Gnuplot software

using the Levenberg-Marquardt algorithm [173, 174].

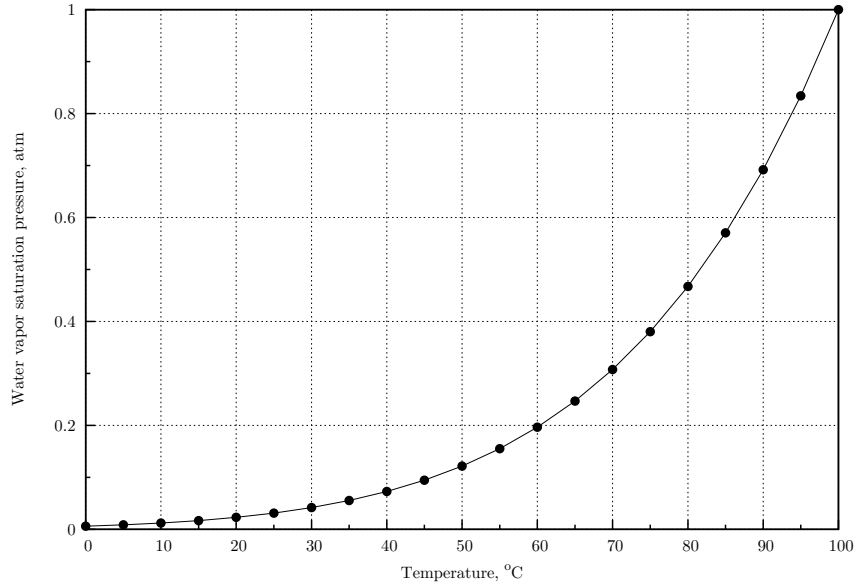


Figure A.1: Saturation pressure of water vapor at low temperatures

A.3 Capillary Pressure Measurement

To capture realistic liquid water transport behavior within the porous media, experimental data is required to relate the variation of liquid phase saturation with capillary pressure. One of the major techniques used in the measurement of capillary pressure data is gravimetric method, in which water is forced through pores by the gravitational force. Pressure data are recorded to detect capillary pressure created by water displacement. Figure A.2 represents a typical capillary pressure variation for different materials of choice [144].

Shape of the capillary pressure curve does depend on the structural properties and wetting properties of the material. The span in the capillary pressure curves (Figure A.2) explain the reason why higher phase saturation levels are observed in the catalyst layers and microporous layers as compared to gas diffusion layer. Microporosity and hydrophobicity in MPL and CL increase the liquid phase saturation. Base case model fitting parameters for these capillary pressure data are tabulated in section 4.5.

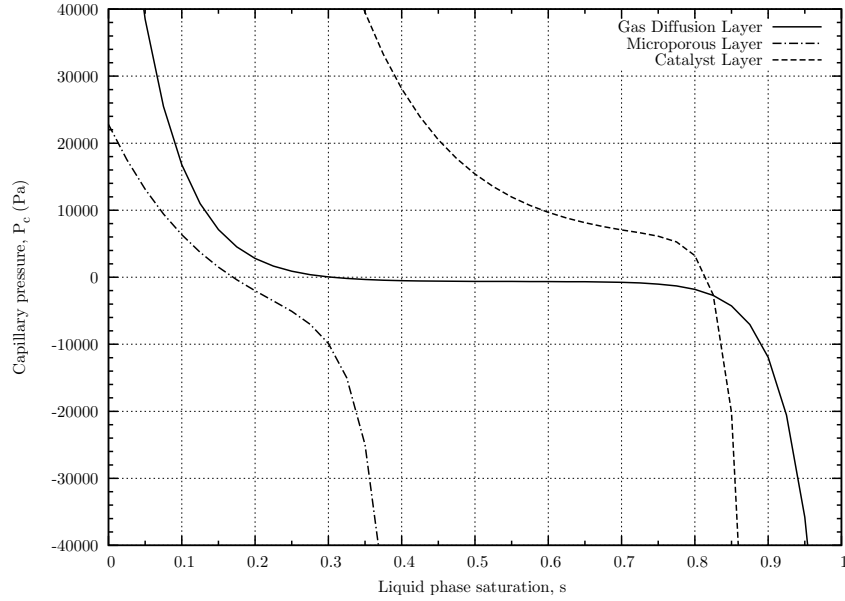


Figure A.2: Capillary pressure variation with respect to liquid phase saturation level for different components at ambient temperature

A.4 Water Uptake of the Electrolyte

In order to estimate ionic conductivity, water diffusion coefficient within the solid polymer electrolyte, it is critical to have data for water uptake of the electrolyte for various temperature. Generally, an historical data published previously have been used for the electrolyte water content estimation [21]. Figure A.3 shows the variation of membrane water content as function water activity at 30 °C.

Although membrane water uptake curve presented in Figure A.3 is for 30 °C, it was assumed that the water uptake curve empirical correlation given in equation (4.30) could be used at higher operating temperatures.

A.5 Proton Exchange Membrane Ionic Conductivity

Ionic conductivity data for the solid polymer electrolyte is critical for the computation of variable profiles within the membrane. Below Figure A.4 shows the variation of ionic conductivity of Nafion[®] 117 membrane for different hydration states at 30 °C [175].

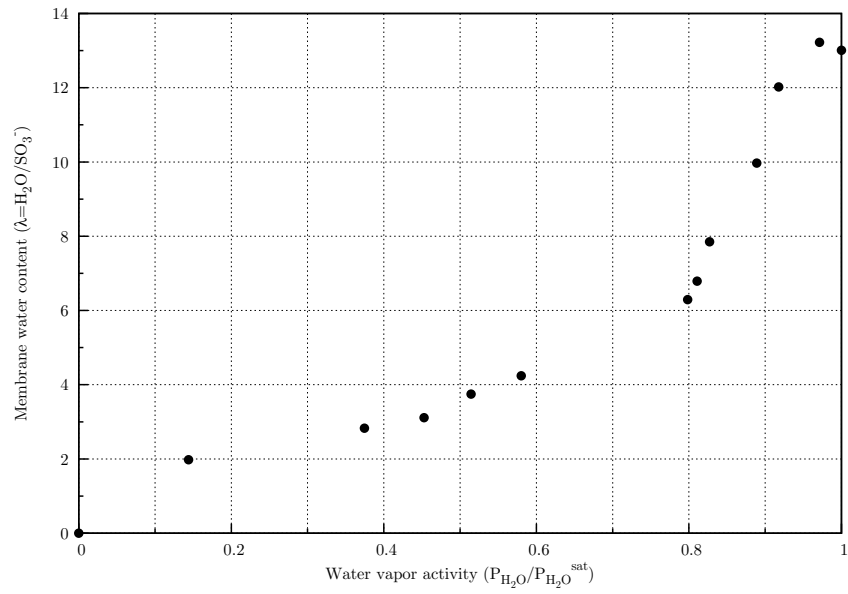


Figure A.3: Water content of Nafion[®] 117 membrane as function of water activity at 30 °C

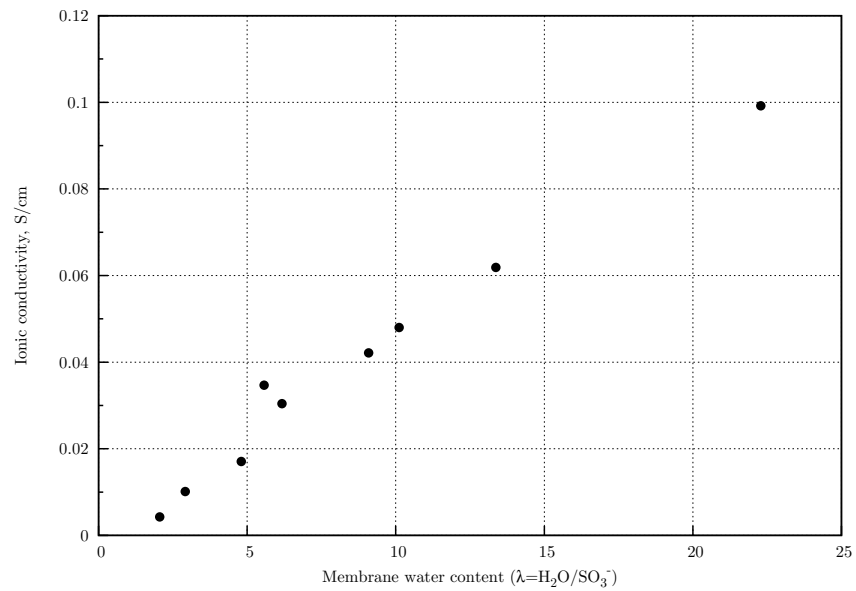


Figure A.4: Ionic conductivity of Nafion[®] 117 membrane as function of water content at 30 °C

Since most of the ohmic potential loss is due to the electrolyte, accurate prediction of the ionic conductivity inside the electrolyte is important. There is still a need for the measurement of ionic conductivity of various candidate electrolytes as function of humidity and temperature with the use of novel experimental methods (see section 6.5).

APPENDIX B

ELECTROCHEMICAL REACTION MECHANISMS

B.1 Oxygen Reduction Reaction Mechanism

In the proposed reaction mechanism, 4.46a considered to be the rate determining step. The following reaction rate can be written for a reversible reaction:

$$r = k_{1f}[O_2][s] - k_{1b}[O_2 \cdot s] \quad (\text{B.1})$$

One can define the total site available in terms of vacant site and oxygen adsorbed at reaction and equilibrium conditions respectively as follows:

$$S_t = [s] + [O_2 \cdot s] \quad (\text{B.2})$$

$$S_t = [s]_o + [O_2 \cdot s]_o \quad (\text{B.3})$$

We can define $\theta = [O_2 \cdot s]/S_t$ and $[s]/S_t = (1 - \theta)$ as oxygen surface coverage and available vacant sites at reaction conditions. Similarly, one can define $\theta_o = [O_2 \cdot s]_o/S_t$ and $[s]_o/S_t = (1 - \theta_o)$ at the equilibrium conditions. Using the Faraday's law, we can rewrite rate expression in terms of current density:

$$i = nF(k_{1f}[O_2][s] - k_{1b}[O_2 \cdot s]) \quad (\text{B.4})$$

At the equilibrium, forward and backward rate are assumed to be equal and they are equal to the initial rate constant, which is defined as the exchange current density:

$$i_o = nFk_{1f}[O_2]_o[s]_o \quad (\text{B.5a})$$

$$i_o = nFk_{1b}[O_2 \cdot s]_o \quad (\text{B.5b})$$

Substituting forward and backward rate in terms of exchange current density and equilibrium concentrations:

$$i = nF \left(\frac{i_o}{nF[O_2]_o[s]_o} [O_2][s] - \frac{i_o}{nF[O_2 \cdot s]_o} [O_2 \cdot s] \right) \quad (B.6)$$

Rearranging the terms;

$$i = i_o \left[\left(\frac{[O_2]}{[O_2]_o} \right) \frac{[s]}{[s]_o} - \frac{[O_2 \cdot s]}{[O_2 \cdot s]_o} \right] \quad (B.7)$$

Rewriting the current rate in terms of oxygen coverage, the rate equation reads:

$$i = i_o \left[\left(\frac{[O_2]}{[O_2]_o} \right) \frac{(1 - \theta)}{(1 - \theta_o)} - \frac{\theta}{\theta_o} \right] \quad (B.8)$$

In order to be able to use equation B.8, oxygen coverage at the reaction condition should be expressed in terms of equilibrium oxygen coverage. Since Adsorption is the rate determining step for ORR, one can think of the other reactions are in quasi equilibrium. Using reaction 4.46b, we can write the electrode potential and equilibrium potential with respect to a reference state as follows:

$$E_2 = E_2^o - \frac{RT}{F} \ln \frac{[O_2H \cdot s]}{[O_2 \cdot s][H^+]} \quad (B.9a)$$

$$E_2^{eq} = E_2^o - \frac{RT}{F} \ln \frac{[O_2H \cdot s]_o}{[O_2 \cdot s]_o[H^+]_o} \quad (B.9b)$$

By definition of the overpotential and the difference between two electrode reactions relates the overpotential to intermediates as follows:

$$e^{-\frac{F}{RT}\eta_2} = \ln \left(\frac{[O_2H \cdot s]}{[O_2 \cdot s][H^+]} \frac{1}{K_2} \right) \quad (B.10)$$

where overpotential and equilibrium constants are defined as:

$$\eta_2 = E_2 - E_2^{eq} \quad (B.11a)$$

$$K_2 = \frac{[O_2H \cdot s]_o}{[O_2 \cdot s]_o[H^+]_o} \quad (B.11b)$$

Solving for the $[O_2H \cdot s]$ reads:

$$[O_2H \cdot s] = K_2 [O_2 \cdot s][H^+] e^{-\frac{F}{RT}\eta_2} \quad (B.12)$$

In a similar way, for reaction 4.46c we can write the intermediate concentration as follows:

$$[O_2H \cdot s]^- = K_3[O_2H \cdot s]e^{-\frac{F}{RT}\eta_3} \quad (\text{B.13})$$

In the reaction mechanism, reaction 4.46d is in a quasi equilibrium since we assumed that the first reaction is rate determining. The following is considered to hold near OHP:

$$[O_2H_2 \cdot s] = K_4[O_2H \cdot s]^- [H^+] \quad (\text{B.14})$$

Reformation of the intermediate molecule by bond breaking, the following holds for reaction 4.46e:

$$[OHOH \cdot s] = K_5[O_2H_2 \cdot s] \quad (\text{B.15})$$

In the final reaction in the pathway, it is expected a fast electronation and protonation as follows:

$$[s][OH_2]^2 = K_6[OHOH \cdot s][H^+]^2 e^{-\frac{2F}{RT}\eta_6} \quad (\text{B.16})$$

Now, one can back substitute the concentration for the last 5 reactions to obtain an expression in terms of vacant sites:

$$[s][OH_2]^2 = K_2K_3K_4K_5K_6[O_2 \cdot s][H^+]^2 e^{-\frac{F}{RT}(\eta_2+\eta_3+2\eta_6)} \quad (\text{B.17})$$

Solving for the adsorbed oxygen reads:

$$\theta = \frac{[OH_2]^2}{1 + K[H^+]^4 e^{-\frac{F}{RT}(\eta_2+\eta_3+2\eta_6)}} \quad (\text{B.18})$$

where overall equilibrium constant and vacant site coverage are defined as:

$$K = K_2K_3K_4K_5K_6 \quad (\text{B.19a})$$

$$[s]/S_t = (1 - \theta) \quad (\text{B.19b})$$

The expression for the adsorbed oxygen coverage in equation can now be replaced. For unity activity of protons and water the current rate turns out as follows:

$$i = i_o \frac{K \left[\left(\frac{C_{O_2}}{C_{O_2}^o} \right) \frac{\theta_o}{1-\theta_o} - 1 \right] e^{-\frac{F}{RT}(\eta_2+\eta_3+2\eta_6)}}{\theta_o \left(1 + K e^{-\frac{F}{RT}(\eta_2+\eta_3+2\eta_6)} \right)} \quad (\text{B.20})$$

if we rewrite in terms of single overpotential η the final form of the rate would be :

$$i = i_o \frac{\left[\left(\frac{C_{O_2}}{C_{O_2}^o} \right) \frac{\theta_o}{1-\theta_o} - 1 \right] e^{-\frac{F}{RT}\eta}}{\theta_o \left(\frac{1}{K} + e^{-\frac{F}{RT}\eta} \right)} \quad (\text{B.21})$$

In order to see the limits of the rate we can think two limiting cases. If K is too large compared to the potential driving force in the denominator the rate turns out to be:

$$i = i_o \left[\left(\frac{C_{O_2}}{C_{O_2}^o} \right) \frac{1}{1-\theta_o} - \frac{1}{\theta_o} \right] \quad (\text{B.22})$$

If K is too small compared to the potential term, then the following rate expression is obtained:

$$i = \frac{i_o K}{\theta_o} \left[\left(\frac{C_{O_2}}{C_{O_2}^o} \right) \frac{\theta_o}{1-\theta_o} - 1 \right] e^{-\frac{F}{RT}\eta} \quad (\text{B.23})$$

B.2 Hydrogen Oxidation Reaction Mechanism

Reaction rate can be written using (4.37a) as :

$$r = k_{1f}[H_2][s]^2 - k_{1b}[H \cdot s]^2 \quad (\text{B.24})$$

Where k_{1f} and k_{1b} are the forward and backward rate constants for the Tafel reaction respectively. In the reaction and rate expression s is illustrating the available site for

the reaction. In this case particularly it can be considered as the active Platinum sites at any time during the course of the reaction. In order to convert the rate expression into current density, the following Faraday's law can be introduced:

$$r = \frac{i}{nF} \quad (\text{B.25})$$

From B.24 and B.25, rate is rewritten in terms of current density as:

$$i = nF (k_{1f}[H_2][s]^2 - k_{1b}[H \cdot s]^2) \quad (\text{B.26})$$

If S_t is denoting the total active site when there is no hydrogen adsorption over the surface, the following relation holds for the reaction mechanism:

$$S_t = [s] + [H \cdot s] \quad (\text{B.27})$$

Where $[s]$ is the total vacant site at any time and $[H \cdot s]$ is the total site covered by hydrogen. Same relation could be written at the equilibrium conditions as follows:

$$S_t = [s]_o + [H \cdot s]_o \quad (\text{B.28})$$

Similarly, these are the vacant site and used hydrogen site at the equilibrium. Since equilibrium surface coverage is an experimentally detectable parameter, the idea is to express the rate in terms of measurable quantities. At the equilibrium conditions, rate is equal to zero. In other words, forward and backward rates are equal and following relation can be written for equilibrium current density or exchange current density:

$$i_o = nFk_{1f}[H_2]_o[s]_o^2 \quad (\text{B.29a})$$

$$i_o = nFk_{1b}[H \cdot s]_o^2 \quad (\text{B.29b})$$

Using B.29a and B.29b forward and backward rates are substituted into B.26:

$$i = nF \left(\frac{i_o}{nF[H_2]_o[s]_o^2} [H_2][s]^2 - \frac{i_o}{nF[H \cdot s]_o^2} [H \cdot s]^2 \right) \quad (\text{B.30})$$

If we simplify B.30 and introduce B.27 and B.28 for expressing the equation in terms of adsorbed hydrogen sites:

$$i = i_o \left[\left(\frac{[H_2]}{[H_2]_o} \right) \frac{(S_t - [H \cdot s])^2}{(S_t - [H \cdot s]_o)^2} - \frac{[H \cdot s]^2}{[H \cdot s]_o^2} \right] \quad (\text{B.31})$$

Another way to express the hydrogen adsorbed sites is to express them in terms of fractional hydrogen coverage. The following equation can be written for the fractional surface coverage:

$$\theta + \frac{s}{S_t} = 1 \quad (\text{B.32})$$

where θ indicates the fractional hydrogen coverage of the surface at any time and θ_o is the same parameter described at the equilibrium conditions. Rewriting B.31 in terms of fractional coverage, the following equation is obtained:

$$i = i_o \left[\left(\frac{[H_2]}{[H_2]_o} \right) \frac{(1 - \theta)^2}{(1 - \theta_o)^2} - \frac{\theta^2}{\theta_o^2} \right] \quad (\text{B.33})$$

Electrode potential for the Volmer reaction (4.37b) can be defined as follows:

$$E = E^o + \frac{RT}{2F} \ln \frac{[s]^2 [H^+]^2}{[H \cdot s]^2} \quad (\text{B.34})$$

Electrode potential can be defined similarly at the equilibrium condition by using the equilibrium concentrations:

$$E^{eq} = E^o + \frac{RT}{2F} \ln \frac{[s]_o^2 [H^+]_o^2}{[H \cdot s]_o^2} \quad (\text{B.35})$$

The potential difference between the electrode and equilibrium potential is so called overpotential and defines as follows:

$$\eta = E - E^{eq} \quad (\text{B.36})$$

Considering unity proton concentration and using the definition of overpotential, the following equation can be written to relate overpotential to hydrogen coverage and vacant sites.

$$e^{\frac{F}{RT}\eta} = \frac{[s] [H \cdot s]_o}{[s]_o [H \cdot s]} \quad (\text{B.37})$$

Using the total site definitions and converting to fractional hydrogen coverage, the following form of the equation is obtained:

$$e^{\frac{F}{RT}\eta} = \frac{1 - \theta}{1 - \theta_o} \frac{\theta_o}{\theta} \quad (\text{B.38})$$

Solving for θ the following equation reads:

$$\theta = \frac{\theta_o}{\theta_o + (1 - \theta_o) e^{\frac{F}{RT}\eta}} \quad (\text{B.39})$$

Now, we have an expression for adsorbed hydrogen in terms of overpotential and equilibrium hydrogen surface coverage. Substituting this relation into B.33, we get the following final form of rate in terms of measurable quantities:

$$i = i_o \left[\left(\frac{[H_2]}{[H_2]_o} \right) e^{\frac{2F}{RT}\eta} - 1 \right] \left(\frac{1}{\theta_o + (1 - \theta_o)e^{\frac{F}{RT}\eta}} \right) \quad (\text{B.40})$$

APPENDIX C

ELECTROCATALYST SYNTHESIS ROUTE

Figure C.1 depicts the procedure for electrocatalyst synthesis and characterization. First, solid core mesoporous shell silica was synthesized. Second, with the use of alternative carbon precursors, hollow core mesoporous shell carbon spheres were produced. After that, electrocatalysts were synthesized by microwave irradiation method under different synthesis conditions. Various *ex situ* and *in situ* characterization methods were employed to gain structural and electrochemical information on the novel electrocatalysts.

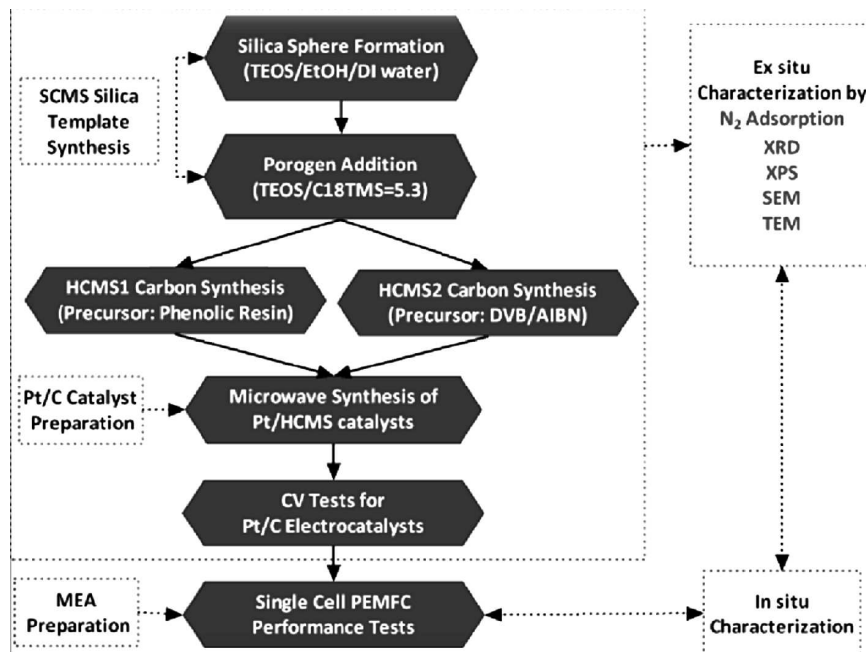


Figure C.1: PEM fuel cell electrocatalyst synthesis and characterization route

APPENDIX D

EXPERIMENTAL DATA FOR PEM FUEL CELL TESTS

Polymer electrolyte membrane fuel cell tests were conducted with a home-made test station. A commercial fuel cell test fixture (Electrochem[®], FC05-01 SP REF) was used for recording the polarization data with potentiostatic measurement technique. Flow field architecture of the composite graphite plate was serpentine type. Active area of the test cell hardware was 5 cm².

Membrane electrode assembly (MEA) was composed of Nafion[®] 112 solid polymer electrolyte, Sigracet[®] SGL 30 BC diffusion media (kept same for anode and cathode), and a catalyst layer. Catalyst layer was produced on top of the microporous layer of the diffusion media by spraying method as described in the experimental section. Only catalyst layers on anode and cathode were altered and tested for various electrocatalysts.

Test cell was heated up to the test temperature with the aid of the heaters attached to gold-coated copper plates. Flow rates were adjusted to 100 cm³/min for both hydrogen (fuel) and oxygen (oxidant) with the use of mass flow controllers. Fuel cell temperature was set to 70 °C and atmospheric pressure for all runs. Temperature of the humidifier chambers were adjusted to 70 °C to supply a saturated gas stream at both electrodes (e.g. RH=100% at anode and cathode).

All lines prior to the fuel cell was heated to feed a saturated gas stream at the anode and cathode. After operating the fuel cell several hours at 0.6 V and 0.4 V, steady state potentiostatic measurements were recorded in 5 min. intervals.

Table D.1: Experimental H₂/O₂ PEM fuel cell test data for the polarization curve (Anode catalyst: 20% Pt/C (EOTEK[®]), Cathode catalyst: 20% Pt/HCMS1, T=70 °C, P=1 atm, RH_a=100%, RH_c=100%, H₂ Flow Rate = 100 cm³/min, O₂ Flow Rate = 100 cm³/min)

Current Density (mA/cm ²)	Potential (V)	Power Density (W/cm ²)
0.0	0.95	0.000
5.7	0.89	0.005
22.2	0.84	0.019
52.6	0.79	0.042
93.0	0.74	0.069
129.9	0.70	0.091
180.0	0.65	0.117
233.3	0.60	0.140
288.4	0.55	0.159
343.8	0.50	0.172
398.4	0.45	0.179
451.3	0.40	0.180
500.7	0.35	0.175
549.7	0.30	0.165
595.9	0.25	0.149
639.9	0.20	0.128

Table D.2: Experimental H₂/O₂ PEM fuel cell test data for the polarization curve (Anode catalyst: 20% Pt/C (EOTEK[®]), Cathode catalyst: 20% Pt/HCMS2, T=70 °C, P=1 atm, RH_a=100%, RH_c=100%, H₂ Flow Rate = 100 cm³/min, O₂ Flow Rate = 100 cm³/min)

Current Density (mA/cm ²)	Potential (V)	Power Density (W/cm ²)
0.0	0.96	0.000
8.4	0.89	0.007
34.5	0.84	0.029
78.2	0.79	0.062
134.0	0.74	0.099
198.0	0.69	0.137
328.8	0.60	0.197
453.5	0.50	0.227
560.1	0.40	0.224
655.3	0.30	0.197
734.7	0.20	0.147

Table D.3: Experimental H₂/O₂ PEM fuel cell test data for the polarization curve (Anode catalyst: 20% Pt/C (E TEK[®]), Cathode catalyst: 20% Pt/VX, T=70 °C, P=1 atm, RH_a=100%, RH_c=100%, H₂ Flow Rate = 100 cm³/min, O₂ Flow Rate = 100 cm³/min)

Current Density (mA/cm ²)	Potential (V)	Power Density (W/cm ²)
0.0	0.93	0.000
6.0	0.89	0.005
29.8	0.84	0.025
86.2	0.79	0.068
273.2	0.69	0.189
474.0	0.59	0.280
660.0	0.49	0.323
836.0	0.40	0.334

Table D.4: Experimental H₂/O₂ PEM fuel cell test data for the polarization curve (Anode catalyst: 20% Pt/C (E TEK[®]), Cathode catalyst: 20% Pt/Regal, T=70 °C, P=1 atm, RH_a=100%, RH_c=100%, H₂ Flow Rate = 100 cm³/min, O₂ Flow Rate = 100 cm³/min)

Current Density (mA/cm ²)	Potential (V)	Power Density (W/cm ²)
0	0.92	0.000
4	0.84	0.003
16	0.80	0.013
74	0.69	0.051
200	0.60	0.120
430	0.50	0.215
606	0.40	0.242
822	0.30	0.247

Table D.5: Experimental H₂/O₂ PEM fuel cell test data for the polarization curve (Anode catalyst: 20% Pt/C (E TEK[®]), Cathode catalyst: 20% Pt/BP2000, T=70 °C, P=1 atm, RH_a=100%, RH_c=100%, H₂ Flow Rate = 100 cm³/min, O₂ Flow Rate = 100 cm³/min)

Current Density (mA/cm ²)	Potential (V)	Power Density (W/cm ²)
0.0	0.88	0.000
2.0	0.84	0.002
6.4	0.80	0.005
18.6	0.74	0.014
38.0	0.69	0.026
100.0	0.60	0.060
186.0	0.50	0.093
310.0	0.40	0.124
586.0	0.30	0.176

Table D.6: Experimental H₂/O₂ PEM fuel cell test data for the polarization curve (Anode catalyst: 20% Pt/C (E TEK[®]), Cathode catalyst: 20% Pt/C (E TEK[®]), T=70 °C, P=1 atm, RH_a=100%, RH_c=100%, H₂ Flow Rate = 100 cm³/min, O₂ Flow Rate = 100 cm³/min)

Current Density (mA/cm ²)	Potential (V)	Power Density (W/cm ²)
0	0.96	0.000
110	0.79	0.087
320	0.69	0.221
524	0.59	0.309
682	0.50	0.341
808	0.40	0.323
912	0.30	0.274
1006	0.20	0.201

Table D.7: Experimental H₂/O₂ PEM fuel cell test data for the polarization curve (Anode catalyst: 20% Pt/C (E TEK[®]), Cathode catalyst: Pt(15)Pd(5)/HCMS1 (E TEK[®]), T=70 °C, P=1 atm, RH_a=100%, RH_c=100%, H₂ Flow Rate = 100 cm³/min, O₂ Flow Rate = 100 cm³/min)

Current Density (mA/cm ²)	Potential (V)	Power Density (W/cm ²)
0.	0.94	0.000
4.5	0.89	0.004
20.4	0.84	0.017
54.4	0.79	0.043
99.8	0.74	0.074
149.7	0.69	0.103
206.4	0.64	0.132
265.3	0.60	0.159
331.1	0.55	0.182
399.1	0.50	0.200
464.9	0.44	0.205
530.6	0.40	0.212
594.1	0.35	0.208
655.3	0.30	0.197
709.8	0.25	0.177
771.0	0.20	0.154
882.1	0.10	0.088

Table D.8: Experimental H₂/O₂ PEM fuel cell test data for the polarization curve (Anode catalyst: 20% Pt/C (E TEK[®]), Cathode catalyst: Pt(10)Pd(10)/HCMS1 (E TEK[®]), T=70 °C, P=1 atm, RH_a=100%, RH_c=100%, H₂ Flow Rate = 100 cm³/min, O₂ Flow Rate = 100 cm³/min)

Current Density (mA/cm ²)	Potential (V)	Power Density (W/cm ²)
0.0	0.89	0.000
3.0	0.85	0.003
6.1	0.80	0.005
15.2	0.75	0.011
33.6	0.70	0.024
61.9	0.65	0.040
100.0	0.60	0.060
137.6	0.55	0.076
193.0	0.50	0.097
264.4	0.45	0.119
342.9	0.40	0.137
402.0	0.35	0.141
430.4	0.30	0.129
480.7	0.25	0.120
524.5	0.20	0.105

Table D.9: Experimental H₂/O₂ PEM fuel cell test data for the polarization curve (Anode catalyst: 20% Pt/C (E TEK[®]), Cathode catalyst: Pt(5)Pd(15)/HCMS1 (E TEK[®]), T=70 °C, P=1 atm, RH_a=100%, RH_c=100%, H₂ Flow Rate = 100 cm³/min, O₂ Flow Rate = 100 cm³/min)

Current Density (mA/cm ²)	Potential (V)	Power Density (W/cm ²)
0.0	0.88	0.000
2.3	0.84	0.002
6.4	0.81	0.005
14.3	0.78	0.011
32.0	0.74	0.024
49.4	0.71	0.035
69.8	0.68	0.048
100.5	0.65	0.065
125.4	0.61	0.077
150.6	0.59	0.089
168.3	0.57	0.096
196.2	0.53	0.104
234.7	0.50	0.117
264.0	0.47	0.124
283.9	0.45	0.128
303.9	0.43	0.131
334.7	0.40	0.134
364.0	0.37	0.135
383.0	0.35	0.134
402.3	0.33	0.133
432.2	0.30	0.130
461.9	0.27	0.125
481.2	0.25	0.120
499.6	0.23	0.115
528.8	0.20	0.106

Table D.10: Experimental H₂/O₂ PEM fuel cell test data for the polarization curve (Anode catalyst: 20% Pt/C (ETEK[®]), Cathode catalyst: 20% Pd/HCMS1 (ETEK[®]), T=70 °C, P=1 atm, RH_a=100%, RH_c=100%, H₂ Flow Rate = 100 cm³/min, O₂ Flow Rate = 100 cm³/min)

Current Density (mA/cm ²)	Potential (V)	Power Density (W/cm ²)
0.	0.75	0.000
4.5	0.69	0.003
13.6	0.64	0.009
31.8	0.59	0.019
61.2	0.54	0.033
99.8	0.49	0.049
151.9	0.44	0.067
215.4	0.40	0.086
288.0	0.34	0.098
367.4	0.29	0.107
455.8	0.25	0.114
544.2	0.20	0.109

Table D.11: Experimental H₂/O₂ PEM fuel cell test data for the polarization curve (Anode catalyst: 20% Pt/C (E TEK[®]), Cathode catalyst: Pt(15)Pd(5)/HCMS2 (E TEK[®]), T=70 °C, P=1 atm, RH_a=100%, RH_c=100%, H₂ Flow Rate = 100 cm³/min, O₂ Flow Rate = 100 cm³/min)

Current Density (mA/cm ²)	Potential (V)	Power Density (W/cm ²)
0.	0.95	0.000
2.0	0.92	0.001
7.7	0.89	0.002
26.1	0.85	0.003
48.3	0.82	0.007
75.3	0.79	0.012
106.6	0.76	0.020
141.0	0.73	0.029
188.7	0.69	0.040
251.0	0.65	0.052
275.1	0.63	0.063
310.9	0.60	0.076
345.8	0.57	0.087
379.6	0.54	0.105
401.4	0.52	0.117
422.7	0.50	0.133
444.0	0.48	0.145
464.6	0.46	0.152
495.2	0.43	0.172
526.3	0.40	0.180
557.1	0.37	0.184
587.1	0.34	0.192
607.7	0.32	0.175
627.7	0.30	0.136

Table D.12: Experimental H₂/O₂ PEM fuel cell test data for the polarization curve (Anode catalyst: 20% Pt/C (E-TEK[®]), Cathode catalyst: Pt(10)Pd(10)/HCMS2 (E-TEK[®]), T=70 °C, P=1 atm, RH_a=100%, RH_c=100%, H₂ Flow Rate = 100 cm³/min, O₂ Flow Rate = 100 cm³/min)

Current Density (mA/cm ²)	Potential (V)	Power Density (W/cm ²)
0.0	0.92	0.000
6.4	0.86	0.005
8.6	0.84	0.007
17.5	0.82	0.014
25.6	0.79	0.020
42.2	0.77	0.032
53.1	0.74	0.039
66.0	0.72	0.048
86.6	0.69	0.060
124.7	0.64	0.080
140.4	0.62	0.087
164.2	0.60	0.099
207.0	0.54	0.112
252.2	0.49	0.124
280.1	0.46	0.129
309.1	0.43	0.133
349.2	0.40	0.140
400.0	0.35	0.140
453.1	0.30	0.136
502.3	0.25	0.126
552.4	0.20	0.110
598.6	0.15	0.090
642.6	0.10	0.064
681.0	0.05	0.034
690.7	0.03	0.021

Table D.13: Experimental H₂/O₂ PEM fuel cell test data for the polarization curve (Anode catalyst: 20% Pt/C (E TEK[®]), Cathode catalyst: Pt(5)Pd(15)/HCMS2 (E TEK[®]), T=70 °C, P=1 atm, RH_a=100%, RH_c=100%, H₂ Flow Rate = 100 cm³/min, O₂ Flow Rate = 100 cm³/min)

Current Density (mA/cm ²)	Potential (V)	Power Density (W/cm ²)
0.0	0.91	0.000
0.5	0.88	0.0004
1.1	0.86	0.001
2.0	0.84	0.002
3.6	0.82	0.003
6.1	0.80	0.005
10.2	0.78	0.008
15.7	0.76	0.012
22.7	0.74	0.017
31.8	0.72	0.023
43.1	0.70	0.030
56.2	0.68	0.038
81.4	0.65	0.053
137.6	0.60	0.083
216.6	0.55	0.119
302.7	0.50	0.151
380.1	0.45	0.171
471.9	0.40	0.189
532.7	0.35	0.186
602.5	0.30	0.181

Table D.14: Experimental H₂/O₂ PEM fuel cell test data for the polarization curve (Anode catalyst: 20% Pt/C (E TEK[®]), Cathode catalyst: 20% Pd/HCMS2 (E TEK[®]), T=70 °C, P=1 atm, RH_a=100%, RH_c=100%, H₂ Flow Rate = 100 cm³/min, O₂ Flow Rate = 100 cm³/min)

Current Density (mA/cm ²)	Potential (V)	Power Density (W/cm ²)
0.0	0.88	0.000
1.6	0.84	0.001
5.0	0.81	0.004
9.5	0.79	0.008
18.4	0.76	0.014
29.9	0.73	0.022
48.8	0.69	0.034
58.7	0.67	0.039
69.4	0.65	0.045
80.5	0.63	0.051
98.2	0.60	0.059
117.0	0.57	0.067
136.3	0.54	0.074
149.7	0.52	0.078
169.6	0.49	0.083
182.5	0.48	0.088
203.0	0.44	0.089
216.1	0.43	0.093
236.5	0.40	0.095
256.2	0.37	0.095
275.3	0.34	0.094
288.2	0.32	0.092
301.8	0.30	0.091
321.8	0.27	0.087
335.8	0.25	0.084
359.4	0.22	0.079

APPENDIX E

NONLINEAR FIT FOR A LUMPED PEM FUEL CELL MODEL

In order to minimize the function given in equation (3.6), Levenberg–Marquardt Algorithm (LMA) can be used effectively. LMA algorithm provides a numerical solution set for the model parameters appearing in the nonlinear zero dimensional lumped PEM fuel cell model. The main idea is to find optimal model parameters that best match with least square curve fitting. The details of the algorithm were outlined in the literature [173, 174].

LMA algorithm is an iterative procedure with the target of minimizing the function of interest. To find convergent solution set for the nonlinear model, it is very critical to supply initial guesses for the model parameters in the vicinity of the roots; otherwise, one may not get a numerical solution.

Figure E.1 and Figure E.2 show zero dimensional model fits for the experimental data performed with 20% Pt/HCMS1 and 20% Pt/BP2000 cathode electrocatalyst respectively. Anode electrocatalyst was the commercial 20% Pt/C (ETEK[®]) electrocatalyst. Model parameters for these two cases were given in Table 8.1.

For a reasonable lumped model fit, it is essential to provide large set of experimental data to the numerical procedure. When the data points are not sufficient, the model results will not be reliable. Gnuplot software can directly be used to compute model parameters with LMA.

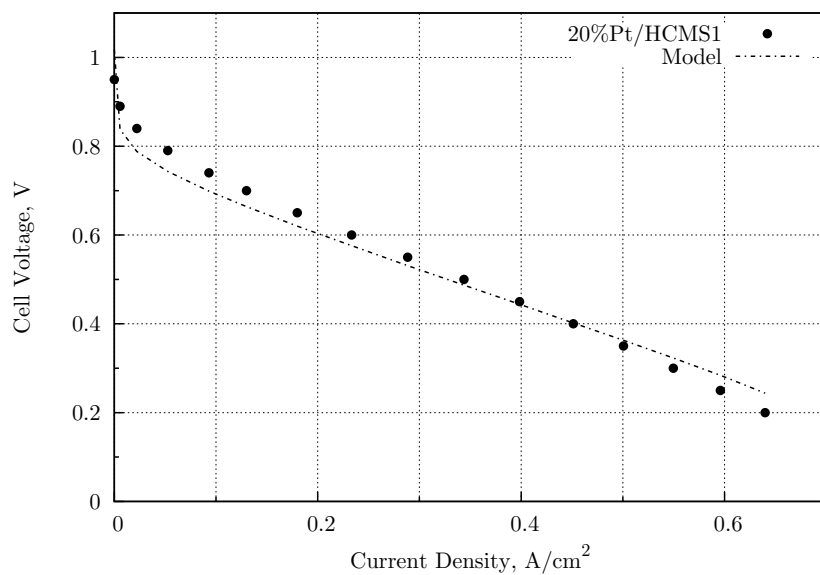


Figure E.1: Zero dimensional model validation for PEMFC with 20% Pt/HCMS1 cathode electrocatalyst ($T=70\text{ }^{\circ}\text{C}$, $P_a=1\text{ atm}$, $P_c=1\text{ atm}$, Anode RH= 100 %, Cathode RH= 100 %)

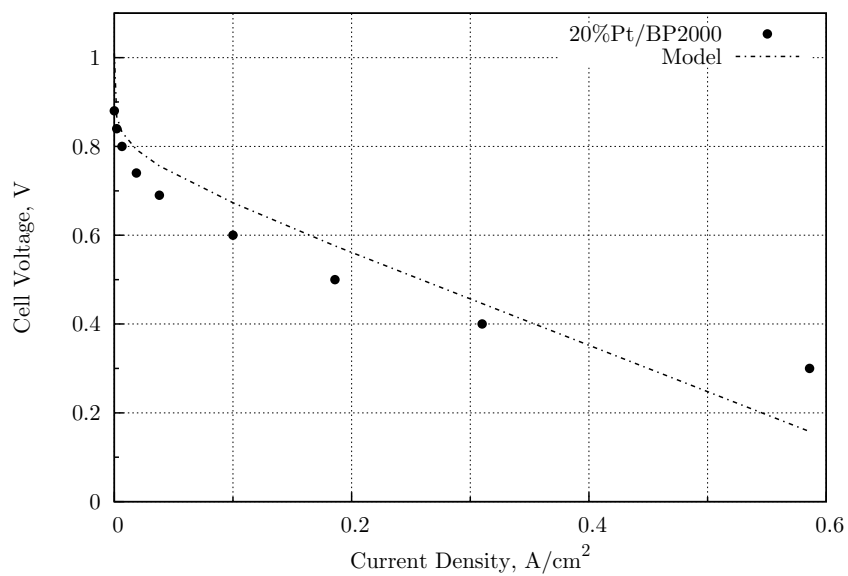


Figure E.2: Zero dimensional model validation for PEMFC with 20% Pt/BP2000 cathode electrocatalyst ($T=70\text{ }^{\circ}\text{C}$, $P_a=1\text{ atm}$, $P_c=1\text{ atm}$, Anode RH= 100 %, Cathode RH= 100 %)

APPENDIX F

FCSIMULATOR PROGRAM

F.1 FCSIMULATOR Program

FCSIMULATOR is a PEM fuel cell simulation program written in FORTRAN 90 code architecture. FORTRAN 90 code is written in "implicit none" form. Therefore, program can run easily in single precision or double precision mode. Main.f90 file is the main program file compiled with gfortran (Version: 4:4.3.2-2, GNU FORTRAN 95 Compiler). Gfortran compiles FORTRAN 90 on platforms supported by the gcc4.3.2-1.1 (GNU compiler collection or GNU C compiler) compiler. It uses the gcc back end to generate optimized code.

FCSIMULATOR program is only tested with the gfortran compiler. There may be some incompatibility in other compilers. FORTRAN code automatically produce the data and plot the data from the routines by making calls to Gnuplot program. In order to make use of plotting routines, a Linux based operating system is necessary. If calls to plot functions and other system calls are omitted, program can run with Windows based operating systems. The program can be compiled by writing the following line in terminal of a Linux based operating system. Here, "target" is the executable file generated from the compiler.

```
$ gfortran -o target global.f90 inputparameter.f90 utility.f90  
    geometry.f90 functions.f90 solver.f90  
    preprocess.f90 dim1.f90 main.f90
```

Typing the following command in the terminal will execute the code:

```
$ ./target
```

Several output files and plots are generated at the end of the code execution related to the variable profiles as well as current–voltage data are written to a file in the scan range.

F.2 FCSIMULATOR Code Architecture

F.2.1 File Information

There is a main program and several modules. In general, subroutines and functions are contained in modules unless otherwise stated. Several tasks are performed by subroutine calls in the modules from different modules. The followings are the file list of the code with some basic explanation.

```
MAIN PROGRAM      : main.f90
```

```
MODULES   : global.f90
```

```
    All global variables are declared and some assignments if necessary
```

```
        : inputparameter.f90
```

```
    Parameter assignments are supplied in this module
```

```
        : utility.f90
```

```
    Plotting routines, system date return, file name generation
```

```
        : geometry.f90
```

```
    Computational grid is generated, grid resolution is adjustable
```

```
        : functions.f90
```

```
    All modeling equations are stored in this module
```

```

: solver.f90
Numerical solvers are stored in the solver module

: preprocess.f90
A module for printing some initial parameters

: dim1.f90
General mathematical model module for PEMFC

```

F.2.2 Program Input Parameter Module

There are various input modules for the program source code. Below is a typical input file for a three layer cathode model simulation for a PEM fuel cell operating isothermally under steady state conditions. There are several modules written for different modes of operation. Interested reader may reach all source files upon request (berker@ficicilar.com).

```

module input_parameter

use global_var
implicit none

!=====
! MODEL INPUT PARAMETERS
!=====
! Cathode inlet gas temperature, [K]
real(pn), parameter :: tcg_in = 343.15_pn, &
! Initial solid phase temperature, [K]
ts_in      = 343.15_pn, &
! Cathode inlet pressure, [atm]
pc_in      = 1._pn, &
! Total gas concentration, [mol/cm^3]

```

```

ct          = pc_in / (r_gas * tcg_in),          &
! Relative Humidity at cathode
rh_c        = 1._pn,                            &
! Water saturation pressure @ Tcg_in, [atm]
psat_in     = exp(-5.0937_pn + 7.1081e-2_pn     &
* (tcg_in - 273.15_pn)                          &
- 2.5155e-4_pn * (tcg_in - 273.15_pn) **2.     &
+ 5.0125e-7_pn * (tcg_in - 273.15_pn) ** 3.), &
! Inlet H2O_g mole fraction
h2o_in      = rh_c * psat_in / pc_in,          &
! Oxygen mole fraction in dry air
o2_dry      = 0.21_pn,                          &
! Cathode inlet o2 mole fraction
o2_in       = o2_dry * (1.-h2o_in),            &
! Cathode inlet liquid phase saturation
s_in        = 0.001_pn,                         &
! Initial estimate for water inside Nafion, [mol/cm^3]
ch2om_in    = 14._pn*1.2e-3_pn,                &
! Initial estimate for ionic phase potential, [V]
phim_in     = -1.e-3_pn,                       &
! Reference cathode exchange current density at 273 K, [A/cm^2]
io_cref     = 1.e-6_pn,                        &
! C_O2_ref = P_O2 / H_O2_N, [mol/cm^3] P_o2 = 1atm @60oC
co2_ref     = 5.56e-6_pn,                      &
! OCV of the cell, [V]
uref        = 1.1_pn,                          &
! Starting applied solid phase potential, [V]
start_scan  = 1._pn,                           &
! End scan of applied potential [V]
end_scan    = 0.295_pn,                        &
! Ramp of the potential scan, [V]
ramp        = 0.001_pn
! Array for constant voltage for data storage

```

```

real(pn),    dimension(5)    :: const_volt = &
(/  0.80_pn,    &
    0.60_pn,    &
    0.50_pn,    &
    0.40_pn,    &
    0.30_pn     /)

!=====
! SAVE DATA
!=====

! Data collection frequency for variable profiles
integer(i4b), parameter :: collect_pf = 10

!=====
! CATHODE GAS DIFFUSION LAYER PROPERTIES
!=====

! Bulk porosity
real(pn), parameter :: e_cgdl = 0.3_pn, &
! Constant capillary gradient, [dyne /cm^2]
cp_cgdl    = 284.2_pn,                &
! Liquid water permeability at 100% sat, [cm^2]
p_cgdl     = 1.e-9_pn ,                &
! Solid phase thermal conductivity, [W /cm.K]
ks_cgdl    = 0.015_pn,                &
! Solid phase electronic conductivity, [S /cm]
cond_cgdl  = 12.5_pn,                 &
! Heat transfer coefficient at cathode GDL, [W/cm^2.K]
h_cgdl     = 25.e-4_pn,                &
! Bulk density of cathode gdl based on toray, [g/cm^3]
ro_cgdl    = 0.49_pn,                 &
! Surface area toray h60, [cm^2/g]
a_gdl      = 0.4_pn * 10000._pn,      &
! Heat transfer area [cm^2/cm^3]

```

```

area_cgdl = a_gdl * ro_cgdl * (1._pn - e_cgdl)

!=====
! CATHODE CATALYST LAYER PROPERTIES
!=====

real(pn), parameter ::      &
! Bulk porosity
e_ccl = 0.06_pn, &
! Constant capillary gradient, [dyne /cm^2]
cp_ccl      = 568.4_pn, &
! Liquid water permeability at 100% sat, [cm^2]
p_ccl      = 3.e-11_pn, &
! Ionomer fraction in the cathode catalyst layer
eps_cn     = 0.393_pn, &
! Radius of cathode catalyst agglomerate, [cm]
rp        = 1.e-5_pn, &
! Nafion film thickness over agglomerate, [cm]
d_n       = 1.e-6_pn, &
! Electroactive area for Pt, [cm^2 /mg]
apt       = 1000._pn, &
! Cathode Pt loading, [mg Pt / cm^2]
mpt       = 0.4_pn, &
! Cathodic charge transfer coef. for Tafel kinetics
alpha_c   = 0.5_pn, &
! Cathodic charge transfer coef. for B-V kinetics (anode)
alpha_ba  = 0.5, &
! Cathodic charge transfer coef. for B-V kinetics (cathode)
alpha_bc  = 0.5, &
! Agglomerate area
a_pt_agg  = apt * mpt /((1._pn - e_ccl) * 0.0016_pn), &
! Catalyst geometry factor
a_r       = 3._pn * (1._pn - e_ccl) / (rp +d_n), &

```

```

! Equilibrium constant for mechanistic approach
keq      = 1._pn,      &
! Equilibrium oxygen surface coverage
theta_o2 = 0.5_pn,    &
! Cathodic charge transfer coef. for L-B-V kinetics
alpha_lbv = 1._pn,    &
! Solid phase thermal conductivity, [W /cm.K]
ks_ccl    = 0.003_pn, &
! Solid phase electronic conductivity, [S /cm]
cond_ccl  = 100._pn,  &
! Heat transfer coefficient at cathode GDL, W/cm^2.K
h_ccl     = 25.e-4_pn, &
! Surface area, [cm^2/g]
a_ccl     = 100._pn * 10000._pn, &
! Bulk density of Vulcan XC72, [g/cm^3]
ro_cb     = 0.264_pn, &
! Heat transfer area [cm^2/cm^3]
area_ccl  = a_ccl * ro_cb * (1._pn - e_ccl)

!=====
! SOLID POLYMER ELECTROLYTE PROPERTIES (NAFION 112)
!=====

real(pn), parameter :: &
! Fixed site charge concentration, [mol/cm^3]
cf      = 1.2e-3_pn, &
! Effective thermal conductivity, [W /cm.K]
km_eff = 0.0025_pn

!=====
! OTHER PARAMETERS
!=====

```

```

real(pn), parameter ::      &
! Bruggemann correction factor
bf          = 1.5_pn,      &
! Condensation rate
rate_cn     = 100._pn,    &
! Evaporation rate
rate_en     = 100._pn,    &
! Factor in D_H2O_m correlation
beta        = 2.2_pn,     &
! Heat of vaporization @ 60 oC, [J/mol]
delta_h2o   = 42479.4_pn, &
! Cp of liquid water at 60 oC, [J / g.K]
cp_w        = 4.185_pn

end module input_parameter

```

VITA

Berker Fıçıcılar was born on August 29, 1977 in Mustafakemalpaşa, Bursa. After graduating from Arı College and Yüce Fen High School in Ankara, his career as a professional student began in 1995 at the Middle East Technical University (METU). He graduated from METU with a Bachelors of Science degree in Chemical Engineering in 2001. In the same year, he started graduate studies [176] under the supervision of Professors Timur Doğu & Gülşen Doğu and received a Master of Science degree from the Chemical Engineering Department of METU in 2004.

Since 2005, the author has been studying with his supervisor Professor İnci Eroğlu for his Ph.D. degree in Chemical Engineering of METU. In 2010, as part of Ph.D. study, he took a leave to conduct research at the University of Kansas for about nine months. He worked in Electrochemical Engineering Laboratory on "*PEM Fuel Cell Modeling and Simulation*" under the supervision of Professor Trung Van Nguyen at the University of Kansas. His current research interests are modeling and simulation of electrochemical systems, support and catalyst design for PEMFCs, and PEMFC diagnostics. Some selected publications out of this dissertation are listed below:

1. B. Fıçıcılar, İ. Eroğlu, and T.V. Nguyen. A Five Layer One-Dimensional PEMFC Model with Detailed Electrode Kinetics. *ECS Transactions*, 33(1):1515–1527, 2010
2. B. Fıçıcılar, A. Bayrakçeken, and İ. Eroğlu. Pt incorporated hollow core mesoporous shell carbon nanocomposite catalyst for proton exchange membrane fuel cells. *International Journal of Hydrogen Energy*, 35(18):9924–9933, 2010
3. B. Fıçıcılar, A. Bayrakçeken, and İ. Eroğlu. Effect of Pd loading in Pd-Pt bimetallic catalysts doped into hollow core mesoporous shell carbon on performance of proton exchange membrane fuel cells. *Journal of Power Sources*, 193(1):17–23, 2009